Phénomènes de cohérence quantique macroscopique dans les jonctions Josephson bosoniques

Giulia Ferrini

Thèse

présentée par

Giulia FERRINI

pour obtenir le grade de

Docteur de l'Université de Grenoble – Grenoble I

Spécialité : **Physique**

MACROSCOPIC QUANTUM COHERENT PHENOMENA IN BOSE JOSEPHSON JUNCTIONS

Thèse préparée au

Laboratoire de Physique et de Modélisation des Milieux Condensés

sous la direction de

Frank W. J. HEKKING et Anna MINGUZZI

Soutenue publiquement le

20 Octobre 2011

Composition du jury :

M^{me}	Wiebke GUICHARD	Institut Néel, Grenoble (France)	Président du jury
M^{r}	Augusto SMERZI	BEC Center, Trento (Italie)	Rapporteur
M^{r}	Nicolas PAVLOFF	LPTMS, Orsay (France)	Rapporteur
M^{r}	Claude FABRE	LKB, Paris (France)	Examinateur
M^{r}	Frank W. J. HEKKING	LPMMC, Grenoble (France)	Directeur de thèse
M^{me}	Anna MINGUZZI	LPMMC, Grenoble (France)	Co-directrice de thèse

"Tanzt, tanzt, sonst sind wir verloren."
Pina Bausch

Introduction

It has been realized in the last decade that confined ultracold atomic gases offer the possibility to manipulate coherently entangled many-body quantum states. In particular, a major advantage provided by these type of systems is the high degree of control of the relevant experimental parameters, due to the ability of tailoring traps of various geometry [1, 2] and of tuning the interatomic interactions [3]. This has a large interest for applications in quantum information and quantum technology. Recent advances have concerned applications to quantum simulators [4] and high-sensitivity atom interferometry, which can be used for enhancing the precision in atomic clocks and in magnetic field sensors [5–9].

In the latter field, very promising results have been recently demonstrated with the use of a Bose Josephson junction (BJJ) [5–9]. Such a system is formed by two modes of a Bose-Einstein condensate, which may correspond either to two internal states of the condensed atoms in a single potential well or to two spatially separated wave functions in a double well. In an atom interferometer, the two modes of the condensate are left evolving under the interaction with the physical quantity to be measured, which causes a relative phase shift φ on the two modes. From measurements on the output state, e.g. of the relative population of the two modes, the phase shift can be estimated. The Schwinger representation [10] connects the creation and annihilation operators $\hat{a}_i$ and $\hat{a}_i^\dagger$ (for $i = 1, 2$) of the bosons in the two modes to the three components of a collective angular momentum operator $\hat{J} = (\hat{J}_x, \hat{J}_z, \hat{J}_z)$, in terms of which the operations composing the interferometric sequence can be described.

It has been proposed [11, 12] and experimentally demonstrated [7–9, 13] that Bose Josephson junctions allow for the creation of atomic squeezed states, in which the quantum fluctuations of the collective angular momentum operator in a certain direction are reduced to the expense of the fluctuations in another direction. Such non classical states can be used in an interferometric protocol to improve the phase sensitivity $\Delta\varphi$ reducing it below the shot-noise limit $\Delta\varphi \propto 1/\sqrt{N}$ - the limit that one obtains using classical states, N being the number of bosons [14, 15]. This prediction has been recently experimentally demonstrated in a Bose Josephson junction by C. Gross *et al* [8].

A further enhancement of the precision in atom-interferometry has been predicted to be reached by the use of macroscopic superpositions of atomic coherent states [15, 16]. These are highly entangled states, in which a macroscopic number of particles is found in a coherent superposition of different possible states - the "components" of the superposition. These states are often familiarly referred to as "Schrödinger's cat states", and in particular two-component superpositions are also known from other quantum information

contexts as GHZ states [17–20]. Incidentally, macroscopic superpositions are predicted to be a fundamental resource in quantum communication and quantum computation [21], and their experimental realization would also serve as a fundamental test for quantum mechanics at the macroscopic scale. In quantum interferometry, the phase uncertainty which could be reached with the use of these states scales like $1/N$, and corresponds to the "Heisenberg limit" - the highest possible phase sensitivity which can be reached with linear interferometry [15, 16].

The experimental realization of these states is however challenging, because of their fragility with respect to decoherence effects induced by particle losses [22, 23], phase noise - due to stochastic fluctuations of the energies of the two modes [24, 25], collisions with thermal atoms [26, 27], interaction with the electromagnetic field [28, 29], and random fluctuations of the trapping potentials [30]. The two former phenomena, in particular, are the main noise sources in the experiments of Ref. [8, 9, 13].

In this thesis, we study protocols for the creation, detection and exploitation in atom interferometry of atomic squeezed states and macroscopic superposition in Bose Josephson junctions, in the presence of phase noise and particle losses.

After introducing in Chap.1 the system under study - the Bose Josephson junction - and its main features, we address in Chap.2 how squeezed states and macroscopic superpositions can be created in a BJJ by means of dynamical and adiabatic methods, in the absence of external noise sources. We especially focus on dynamical protocols. We first demonstrate the formation of macroscopic superpositions during the dynamics of the BJJ which follows a quench of the coupling between the two modes; then, we address an optimal control protocol, with the goal of lowering the time of formation of the superposition states. In Chap.3 we study how macroscopic superpositions can be detected by means of repeated measurements of the collective angular momentum operator in various directions, which is an observable accessible in the experiments. In Chap.4 we address the applications to quantum metrology, studying the degree of *usefulness* for sub-shot noise interferometry of the quantum state produced during the quenched dynamics of the BJJ. Finally, in Chap.5 we address the effect of phase noise and particle losses on the above-mentioned protocols. We analyze how the presence of noise affects the formation of squeezed states and macroscopic superpositions, studying in detail the decoherence processes to which the latter states undergo.

The results presented in this thesis have been the subject of four scientific publications in Physical Review A [24, 25, 31, 32], and of one preprint recently submitted for publication [33].

Les gaz d'atomes ultrafroids offrent la possibilité de manipuler de façon cohérente des états intriqués à beaucoup de particules. En particulier, un avantage relevant de ce type de systèmes est l'énorme capacité à contrôler les paramètres expérimentaux, tels que la forme du piège [1, 2] ou la force des intéractions inter-atomiques [3]. Cela a un grand interêt pour les applications en information quantique. Des progrès récents ont concerné les simulateurs quantiques [4] et l'interférométrie atomique à grande sensibilité, qui peut être utilisée pour augmenter la précision des horloges atomiques et des capteurs magnétiques [5–9].

Dans ce dernier champ d'application, des résultats expérimentaux très promet-

teurs ont été achevés à l'aide d'une jonction Josephson bosonique (BJJ) [5–9]. Ce système est formé par deux modes d'un condensat de Bose-Einstein, qui peuvent correspondre soit à deux états internes distincts des atomes condensés, soit aux deux fonctions d'ondes d'atomes séparés spatialement, dans un double puits de potentiel. En interférométrie atomique les deux modes du condensat évoluent sous l'effet de l'interaction avec la quantité physique à mesurer; cela cause un déphasage relatif φ des deux modes. à partir de mesures sur l'état de sortie, par exemple de la différence de population entre les deux modes, le déphasage peut être estimé. La représentation de Schwinger [10] relie les opérateurs de création et annihilation $\hat{a}_i$ et $\hat{a}_i^\dagger$ (avec $i = 1, 2$) des bosons dans les deux modes aux trois composantes d'un opérateur de moment angulaire collectif $\hat{J} = (\hat{J}_x, \hat{J}_z, \hat{J}_z)$, en termes du quel les opérations qui composent la séquence interférométrique peuvent être décrites.

Il a été proposé [11, 12] et expérimentalement démontré [7–9, 13] que les jonctions Josephson bosoniques permettent de créer des états atomiques comprimés, c'est-à-dire des états dans lesquels les fluctuations quantiques du moment angulaire collectif selon une certaine diréction sont réduites, au détriment des fluctuations dans la direction perpendiculaire. Ces états non-classiques peuvent être utilisés dans une séquence interférométrique pour améliorer la sensibilité de phase $\Delta\varphi$ en la réduisant au dessous de la limite quantique standard $\Delta\varphi \propto 1/\sqrt{N}$, c'est-à-dire la limite qu'on obtient en utilisant des états classiques, N étant le nombre de bosons [14, 15]. Cette prédiction a été récemment démontrée expérimentalement avec une jonction Josephson bosonique par C. Gross et al [8].

Il a été prédit qu'il est possible d'obtenir une augmentation supplémentaire de la précision à l'aide de superpositions macroscopiques d' états cohérents [15, 16]. Celles-ci sont des états hautement intriqués, dans lesquels les atomes se trouvent dans une superposition d'états macroscopiquement différents, les composantes de la superposition. Ces états sont familièrement appelés "chats de Schrödinger", et en particulier des superpositions à deux composantes sont aussi connus dans d'autres contextes en information quantique comme états GHZ [17–20]. Par ailleurs, il est prédit que les superpositions macroscopiques sont une ressource fondamentale pour les communications quantiques et pour le calcul quantique [21], et leur réalisation expérimentale serait aussi une épreuve pour la mécanique quantique à échelle macroscopique. En intérférométrie atomique, la sensibilité de phase qui pourrait être achevée à l'aide de ces états suit la lois d'échelle $1/N$, ce qui correspond à la "limite d'Heisenberg", c'est-à-dire la meilleure sensibilité qui peut être atteinte par interférométrie linéaire [15, 16].

La réalisation expérimentale de ces états est néanmoins difficile, à cause de leur fragilité face aux effets de décohérence induits par des pertes de particules [22, 23], par le bruit de phase (dû aux fluctuations stochastiques des énergies des deux modes) [24, 25], par des collisions avec des atomes thermiques [26, 27], des interactions avec les champs électromagnétiques [28, 29], ou des fluctuations des potentiels réalisant le piège [30]. En particulier, les deux premiers phénomènes sont les sources principales de bruit dans les expériences de Refs. [8, 9, 13].

Dans cette thèse nous étudions des protocoles pour la création, la détection et pour l'exploitation en interférométrie atomique d'états comprimés d'une part et des superpositions macroscopiques d'autre part, dans les jonctions Josephson bosoniques, en présence de bruit de phase et pertes des particules.

*Après avoir introduit dans le premier chapitre le système étudié, la jonction Josephson bosonique, et ses caractéristiques principales, nous étudions dans le chapitre 2 comment des états comprimés et des superpositions macroscopiques peuvent être créés dans une BJJ par des méthodes dynamiques et adiabatiques, en absence de bruits extérieurs. Nous nous focalisons particulièrement sur les protocoles dynamiques. Nous commençons par démontrer que des superpositions macroscopiques peuvent être créées pendant la dynamique qui suit un arrêt soudain du couplage (une "trempe") entre les deux modes; par la suite, nous étudions un protocole de contrôle optimal, dans le but de réduire le temps de formation des superpositions. Dans le chapitre 3 nous étudions comment les superpositions macroscopiques peuvent être détectées à l'aide de mesures répétées du moment angulaire collectif selon différentes directions, qui est une observable accessible dans les expériences. Dans le chapitre 4 nous abordons les applications à la métrologie quantique, en étudiant le degré d'*utilité *pour l'interférométrie en dessous de la limite quantique standard de l'état quantique produit pendant la dynamique de la BJJ. Enfin, dans le chapitre 5 nous abordons l'effet du bruit de phase et de la perte de particules sur les protocoles mentionnés plus haut. Nous analysons comment la présence de bruit affecte la formation des états comprimés et des superpositions macroscopiques, en étudiant en détail le processus de décohérence auxquels ces derniers sont subjets.*

Les résultats présentés dans cette thèse ont fait l'objet de quatre publications scientifiques dans Physical Review A [24, 25, 31, 32], et d'une pré-publication [33] récemment soumise.

Contents

Chapter 1

The Bose Josephson Junction

In this chapter we present the system studied in this thesis: a Bose Josephson Junction (BJJ). This system, made out of bosons which can occupy two modes, is realized by coupling two trapped Bose-Einstein condensates, allowing for an exchange of particles between them. As we will briefly recall in the following, the name "Josephson" comes from the analogous superconducting system, in which Cooper pairs tunnel through two weakly coupled superconducting electrodes [34].

After a general introduction on quantum gases, we review the possible experimental realizations of a BJJ. Then, we detail its theoretical description within the two-mode approximation, presenting the ground state properties of this model. Among them, we especially discuss the fluctuations of the number operator describing the population imbalance between the two-modes and the momentum distribution; these results have been published in Ref. [31]. Finally, we introduce the semi-classical approximation for the BJJ.

Dans ce chapitre, nous présentons le système étudié: la jonction Josephson bosonique (BJJ). Ce système, composé par des bosons qui peuvent occuper deux modes, est réalisé en couplant deux condensats de Bose-Einstein piégés, permettant un échange de particules entre eux. Comme on le rappellera brièvement dans la suite, le nom "Josephson" est donne par analogie au système supraconducteur, dans lequel des paires de Cooper peuvent passer par effet tunnel entre deux électrodes supraconductrices faiblement couplées [34]. Aprés une introduction générale sur les gaz quantiques, nous rappelons les possibles réalisations expérimentales d'une BJJ. Ensuite, nous détaillons sa description théorique dans le cadre de l'approximation à deux modes, en présentant les propriétés de l'état fondamental de ce modèle. Parmi celles-ci, nous discutons en particulier les fluctuations de l'opérateur nombre qui décrit le déséquilibre de population atomique entre les deux modes de la jonction; ces résultats ont été publiés en Ref. [31]. Enfin, nous introduisons l'approximation semiclassique pour la BJJ.

1.1 Quantum gases: an overview

Quantum gases are ultracold metastable vapors of alkali atoms in the quantum degenerate regime. For such vapors the atomic density n and the thermal De Broglie length $\lambda_{dB} = \sqrt{\frac{\hbar^2}{mK_BT}}$ satisfy the relation $n\lambda^3 \gtrsim 1$. In this regime, since the thermal wavelength is comparable to the inverse inter-particle density, Boltzmann statistics does not apply and quantum mechanics is required for a proper description of the system. We use the term "metastable" in the sense that thermodynamic equilibrium, under these conditions of temperatures and pressure, corresponds to the solid phase for alkali atoms; to keep the gaseous state, atoms need to be kept at very low density (which prevents three-body collisions to happen), and far from any material wall, which would favor the formation of molecules.

In a non-interacting Bose gas, as an effect of its quantum statistics, at low temperatures all the particles "condense" in the lowest energy state. This can be understood as follows [35]. The average occupation of the single particle levels ϵ_i in an ideal gas of bosons follows the distribution $\overline{n}_i(\mu, T) = 1/(e^{\beta(\mu-\epsilon_i)})$, in the grand-canonical ensemble. The chemical potential μ is bounded from below by ϵ_0 to prevent negative occupation numbers. When μ approaches ϵ_0, the occupation of the lowest energy level $N_0 \equiv \overline{n}_0$ diverges (see figure 1.1). The chemical potential is fixed by the normalization condition $N_T(\mu, T) \equiv \sum_{i\neq 0} \overline{n}_i(\mu, T) = N - N_0$. When the value of $N_T(\mu = \epsilon_0, T)$ is larger than N, then the normalization condition is satisfied for values of $\mu < \epsilon_0$, and the occupation of the ground state is negligible (see again figure 1.1). Since $N_T(\mu = \epsilon_0, T)$ is growing monotonously with T, this happens at high temperatures. When $N_T(\mu = \epsilon_0, T) < N$, in order to satisfy the normalization condition it is required that $\mu \sim \epsilon_0$, leading to a macroscopic occupation of the lowest level. The condition for such a "condensation" is hence given by $N_T(\mu = \epsilon_0, T_C) = N$, which defines the critical temperature [35].

Such a condensation in energy space, known as Bose-Einstein Condensation (BEC), has been theoretically predicted by Bose and Einstein in 1925[1] and experimentally achieved with a weakly-interacting gas for the first time in 1995 (seventy years later) for Rubidium [36] and Sodium [37], for which Eric Cornell, Carl Wiemann and Wolfgang Ketterle earned the 2001 Nobel Prize in Physics. In subsequent years, many other atomic species have been condensed (namely ^{7}Li, ^{40}Ca, ^{4}He, ^{39}K, ^{41}K, ^{133}Cs, ^{174}Yb, ^{52}Cr, ^{84}Sr, ^{86}Sr, ^{88}Sr, H).

A rough estimate of the critical temperature below which the atomic gas undergoes the BEC transition can be given via dimensional arguments: for a uniform gas of free particles in the degenerate regime, the relevant quantities are the particle mass m, the density n, and the Plank constant $h = 2\pi\hbar$. The only way to combine them to form an energy is $\frac{\hbar^2 n^{2/3}}{m}$, which has to be compared to the energy k_BT_C, so that the estimate for the critical temperature gives

$$T_C = c\,\frac{\hbar^2 n^{2/3}}{mk_B}, \tag{1.1}$$

where c is a dimensionless constant and its numerical value turns out to be approximately 3.3 for a Bose gas confined in a three dimensional box [35]. In experiments, however, the typical confinement is rather harmonic. Let us indicate with ω_0 the frequency of the harmonic potential. The density of the gas in the cloud can be estimated as $n \sim \frac{N}{R^3}$, where

[1] Bose's paper dealt with photons; Einstein extended Bose's treatment to massive bosons.

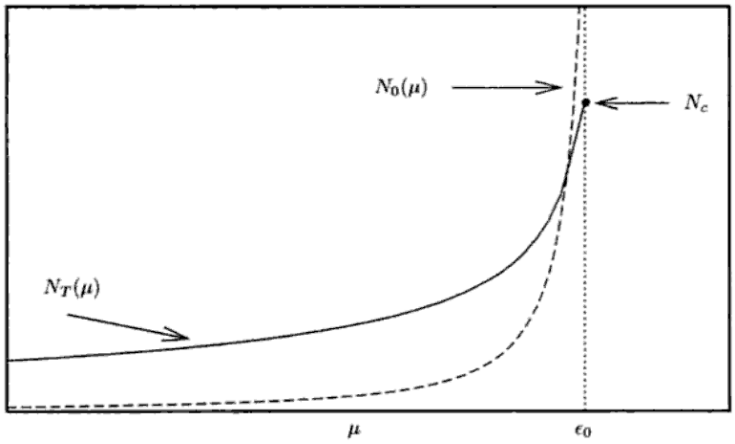

Figure 1.1: Number of particles out of the condensate N_T and number of particles in the condensate N_0 as a function of the chemical potential μ in the ideal gas model, from Ref. [35].

N is the number of particle and $R \sim \left(\frac{k_B T}{m\omega_0^2}\right)^{1/2}$ is the size of the atomic cloud; then the transition temperature is obtained substituting this expression for the density in Eq. (1.1)

$$k_B T_C = C_1 \hbar \omega_0 N^{1/3}, \tag{1.2}$$

where the constant C_1 is of the order of unity [2].

In practice, atomic gases are not ideal but often weakly interacting. The atomic interaction potential between atoms is the standard Van der Waals one, with a hard-core repulsive part at short distances, which results from the Coulomb repulsion of the two electronic clouds, and a weak attractive contribution at larger distances due to the dipole-dipole interactions. However, at very low temperatures, interactions are properly accounted by the s-wave scattering length a, as higher partial-wave contributions would require to overcome the centrifugal barrier and are hence negligible. Under the diluteness condition $na^3 \ll 1$ a partial condensation takes place in a level modified with respect to the non-interacting ground state [35], but depleted even at $T = 0$ by a fraction $\propto \sqrt{na^3}$. In what follows, we will always suppose that the diluteness condition is fulfilled.

Typical parameters necessary to observe BEC involve temperatures of $10 - 100\ nK$ and densities of the order of $10^{13} - 10^{14} cm^{-3}$ (quite low compared to the typical density of molecules in air at atmospheric pressure and room temperature, of about $10^{19}\ cm^{-3}$). Typically, these densities correspond to a number of atoms of $10^3 - 10^6$ confined in spaces of linear dimension of $10\ \mu m - 1\ mm$. The lifetime of an atomic condensed cloud is about 10 seconds; this enables one to measure both static and dynamical properties before loss mechanisms, which we will discuss in Sec. 5.2, eventually destroy the condensate.

1.1.1 Trapping quantum gases

In order to achieve the densities and temperatures required to observe the BEC, one has to cool and to trap atoms. In typical experiments, the starting point is a room temperature

[2] A more rigorous calculation of the critical temperature for atoms confined in a three dimensional harmonic potential can be found in [35] and provides $k_B T_C = C_1 \hbar (\omega_1 \omega_2 \omega_3)^{1/3} N^{1/3}$, where ω_i is the angular frequency corresponding to the i direction and $C_1 \simeq 0.94$.

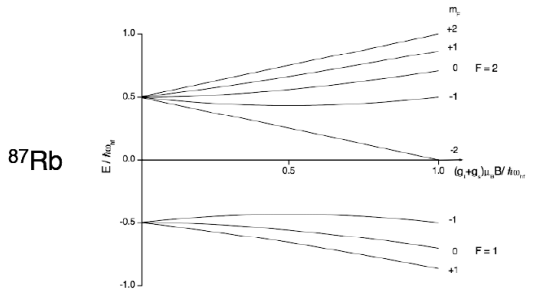

Figure 1.2: Splitting of the hyperfine levels of Rb as a function of the magnetic field.

atomic gas which is first pre-cooled to about 10 μK with a laser, then transferred into a magnetic trap, and finally cooled down to hundreds of nK via evaporative cooling. The way of combining the steps of cooling and trapping varies from experiment to experiment, but the physical principles exploited are generally based on the interaction of atoms with electric and magnetic fields. A review of these methods can be found, for example, in [38]. We briefly review here the main mechanisms underlying the trapping of alkali atoms, as this will allow us to introduce some notions which will be useful in the rest of the thesis.

1.1.1.a Hyperfine structure and magnetic traps

Magnetic trapping of neutral atoms relies on the use of the interactions of their spin properties with inhomogeneous magnetic fields. Alkali atoms have a simple electronic configuration, characterized by closed shells except for the outermost, occupied by a single electron. As the orbital momentum is zero in the ground state, the total electronic angular momentum J is equal to $1/2$; the nuclear spin I depends on the isotope. Hence, there are two possibilities for the resulting total angular momentum: $F = I \pm 1/2$. In the absence of an external magnetic field, the interaction between the nuclear spin and the outermost electron one (the hyperfine interaction, $H_{hf} = A\,\vec{I}\cdot\vec{J}$, where A is the relevant coupling constant) removes the degeneracy of the two configurations.

When an external magnetic field is applied (say in the $\hat{z}$ direction) the total Hamiltonian is

$$H = A\,\vec{I}\cdot\vec{J} + 2\,\mu_B\,J_z\,B(\vec{r}) \tag{1.3}$$

where μ_B is the Bohr magneton. Since $\vec{I}\cdot\vec{J} = 1/2\,(I^2 + J^2)$, the eigenstates of the hyperfine Hamiltonian are eigenstates of J^2, I^2, F^2 and F_z. Treating the magnetic field as a perturbation, to first order the corrections to the energy levels are

$$\langle F, m_F|2\mu_B J_z B|F, m_F\rangle = g_L\,\mu_B\,m_F\,B \;\equiv\; -\mu_F\,B \tag{1.4}$$

where g_L is the Landé factor and m_F is the eigenvalue of F_z. The resulting splitting of ^{87}Rb levels is depicted in figure 1.2. We obtain from Eq. (1.4) that the magnetic contribution to the energy provides a potential energy $-\mu_i B$, where $-\mu_i$ can be either positive or negative, depending on the unperturbed hyperfine state. When the magnetic field is inhomogeneous, if the magnetic moment is positive, the atom is driven to regions of higher field (these states are referred to as "high-field-seeker"), while if it is negative, it will move towards regions of lower field ("low-field-seeker" states). Since the modulus of a static magnetic field cannot have a maximum in vacuum, high-field seeker states can never be magnetically trapped - they can be optically trapped, though. Thus, the task of constructing a magnetic

trap relies on the design of magnetic field configurations with a local minimum, e.g. a quadrupole potential. Recently a versatile way of implementing magnetic trapping has been provided by atom chips [39]. These are miniaturized current conductors which allow for the generation of magnetic fields of almost arbitrary geometry. They can also combine with optical methods, allowing for the generation of special potentials such as lattices, potential barriers, and single- or double-well potentials. They have been recently used for matter-wave interferometry [40], or for the generation of atomic squeezed states [9, 41, 42].

1.1.1.b Optical traps

Another option for trapping atoms is the use of optical traps. These are based on the following principle. Since the wavelength of the laser radiation is much larger then the atomic size, the interaction of the atom with the laser field can be treated with high accuracy in the dipole approximation, and can be expressed as

$$V(\vec{r},t) = -\vec{D}\cdot\vec{E}(\vec{r},t), \tag{1.5}$$

where $\vec{D}$ is the electric dipole and $\vec{E}(\vec{r},t)$ is the time-dependent oscillating electric field. The interaction given above produces a polarization $\alpha(\omega)$ of the atom oscillating with the same frequency as the electric field. Because of the Stark effect, atomic levels undergo a shift which can be calculated with second order perturbation theory and which can be regarded as an effective potential

$$U(\vec{r}) = -\frac{1}{2}\alpha(\omega)\overline{E^2(\vec{r},t)}, \tag{1.6}$$

where the time average is taken because the frequency of the laser field is much higher than the inverse typical time of the atomic motion. If the intensity of the radiation field varies with the position, the interaction energy above gives rise to a force. The sign of the polarizability and hence of the energy shift depends on the frequency of the radiation, and turns out to be positive above the characteristic dipole resonance frequency and negative below, so that the atom will be attracted or repelled from the regions of higher field, depending on the frequency of the laser. Hence, by focusing a laser beam with frequency detuned in such a way that the energy of a ground state atom has a minimum in space, it is possible to trap the atoms.

The main advantage of optical traps is that the trapping is not limited to specific magnetic states (as it is in the case of magnetic traps). As we will detail in Sec.1.2, this has allowed to study spinor Bose-Einstein condensates, i.e. mixtures of atoms condensed in different hyperfine states. A second advantage is the following: the interaction strength can be tuned by applying a magnetic field through the so called "Feschbach resonances" [3, 38]; this has been largely exploited in the experimental realizations of bosonic condensates and also allowed to condense fermionic pairs, since interactions between fermions can be adjusted to form weakly bound molecules [43, 44]. This is achieved by applying a uniform magnetic field to atoms in an optical trap. Thus, this technique is impractical in magnetic traps, where the inhomogeneity of the field is necessary for trapping. Note however that tunable interatomic interactions have been recently achieved with atoms in a magnetic trap in the experiment of Ref. [9, 41], via manipulation of the spatial modes of the condensate (see discussion in Sec.1.3.1, in particular Eq.(1.20)).

1.1.2 Probing quantum gases

Quantum gases are most directly probed by accessing to their density profile. One way to measure the density is absorption imaging of an atomic cloud released from the trap and allowed to expand freely [45]. Light at a resonant frequency is shone across the cloud and is absorbed passing through it; thus, by measuring the absorption profile, one can obtain information about the density distribution. Note that this is a "two-dimensional column density profile", in the sense that the density is integrated over the direction of the light beam: if the light beam is directed along x, one can measure $n(y,z) = \int dx\, n(x,y,z)$. This method is destructive, since absorption of light changes the internal state of atoms and heats the cloud significantly. To study time-dependent phenomena, it is therefore necessary to prepare a new cloud for each time point ("shot").

If the expansion occurs in absence of interactions, the density profile after the expansion at times t much larger than the inverse of the oscillator frequencies related to the confinement, $\omega_i t \gg 1$, is proportional to the momentum distribution of the cloud before the expansion ("time of flight" imaging). A demonstration of this fact, as well as the discussion of the interacting case, are discussed for example in Ref. [35, 46]. This is often exploited to obtain the initial momentum distribution of the atomic cloud, with the further advantage that measurements performed after the expansion of the condensate provide a gain in spatial resolution.

An alternative technique is phase-contrast imaging. This exploits the fact that the refractive index of the gas depends on its density, and therefore, by allowing a laser beam which is passed through the gas to interfere with a reference one, one can gain information on the density profile of the gas by looking at the interference fringes produced. An advantage of this method is that it is almost non destructive, and it is therefore possible to study time-dependent phenomena using a single cloud.

1.2 The Bose Josephson junction: experimental realizations

The realization of the Josephson effect with cold atoms has been theoretically proposed by J. Javanaien in 1986 [47] (ten years before the BEC realization), who suggested that *"when two traps containing the condensates are brought close to each other, an oscillatory exchange of particles governed by the phase of the macroscopic wave functions of the two atomic gases should result."*. The analogy with the superconducting Josephson effect has been pursued in theoretical references [48–50], and in the experimental work of Ref. [51] (see also Sections 1.6.1.c and 1.6.2.c).

The first experimental realization of a Josephson junction with bosons confined in a double-well potential was obtained in 2005 by Albiez et al. [52]. In their experiment, the double-well potential was realized by superimposing a three-dimensional harmonic confinement and a one-dimensional optical lattice, thus optically trapping a thousand of ^{87}Rb atoms. This system undergoes the name of "external Bose Josephson Junction", since the two relevant modes correspond to the lowest-energy spatial modes in each well. Other experiments realizing an external BJJ via optical trapping are reported in Ref. [51], while a magnetic atom chip-based double-well potential has been realized in the experiment of Ref. [42].

Another possible experimental realization of a BJJ consists of trapping in a single harmonic potential a mixture of ^{87}Rb atoms in two distinct hyperfine states, which can be coupled by means of a resonant radiofrequency-microwave field. This realizes an "internal

BJJ". Such a system has been experimentally achieved for the first time at JILA [53], and has been later available also in Heidelberg [8] and in Munich [9, 41].

In both the external and the internal BJJs, the accessible observables are typically the number imbalance between the two modes, obtained by absorption imaging as described in Sec.1.1.2, and the "phase coherence" between the two modes, i.e. the relative phase between the wave functions of the atoms in the two modes. The latter property is typically probed by fitting a time-of-flight density profile with a cosine function (see Sec. 1.1.2, Eqs.(1.44) and (1.55) and Refs. [54, 55]). Note that in each realization of such an experiment the momentum distribution displays oscillations, which lead to the extraction of a specific value of the phase [54, 56, 57]. Roughly, this happens because in the thermodynamic limit the eigenstates of the momentum distribution have a well-defined phase [54], and hence a "phase" is built up in the measurement process even if the two condensates were initially independent; if this is the case, the phase obtained fluctuates from shot to shot. Hence, the determination of the existence of a well-defined relative phase between the two modes requires averaging over many realizations of the described experiment [3].

In the remainder of this thesis, when having in mind experimental aspects, we will focus more specifically on the Heidelberg experimental setups, described in Refs. [13, 52, 57] (external BJJ) and [8, 61, 62] (internal BJJ).

1.3 Theoretical description: modeling the BJJ

We now introduce the theoretical model suitable for describing the system presented in the previous section. Its description in the quantum regime requires in principle the use of the general many-body Hamiltonian, describing a system of interacting bosons in an external potential $V_{ext}(\vec{r})$. However, by means of the two-mode approximation on the field operator, its expression can be considerably simplified. We present here the derivation of the Hamiltonian in the two-mode approximation, following Refs. [35, 63].

1.3.1 The external BJJ

Let us first focus on an external Bose Josephson junction. We start from the general many-body Hamiltonian,

$$\begin{aligned} H &= \int d^3r \frac{\hbar^2}{2m} \nabla\hat{\Psi}^\dagger(\vec{r})\nabla\hat{\Psi}(\vec{r}) + \hat{\Psi}^\dagger(\vec{r})V_{ext}(\vec{r})\hat{\Psi}(\vec{r}) + \\ &+ \frac{1}{2}\int d^3r \int d^3r' \hat{\Psi}^\dagger(\vec{r})\hat{\Psi}^\dagger(\vec{r'})U(r-r')\hat{\Psi}(\vec{r})\hat{\Psi}(\vec{r'}) \end{aligned} \tag{1.7}$$

where $\hat{\Psi}(\vec{r})$, $\hat{\Psi}^\dagger(\vec{r})$ are bosonic field operators satisfying the standard commutation relation $\left[\hat{\Psi}(\vec{r}), \hat{\Psi}^\dagger(\vec{r'})\right] = \delta^3(\vec{r}-\vec{r'})$, and $U(r-r')$ is the interaction potential. We may consider for simplicity an external double-well potential V_{ext} resulting from the superposition of a three-dimensional harmonic confinement and a cosine potential, i.e.

$$V_{ext}(\vec{r}) = \frac{1}{2}m\omega_x^2x^2 + \frac{1}{2}m\omega_y^2y^2 + \frac{1}{2}m\omega_z^2z^2 + \frac{V_0}{2}\left(1+\cos\left(\frac{2\pi x}{d}\right)\right), \tag{1.8}$$

[3] Properly speaking, no hermitian operator is associated to the phase [58–60], and the notion of a "well-defined" phase is better formulated in terms of coherent state, as we shall define in Sec.1.4.3

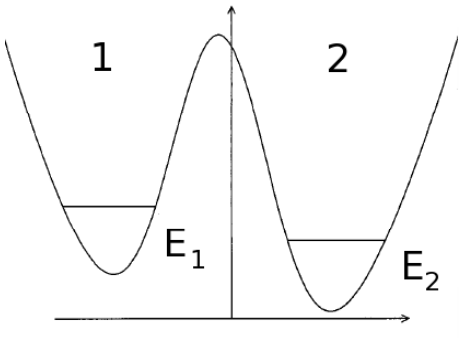

Figure 1.3: A schematic representation of the double well potential.

with d a parameter defining the spatial periodicity of the potential, typically amounting to a few micrometer. Such an external potential is sketched in Fig.1.3. At the bottom of each of the two central wells, the cosine potential can be expanded to the quadratic order, leading to an effective local harmonic potential with an effective frequency along the axes of the double well $\omega_{x_eff}^2 = \omega_x^2 + \frac{V_0 4\pi^2}{m d_{dw}^2}$. The single particle levels in such a double-well potential satisfy the Schrödinger equation

$$\left(-\frac{\hbar}{2m}\nabla^2 + V_{ext}(\vec{r})\right)\phi(\vec{r}) = E\phi(\vec{r}). \tag{1.9}$$

If the tunneling through the barrier is negligible, the solution is given by two degenerate levels $\phi_{1,2}(\vec{r}) = \phi_0(\vec{r} - \vec{r}_{1,2})$ (where $\vec{r}_{1,2}$ are the coordinates of the center of each well), each of them being the displacement of $\phi_0(\vec{r})$, corresponding to the ground state of a three-dimensional harmonic oscillator with frequencies $\omega_{x_eff}, \omega_y, \omega_z$. We will indicate the energy of these two levels with E_0. The inclusion of tunneling across the barrier lifts the degeneracy. Treating the tunneling K with degenerate perturbation theory, the energy eigenstates are given by the symmetric and antisymmetric combinations

$$\phi_\pm(\vec{r}) = \frac{1}{\sqrt{2}}\left(\phi_1(\vec{r}) \pm \phi_2(\vec{r})\right), \tag{1.10}$$

with corresponding eigenvalues $E_\pm = E_0 \mp K$.

Now let us come back the many-body problem. Due to the diluteness of the gas, the average distance between two particles is large with respect to the scattering length a, and the microscopic details of the interaction potential do not need to be specified anymore. We can therefore replace the true potential $U(r)$ by an effective one $U_{eff}(r)$ without affecting the analysis of the macroscopic properties of the gas, provided that the effective potential leads to the same scattering length. It is common to adopt as an effective potential the contact pseudo-potential

$$U_{eff}(\vec{r} - \vec{r'}) = g\delta(\vec{r} - \vec{r'}). \tag{1.11}$$

The parameter g is connected to the s-wave scattering length a in the Born approximation by

$$g = \frac{4\pi\hbar^2 a}{m}. \tag{1.12}$$

Using Eq. (1.11), the Hamiltonian of the system becomes

$$H(t) = \int d^3r [\frac{\hbar^2}{2m} \nabla\hat{\Psi}^\dagger(\vec{r})\nabla\hat{\Psi}(\vec{r}) + \hat{\Psi}^\dagger(\vec{r})V_{ext}(\vec{r})\hat{\Psi}(\vec{r}) + \frac{g}{2}\hat{\Psi}^\dagger(\vec{r})\hat{\Psi}^\dagger(\vec{r})\hat{\Psi}(\vec{r})\hat{\Psi}(\vec{r})]. \quad (1.13)$$

Now, in the two-mode approximation we describe the many-body state of the system by giving the occupation number of the two single particle states (1.10); this allows to write the field operator in the form

$$\hat{\Psi}(\vec{r}) = \hat{a}_+\phi_+(\vec{r}) + \hat{a}_-\phi_-(\vec{r}), \quad (1.14)$$

where we introduced the annihilation operators $\hat{a}_\pm(t) = \int d^3r\phi^*_\pm(\vec{r})\hat{\Psi}(\vec{r},t)$. By means of the simple transformation $\hat{a}_{1,2} = \frac{1}{\sqrt{2}}(\hat{a}_+ \pm \hat{a}_-)$ we are able to rewrite the field operator as

$$\hat{\Psi}(\vec{r}) = \hat{a}_1\phi_1(\vec{r}) + \hat{a}_2\phi_2(\vec{r}), \quad (1.15)$$

where $\hat{a}_{1,2}$ annihilate particles in wells $1, 2$. Substituting Eq.(1.15) in the Hamiltonian (1.13) and integrating over the spatial degrees of freedom we obtain

$$H_{ext} = E_1\hat{a}_1^\dagger\hat{a}_1 + E_2\hat{a}_2^\dagger\hat{a}_2 + \frac{U_1}{2}\hat{a}_1^\dagger\hat{a}_1^\dagger\hat{a}_1\hat{a}_1 + \frac{U_2}{2}\hat{a}_2^\dagger\hat{a}_2^\dagger\hat{a}_2\hat{a}_2 - K(\hat{a}_2^\dagger\hat{a}_1 + \hat{a}_1^\dagger\hat{a}_2) \quad (1.16)$$

where we have discarded the terms involving the overlap of the two modes. The parameters entering in Eq.(1.16) are given by

$$\begin{aligned} E_i &= \int d^3r \frac{\hbar^2}{2m}(\nabla\phi_i(\vec{r}))^2 + \phi_i^2(\vec{r})V_{ext} \\ U_i &= g\int d^3r\phi_i^4(\vec{r}) \\ K &= -\int d^3r \frac{\hbar^2}{2m}(\nabla\phi_1(\vec{r})\nabla\phi_2(\vec{r})) + \phi_1(\vec{r})\phi_2(\vec{r})V_{ext} \end{aligned} \quad (1.17)$$

Hamiltonian (1.16) is a two-sites Bose Hubbard Hamiltonian, and has been extensively used to study the properties of bosonic Josephson junctions (see for instance Ref. [63]).

1.3.1.a Validity of the two-mode approximation

As it was implicit in the previous discussion, two approximations are actually involved in the two-mode approximation [63]. The first is that the tunneling is weak (which allows to treat it pertubatively at the single particle level), so that the single particle energy spectrum is given by the first two levels well separated from the higher ones. The second one is that interactions are weak enough so that they do not affect considerably the single particle orbitals $\phi_{1,2}(\vec{r})$. Taking the case of isotropic wells $\omega_{x_{eff}} \approx \omega_y \approx \omega_z \equiv \omega_0$, this is a good approximation if both the tunneling energy and the interaction energy are much smaller with respect to the trap frequency ω_0, which characterizes the oscillations of the condensate within each trap, i.e.

$$\begin{aligned} K &\ll \hbar\omega_0 \\ NU_i &\ll \hbar\omega_0. \end{aligned} \quad (1.18)$$

For the temperature not to excite higher levels we have also to assume the requirement $k_B T \ll \hbar\omega_0$.

If the interactions are not so weak, an improvement over such an approximation is obtained by taking as orbitals $\phi_i(\vec{r})$ the time-independent solutions of the Gross-Pitaevski equation (see Sec.1.6) with $N/2$ atoms in each well, normalized to unity [48]. In a further improvement, time-dependent orbitals are considered, which provides the parameters K and χ with a dependence on the mode occupation, and leads them to vary during the dynamical evolution [23].

A comparison of the two-mode model with the full quantum dynamics derived from the Hamiltonian in Eq.(1.7) via a MCTDHB analysis (multiconfigurational time-dependent Hartree for bosons) has been carried out in Refs. [64, 65] for a one-dimensional Bose Josephson junction, with the result that the two-mode dynamics qualitatively reproduces the full quantum dynamics in a vast regime of the parameters.

1.3.2 Internal BJJ

For the internal case, the derivation of the two-mode model is analogous. The main difference with the external case is that the cross-interaction term, involving the overlap of the two different atomic-species orbitals $\phi_{1,2}(\vec{r})$, cannot be neglected in this case, since both of the two species are trapped in the the same harmonic potential. Furthermore, the scattering length of atoms in different hyperfine states can be in principle different for the two species, i.e. $a_{11} \neq a_{22}$ a priori (which is e.g. the case of the states $|F = 1, m_F = 1\rangle$ and $|F = 2, m_F = -1\rangle$ of ^{87}Rb, used in the experiment of Ref. [8]). On the other hand, this allows us to assume that the spatial mode of the two hyperfine states is the same, i.e. $\phi_1(\vec{r}) \simeq \phi_2(\vec{r}) \simeq \phi_0(r)$, the latter being the spatial mode of the harmonic potential. Furthermore, the K parameter represents here the coupling with microwave and radiofrequency fields, which can be tuned both in amplitude and phase. In the basis of the two hyperfine levels, the dipole operator in Eq.(1.5) reads $\vec{D} = \vec{d}(\hat{a_1}^\dagger \hat{a}_2 + \hat{a_2}^\dagger \hat{a}_1)$. By decomposing also the oscillating electrical field $\vec{E} = \vec{E^+} + \vec{E^-}$ with $\vec{E}^\pm = \vec{E}_0 e^{\pm i(\vec{k}\cdot\vec{r}-\omega t)}$, if the field is resonant for the hyperfine transition, in the rotating-wave approximation we are left with $V = -(K\hat{a_1}^\dagger \hat{a}_2 + K^* \hat{a_2}^\dagger \hat{a}_1)$, where we identified $K = -\vec{d}\cdot\vec{E^+}$ and $K^* = -\vec{d}\cdot\vec{E^-}$.

Hence, in this case the Hamiltonian is

$$H_{int} = E_1 \hat{a}_1^\dagger \hat{a}_1 + E_2 \hat{a}_2^\dagger \hat{a}_2 + \frac{U_1}{2}\hat{a}_1^\dagger \hat{a}_1^\dagger \hat{a}_1 \hat{a}_1 + \frac{U_2}{2}\hat{a}_2^\dagger \hat{a}_2^\dagger \hat{a}_2 \hat{a}_2 + U_{12}\hat{a}_1^\dagger \hat{a}_1 \hat{a}_2^\dagger \hat{a}_2 - K\hat{a}_1^\dagger \hat{a}_2 + K^* \hat{a}_2^\dagger \hat{a}_1 \tag{1.19}$$

with interaction parameters given by

$$\begin{aligned} U_i &= g_{ii} \int d^3 r \phi_i^4(\vec{r}) \approx g_{ii} \int d^3 r \phi_0^4(\vec{r}) \\ U_{12} &= g_{12} \int d^3 r \phi_1^2(\vec{r}) \phi_2^2(\vec{r}) \approx g_{12} \int d^3 r \phi_0^4(\vec{r}), \end{aligned} \tag{1.20}$$

where $g_{ij} = 4\pi\hbar^2 a_{ij}/m$.

1.4 Mapping onto a spin model

The two-mode Hamiltonians (1.16) and (1.19) derived in the previous section can be mapped on a spin Hamiltonian, by means of the Schwinger representation [10]. After

presenting this mapping, we introduce the state basis which are suitable to describe the system, and which we will extensively use throughout the present thesis.

1.4.1 Rewriting the Hamiltonian

In the Schwinger representation [10], a system of N two-mode bosons can be mapped on a system of N 1/2-spins. This mapping, suggested for the BJJ in Ref. [63], is based on the identification of the two modes of the BJJ, accessible to each of the N bosons, with two spin states, $\pm 1/2$. As a consequence, a collective angular momentum operator can be defined in terms of the creation and annihilation operators of the bosons in the each of the two modes. The ladder operators are defined as

$$\begin{aligned} \hat{J}_+ &= a_1^\dagger \hat{a}_2 \\ \hat{J}_- &= a_2^\dagger \hat{a}_1, \end{aligned} \tag{1.21}$$

leading to

$$\begin{aligned} \hat{J}_x &= \frac{\hat{J}_+ + \hat{J}_-}{2} \\ \hat{J}_y &= \frac{\hat{J}_+ - \hat{J}_-}{2i} \\ \hat{J}_z &= \frac{\hat{a}_1^\dagger \hat{a}_1 - \hat{a}_2^\dagger \hat{a}_2}{2}. \end{aligned} \tag{1.22}$$

In particular, the operators thus defined satisfy the usual commutation relations $\left[\hat{J}_i, \hat{J}_j\right] = i\epsilon_{ijk}\hat{J}_k$ where ϵ_{ijk} is the Levi-Civita symbol, as well as the Heisenberg uncertainty relation

$$\Delta J_i^2 \Delta J_j^2 \geq \frac{1}{4}\langle \hat{J}_k \rangle^2, \tag{1.23}$$

where $\Delta J_i^2 = \langle \hat{J}_i^2 \rangle - \langle \hat{J}_i \rangle^2$ is the variance of the operator $\hat{J}_i^2$. From Eq.(1.22) we can interpret the operator $\hat{J}_x$ as the tunneling operator, $\hat{J}_y$ as the current operator and $\hat{J}_z$ as the population imbalance between the two wells, i.e. the relative number operator; in the following we will often omit the adjective "relative", referring to $\hat{J}_z$ simply as to the "number operator".

By means of Eq.(1.22), both Hamiltonians in Eq.(1.16) and Eq.(1.19) can then be mapped on the spin-like Hamiltonian

$$\hat{H} = \chi \hat{J}_z^2 - \lambda \hat{J}_z - 2K\hat{J}_x \tag{1.24}$$

where we have discarded a constant factor depending on the total number of particles. For the external BJJ χ is the half of the sum of the interaction energies U_i in the two modes, whereas for the internal BJJ $\chi = (U_1 + U_2)/2 - U_{12}$, also depending on the inter-species interaction U_{12}. In both cases, λ is related to the difference $\Delta E = E_2 - E_1$ between the energies of the two modes and to the difference of the interactions by

$$\lambda = \Delta E + (N-1)(U_2 - U_1)/2. \tag{1.25}$$

We have considered here that the coupling in Eq.(1.19) is real and positive, in order to map both the Hamiltonians in the same expression (1.24). Note however that in

the internal BJJ case it is possible to exploit, if needed, the phase of the complex field $K = |K|e^{-i\gamma}$ to engineer a more general form of the coupling term, leading from Eq.(1.19) to $Ke^{-i\gamma}\hat{a}_1^\dagger\hat{a}_2 + K^*e^{i\gamma}\hat{a}_2^\dagger\hat{a}_1 = -|K|(\hat{J}_x\cos\phi - \hat{J}_y\sin\phi)$. We will use this property of the internal BJJ in Chap.2, to provide a protocol for the efficient generation of macroscopic superpositions. For the sake of completeness, we also mention that in the external BJJ setup engineering a negative coupling constant K is also possible, by applying a drive to the trapping potential [66, 67].

For $\lambda = 0$ the Hamiltonian (1.24) belongs to a class of models introduced in nuclear Physics by Lipkin, Meshkov and Glick [68], and also correspond of the continuous-kick limit of the kicked top model [69].

1.4.2 Fock states

Supposing that the total number of bosons $N = a_1^\dagger a_1 + a_2^\dagger a_2$ is constant[4], the dimension of the Hilbert space is $N+1$. A basis for the Hilbert space is provided by the Fock states $|n\rangle \equiv |n_1 = N/2+n, n_2 = N/2-n\rangle$ (also called "Dicke states"), which are the eigenstates of the number imbalance operator, i.e. they satisfy the equation

$$\hat{J}_z|n\rangle = n|n\rangle. \tag{1.26}$$

The variable

$$n = \frac{n_1 - n_2}{2} \tag{1.27}$$

represents hence the imbalance in the occupations of the two modes, and is bounded by $-N/2 \leq n \leq N/2$. For small imbalance $n \ll \pm N/2$, such states represent fragmented states of the condensate, i.e. states in which the two single-particle wave functions $\phi_1(\vec{r})$ and $\phi_2(\vec{r})$ are both macroscopically occupied. As the two wave functions are in this case spatially separated, the phase coherence over the spatial extent of the entire system is lost [70].

1.4.3 Atomic coherent states

Another useful set of states for such a model is given by $SU(2)$ coherent states (also referred to as "atomic coherent" states or "Bloch states"). In what follows we briefly review their possible equivalent definitions and their main properties, following Refs. [71, 72].

1.4.3.a Definition

SU(2) coherent states are defined in terms of the Fock states (1.26) as

$$|\theta,\phi\rangle = \sum_{n=-N/2}^{N/2} \binom{N}{\frac{N}{2}+n}^{\frac{1}{2}} \frac{\alpha^{n+\frac{N}{2}}}{(1+|\alpha|^2)^{\frac{N}{2}}}|n\rangle \equiv |\alpha\rangle \tag{1.28}$$

with $\alpha = e^{-i\phi}\tan\theta/2$, where the conventions for two angles are defined in figure 1.4. An equivalent expression for the same state is

$$|\theta,\phi\rangle = \frac{\left(\cos\frac{\theta}{2}\hat{a}_1^\dagger + \sin\frac{\theta}{2}e^{-i\phi}\hat{a}_2^\dagger\right)^N}{\sqrt{N!}}|0\rangle, \tag{1.29}$$

[4]This hypothesis will be released in Chapter 5, where we will treat particle losses.

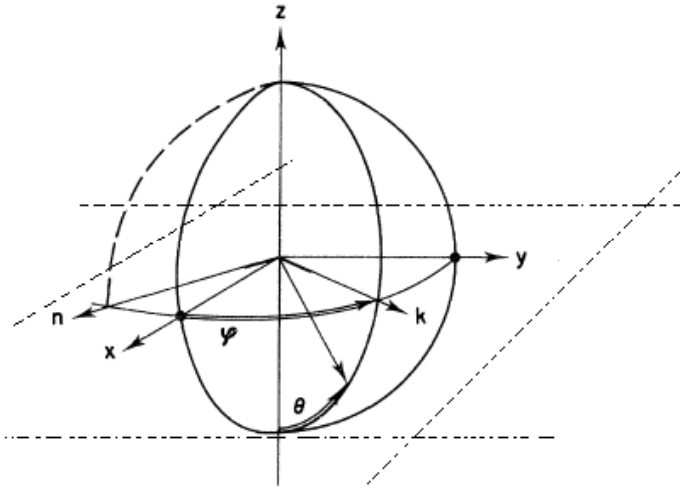

Figure 1.4: Bloch sphere and convention for the two angles θ and ϕ.

from which it is apparent that in a coherent state all of the atoms occupy the same one-particle state $\cos(\theta/2)\phi_1(\vec{r}) + \sin(\theta/2)e^{-i\phi}\phi_2(\vec{r})$. It is therefore a macroscopically occupied state, which realizes the closest classical analog, similarly as quantum optics coherent states.

1.4.3.b Visualization

A coherent state can be visualized as a circle on the Bloch sphere, whose center coordinates is given by the expectation values of the angular momentum operators, i.e.

$$\begin{aligned} \langle\theta,\phi|\hat{J}_x|\theta,\phi\rangle &= \frac{N}{2}\sin\theta\cos\phi \\ \langle\theta,\phi|\hat{J}_y|\theta,\phi\rangle &= \frac{N}{2}\sin\theta\sin\phi \\ \langle\theta,\phi|\hat{J}_z|\theta,\phi\rangle &= -\frac{N}{2}\cos\theta \equiv n. \end{aligned} \tag{1.30}$$

Since the quantum fluctuations (the variance) of the angular momentum operators in each direction in the plane tangential to the sphere in the point $\langle\theta,\phi|\vec{J}|\theta,\phi\rangle$ are given by $(\Delta J_i)^2 = N/2$, as an order of magnitude for the radius of the circle we can take $\sigma = \sqrt{N}$. Such fluctuations are isotropic and "minimal", in the sense that they satisfy Eq. (1.23) with the equal sign.

From the third line in Eq.(1.30) we see that the angle θ is related to the number imbalance variable n by a cosine function (see also Fig.1.4). For example the coherent state with $\theta = 0$, i.e. at the south pole of the Bloch sphere, corresponds to the maximally unbalanced Fock state $|n = -N/2\rangle$, while coherent states with $\theta = \pi/2$ lie on the equator and correspond to an average symmetric occupation of the two modes. The latter set of states will be referred to in what follows as *phase states*.

From Eq.(1.29) we see that the angle ϕ is the phase difference between the two-modes. This is better understood in the semi-classical limit of the two-mode BJJ model, which will be developed in Sec.1.6.

1.4.3.c Non orthonormality

The set of states introduced is not orthonormal but overcomplete [71, 72]. Indeed, the overlap of two coherent states is given by

$$\langle \theta', \phi' | \theta, \phi \rangle = \left(\frac{(1 + \alpha^* \alpha')^2}{(1 + |\alpha|^2)(1 + |\alpha'|^2)} \right)^{\frac{N}{2}}, \tag{1.31}$$

which tends to $\delta(\theta - \theta')\delta(\phi - \phi')$ only in the large N limit.

1.4.3.d Coherent states as displacement of a reference state

Like their analog in quantum optics, SU(2) coherent states can be obtained from a reference state, for example the above mentioned south pole of the Bloch sphere $|n = -\frac{N}{2}\rangle$, via the action of a displacement operator [72], i.e.

$$|\theta, \phi\rangle = e^{-i\theta \hat{J}_r} |n = -\frac{N}{2}\rangle \equiv \hat{R}(\zeta) |n = -\frac{N}{2}\rangle, \tag{1.32}$$

with $\zeta = \theta/2 e^{-i\phi}$,

$$\hat{J}_r = \hat{J}_x \sin\phi - \hat{J}_y \cos\phi = \vec{J} \cdot \hat{r} \tag{1.33}$$

and $\hat{r}$ being the unit vector identifying the direction

$$\hat{r} = \sin\phi \hat{x} - \cos\phi \hat{y}. \tag{1.34}$$

Hence, each atomic coherent state is the minimal eigenstate of the angular momentum operator rotated with respect to $\hat{J}_z$ by an angle θ around the direction $\hat{r}$. Indeed, multiplying each member of Eq. (1.26) for $n = -N/2$ by $\hat{R}(\zeta)$ and inserting the identity $\hat{R}(\zeta)^{-1}\hat{R}(\zeta)$ in the first member, we obtain

$$\hat{R}(\zeta)\hat{J}_z\hat{R}(\zeta)^{-1} |\theta, \phi\rangle \equiv \hat{J}_r |\theta, \phi\rangle = -\frac{N}{2} |\theta, \phi\rangle. \tag{1.35}$$

Equation (1.35) is analogous to the quantum optics equation $\hat{a}|\alpha\rangle = \alpha|\alpha\rangle$, in the sense that it is an eigenstate equation for the angular momentum operator (annihilation operator) $\hat{J}_r$ ($\hat{a}$).

1.4.4 Experimental implementations of the observables

Arbitrary rotations of the kind (1.33) can be experimentally implemented, in principle both in the external and internal set-up. This requires switching off the interatomic interaction, i.e. setting $\chi = 0$. In the external model, this can be done by exploiting the Feschbach resonance technique. In the internal set-up, because of the combination of the scattering lengths a_{ij} of the different atomic species in Rubidium, it is found that typically χ is very small, and Feschbach resonances are rather employed when non-zero interactions are desired [8, 62]. Then one exploits the linear part of the Hamiltonian Eq.(1.24), to evolve the state during a time which matches the desired angle of rotation [73]. In particular, in the internal set-up this is done in a very fast and controlled way by tuning the amplitude and the phase of the resonant field coupling the two modes. More severe limitations in the speed of such operations apply for the external BJJ setup [62].

As a consequence, the angular momentum operator is an observable accessible in experiments for each generic direction: this can be achieved by measuring the population

imbalance $\hat{J}_z$ between the two modes after proper rotations of the state over the Bloch sphere [74]. For instance, the measurement of the angular momentum operator in a direction contained in the equator as in Eq.(1.33) on the quantum state $|\psi\rangle$ is achieved by measuring $\hat{J}_z$ on the rotated state $e^{i\pi J_x/2}e^{i\phi J_z}|\psi\rangle$.

1.5 Ground state properties

In this section we briefly review the properties of the ground state of the Bose Josephson junction, in the different regimes of the parameters of Hamiltonian (1.24). We present in particular the calculation of the number fluctuations and of the momentum distribution.

1.5.1 Ground state of the model

Let us define the dimensionless parameter

$$\Lambda = \chi N/(2K). \tag{1.36}$$

Following Ref. [57, 75], three different regimes of the parameters can be distinguished, in which the ground state of the BJJ has different qualitative properties.

- *Rabi regime*: $\Lambda \ll 1$ (strong coupling)

  When the two modes are strongly coupled, a well defined relative phase is established between them, while the number imbalance operator is fluctuating. By this, we mean that in this regime the ground state is close to a phase state. To be convinced of this point, let us consider the limiting case $\Lambda = 0$. In this limit, from Eq.(1.24) it is clear that the energy is minimal for the maximal eigenstate for the $\hat{J}_x$ operator, satisfying $\hat{J}_x|N/2\rangle_x = N/2|N/2\rangle_x$, i.e.

  $$|\psi_{GS}\rangle = |\frac{N}{2}\rangle_x = |\theta = \frac{\pi}{2}, \phi = 0\rangle = |\alpha = 1\rangle, \tag{1.37}$$

  which coincides with the phase state parameterized by $\alpha = 1$, as expressed by the last equality. The ground state (1.37) can be visualized in the left panel of Fig. 1.5. In this regime the number fluctuations amount to $\Delta J_z = \sqrt{N}/2$.

- *Fock regime*: $\Lambda \gg N^2$ (strong interactions)

  In the strongly interacting regime, the ground state is close to a Fock state. In the limiting situation $\Lambda \to \infty$, the ground state is easily determined by completing the square in Eq.(1.24), leading to the Hamiltonian in the non coupled regime $H = \chi\left(n - \frac{\lambda}{2\chi}\right)^2$. The ground state in this case is the Fock state minimizing the energy, and hence it depends on the integer value of the energy imbalance between the two modes renormalized by the interactions, i.e.

  $$|\psi_{GS}\rangle = \begin{cases} |n = \mathrm{Int}\left[\frac{\lambda}{2\chi}\right]\rangle & \text{if } |\frac{\lambda}{2\chi}| < \frac{N}{2} \\ |n = \pm\frac{N}{2}\rangle & \text{resp. for } \frac{\lambda}{2\chi} > \frac{N}{2} \text{ or } \frac{\lambda}{2\chi} < -\frac{N}{2}\ . \end{cases} \tag{1.38}$$

  In particular, for $\lambda = 0$ the ground state is the symmetric Fock state $|n = 0\rangle = |n_1 = N/2, n_2 = N/2\rangle$, also said *Twin-Fock state* [76]. In this regime, the number operator has zero fluctuations, while the phase is completely undefined (see the right panel

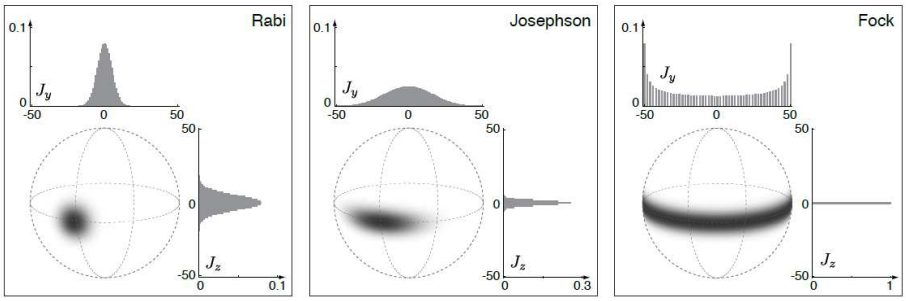

Figure 1.5: Visualization of the ground state of the BJJ on the Bloch sphere, as well as distribution of the number operator in the various regimes of the parameters at $\lambda = 0$, taken from Ref. [62].

in Fig. 1.5). In Sec. 3.1 we will be able to reformulate this in terms of the shape of the Husimi distribution of a Fock state, which is a "crown", completely isotropic in the ϕ angle, and with a value of θ given by the last equation in the set (1.30).

- *Josephson regime*: $1 \ll \Lambda \ll N^2$

  This intermediate regime is characterized by reduced number fluctuations, while the phase coherence is still quite large (see the middle panel in figure 1.5) [57, 62]. We shall see in Section 2.4.1 that the ground state of the BJJ in this regime is a squeezed state.

1.5.1.a Phase diagram of the number fluctuations

In order to have a "pictorial view" of the different regimes for the ground state, we present in Fig.1.6 the plot of the number fluctuations in color scale, calculated numerically as a function of the ratio between the coupling and the interactions, and of the asymmetry of the BJJ λ. These findings are contained in our work Ref. [31]. The black/blue colors correspond to low number fluctuations, while red-yellow colors indicate high fluctuations. We see that this figure exhibits lobes, reminiscent of the phase diagram of the Bose-Hubbard model [77, 78], in which the fluctuations of the number n in the plane of the chemical potential and the strength of the atomic interactions show the Mott-insulator/superfluid transition. Note however that our system does not display a real phase transition but rather a "crossover", because it involves only two modes, and hence the lobes are not bounded by a line which separates the two phases. Furthermore, lobes do not refer to the number of particles in each mode, but to the atomic population imbalance between the two modes at constant total number of atoms. The presence of lobes is a consequence of the double degeneracy of the spectrum of the Hamiltonian (1.24) in the regime of strong interactions. Indeed, at half integer $\lambda/(2\chi)$ two degenerate Fock states minimize the energy, resulting in enhanced number fluctuations. Note also that the size of the lobes increases with increasing imbalance λ. This effect is a direct consequence of the effective nonlinear Josephson coupling, which decreases as $\lambda/(2\chi)$ approaches $N/2$ (see Eq.(1.53)), and is absent in the analogous diagram for superconducting Josephson junctions. The green curve represents an analytical calculation of the number fluctuations, obtained by

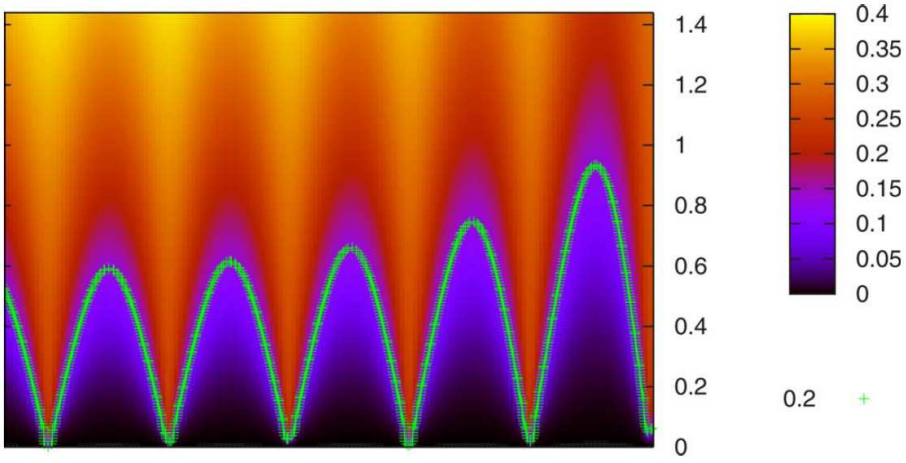

Figure 1.6: Relative number fluctuations in color scale as a function of the parameters $\lambda/(2\chi)$ (x-axes) and $N^2/(2\Lambda) = 2KN/\chi$ (y-axes), for $N = 12$ bosons. The green line corresponds to the value of the number fluctuations of 0.2. From Ref. [31]

treating the coupling perturbatively to the second order, leading to

$$\langle \Delta \hat{J}_z^2 \rangle = \left(\frac{K}{\chi}\right)^2 \left[\frac{\left(\frac{N}{2} - \bar{n_0}\right)\left(\frac{N}{2} + \bar{n_0} + 1\right)}{E_+} + \frac{\left(\frac{N}{2} + \bar{n_0}\right)\left(\frac{N}{2} - \bar{n_0} - 1\right)}{E_-} \right] \tag{1.39}$$

with and $\bar{n_0} \equiv \mathrm{Int}\left[\lambda/(2\chi)\right]$ and $E_\pm = \pm 2(n_0 - \bar{n_0}) - 1$ (see also appendix C.1).

1.5.2 Momentum distribution for the external BJJ

As we have anticipated in Sec.1.2, the coherence of the system is reflected in the presence of fringes in the momentum distribution. Let us now demonstrate this for the external BJJ. With the use of Eq.(1.15), the one-body density matrix of the system in the two-mode approximation is given by

$$\rho(\vec{r}, \vec{r'}) = \langle \hat{\Psi}^\dagger(\vec{r}) \hat{\Psi}(\vec{r'}) \rangle = \sum_{i,j}^{2} \phi_i^*(\vec{r}) \phi_j(\vec{r'}) \langle \hat{a_i}^\dagger \hat{a_j} \rangle. \tag{1.40}$$

The momentum distribution is properly defined as the Fourier transform of the one-body density matrix with respect to the relative variable $\vec{r} - \vec{r'}$ [35], and is thus given by

$$n(\vec{p}) = \frac{1}{2\pi^3} \int d\vec{r} d\vec{r'} e^{-i\vec{p}(\vec{r} - \vec{r'})} \rho(\vec{r}, \vec{r'}), \tag{1.41}$$

where we have set $\hbar = 1$. Substituting the one-body density matrix (1.40) in Eq.(1.41) leads to

$$\begin{aligned} n(\vec{p}) &= \sum_{i,j=1}^{2} \left(\frac{1}{2\pi^{3/2}} \int d\vec{r} e^{-i\vec{p}\vec{r}} \phi_i^*(\vec{r}) \right) \left(\frac{1}{2\pi^{3/2}} \int d\vec{r'} e^{i\vec{p}\vec{r'}} \phi_j(\vec{r'}) \right) \langle \hat{a_i}^\dagger \hat{a_j} \rangle = \\ &= \sum_{i,j=1}^{2} \mathcal{F}[\phi_i(\vec{r})] \mathcal{F}[\phi_j(\vec{r'})]^* \langle \hat{a_i}^\dagger \hat{a_j} \rangle, \end{aligned} \tag{1.42}$$

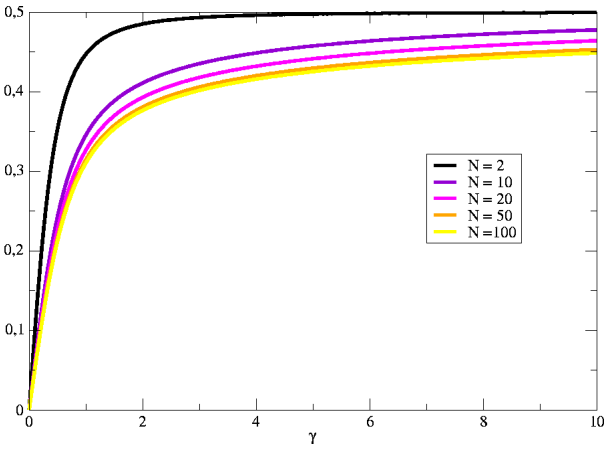

Figure 1.7: Visibility $\nu/2$ evaluated on the ground state and as a function of the parameter $N^2/(2\Lambda) = 2KN/\chi$ for different values of N, and $\lambda = 0$.

where $\mathcal{F}[h(r)]$ denotes the Fourier transform of the function $h(r)$. In the symmetric configuration, the spatial wave functions on each mode are expressed by $\phi_{1,2}(\vec{r}) = \phi_0(\vec{r} \pm \frac{d}{2}\hat{i})$, and their Fourier transform can be easily computed as $\phi_{1,2}(\vec{p}) = \mathcal{F}[\phi_0(\vec{r} \pm \frac{d}{2})] = e^{\pm i p_x \frac{d}{2}}\phi_0(\vec{p})$, where we chose the axes along the two condensates being the x-axes, and where $\phi_0(\vec{p}) = \mathcal{F}[\phi_0(\vec{r})]$ is the Fourier transform of the mode. Then, substituting the previous expression in Eq. (1.42) and using Eq.(1.21) we obtain

$$n(\vec{p}) = |\phi_0(\vec{p})|^2(N + e^{ip_x d}\langle \hat{J}_+\rangle + e^{-ip_x d}\langle \hat{J}_-\rangle), \tag{1.43}$$

where we have used the fact that ϕ_0 is an even function. With the help of Eqs. (1.22), we can finally rewrite the momentum distribution (1.43) as

$$n(\vec{p}) = |\phi_0(\vec{p})|^2(N + \langle \hat{J}_x\rangle \cos(p_x d) - \langle \hat{J}_y\rangle \sin(p_x d)). \tag{1.44}$$

In the ground state, there is no current flowing across the two wells and $\langle \hat{J}_y\rangle$ is zero. Therefore, from Eq. (1.44), we see that the presence or absence of fringes in the momentum distribution is determined by the expectation value of $\langle \hat{J}_x\rangle$, and we expect deviations from the smooth gaussian shape when $\langle \hat{J}_x\rangle$ is not zero. This quantity, renormalized by $N/2$, is indeed called the "coherence factor" or "visibility", and is denoted as [14, 57]

$$\nu = \frac{\langle \hat{J}_x\rangle}{N/2}. \tag{1.45}$$

This is not surprising due to the first equality in Eq.(1.30), which shows that $\langle \hat{J}_x\rangle$ is proportional to the cosine of the phase. Hence, it is maximal in the Rabi regime in which the ground state is a phase state ($\langle \hat{J}_x\rangle = N/2$), while it is zero in the Fock regime in which the phase is completely undetermined. In figure (1.7) we show the numerical evaluation of the visibility of the system $\langle \hat{J}_x\rangle/N$ and as function of the ratio $N^2/(2\Lambda) = 2KN/\chi$, for $\lambda = 0$.

In Fig. 1.8 we present instead a numerical evaluation of the longitudinal momentum distribution $\nu(p_x) = \int dp_y dp_z n(\vec{p})$ for different values of the parameter Λ. We see that, according to Eq.(1.44) and to the considerations on the visibility, the momentum distribution exhibits fringes in the coherent regime of high coupling, reflecting the existence of

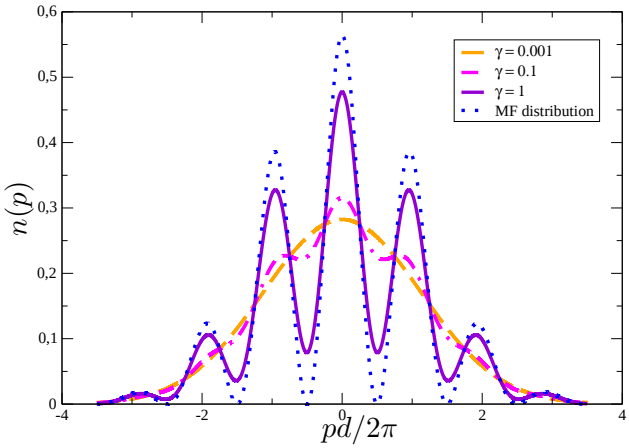

Figure 1.8: Momentum distribution for different values of the parameter $N^2/(2\Lambda) = 2KN/\chi \equiv \gamma$; the distribution exhibits fringes in the coherent regime while interference effects are washed out when the coupling is small. We used $N = 10$, $\chi = 1$, $K = 10^{-4}\chi$, $10^{-2}\chi$, $10^{-1}\chi$. As single particle wave function we choose the gaussian $\phi_0(\vec{r}) = 1/c^3 e^{(x^2+y^2+z^2)/(2\sigma^2)}$ normalized to unity, with $c = (\sqrt{\pi}\sigma)^{1/2}$ and $\sigma = d/10$.

a well defined relative phase between the two condensates, while interference effects are washed out when the coupling is small.

The phase diagram for the fluctuations $\langle \Delta \hat{J}_x^2 \rangle$ of the "coherence factor" is complementary with respect to Fig. 1.6, as presented in Fig. 1.9. That is of course because of the underlying uncertainty principle expressed by Eq.(1.23).

1.6 The semi-classical limit

1.6.1 Semi-classical Hamiltonian and equations of motion

Let us now address the mean field approximation. If the number of particles is large, the fluctuations are negligible with respect to the expectation value of the physical observables, so that we are allowed to treat the field operator as a c-number, i.e.

$$\hat{\Psi}(\vec{r}, t) \to \psi_i(\vec{r}, t). \tag{1.46}$$

This complex field is also called the *order parameter* or the *condensate wave function*. The replacement (1.46) in the Hamiltonian (1.13) leads to the energy functional $E = \int d^3r [\frac{\hbar^2}{2m}|\nabla\psi|^2 + V_{ext}|\psi| + \frac{g}{2}|\psi|^4]$, which by using a variational principle generates the equation [35]

$$-\frac{\hbar^2\nabla^2}{2m}\psi + V_{ext}\psi + g|\psi(r)|^2\psi = i\hbar\partial_t\psi. \tag{1.47}$$

This non-linear time-dependent Schroedinger equation for the wave function of the condensate is known as the "Gross-Pitaevskii" equation (GPE). It has been originally derived in Refs. [79] and [80], and it is the main theoretical tool for investigating nonuniform dilute Bose gases at low temperatures. One should not confuse the solution of the GPE $\psi(r)$, which is normalized to the total number of particle in the condensate, with the many-body

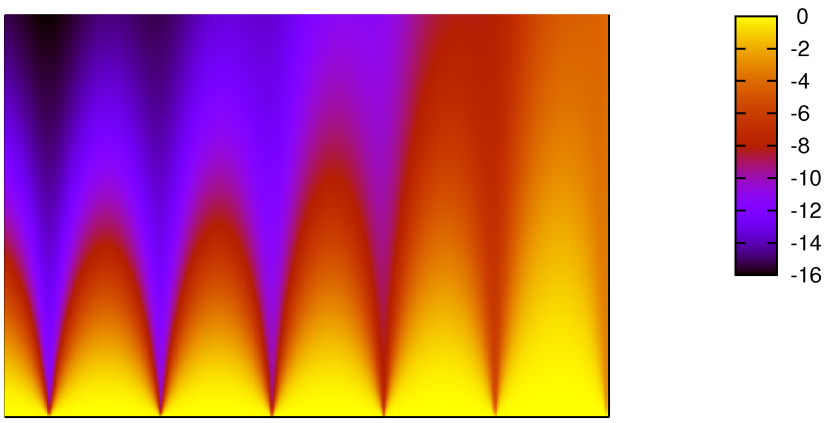

Figure 1.9: Fluctuations $\langle \Delta \hat{J}_x^2 \rangle$ in color scale as a function of the parameters $\lambda/(2\chi)$ (x-axes) and $N^2/(2\Lambda) = 2KN/\chi$. For $N = 12$ bosons.

wave function of the system, readily obtained from $\psi(r)$ taking the symmetric product

$$\Psi_{MB}(\vec{r_1}, \vec{r_2}..., \vec{r_N}) = \left(\frac{1}{\sqrt{N}}\psi(\vec{r_1})\right)\left(\frac{1}{\sqrt{N}}\psi(\vec{r_2})\right).....\left(\frac{1}{\sqrt{N}}\psi(\vec{r_N})\right), \tag{1.48}$$

and which is normalized to unity [35].

In terms of the creation and annihilation operators, the replacement (1.46) amounts to the identification

$$\hat{a}_i \to \langle \hat{a}_i \rangle \simeq \sqrt{n_i} e^{i\theta_i} \equiv \psi_i \tag{1.49}$$

where n_i and θ_i are the number of particles and the phase of the condensate in each mode. With this prescription, the field operator $\hat{\psi}$ in Eq. (1.15) is replaced by the classical field

$$\psi(\vec{r}, t) = \psi_1(t)\phi_1(\vec{r}) + \psi_2(t)\phi_2(\vec{r}). \tag{1.50}$$

Substituting the explicit two-mode expression for ψ given in Eq.(1.50) in the GPE, the time evolution of the particle numbers $n_{1,2}$ and of the phases $\theta_{1,2}$ in each condensate can be derived [48]. In order to proceed further, it is convenient to define the relative variables

$$\begin{aligned} n &= \frac{n_1 - n_2}{2} \\ \phi &= \theta_2 - \theta_1, \end{aligned} \tag{1.51}$$

so that n represents the classical imbalance in the atomic population of the two wells, coinciding with the definition in Eq.(1.27), and ϕ is the relative phase between the two condensates. In terms of these variables, the semi-classical equations of motion are

$$\partial_t n = -2K\sqrt{\left(\frac{N}{2}\right)^2 - n^2}\sin\phi \tag{1.52a}$$

$$\partial_t \phi = 2\chi\left(n - \frac{\lambda}{2\chi}\right) + K\frac{2n}{\sqrt{\left(\frac{N}{2}\right)^2 - n^2}}\cos\phi \tag{1.52b}$$

in which n and ϕ are regarded as commuting variables, conjugate in the classical sense of Poisson bracket, and in which the parameters K, χ and λ are defined as in Secs.1.3 and 1.4. This is a good approximation in the strongly coupled (Rabi) regime, and for $N \gg 1$. The corresponding semi-classical Hamiltonian is

$$H = \chi n^2 - \lambda n - 2K\sqrt{\left(\frac{N}{2}\right)^2 - n^2}\cos\phi. \tag{1.53}$$

1.6.1.a Equivalent derivation

An equivalent way of obtaining the semi-classical Hamiltonian (1.53) (and consequently Eqs. (1.52a) and (1.52b) is projecting the Hamiltonian Eq.(1.24) on the coherent state Eq.(1.28), leading to $\langle\theta, \phi|\hat{H}|\theta, \phi\rangle$. Using the expectation values (1.30), by evaluating also $\langle\theta, \phi|\hat{J}_z^2|\theta, \phi\rangle = n^2(1 - 1/N) + N/4$ we obtain

$$\langle\theta, \phi|\hat{H}|\theta, \phi\rangle = \chi n^2\left(1 - \frac{1}{N}\right) - \lambda n - 2K\sqrt{\left(\frac{N}{2}\right)^2 - n^2}\cos\phi, \tag{1.54}$$

where we used that $N \sin\theta/2 = \sqrt{(N/2)^2 - n^2}$, from Eq.(1.24).

Equation (1.54) reproduces to $O(1/N)$ the mean field result Eq.(1.53) (the inessential constant term $\chi N/4$ has been discarded). In particular, the equivalence of the coupling operator projected over coherent states as in Eq.(1.30), together with the coupling part of the semi-classical Hamiltonian (1.53) justifies the interpretation of the ϕ angle of an atomic coherent state as the physical phase difference of the junction in the semi-classical limit, as anticipated in Sec.1.4.3.

1.6.1.b Semi-classical momentum distribution

Similarly, by using the expectation values Eq.(1.30) we can obtain from Eq.(1.44) the momentum distribution in the semiclassical limit

$$n(\vec{p}) = |\phi_0(\vec{p})|^2 (N + 2\sqrt{\left(\frac{N}{2}\right)^2 - n^2}\cos(\phi + p_x d)), \tag{1.55}$$

as can be found in Ref. [54]. We see that, as we expected, the momentum distribution in the semiclassical limit shows maximal fringes, corresponding to the Rabi regime.

1.6.1.c Analogy with the superconducting case

By adding a constant term irrelevant for the dynamics, we can rewrite the semi-classical Hamiltonian (1.53) as $H = \chi\left(n - \frac{\lambda}{2\chi}\right)^2 - 2K\sqrt{\left(\frac{N}{2}\right)^2 - n^2}\cos\phi$. We can then note the similarity of Eq.(1.53) with the Hamiltonian of a superconducting Josephson junction in a Cooper-pair box circuit (SJJ) $H_{SJJ} = E_C(n - n_g)^2 - E_J\cos\phi$ [81], where the charging energy E_C can be identified with the interaction energy χ, the role of the gate parameter $n_g = C_g V_g/(2e)$ is played by λ, and the tunneling energy E_J can be obtained by linearizing the square-root term in (1.53), leading to KN. The presence of the latter term in Eq.(1.53) represents the main difference with the superconducting case, in which strong charge imbalances are suppressed by the external circuit, and one can only access the linear regime. As a consequence, the classical SJJ system maps on the problem of a rigid pendulum, while the BJJ maps on the non-rigid pendulum, in which the length of the pendulum depends on its momentum. This new feature is responsible for a rich variety of dynamical regimes which are absent in the superconducting case, and which we recall in the following sections.

1.6.2 Dynamical regimes

The full solution of Eqs.(1.52a), (1.52b) can be given in terms of jacobian elliptic functions and can be found in Ref. [49]. Let us restrict to the symmetric case $\lambda = 0$, and describe briefly the main features of such a solution. Before doing so, we need two ingredients: the structure of the fixed points of the system and the notion of Macroscopic Quantum Self Trapping (MQST), which we introduce below.

1.6.2.a Fixed points

The fixed points of the system, defined as the values of the number and phase variables which remain constant during the evolution if chosen as initial conditions, can be easily

identified by imposing $\partial_t \phi = 0$ and $\partial_t n = 0$ in the equations of motion (1.52a),(1.52b). Depending on the parameter Λ defined in Eq.(1.36), this yields the fixed points

$$\begin{aligned}
&(i)\, F_0 = (\theta = \pi/2, \phi = 0), \text{ stable;} \\
&(ii)\, F_\pi = (\theta = \pi/2, \phi = \pi), \text{ stable if } \Lambda < 1 \text{ (Rabi regime) unstable if } \Lambda > 1 \text{ (Josephson} \\
&\quad \text{regime); in the latter case, two stable fixed points are located at} \\
&(iii)\, F_\pm = \left(n_\pm = \pm \left(\frac{N}{2}\right) \sqrt{1 - \frac{1}{\Lambda^2}}, \phi = \pi \right) \text{ (Josephson regime only).}
\end{aligned} \tag{1.56}$$

Indeed, at $\Lambda = 1$ a bifurcation occurs in the model and the fixed points of the system change.

1.6.2.b Macroscopic quantum self trapping

Let us introduce the rescaled variable $z = 2n/N$, and rescale the Hamiltonian (1.53) by the factor KN, obtaining the Hamiltonian given in Ref. [48]

$$H_{sc} = \frac{H}{KN} = \frac{\Lambda}{2} z^2 - \sqrt{1 - z^2} \cos\phi. \tag{1.57}$$

Under certain conditions, trajectories in which the number imbalance can not be reduced to zero, i.e. for which the equation $z(t) = 0$ has no solution, are allowed. This regime is known as *macroscopic quantum self-trapping*. The condition to enter this regime can be found using the fact that the energy is conserved during the evolution, i.e.

$$H_{sc}(0) = \frac{\Lambda}{2} z(0)^2 - \sqrt{1 - z(0)^2} \cos\phi(0) = \frac{\Lambda}{2} z^2 - \sqrt{1 - z^2} \cos\phi \tag{1.58}$$

which, solved for z^2, gives

$$z^2 = \frac{2}{\Lambda^2} \left[(\Lambda H_{sc}(0) - \cos^2\phi) \pm |\cos\phi| \sqrt{\cos^2\phi - 2\Lambda H_{sc}(0) + \Lambda^2} \right]; \tag{1.59}$$

asking for $z = 0$ then leads from (1.59) to the condition

$$\Lambda H_{sc}(0) - \cos^2\phi = \mp |\cos\phi| \sqrt{\cos^2\phi - 2\Lambda H_{sc}(0) + \Lambda^2}, \tag{1.60}$$

which after some algebras leads to $|H_{sc}(0)| = |\cos\phi|$. It is then clear that for

$$H_{sc}(0) > 1 \tag{1.61}$$

Eq.(1.60) has no solution, i.e. $z(t) = 0$ cannot be satisfied at any time (the other condition $H(0) < -1$ has to be discarded because it is not allowed by Eq.(1.58)). The condition for the MQST therefore is (1.61).

1.6.2.c Dynamical regimes

We shall now review in what follows more in detail the possible trajectories associated to the different regimes [48, 49, 61].

In the in the Rabi regime ($\Lambda < 1$), small oscillations around the two fixed points F_0 and F_π are allowed. Their frequency can be obtained by linearizing Eqs.(1.52a,1.52b),

leading respectively to $\omega_0 = 2K\sqrt{1+\lambda}$ for the oscillations around F_0 (blue trajectories in Fig.1.10a) and to $\omega_\pi = 2K\sqrt{1-\lambda}$ for the oscillations around F_π (red trajectories in Fig.1.10a) .

For $\Lambda > 1$, entering the Josephson regime, the trajectories around F_π become broader (red trajectories in Fig.1.10b), while small oscillations around $F_\pm$ appear (green trajectories in Fig.1.10b), which are an example of self-trapped trajectories as discussed in Sec. 1.6.2.b.

From Eq.(1.58) we see that for $\Lambda > 2$, the condition for the MQST (1.61) can be fulfilled with no need for the phase to be confined to a small interval around π, and then other MQST trajectories appear (orange trajectories in Fig.1.10c), in which the phase is growing with the time. For this reason these trajectories are known as "running states", and they are the analog of the AC Josephson effect in superconducting junctions [34, 51].

An experimental verification of all of the regimes presented above is given in Ref. [61], from which Fig. 1.10 is taken.

1.6.2.d Equation of the separatrix

From the above discussion, it is clear that for each value $\Lambda > 1$ there exists a special trajectory which separates the macroscopic quantum self-trapping trajectories from the oscillations in which the number imbalance can take the zero value. This special trajectory passes through F_π, is eight-shaped and is called the "separatrix" (black line in Figs. 1.10 b and c). The equation of the separatrix can be found from the MQST condition given in Eq.(1.61). By using the third line in Eq.(1.30) and the fact that $\sqrt{(N/2)^2 - n^2} = N\sin\theta/2$, from Eq.(1.58) we find that the condition (1.61) translates in terms of the variable θ and ϕ into

$$\frac{\Lambda}{2}\cos^2\theta - \sqrt{1-\cos^2\theta}\cos\phi = 1, \tag{1.62}$$

or, by solving for $\sin\theta$,

$$|\sin\theta| = -\frac{1}{\Lambda}\cos\phi \pm \frac{1}{\Lambda}\sqrt{\cos^2\phi - 2\Lambda + \Lambda^2} \tag{1.63}$$

(for $\Lambda \geq 2$ only the plus sign can be taken, while for $\Lambda < 2$ both signs are allowed). The separatrix can be exploited to produce macroscopic superpositions of coherent states, as will be detailed in Chapter 2.

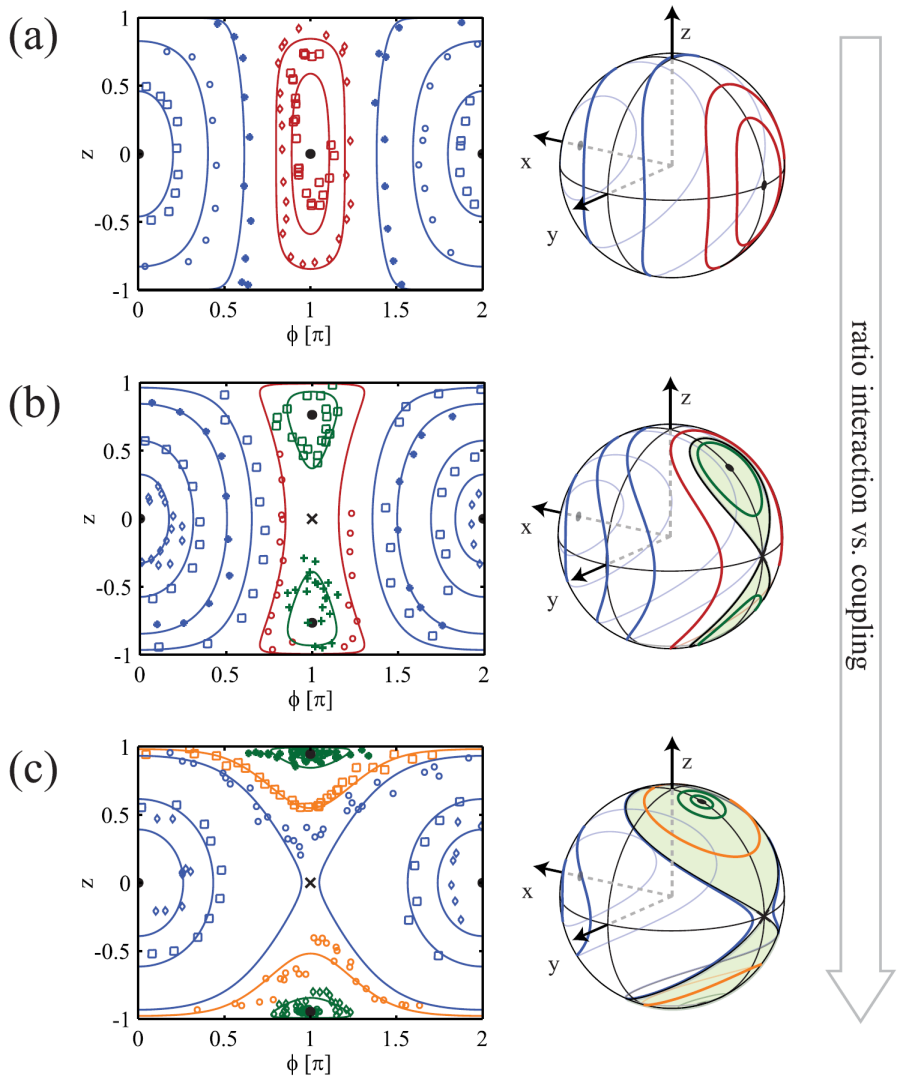

Figure 1.10: Experimental observation of the dynamical regimes of the BJJ, from Ref. [61].

Chapter 2

Creation of entangled states in a Bose Josephson junction

In this chapter we focus on the creation of entangled states in Bose Josephson junctions. After introducing in Sec. 2.1 the notion of multiparticle entanglement and some criteria for its detection in bosonic systems, we will consider some specific entangled states, such as squeezed states, macroscopic superpositions of coherent states and Fock states. We will then explain how it is possible to create such entangled states in a BJJ. We will first briefly review the protocols to realize adiabatically squeezed states and macroscopic superpositions of coherent states. Then, we will discuss how a known protocol leading to the formation of squeezed states can be extended to create macroscopic superpositions of coherent states [31]. The latter result has been the subject of our work Ref.[31]. An improved protocol involving optimum control will be finally presented; more details about this work can be found in our pre-print Ref. [33]

Dans ce chapitre nous nous focalisons sur la création d'états intriqués dans les jonctions Josephson bosoniques. Après avoir introduit en Sec. 2.1 la notion d'intrication pour des systèmes à grand nombre de particules et quelques critères pour sa détection dans les systèmes bosoniques, nous considérerons quelques états intriqués en particulier, tels que les états comprimés, les superpostions macroscopiques d'états cohérents, et les états de Fock. Ensuite nous expliquerons comment il est possible de créer ces états dans une BJJ. Nous rappellerons d'abord les protocoles permettants de réaliser de façon adiabatique les états comprimés et les superpostions macroscopiques. Ensuite, nous discuterons comment un protocole dynamique connu qui permet de créer des états comprimés peut être étendu pour générer des superpositions macroscopiques d'états cohérents [31]. Ce dernier résultat a fait l'objet de notre publication Ref.[31]. Un protocole amélioré basé sur le contrôle optimal sera enfin présenté; plus de détails sur ce travail peuvent être trouvés dans la pre-publication Ref. [33].

2.1 Multiparticle entanglement

In this thesis we use the following definition multiparticle entanglement [12, 82]: a general density matrix $\hat{\rho}$ describing the state of the N atoms in the BJJ is said to be *entangled* if it cannot be written as a separable density matrix, i.e. if

$$\hat{\rho} \neq \hat{\rho}_{sep}, \tag{2.1}$$

where

$$\hat{\rho}_{sep} = \sum_k p_k \hat{\rho}_k^{(1)} \times \hat{\rho}_k^{(2)} \dots \hat{\rho}_k^{(N)}, \tag{2.2}$$

each density matrix $\hat{\rho}_k^{(i)}$ referring to the i^{th}-boson, and $p_k \geq 0$ being a probability such that $\sum_k p_k = 1$. Note that the states appearing in the definition (2.2) are symmetric for the exchange of particles. Indeed, the $(N+1)$-dimensional Hilbert space which accounts for our system of indistinguishable bosons in the two-mode approximation is the restriction to the symmetric subspace of the Hilbert space of all the possible 2^N states which would be obtained with N distinguishable two-mode particles ("qubits").

The definition in Eq.(2.2) leads to consider as entangled some states for which the non-separability is due to the symmetrization over the particles of the bosonic state. This point has been a source of confusion and controversy [83–85]; some comments related to this issue will be given in Sec.2.3.3.

Note also that a coherent state of the form (1.28) is separable according to the definition above, since by (1.32) it can be written as a product state, despite the fact that it is non-separable according to the bipartition on the modes of the BJJ (see table 2.3.3).

2.2 Criteria for multiparticle entanglement

Motivated by the fact that in the experiments only few moments $\langle \hat{J}_i^k \rangle$ of the total distribution of the angular momentum operators are typically accessible, a full set of inequalities allowing to witness entanglement by means of first and second moments only has been derived in Ref. [82]. These inequalities regroup several criteria which were derived independently [12, 86]. Violation of any of the following inequalities implies entanglement:

$$\begin{aligned}
&\langle \hat{J}_x^2 \rangle + \langle \hat{J}_y^2 \rangle + \langle \hat{J}_z^2 \rangle \leq \frac{N(N+2)}{4} \\
&(\Delta \hat{J}_x)^2 + (\Delta \hat{J}_y)^2 + (\Delta \hat{J}_z)^2 \geq \frac{N}{2} \\
&\langle \hat{J}_i^2 \rangle + \langle \hat{J}_j^2 \rangle - \frac{N}{2} \leq (N-1)(\Delta \hat{J}_k)^2 \\
&(N-1)\left[(\Delta \hat{J}_i)^2 + (\Delta \hat{J}_j)^2\right] \geq \langle \hat{J}_k^2 \rangle + \frac{N(N-2)}{4}.
\end{aligned} \tag{2.3}$$

These inequalities identify in the space of the expectation values $\langle \hat{J}_x^2 \rangle, \langle \hat{J}_y^2 \rangle, \langle \hat{J}_z^2 \rangle$ a "polyptote", represented in Fig.2.1 for $N = 6$ particles. If a state lies outside the polyptote, i.e. if it violates one of the inequalities in Eq.(2.3), then it is necessarily entangled according to the definition (2.1), however inside the polyptote both separable and entangled states can be found. These inequalities are however complete in the macroscopic limit in the sense that no other entangled states can be detected with only first and second moments (see also remarks in Sec.4.1.4).

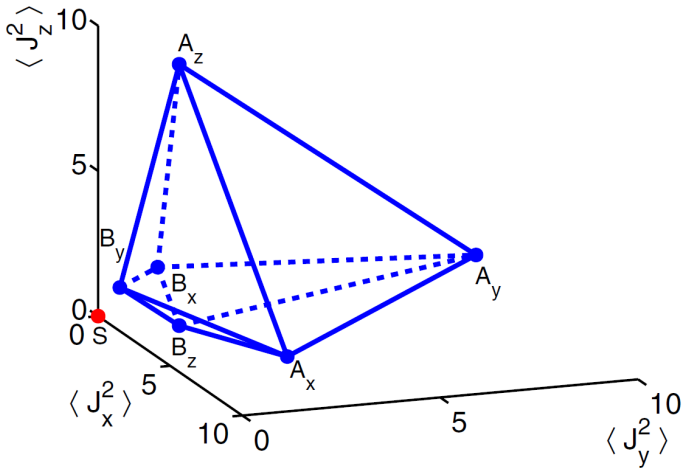

Figure 2.1: Polyptote delimiting the set of entangled states. The points which lie outside the polyptote violate one of inequalities in Eq.(2.3) and are hence entangled according to the definition (2.1) (from Ref. [82]).

We remark that the inequalities (2.3) were originarily derived for a general state of N-qubits, not necessarily symmetric like in the case of our states of indistinguishable particles. In Ref. [82] it has been proven that the inequalities in Eq.(2.3) can not only detect bipartite entanglement (i.e. the non-separability of the reduced density matrix $\hat{\rho}_{A,B} = \mathrm{tr}_{i=1...N, i\neq A,B}[\hat{\rho}]$), but they can also detect entangled states which have a separable two-body density matrix, despite the fact that they are based on first and second moments only [82][1].

A quantity which serves to estimate the number of non-separable particles by disposing only of first and second moments as in Eq.(2.3), the *depth of entanglement*, has been introduced in Ref. [87].

We stress that the criteria provided by Eqs. (2.3) are not restricted to pure states, but they are valid for a general density matrix.

Finally we mention that these inequalities have been recently generalized to the case of a system of N-"qudits" (i.e., individual particles which can occupy more than two states) [88].

2.2.1 Linear entropy

We just mention here an entanglement measure commonly used for pure states, which quantifies the bipartite entanglement of a subsystem $\hat{\rho}_A = \mathrm{tr}_B\hat{\rho}$ with the rest of the system, $\hat{\rho}_B = \mathrm{tr}_A\hat{\rho}$. This is known as the *Von Neumann Entropy* $S_N(\hat{\rho}_A) = -\mathrm{tr}(\hat{\rho}_A \log \hat{\rho}_A)$ [30, 89], satisfying $S_N(\hat{\rho}_A) = S_N(\hat{\rho}_B)$. The linearization of $S_N(\hat{\rho}_A)$ leads to the linearized entropy

$$S_N(\hat{\rho}_A) = 1 - \mathrm{tr}(\hat{\rho}_A^2). \tag{2.4}$$

[1] To illustrate this fact, a non-symmetric state of distinguishable particles was chosen in Ref. [82]. We note that this is also true for the W state, which will be discussed in Sec.2.3.3; such a state belongs rather to the symmetric (bosonic) subspace, is genuinely multipartite entangled and is detected by the inequalities (2.3).

Taking the subsystem to be a single particle, the linearized entropy can be related to the expectation values of collective spins as [69]

$$S_N = \frac{1}{2}\left[1 - \frac{4}{N^2}(\langle \hat{J}_x\rangle^2 + \langle \hat{J}_y\rangle^2 + \langle \hat{J}_z\rangle^2)\right]. \tag{2.5}$$

Its values range from 0 for separable states to 1/2 for maximally entangled states.

2.3 Relevant multiparticle entangled states in a BJJ

We focus in the following on specific entangled states such as squeezed states, macroscopic superpositions of coherent states and Fock states, introducing their main features.

2.3.1 Coherent spin squeezing and squeezed states

Let us introduce the *coherent spin squeezing parameter* $\xi_{\hat{n}}$ as in Ref. [12]. This parameter is related to the angular-momentum fluctuations along the direction $\hat{n}$ according to

$$\xi^2_{\hat{n}}\left[\hat{\rho}_{\rm in}, \hat{J}_n\right] = \frac{N(\Delta \hat{J}_n)^2}{\langle \hat{J}_{p_1}\rangle^2 + \langle \hat{J}_{p_2}\rangle^2}, \tag{2.6}$$

where

$$\begin{aligned} \hat{p}_1 &= \cos\phi\,\hat{x} + \sin\phi\,\hat{y} \\ \hat{p}_2 &= -\cos\theta\sin\phi\,\hat{x} + \cos\theta\cos\phi\,\hat{y} + \sin\theta\,\hat{z} \end{aligned} \tag{2.7}$$

are the unit vectors perpendicular to

$$\hat{n} = \sin\theta\sin\phi\,\hat{x} - \sin\theta\cos\phi\,\hat{y} + \cos\theta\,\hat{z}, \tag{2.8}$$

and $\langle\cdot\rangle = \mathrm{tr}(\cdot\hat{\rho}_{\rm in})$ is the expectation value in state $\hat{\rho}_{\rm in}$.

A state $\hat{\rho}_{\rm in}$ is said to be *coherent spin squeezed*, or simply *squeezed* in the direction $\hat{n}$ if the corresponding coherent spin squeezing parameter satisfies

$$\xi^2_{\hat{n}}\left[\hat{\rho}_{\rm in}, \hat{J}_n\right] < 1. \tag{2.9}$$

Hence, in a squeezed state the fluctuations of the angular momentum operator are reduced in a certain direction, at the expense of the orthogonal direction, so that the uncertainty principle Eq.(1.23) is still satisfied with the equal sign, as it happens for squeezed states in quantum optics.

As pointed out in Ref. [82], the squeezing criterion Eq.(2.9) is equivalent to the last inequality in Eq.(2.3) in the limit of large number of particles. Hence, squeezed states are multiparticle entangled in the sense of Sec.2.1, which was earlier demonstrated in Ref. [12].

Squeezed states have been realized in BJJ systems in the experiments of Refs. [6, 8, 9, 13]. In Sec.4.1.2 we will see how squeezed states can be employed in atomic interferometry to overcome classical limits of precision. In this context, it is common to express squeezing in decibel, i.e. $\xi^2_{\rm dB} = 10\log_{10}\xi^2$.

In order to quantify the intrinsic correlations of a quantum state, regardless of the direction in which the correlations are manifest, we will introduce an optimized version of the coherent spin squeezing parameter in Sec.4.2.

2.3.1.a Other definitions of spin squeezing

An alternative definition of spin squeezing has been introduced by Kitagawa and Ueda in Ref. [11]. According to their definition, the state is squeezed in a certain direction $\hat{n}$ if

$$\xi^2_{U,\hat{n}}\left[\hat{\rho}_{\rm in}, \hat{J}_n\right] = \frac{4(\Delta \hat{J}_n)^2}{N}. \tag{2.10}$$

In the case in which the direction of minimal fluctuations is the $\hat{z}$ direction, the state is said to be "number squeezed" [13, 90]. According to this definition, any Fock state is squeezed along the $\hat{z}$ direction, including the coherent states at the poles. The main difference with respect to the definition in Eq.(2.6) is indeed that in (2.10) the expectation value of the spin in the direction perpendicular to the one of squeezing does not appear in the denominator, and hence the "coherence" of the state, meaning the expectation value of the total spin $\langle \hat{J} \rangle$, is not taken into account. The two definitions coincide when the expectation value of the spin operators in the perpendicular directions is maximal, i.e. when $\langle \hat{J}_{\hat{p}_1} \rangle^2 + \langle \hat{J}_{\hat{p}_2} \rangle^2 = N^2/4$, as can be seen by comparing Eq.(2.6) and (2.10). Note that when this is not the case the two definitions may instead lead to drastically different results. Consider for example a coherent state, say the phase state $|\theta = \pi/2, \phi = 0\rangle$; for this state the coherent spin squeezing (2.6) is minimized in the (yOz) plane and its value is $\xi^2_y = \xi^2_z = 1$. The incoherent version (2.10) instead allows to take the direction $\hat{x}$ as minimizing direction, leading to best squeezing $\xi^2_{U,x} = 0$.

We remark furthermore that the condition analogous to Eq.(2.9), i.e.

$$\xi^2_{U,\hat{n}}\left[\hat{\rho}_{\rm in}, \hat{J}_n\right] < 1, \tag{2.11}$$

generally does not imply entanglement. A counter-example is indeed provided by any coherent state, e.g. the ones at the poles, which are number squeezed but separable. However, if Eq.(2.11) is satisfied for a certain direction $\hat{n}$ and simultaneously $\langle J_n \rangle = 0$, then it implies entanglement in the sense of Eq.(2.1) [86]. This can be seen by noticing that for symmetric states $\langle \hat{J}^2_x \rangle + \langle \hat{J}^2_y \rangle + \langle \hat{J}^2_z \rangle = N(N+2)/4$, so that the second inequality in Eq.(2.3) can be rewritten as

$$\frac{4(\Delta J_n)^2}{N} \geq 1 - \frac{4\langle J_n \rangle^2}{N^2}, \tag{2.12}$$

the violation of which renders the criterion Eq.(2.11) provided $\langle J_n \rangle = 0$.

It has also been demonstrated that violation of Eq.(2.12) for symmetric states constitutes a necessary and sufficient condition for bipartite entanglement. As a corollary, for the states which satisfy $\langle J_n \rangle = 0$, the condition (2.11) is also a necessary and sufficient condition for bipartite entanglement, which is not the case for Eq.(2.9).

2.3.2 Macroscopic superpositions of coherent states

In the context of this thesis, we will designate with the term *macroscopic superposition* a superposition of two or more coherent states. Since in each coherent state all the atoms are in the same one-particle state as described in Sec 1.4, then a superposition of coherent states is a superposition of macroscopically distinguishable configurations, also said a "Schrödinger's cat state". We will often use this equivalent more familiar designation in the following.

For example, the state

$$|\psi_{\rm NOON}\rangle = \frac{1}{\sqrt{2}}(|\theta=0,\phi=0\rangle + |\theta=\pi,\phi=0\rangle) \tag{2.13}$$

is the superposition of the two coherent states at the poles of the Bloch sphere. Such a state is also know as a "NOON state", because of its equivalent expression on the basis of the mode occupation $|n_1,n_2\rangle$, which gives $|\psi_{\rm NOON}\rangle = 1/\sqrt{2}(|N,0\rangle + |0,N\rangle)$. The rotation of the previous state by $\pi/2$ around an axes in the $(x0y)$ plane leads to the two-component "phase cat state" $\frac{1}{\sqrt{2}}(|\theta=\pi/2,\phi\rangle + |\theta=\pi/2,\phi+\pi\rangle)$ i.e. the superposition of two coherent states located on the equator of the Bloch sphere. In particular, rotation around the y axes leads to the state

$$|\psi_{\rm PHASE}\rangle = \frac{1}{\sqrt{2}}(|\theta=\pi/2,\phi=0\rangle + |\theta=\pi/2,\phi=\pi\rangle). \tag{2.14}$$

Such states are highly entangled. The NOON state is maximally entangled both in the sense of the bipartition on the BJJ-modes and on the particles, i.e. according to the definition (2.1) (see Table 2.3.3). The other two-component cat states, such as the two-component phase cat state (2.14), are maximally entangled on the particles and in the sense of a bipartition according to a combination of the modes which depends on the coherent states composing the superposition, as expressed by Eq.(1.29).

Two-component macroscopic superposition states are known from other contexts as GHZ states (see [17–20] and references therein). They are maximally entangled states according to many entanglement measures, e.g. the linearized entropy defined in Eq.(2.5), which takes the maximal value $S_N = 1/2$; indeed, since such states are genuinely N-entangled, then each single particle is (maximally) entangled with the others. They also maximize the quantum Fisher information, an entanglement parameter which will be introduced in Sec.4.1.3. Note however that for $N > 2$ the definition of a multipartite entanglement measure is not univocal, and there exist multipartite entanglement measures for which such states are not the maximally entangled ones, such as the geometric entanglement [91, 92] or the "Quantumness" [93].

Macroscopic superpositions do not violate any of the equations (2.3). This is because, as recalled in Sec.2.2, such inequalities are based on expectation values depending only on two-body correlations between particles of the state, which for the NOON or GHZ states are consistent with those of a separable state (contrarily to W states). Information from N-order moments like $\langle \hat{J}_k^N \rangle$ is needed to verify entanglement in a N-particle macroscopic superposition (see also Chap. 3).

2.3.3 Fock states

The Fock states introduced in Eq.(1.26) are also entangled in the sense of Eq.(2.1) (indeed they violate the third inequality in Eq.(2.3)), except for $n = \pm N/2$, where one recovers the coherent states at the poles of the Bloch sphere, which are separable as already mentioned. For example, in the Fock states labeled by $n = \pm N/2 \mp 1$ all the particles except one occupy the same of the two modes, which leads in first quantization to

$$|n = N/2-1\rangle = \frac{1}{\sqrt{N}}(|2;1;1;1;...1\rangle + |1;2;1;1;...1\rangle + ... + |1;1;1;1;...2\rangle), \tag{2.15}$$

where we have taken the case $n = N/2-1$. Such a state is know as a W state [94], and is also genuinely N-particle entangled. Increasing the number of "excitations" allows to

	Phase state ($\alpha = 1$) $(\hat{a}_1^\dagger + \hat{a}_2^\dagger)^N\|0\rangle$ Eq.(1.28)	Twin-Fock state $\hat{a}_1^{\dagger\frac{N}{2}}\hat{a}_2^{\dagger\frac{N}{2}}\|0\rangle$ Eq.(1.26)	Phase cat state $(\hat{a}_1^{\dagger N} + \hat{a}_2^{\dagger N})\|0\rangle$ Eq.(2.14)
two-mode entanglement	yes	no	yes
N-particle entanglement	no	yes	yes

Table 2.1: Entanglement of a phase state, a Fock state and a macroscopic superposition with respect to the bipartition on the modes or on the particles.

span the other Fock states, reaching half way the symmetric state (in the sense of the population of the two modes), i.e. the Twin-Fock state $|n = 0\rangle$. For $N = 2$, the latter state reads in first quantization

$$|\psi\rangle = \frac{1}{\sqrt{2}}\left(|1;2\rangle + |2;1\rangle\right). \tag{2.16}$$

Eqs. (2.15) and (2.16) allow us to stress that such states are not entangled in the sense of a partition *on the two modes*, but in the sense of the partition *on the particles*, due to the symmetrization of the bosonic state [76, 85, 95] (see table 2.3.3). Some authors in the quantum information community use different definitions with respect to Eq.(2.1), and reject that Fock states are "entangled", claiming that the correlations coming from the symmetrization of the wave function of indistinguishable particles are "unphysical" [20, 83]. The main reason for this is that such correlations cannot be exploited to do quantum computation since individual particles cannot be individually addressed, nor could be Bell inequalities violated (see [85] and references therein). Furthermore, such correlations do not affect the physical observables when the particles are taken far apart each other [10]. However other authors [76, 85] stress the fact that entanglement due to the symmetrization can be a useful resource every times that "collective local operations" only are required, i.e of the type

$$\hat{J}_k = \sum_{i=1}^{N} \hat{\sigma}_k^{(i)}. \tag{2.17}$$

instead of "local" operations $\hat{\sigma}_k^{(i)}$ [2]. An example of a quantum information protocol in which only collective local operations are required is phase estimation, which will be discussed in Sec.4.1.3. The issue of the entanglement for indistinguishable particles in this context, as well as the dependence of the correlations on the spatial distance between the two modes when also internal degrees of freedom are involved are discussed in Ref. [85].

2.4 Adiabatic protocols for the creation of entangled states in BJJs

We now review methods for the generation of entangled states in a BJJ, starting with adiabatic methods.

[2] Note that the nomenclature "local" for operation of the type $\hat{\sigma}_k^{(i)}$ was introduced for spin systems, in which i labels the spin site, individually addressable (see e.g. [76]). However in the external Bose Josephson set-up the operators $\hat{\sigma}_{x,y}$ are non-local in the sense of space, i.e. it is not true that the matrix element over eigenstates of the position $\langle\vec{r}|\hat{\sigma}_{x,y}|\vec{r}'\rangle$ is proportional to $\delta(\vec{r} - \vec{r}')$.

2.4.1 Spin squeezing in the ground state

As can be seen in Fig.1.6, the ground state of the BJJ in the regime in which the interactions are dominant with respect to the tunneling (see Sec. 1.5.1) is number squeezed. With the numerical values considered in the figure for the total number of particles, $N = 12$, the number squeezing condition Eq.(2.11) reads $(\Delta J_z)^2 < 3$, always satisfied in the regime plotted in the figure. Indeed only in the limiting case in which the interactions are zero the state would not be number squeezed, reaching its worst value $\xi^2_{U,z} = 1$ for the phase state $|\theta = \pi/2, \phi = 0\rangle$ ($\alpha = 1$), corresponding to the ground state in the Rabi regime. In particular Fock states, yielding the ground state along the x axes of the diagram presented in the figure, are also number squeezed according to the definition in Eq.(2.10).

It can be shown that in the squeezing regions the ground state is indeed coherent spin squeezed [96]. A plot of the coherent spin squeezing leads to a result qualitatively similar to Fig.1.6. On the axes $\lambda = 0$ of the diagram in Fig.1.6, the coherent spin squeezing in the $\hat{z}$-direction decreases from 1 for the phase state $|\theta = \pi/2, \phi = 0\rangle$, corresponding to the Rabi regime, to zero, deeply inside the Fock regime. Despite the fact that the coherence of the state goes to zero at $K = 0$, the coherent spin squeezing reaches a minimum value when the ground state becomes eventually a Fock state. This will be demonstrated in Sec.4.3, where we will discuss the implications of ground state squeezing for quantum metrology.

Hence, one could think of preparing the state as a coherent state, and then lowering the coupling between the two modes adiabatically, entering the squeezing regime. In an external BJJ the decrease of the coupling between the two modes can be realized by increasing the barrier separating the two wells. The conditions for adiabaticity of the splitting process have been discussed in Ref. [97], in which the spatial dependence of the mode functions on the form of the potential has been taken into account with a variational ansatz. An experiment of this type has been performed with an external BJJ by the group of M. Oberthaler in Heidelberg, as reported in Ref. [13], leading to a squeezing of $\xi^2_z = -3.8$dB. [3]. The measurement of the number fluctuations and of the coherence factor allowed to experimentally determine both the coherent spin squeezing and the Ueda spin squeezing. The dependence of the actual squeezing on the ramping time has also been addressed in the same work (see also Ref. [90] for further discussions). Limitations due to the temperature are discussed in Ref. [62], and will be also addressed in Appendix C.

2.4.2 Ground state of the attractive BEC

A macroscopic superposition of two coherent states (Eq.(2.13)) can be in principle created by preparing the system in a coherent state and by tuning the interatomic interactions adiabatically to strongly negative values [28, 98, 99]. This could be achieved by exploiting Feschbach resonances, as recalled in Chap.1. Indeed, the ground state of the model Hamiltonian (1.24) in the regime of strongly attractive interactions and for symmetric modes $\lambda = 0$ is exactly the NOON state; this is easily understood noticing that in this regime the energy is minimized by the configurations in which all the atoms occupy the same mode, and the two situations corresponding to the maximal occupation of each of the two modes are degenerate.

[3] Technically this result has been achieved with a slightly less shallow harmonic potential, which leads to the occupation of six neighboring wells. The analogous measurement for the rigorously double-well set-up leads to −2.3dB

However this method suffers from some disadvantages. For instance, the strength of the interactions should not increase above a critical threshold, otherwise the gas becomes unstable, and collapses under the effect of the attraction among the atoms [28, 98]. On the other hand, since the first excited state is separated from the ground state by an energy χ, too weak an interaction renders perfect adiabaticity difficult to reach. Issues related to the experimental feasibility of such a protocol are discussed in Ref. [98].

2.5 Dynamical protocols

2.5.1 Creation of squeezed states and macroscopic superpositions of phase states by a quenched dynamics of the BJJ

Let us now address how one can dynamically create squeezed states and macroscopic superpositions of coherent states in a BJJ by a quenched dynamics. Let us take as initial state a coherent state, $|\alpha\rangle$. We focus for the moment on the case of an even total number of particles, and $\lambda = 0$ (symmetric modes). Let us consider the situation where a "quench" occurs, i.e. the coupling between the two modes is suddenly switched off. Then the system evolves under the interaction part of the Hamiltonian only, i.e.

$$H = \chi \hat{J}_z^2. \tag{2.18}$$

Equation (2.18) is analogous to the Kerr Hamiltonian in quantum optics $H_{kerr} \propto \hat{n}(\hat{n}-1)$, where $\hat{n}$ is the photon number [95, 100]. Note also that the Hamiltonian (2.18) conserves the number operator. Hence, the dynamics takes place on a parallel of the Bloch sphere corresponding to the angle θ which parameterizes the initial coherent state, i.e. such that $\alpha = e^{-i\phi}\tan\theta/2$. In particular, if we take as initial state the phase state $|\theta = \pi/2, \phi = 0\rangle = |\alpha = 1\rangle$, which as we have seen corresponds to the ground state of the BJJ in the Rabi regime, the dynamics is restricted to the equator of the Bloch sphere.

A qualitative picture of the dynamics of the state under the action of the Hamiltonian (2.18) view from the top of the Bloch sphere is given in Fig.2.2. By using the expansion of the coherent state on the Fock states given in Eq.(1.28) the action of the time evolution operator on the state can be expressed as

$$|\psi(t)\rangle = e^{-i\chi \hat{J}_z^2 t}|\alpha\rangle = \sum_{m=-N/2}^{N/2} \binom{N}{\frac{N}{2}+m}^{1/2} \frac{\alpha^{m+\frac{N}{2}}}{(1+|\alpha|^2)^{\frac{N}{2}}} e^{-i\chi m^2 t}|m\rangle. \tag{2.19}$$

As it can be seen from Eq.(2.19), the state of the system is periodic as a function of time. Indeed, when all the phases $e^{-i\chi m^2 t}$ are equal to 1, the BJJ is found in the initial coherent state. This happens for $T_{even} = 2\pi/\chi \equiv T$. Decomposing the time evolution operator as $e^{-i(\chi t \hat{J}_z)\hat{J}_z}$ allows us to discuss qualitatively the effect of the atomic interactions on the initial coherent state. This operator indeed performs a rotation around the z-axes, but with a speed which depends on $\hat{J}_z$. To fix the ideas, consider e.g. the case of an initial phase state with $\alpha = 1$, i.e. placed on the equator of the Bloch sphere. In a semi-classical picture in which the uncertainty associated to the initial coherent state is assimilated to a classical distribution of points, the result is that points above the equator evolve rotating in one direction, while points under the equator are rotated in the other direction; the farther they are from the center, the faster is their evolution. Hence, as a result, the state is stretched along the equator of the Bloch sphere. This leads at short times to a coherent

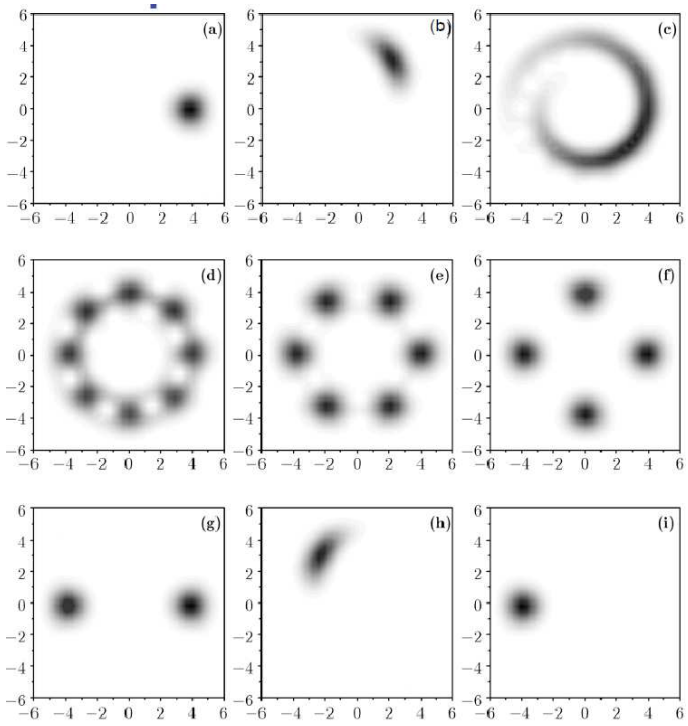

Figure 2.2: Dynamics of the state on the parallel at angle θ of the Bloch sphere (top view) under the action of the Hamiltonian (2.18), taken from Ref. [95].

spin squeezed state (see panel (b) in Fig.2.2). The value of the squeezing parameter as well as the direction of optimization have been determined in Ref. [11]. In section 4.4 we will present an equivalent derivation of these results. As a consequence of this phase diffusion, the visibility $\nu(t)$ introduced in Eq.(1.45) decreases, and a simple calculation yields (here for $\alpha = 1$)

$$\frac{N}{2}\nu(t) = \langle \hat{J}_x \rangle_t = \frac{N}{2}\cos^{N-1}\Big(\frac{2\pi t}{T}\Big). \tag{2.20}$$

At later times, the classical distribution of points fills the entire parallel of the Bloch sphere (see panel c) of Fig.2.2). Quantum-mechanically, interference effects take place. Let us discuss this point more in detail, considering specific times corresponding to fractions of the period T as $t_q = T/(2q)$, with q an even integer. From Eq.(2.19), the state at times t_q is given by

$$|\psi(t_q)\rangle = \sum_{m=-N/2}^{N/2} \binom{N}{\frac{N}{2}+m}^{1/2} \frac{\alpha^{m+\frac{N}{2}}}{(1+|\alpha|^2)^{\frac{N}{2}}} e^{-i\frac{\pi m^2}{q}} |m\rangle. \tag{2.21}$$

Let us denote the phase factor in the previous expression by $e^{-i\frac{\pi m^2}{q}} \equiv U_q(m)$. The function $U_q(m)$ is periodic in m with period q, as can be readily verified by evaluating explicitly $U_q(m+q) = e^{-i\frac{\pi(m+q)^2}{q}} = (-1)^q e^{-i\frac{\pi m^2}{q}} = U_q(m)$. Therefore the function $U_q(m)$

can be expanded according to the discrete Fourier series[4]

$$U_q(m) = \sum_{k=0}^{q-1} e^{-i\frac{2\pi km}{q}} u_k \tag{2.22}$$

with

$$u_k = \frac{1}{q}\sum_{m=0}^{q-1} g_k(m), \tag{2.23}$$

where we have defined $g_k(m) = e^{-i\frac{\pi m^2}{q}} e^{i\frac{2\pi km}{q}}$. These coefficients can be re-written by noticing that $\sum_{m=0}^{q-1} g_k(m) = \sum_{m=0}^{q-1} g_k(m+k) = e^{i\frac{\pi k^2}{q}} \sum_{m=0}^{q-1} g_0(m)$. Hence we obtain from Eq.(2.23)

$$u_k = u_0 e^{i\pi\frac{k^2}{q}} \tag{2.24}$$

where we have defined $u_0 = 1/q \sum_{m=0}^{q-1} g_0(m) = 1/q \sum_{m=0}^{q-1} e^{-i\frac{\pi m^2}{q}}$. Substituting expressions (2.22) and (2.24) in Eq.(2.21) and exchanging the two sums we obtain

$$|\psi(t_q)\rangle = u_0 \sum_{k=0}^{q-1} c_k |e^{-i\frac{2\pi k}{q}}\alpha\rangle \tag{2.25}$$

where we defined $e^{i\frac{\pi k(N+k)}{q}} = c_k$. Hence, the system at times t_q is found in a superposition of coherent states, located symmetrically on the parallel of the Bloch sphere at azimutal angle θ - the equator if $\alpha = 1$. This result has been published in our work [31], and simultaneously in Ref.[101].

This effect was first described for quantum-optics coherent states by B. Yurke in Ref. [102], and in the context of superconducting Josephson junctions by C. C. Gerry [103]. The formation of macroscopic superpositions of coherent states has also been addressed in optical lattices trapping cold atoms in the N-sites Bose-Hubbard model in Ref. [104] (see also discussion in Chap.6). For example, at time t_2 the system is in the two-component macroscopic superposition

$$|\psi(t_2)\rangle = \frac{1}{\sqrt{2}}\left(e^{-i\pi/4}|\alpha\rangle + e^{i\pi/4}(-1)^{N/2}|-\alpha\rangle\right); \tag{2.26}$$

for $\alpha = 1$, this is a "phase cat" state, which only differs from Eq.(2.14) by the presence of a relative phase between the components (see also panel g) in Fig.2.2).

The expression of the macroscopic superpositions with an odd number of components q analogous to Eq.(2.25) is

$$\begin{aligned} |\psi(t_q)\rangle &= \tilde{u}_0 \sum_{k=0}^{q-1} \tilde{c}_k |e^{-i\frac{2\pi k}{q} - i\frac{\pi}{q}}\alpha\rangle \\ \tilde{u}_0 &= \frac{1}{q} e^{\frac{i\pi N}{2q}} \sum_{m=0}^{q-1} e^{-i\frac{\pi m(m-1)}{q}} \\ \tilde{c}_k &= e^{i\frac{\pi k(N+k+1)}{q}}. \end{aligned} \tag{2.27}$$

[4]The general definition is the following: if $f(n) = f(n+L)$, then $f(n) = \sum_{k=0}^{L-1} e^{-i\frac{2\pi kn}{L}} u_k$ with $u_k = \frac{1}{L}\sum_{n=0}^{L-1} e^{i\frac{2\pi kn}{L}} f(n)$

As a special case, note that Eq. (2.27) for $q = 1$ yields a coherent state reversed with respect to the initial one, i.e. rotated by π (see also panel i) in Fig.2.2), appearing at a half of the period $t_1 = T/2$. Such a time interval is said "revival" time because at t_1 the visibility given in Eq.(2.20) takes the initial value 1.

The higher is the number of components of cat state of the form (2.25),(2.27), the shorter is the time at which it appear. For instance, for $\alpha = 1$ we can estimate time of formation of the "first" (in chronological order) multicomponent superposition by the following simple argument: the largest number of phase states of size $\sqrt{N}/2$ (see Sec.1.4.3.b) which can be put on the equator of the Bloch sphere of radius $N/2$ is $q_{\max} \simeq 2\pi N/\sqrt{N} = 2\pi\sqrt{N}$. The time of formation of the multicomponent superposition with the highest number of phase states is $t_{fs} = T/(2q_{\max})$, leading to

$$t_{fs} \sim T/\sqrt{N}. \tag{2.28}$$

Since a decrease in the visibility (2.20) is associated to the appearance of cat state, the time t_{fs} is also known as *phase diffusion time*.

Other cat states can form at other fractions of the period, e.g. at times $\tilde{t_q} = T/(2q + 1)$ [31]. Note that in the case of an odd total number of particles N, the period is $T_{odd} = \pi/\chi = T/2$ [101]. The times of formation of cat states correspond to the ones of the even$-N$ case; the components of these states are however rotated in the parallel of the Bloch sphere with respect to the even case [25, 101].

As a final remark, we point out that states similar to the ones described by Eqs.(2.25) and (2.27) are generated in the dynamics of an ensemble of N two-level atoms in a dispersive cavity [105].

2.5.1.a Effect of an asymmetry on the BJJ parameters

We discuss here the effect of an imbalance λ, describing an asymmetry of the two modes of the BJJ as defined in Eq.(1.25), over the creation of cat states. This is readily found by noticing that the interaction part $\chi\hat{J}_z^2$ and the asymmetry part $\lambda\hat{J}_z$ in the Hamiltonian (1.24) commute. Hence, the state in the presence of imbalance is given by

$$|\psi(t)\rangle_\lambda = e^{-i\phi(t)\hat{J}_z}|\psi^{(0)}(t)\rangle, \tag{2.29}$$

where $|\psi^{(0)}(t)\rangle$ is the state of the symmetric two-mode system at time t under the action of the Hamiltonian (2.18), as given in Eq.(2.19), and where we have defined $\phi(t) \equiv -\int_0^t d\tau\lambda(\tau)$, taking into account a possible time-variation of the asymmetry parameter λ. From Eq.(2.29) one deduces that at each time t the effect of such an asymmetry is a rigid rotation of the state around the z-axes of the Bloch sphere (i.e., in the equatorial plane for the initial coherent state with $\alpha = 1$) with respect to the symmetric case, by an angle which depends on time.

Consider as an example the sinusoidal driving $\lambda(t) = \lambda_0 + \delta\sin(\omega t)$. Using Eq.(2.29), the angle of rotation of the cat state formed at time t_q is given by $\phi(t_q) = -t_q(\lambda_0 + \delta(1 - \cos(\omega t_q))/(\omega t_q))$. In particular, for frequency and drive amplitudes such that the condition $\phi(t_q) = 2\pi$ is matched, the q-component cat state is formed as if no drive were applied[5].

The effect of a stochastic fluctuation of the asymmetry λ on the formation of macroscopic superpositions of phase states will be explicitly considered in Sec.5.1.3.

[5]In Ref. [67] such a sinusoidal drive has been studied for the external BJJ in the context of transport, by looking at the time-averaged transferred population after preparing the system in an initial state in

2.5.2 Dynamical creation of macroscopic superpositions in a BJJ: semi-classical argument

A protocol for the dynamical creation of a NOON state has been suggested in Ref. [108]. Contrarily to the proposal for the creation of macroscopic superpositions of phase states presented in Sec.2.5.1, such a protocol makes use of a non-zero coupling between the two modes of the BJJ. The prediction is based on a semi-classical argument, relying on the mean-field dynamics of the system introduced in Sec.1.6, and is briefly reviewed here below.

Let us consider as initial state of the quantum dynamics a coherent state identified by the angles $(\theta = \pi/2, \phi = \pi)$, i.e. the phase state $|\alpha = -1\rangle$, which is centered in F_π (see Eq.(1.56)). As recalled in Sec. 1.4.3.b, the width associated to its fluctuations is $\sigma = \sqrt{N}$. In the semi-classical picture introduced in Sec.2.5.1, such a state can be viewed as a cloud of points evolving according to the classical trajectories. As we have seen in Sec.1.6, for $\Lambda > 1$ (Josephson and Fock regime) the separatrix passes across F_π. Hence in this regimes the initial wave packet evolves along the separatrix by splitting into two outgoing parts, one stretching towards the northern hemisphere of the Bloch sphere, and the other one in the southern part.

Depending on the value of the parameter Λ defined in Eq.(1.36) the following two qualitatively different situations can occur. As can be seen from Eq.(1.63), in the strong coupling regime, for $1 \leq \Lambda \leq 2$, the maximal separation of the two outgoing wave packets is obtained for $\sin\theta[\phi = \pi]$, i.e. for $\theta_\pm = \pm \arcsin \frac{2-\Lambda}{\Lambda}$ (see the separatrix in Fig.1.10b), corresponding qualitatively to a superposition of two coherent states $1/\sqrt{2}(|\theta_+, \phi = \pi\rangle + |\theta_-, \phi = \pi\rangle)$ [108]. In the weak coupling regime, i.e. for $\Lambda \geq 2$, the maximal separation is obtained at $\sin\theta[\phi = 0]$, which gives $\cos\theta_+ = 2/\Lambda\sqrt{\Lambda - 1}$ (see the separatrix in Fig.1.10c), leading to a superposition of two Fock states of the form $1/\sqrt{2}(|n = N/2\cos\theta_+\rangle + |n = -N/2\cos\theta_+\rangle)$ [108].

Precisely at $\Lambda = 2$ the separatrix touches the two poles of the Bloch sphere, leading to the best possible superposition state, i.e. the NOON state given in Eq.(2.13) (note indeed that for this value of Λ we obtain $\theta_+ = \pi$) [33, 108].

The time T_c that it takes for a point initially in F_π to travel along the separatrix and reach one of the poles of the Bloch sphere is [108]

$$T_c \simeq \frac{\chi \ln(8N)}{N}, \tag{2.30}$$

which can be taken as an estimation of the time of formation of the macroscopic superposition.

The accuracy of the semi-classical argument presented above has been checked by performing a quantum calculation of the time evolution of the system under the Hamiltonian (1.24) with parameters corresponding to $\Lambda = 2$ and $\lambda = 0$ [108]. A calculation of the fidelity, i.e. the projection of the state produced on the perfect superposition given in

which all the atoms are in the same well. The tunneling probability exhibits resonances as a function of the driving frequency, reminiscent of the Shapiro-steps in SJJ. To observe this phenomenon the two modes of the BJJ must be coupled, which induces a more complicated dynamics than the one described in Eq.(2.29), as the coupling part does not commute with the rest of the Hamiltonian. Indeed, it has also been shown that such driven coupled dynamics induces chaos in the classical regime, being related to the appearance of entanglement in the quantum regime in Ref. [106]. The transport by driving in such systems has also been addressed in Ref. [107].

Eq.(2.13)

$$\mathcal{F}_1 = |\langle \psi_{\mathrm{NOON}} | \psi(t) \rangle|^2 \tag{2.31}$$

(to be evaluated at the time T_c of formation of the superposition) allows to estimate the quality of the state produced. Such a calculation leads e.g. to $\mathcal{F}_1 = 0.1394$ for $\chi = 1$ and $N = 300$ [33, 108], i.e. the fidelity is quite low, which means that the state formed is only approximatively a NOON state (see second panel in Fig.2.4). We mention that various other quantities, more sensitive to the existence of coherences in the superposition than the fidelity, can be computed to testify the "catness" of the state produced [33]. Among them, we cite the probability distributions of the eigenvalues of angular momentum operators in various directions, which we will extensively treat in Chap. 3, or the quantum Fisher information, which will be discussed in Chap.4.

We note that the time of formation of the NOON state estimated in Eq.(2.30) is much shorter than the time t_2 required to form a two-component macroscopic superposition of phase states by the *quenched dynamics* of the BJJ presented in Sec.2.5.1, providing therefore a speed up with respect to the use of that protocol and leading to a substantial advantage in experiments. Indeed, the fragility of superposition states with a macroscopic number of particles with respect to decoherence induced by various mechanisms renders challenging their experimental realization. Issues related to the decoherence of macroscopic superpositions will be explicitly addressed in Chap. 5. Here we only wish to stress the interest in providing a protocol to create macroscopic quantum superpositions in the shortest time possible, i.e. before decoherence becomes effective, and the question arises whether the solution proposed in Ref. [108] is optimized. This question is addressed in the following section.

2.5.3 Controlled dynamical creation of macroscopic superpositions in a BJJ

In order to study the optimized production of macroscopic superpositions, we have developed a protocol of optimal control in collaboration with D. Sugny and M. Lapert [33]. The general idea is to consider that the parameters of the Hamiltonian (1.24) can be tuned during the time evolution, in order to reach a certain target state (in our case, a macroscopic superposition) in the minimum time possible, or with the best possible fidelity within a fixed time. Since in the internal BJJ setup the coupling K is efficiently controllable both in amplitude and sign by tuning a resonant field, instantaneously with respect to the other time scales of the problem [8, 62] (see also Chap. 1), we choose to keep fixed the parameter χ and to use K as control field. We will have in mind the internal BJJ setup, which appears more suitable for the experimental implementation of our control protocol. In the following we will use a dimensionless version of the coupling K, i.e. $\omega = 2/\Lambda = 4K/(\chi N)$. In terms of this parameter the optimal separatrix of the static protocol presented in the previous section is identified by $\omega = 1$.

2.5.3.a Geometric optimal control approach

We first tackle the problem by means of geometric optimal control theory [109]. In a summarized way, geometric optimal control is a vast domain where the optimal control problems are solved by using tools of geometry and Hamiltonian dynamics. Due to its geometric framework, this method is intrinsically limited to systems with few degrees of freedom. Since as we have seen in Sec.1.6 in the semi-classical limit the BJJ is described

in terms of two classical conjugated variables, i.e. the polar and azimuthal angles of the Bloch sphere of radius $N/2$, the tools of geometric optimal control theory can be applied.

In particular, we solve our time-optimal control problem by applying the Pontryagin Maximum Principle (PMP) [33, 109], which requires to set a bound, m, on the amplitude of the control field: among all the functions $\omega(t)$ allowing to reach the target state, the optimal solution is the one minimizing a given cost, here the duration of the control, within the bound m on the dimensionless parameter ω.

We consider as initial classical state a point on the Bloch sphere at a distance σ from $(\theta = \pi/2,\ \phi = \pi)$, corresponding to the extremum point on the uncertainty circle of the phase state $|\theta = \pi/2, \phi = \pi\rangle$ - the same initial phase state of the protocol presented in Sec. 2.5.2. Without loss of generality, we can choose this point in the upper hemisphere. Then, the optimal sequence to reach in minimum time the north pole of the Bloch sphere is computed. By symmetry of the dynamical equations, the point of the lower hemisphere symmetric with respect to S of the initial state reaches simultaneously the south pole. This classical simultaneous control leads in the quantum domain to the creation of a superposition state.

The minimum time T_{min} for the generation of a macroscopic superposition with this protocol can be estimated analytically for $m \to +\infty$, and results inversely proportional to the total number of particles as the time T_c in Eq.(2.30), differing from it by a numerical factor. The calculation of T_{min} as well as a numerical comparison between T_c and T_{min} are detailed in Ref. [33], resulting in $T_{min} \lesssim T_c$.

The solutions for the optimal fields obtained for three bounds on the field amplitude ω, namely $m = 1,\ 2,\ 100$, are reported in the second panel of Fig.2.3. For $m = 1$ we recover the solution of Ref. [108], which is only composed of a constant field - in the control terminology, a "bang pulse". More complicated solutions can be constructed when the bound m takes larger values. The respective optimal trajectories in the phase space, parameterized by the coordinates θ and ϕ (see Fig. 2.3, and also Refs. [48, 61, 108]) under the field solution $\omega(t)$ are displayed in Fig.2.3. In particular, taking as in Sec.2.5.2 $N = 300$, for $m = 100$ we reach the target in a time $\chi T_{min} = 0.0236$, while for $m = 1$ from Eq.(2.30) one obtains $\chi T_c = 0.0259$. The corresponding fidelities with the state $|\psi_{\rm NOON}\rangle$, obtained by calculating numerically the time-evolution of the quantum state under the solution field $\omega(t)$, are equal to $\mathcal{F}_1 = 0.116$ for $m = 100$, while we recall from Sec.2.5.2 that $\mathcal{F}_1 = 0.139$ for $m = 1$. Table 2.2 lists the numerical results obtained with this approach. Other quantities, sensitive to the correlations, are computed in Ref. [33]. A visualization on the Bloch sphere of the state created is provided in the second panel of Fig.2.4.

Our control protocol can be generalized to create a phase cat $|\psi_{\rm PHASE}\rangle$ (see Eq.(2.14)) in addiction to the state $|\psi_{\rm NOON}\rangle$, which is not possible in the original non-controlled proposal of Ref. [108]. Arguments analogous to the case of a NOON state can be used to describe the optimal trajectories reaching the state $|\psi_{\rm PHASE}\rangle$. Switching the sign of the control field is required here, though, which could be implemented by tuning the microwave and radio-frequency fields as explained in Sec.1.4. Numerical results comparable with those for the state $|\psi_{\rm NOON}\rangle$ are obtained for the minimum time and the projections at various values of the bound, as reported in Table 2.2[6].

The conclusion of this analysis is that both the minimum time of formation of macroscopic superpositions and the respective fidelities obtained with the geometric control protocol developed are comparable to the ones of the static method of Ref. [108]. The

[6]The projection on the phase cat state, analogous to Eq.(2.31), is defined as $\mathcal{F}_2 = |\langle {\rm Cat}_2|\psi(t)\rangle|^2$.

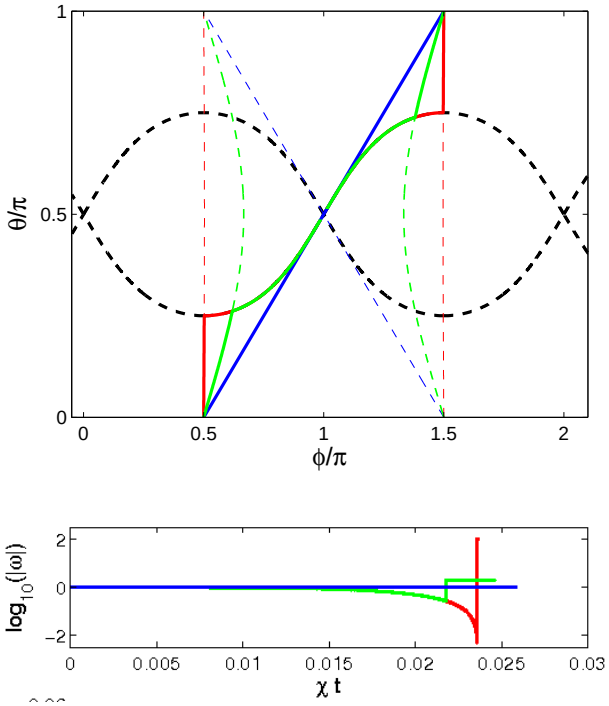

Figure 2.3: (top) Plot in the (θ, ϕ) plane of the optimal trajectory in the semi-classical model for the bounds $m = 1$, $m = 2$ and $m = 100$ in blue (dark), green (light gray) and red (dark gray) respectively. The target state is the cat state $|\psi_{\mathrm{NOON}}\rangle$. The dashed blue, red and green lines represent the position of the separatrix for the different bounds. (bottom) Evolution of the corresponding control fields $\omega(t)$, as a function of the dimensionless time χt.

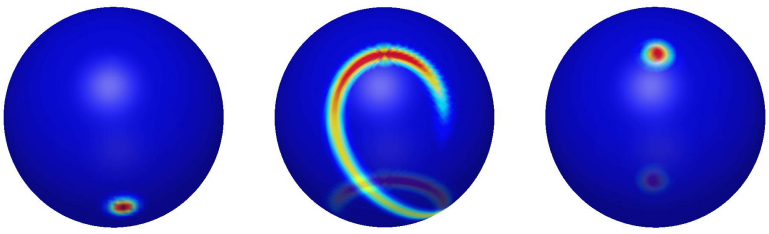

Figure 2.4: Plot of the projections on the Bloch sphere, (i.e. the Husimi function $Q(\theta, \phi) = |\langle \theta, \phi | \psi \rangle|^2$ introduced in Sec.3.1) of the initial state $|\pi/2, 0\rangle$ (left), the final states with the geometric solution for $m = 1$ and $t = T_{min}$ (middle) and with the fully quantum numerical approach with $t = 10\, T_c$ (right).

latter method is hence almost optimal for the creation of a NOON state based on a semi-classical approach, though leading to a poor fidelity. To obtain better results, another approach able to tackle the fully quantum character of the problem has to be used, possibly relaxing a little the time constraint, as detailed in the next section.

	NOON			PHASE		
m	1	2	100	1	2	100
$\chi t(\times 10^{-3})$	25.9	24.6	23.6	25.5	24.6	23.6
$\mathcal{F}_{1,2}$	0.139	0.122	0.116	0.091	0.100	0.116

Table 2.2: Numerical results of the semi-classical control protocol for three different bounds, $m = 1$, 2 and 100. The control duration (χt) and the fidelity ($\mathcal{F}$) are given for the two cat states $|\psi_{\rm NOON}\rangle$ (NOON state) and $|\psi_{\rm PHASE}\rangle$ (Phase state).

2.5.3.b Fully numerical approach

As we have seen in the previous section, the efficiency of the optimal solution based on the semi-classical approach is limited in the original quantum domain. We now determine the solution of the initial quantum problem by using a purely numerical approach, namely the monotonic convergent algorithm, which is a standard approach to solve the optimality equations in quantum mechanics [110].

In this case, we shall rather consider various *fixed* control durations, namely $T' = T_c,\ 5\,T_c$ and $10\,T_c$, multiple of the minimum time T_c of the static control protocol, and we maximize the projection onto the target state at time $t = T'$. In the following computations, we have chosen as parameters of the quantum system $\chi = 1$ and $N = 300$.

In order to guide the numerical optimization, we use the geometric solution as a trial solution for the numerical algorithm. This allows to design a final optimal solution close to the geometric one. Due to the proximity of the results obtained at different values of the bound, we can consider as initial field of the algorithm the constant field $\omega(t) = 1$ in the interval $[0, T']$, corresponding to the bound $m = 1$ of the geometric protocol.

Very good results are obtained, with a final projection larger than 0.88 and 0.99 on the target state $|\psi_{\rm NOON}\rangle$ for $T' = 5\,T_c$ and $T' = 10\,T_c$, respectively. The solution field for this latter case is presented in Fig. 2.5. A visualization on the Bloch sphere of the NOON state created is provided in the third panel of Fig. 2.4. Note that waiting a time $10\,T_c$ with the control field $\omega = 1$ of Ref.[108] would not lead to any improvement, as the quantum state would keep on evolving further from the configuration in the second panel of Fig.4, refocussing at some point in the initial coherent state (the state is indeed periodic). The time T_c is thus the optimum time for creating a cat state with $\omega = 1$. For such a time interval, a projection of 0.2548 is reached with the numerical optimum control protocol, which yields an improvement over the result of Ref.[108], at the price of a more complicated solution.

The same computation has been done for the target state $|\psi_{\rm PHASE}\rangle$, taking again as initial condition for the algorithm the geometrical optimal solution at $m = 1$ (which is no longer static), with a total duration increased by a factor of 1, 5 and 10 as before. The different numerical results are listed in Table 2.3.

To conclude, we have demonstrated that by means of a fully numerical optimization approach it is possible to create a NOON state with a very high fidelity in a time ten times larger than the time of formation of the NOON state in Ref.[108], which led to a very low fidelity. Note that this time interval can still lead to a significative speed-up with respect to the protocol based on the quenched dynamics of the BJJ presented in Sec.2.5.1, where $t_2 = \pi/(2\chi)$ was independent on the number of atoms.

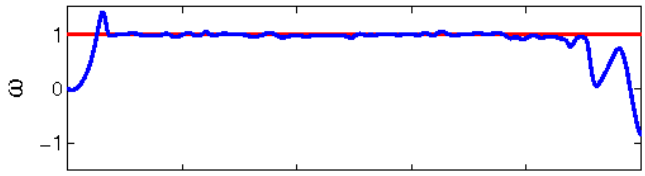

Figure 2.5: Plot of the field solution for $T = 10\,T_c$. The horizontal solid line is the solution of Ref.[108], which is taken as a trial field of the algorithm.

	NOON			PHASE		
n	1	5	10	1	5	10
$\mathcal{F}_{1,2}$	0.255	0.880	0.994	0.245	0.903	0.989

Table 2.3: Same as Table 2.2 but for the quantum protocol. The parameter n represents the ratio of the control duration over the time T_c (see main text).

2.5.3.c Experimental feasibility

Let us discuss the experimental feasibility of our control protocol, starting with the bound on the control. Having in mind the internal BJJ setup (and in particular the experiments of Ref.[8, 62]), typical bounds on the parameter K are $0 < K < 2\pi$KHz, and a typical value for χ is $\chi \approx 2\pi \cdot 0.13$Hz. Fixing this value for the interactions translates the maximum value of the control field which we have used, i.e. $\omega = 100$, into the value of the coupling, $K \approx \pi \cdot 1.95$KHz for $N = 300$ particles, which is within the limit accessible experimentally. Furthermore, the control field can be switched fast compared with the other time scales of the experiments. Note that, from a theoretical point of view, it would be possible to include in our protocol some spectral constraints on the control field [33]. Hence, in ideal conditions it would be possible to implement our control protocol.

However, in realistic conditions the experiments are affected by the presence of noise, which induces dissipation and decoherence, as will be discussed in Chap. 5. Such noise sources have not been taken into account in our protocol, and may change significatively the quantum state reached with the help of the designed control field. In particular, with qualitative arguments we have estimated that, given the experimental parameters of Ref. [8], the atom loss dissipation rate should be lowered by a factor 1000 in order to allow the formation of macroscopic superposition at $10T_c$ without losing any atom - a single loss event causes the decoherence of the NOON state, as it will be shown in Appenxix E.3. Further discussions are provided in the conclusive section of Ref. [33].

Chapter 3

Detection of macroscopic superpositions

The entanglement witnesses presented in the previous chapter allow to detect the presence of entanglement by measuring the collective angular momentum operator in various directions. However, these inequalities do not give any information about the structure of the entangled state. In this chapter, we provide some tools which allow to *visualize* the quantum state of the system, and detect its entanglement in the case of macroscopic superpositions. After briefly presenting the theory of quasi-probability distributions for the SU(2) symmetry group "borrowed" from quantum optics, we introduce the probability distributions of the eigenstates of angular momentum operators in various directions, and we show how they can be used to obtain information about the quantum state of the system. These results are the subject of our publication Ref.[32].

Les critères que nous avons présentés dans le chapitre précédent permettent de détecter l'intrication à l'aide de mesures du moment angulaire collectif dans différentes directions. Cependant, ces inégalités ne donnent pas d'information sur la structure de l'état intriqué. Dans ce chapitre, nous donnons des outils permettant de visualiser *l'état quantique du système, et de détecter l'intrication pour le cas des superpositions macroscopiques d'états cohérents. Après avoir brièvement présenté la théorie des distributions de quasi-probabilité pour le groupe de symétrie SU(2) "emprunté" à l'optique quantique, nous introduisons la distribution de probabilité des valeurs propres de l'opérateur de moment angulaire dans différents directions, et nous montrons que celle-ci peut être utilisée pour obtenir de l'information sur l'état quantique du système. Ces résultats ont fait l'objet de notre publication Ref.[32].*

3.1 Quasi-probabilities distributions in phase space

In quantum optics it can be useful, in order to visualize the quantum state of the system, to introduce quasi-probability distributions in phase space - for the electromagnetic field in a cavity, the complex plane parameterized by the amplitude $\alpha = x + ip$, where $\hat{x} = (\hat{a} + \hat{a}^\dagger)/\sqrt{2}$ and $\hat{p} = (\hat{a} - \hat{a}^\dagger)/(i\sqrt{2})$ are the quadratures of the field. These distributions are thus simultaneous functions of the semiclassical variables x and p, associated with non-commuting observables [72]. Three such phase-space representations can be defined,

namely the Husimi function Q, the Sudahrsan distribution P, and the Wigner function W, each of them in bijective correspondence with the density matrix of the system [72, 111]. Knowledge of each of these representations allows in principle to calculate the other ones by convolution with coherent state overlap functions (similar to Eq.(1.31)), even if the explicit calculation may be impractical (see Ref.[111] and Sec.3.1.2). An interesting feature of these representations is that they allow to convert the calculation of quantum averages to calculations of integrals over phase space. Their definitions can be adapted for the SU(2) algebra, such as to render them suitable to describe our system of N bosons in two modes [71, 72, 111, 112]. As we have seen in the previous chapters, the classical phase space is in this case the Bloch sphere, which can be parameterized by means of the angular variables θ and ϕ. In the following we present the definition of SU(2) phase space distributions.

3.1.1 Husimi distribution Q

The Husimi function is defined as [71, 72]

$$Q(\theta,\phi) = \langle\theta,\phi|\rho|\theta,\phi\rangle, \tag{3.1}$$

with the normalization condition $\frac{(N+1)}{4\pi}\int d\Omega Q(\theta,\phi) = 1$. When the system is in a pure state, i.e. $\rho = |\psi\rangle\langle\psi|$, the Husimi function reduces to the projection over a coherent state, namely $Q(\theta,\phi) = |\langle\theta,\phi|\psi\rangle|^2$. Let us give some examples.

3.1.1.a Husimi distribution of a Fock state

The Husimi distribution of the Fock state $|n\rangle$ is readily calculated by means of Eqs.(1.4.3) and (3.1), and reads

$$Q^{(n)}(\theta,\phi) = \frac{1}{(1+\tan^2\left(\frac{\theta}{2}\right))^N}\binom{N}{\frac{N}{2}+n}\left(\tan^2\left(\frac{\theta}{2}\right)\right)^{2(n+\frac{N}{2})} = Q^{(n)}(\theta). \tag{3.2}$$

As anticipated in Sec.1.5.1, this distribution does not depend on the angle ϕ but only on θ, and for each value of n it is peaked at $\theta = \arccos(-2n/N)$ according to the third line in Eq.(1.30). The Husimi distribution for various Fock states is illustrated in Fig. 3.1.

3.1.1.b Husimi distribution of a coherent state

Due to the definition (3.1), the Husimi distribution of a coherent state is simply calculated by using the expression of the overlap between two coherent states Eq.(1.31). For example, for the phase state $|\theta = \frac{\pi}{2}, \phi = 0\rangle$ we obtain

$$Q(\theta,\phi) = |\langle\theta,\phi|\theta = \frac{\pi}{2}, \phi = 0\rangle|^2 = \frac{1}{2^N}(1+\sin\theta\cos\phi)^N, \tag{3.3}$$

which displays a peak centered around the values $\theta = \frac{\pi}{2}, \phi = 0$ parameterizing the coherent state under consideration.

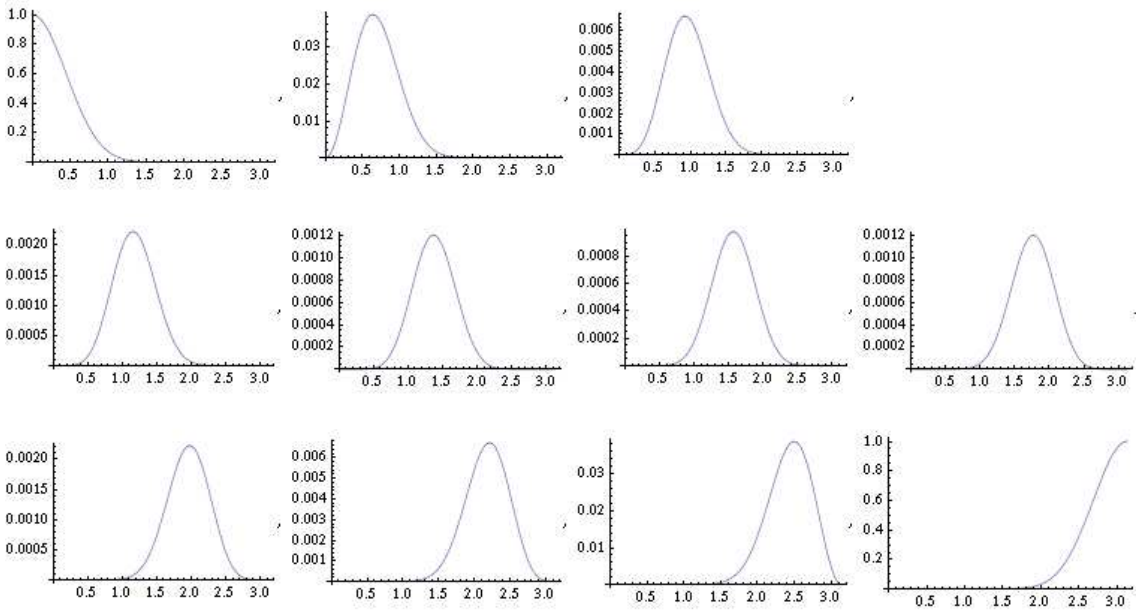

Figure 3.1: Husimi function $Q^{(n)}(\theta)$ of Fock states $|n\rangle$ for $n = -5, -4..., 5$ (with $N = 10$), as given in Eq.(3.2) (panels from left to right, from top to bottom).

3.1.1.c Husimi distribution of cat states

The Husimi distribution of a cat state is also readily obtained by using Eqs.(2.25),(2.27) and the definition (3.1). For phase cat states we will make use in what follows of the restriction of the Husimi distribution to the equator of the Bloch sphere, i.e. $Q(\phi) \equiv Q(\theta = \pi/2, \phi)$. This function displays as many peaks as there are components in the superposition, as can be seen in Fig. 3.2. Some examples of projected Husimi distributions for macroscopic superpositions are given in Ref.[105] and in our work [32]. In Sec.5.1.3.b we will calculate this function explicitly for a two-component cat state formed in the presence of phase noise.

Although the Husimi phase distribution is in one-to-one correspondence with the full density matrix, from a "visual" point of view in practice it is almost insensitive to the difference between a coherent superposition of phase states and the corresponding incoherent mixture of the same coherent states, equally weighted. This is because due to Eq.(3.1) the Husimi distribution can be seen as the diagonal of the density matrix represented over coherent states, while the contributions which allow to distinguish a macroscopic superposition from an incoherent mixture are off-diagonal. This point will be extensively analyzed in Sec.5.1.3.a. As an illustration of this fact, Fig. 3.2 (top panel) shows the Husimi distribution for a three-component superposition of phase states and for the corresponding incoherent mixture, the tiny difference between the two being illustrated in the inset. The need for developing tools to distinguish between coherent superpositions and incoherent mixtures has brought us analyze the eigenvalue distributions which will be presented in Sec. 3.2.1.

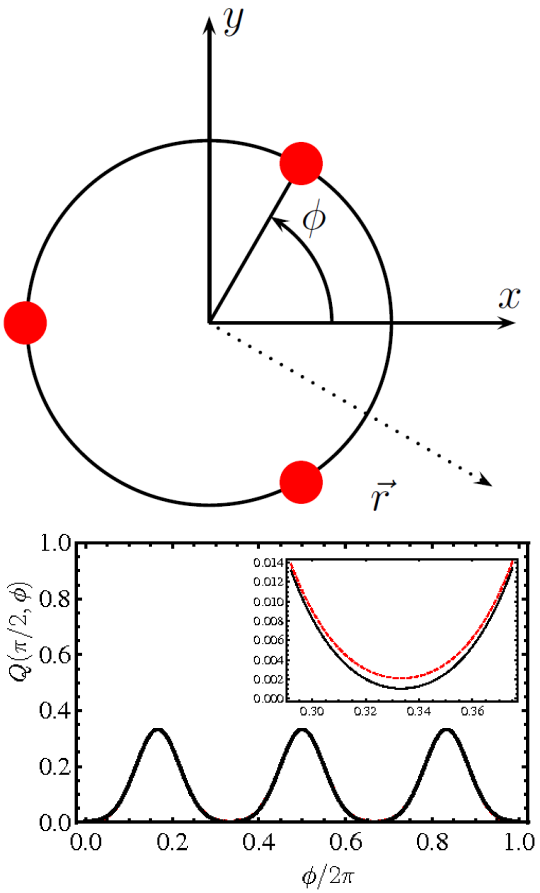

Figure 3.2: Top panel: section of the Bloch sphere on the equatorial plane $\theta = \pi/2$, parameterized by the angle ϕ. The dots indicate schematically the phase of the three coherent states which give rise to the superposition, and correspond to the maxima in the Husimi distribution illustrated in the bottom panel. The vector $\hat{r}$ defines a generic direction of the angular momentum operator for which the probability distribution $P_\phi(r)$ is considered. Our convention for the x, y axes is also indicated. Bottom panel: Dimensionless Husimi distribution $Q(\theta = \pi/2, \phi)$ for a three-component superposition of phase states (solid line) and for the corresponding incoherent mixture (dashed line), as a function of the phase ϕ for N=20 particles. The inset shows a zoom of the same function around $\phi = 2\pi/3$, illustrating the difference between the superposition state and the incoherent mixture. From Ref.[32].

3.1.2 P representation

The P distribution is defined by the implicit relation

$$\rho = \int P(\theta,\phi)|\theta,\phi\rangle\langle\theta,\phi|d\Omega, \tag{3.4}$$

with the normalization condition $(N+1)/(4\pi)\int P(\theta,\phi)d\Omega = 1$ [71, 72].

By projecting Eq.(3.4) over coherent states, one can see that the Q and P representations are related by a "convolution", in which the overlap between coherent states plays the role of a transfer function, i.e.

$$Q(\theta,\phi) = \int P(\theta',\phi')|\langle\theta,\phi|\theta',\phi'\rangle|^2 d\Omega. \tag{3.5}$$

This relation can be inverted, leading to (see Eq.(4.9) in Ref.[112])

$$P(\theta,\phi) = \sum_{l=0}^{2J}\sum_{m=-l}^{l}\frac{(2s+l+1)!}{(2s+l)!}\frac{(2s-l)!}{(2s)!}Y_{l,m}(\theta,\phi)\int d\Omega^{'''}Y^*_{l,m}(\theta^{'''},\phi^{'''})Q(\theta^{'''},\phi^{'''}), \tag{3.6}$$

where $Y_{l,m}(\theta,\phi)$ are the spherical harmonics [71].

This relation allows us to remark explicitly that, due to the overcompleteness of coherent states, the off-diagonal information $\langle\theta',\phi'|\rho|\theta,\phi\rangle$ can be entirely reconstructed solely by employing the diagonal information $\langle\theta,\phi|\rho|\theta,\phi\rangle$, this latter being the Husimi distribution. Indeed from Eq.(3.4) we obtain

$$\langle\theta',\phi'|\rho|\theta,\phi\rangle = \int d\Omega^{''}P(\theta^{''},\phi^{''})\langle\theta',\phi'|\theta^{''},\phi^{''}\rangle\langle\theta^{''},\phi^{''}|\theta,\phi\rangle, \tag{3.7}$$

which, by the use of Eq.(3.6), allows to relate $\langle\theta',\phi'|\rho|\theta,\phi\rangle$ to $Q(\theta,\phi)$.

3.1.3 W representation

The Wigner function for the SU(2) group is defined as [113, 114]

$$W(\theta,\phi) = \mathrm{tr}\left[w(\hat{\theta},\phi)\hat{\rho}\right], \tag{3.8}$$

where the Wigner operator $\hat{w}(\theta,\phi)$ is defined in terms of the spherical tensors $\hat{T}^J_{l,M} = \sqrt{\frac{2l+1}{2J+1}}\sum_{m,m'=-J}^{J}C^{J;m'}_{J,m;l,M}|J,m'\rangle\langle m,J|$ as

$$\hat{w}(\theta,\phi) = \frac{2\pi}{\sqrt{2J+1}}\sum_{l=0}^{2J}\sum_{M=-l}^{l}Y_{l,M}(\theta,\phi)\hat{T}^J_{l,M}. \tag{3.9}$$

Here $C^{J;m'}_{J,m;l,M}$ are the Clebsh-Gordan coefficients and we have explicitly indicated the representation J in the Fock states $|J,m\rangle$. The Wigner function of Fock states, coherent states and squeezed states are explicitly calculated in Ref.[113], while an analogous calculation for macroscopic superpositions is reported in Ref.[29]. In Ref.[115] an experimental tomographic reconstruction of a squeezed state Wigner function in a BJJ has been presented.

An alternative definition of the Wigner function for systems described within a SU(2) formalism has been provided in Ref.[116]. The connection with the usual Wigner function has also been established by the same authors [114]. In that work, the Wigner operator analogous to Eq.(3.9) is defined as

$$\hat{w}_s(\vec{x}) = \int_{SU(2)} d\vec{y} s(\xi) e^{i\vec{y}\cdot\vec{J}} e^{-i\vec{x}\cdot\vec{y}}, \tag{3.10}$$

where $\xi = |\vec{y}|$ and $\vec{y}/\xi = (\sin\theta\sin\phi, \sin\theta\cos\phi, \cos\theta)$, with $0 \leq \xi \leq \pi$, $0 \leq \theta \leq \pi$ and $0 \leq \phi \leq 2\pi$, $\vec{x} \in R_3$, and $s(\xi)$ is a measure; possible choices are the unity measure $s(\xi) = 1$ [116], the left and right invariant measure $s(\xi) = \frac{1}{2}\sin^2\frac{\xi}{2}$ [114], and the De Haar measure $s(\xi) = s_{\text{Haar}}(\xi) = \frac{1}{2\xi^2}\sin^2\frac{\xi}{2}$ [116]. Then, the Wigner function is obtained from the Wigner operator as

$$W_s(\vec{x}) = \text{tr}\left[\hat{w}_s(\vec{x})\hat{\rho}\right] = \int_{SU(2)} d\vec{y} s(\xi) \text{tr}\left[e^{i\vec{y}\vec{J}}\hat{\rho}\right] e^{-i\vec{x}\vec{y}}. \tag{3.11}$$

Among the interesting features of the Wigner function we mention the overlap property, which allows to express the overlap of two states by means of the integral of the product of their Wigner functions. Taking for instance the definition (3.11), this property reads

$$|\langle\Psi|\chi\rangle|^2 \propto \int_{R_3} d\vec{x} W_s^{\Psi}(\vec{x}) W_{\tilde{s}}^{\chi}(\vec{x}) \tag{3.12}$$

with $W_s^{\Psi}(\vec{x}) = \langle\Psi|\hat{w}_s(\vec{x})|\Psi\rangle$ and $s(\xi)\tilde{s}(\xi) = s_{\text{Haar}}(\xi) = \frac{1}{2\xi^2}\sin^2\frac{\xi}{2}$. Note that as a particular case, when the state $|\chi\rangle$ is a generic coherent state, equation (3.12) allows to express the Husimi distribution (3.1) as an integral of the product of the Wigner function with the Wigner function of a coherent state.

Negativities and oscillations of the Wigner function are generally ascribed to the presence of entanglement in the quantum state [29, 117–119], and several works attempt to characterize the non-classicality of a quantum state by means of the negativity of the Wigner function [29, 117–123] (as well as by the non-existence of a well-behaved P function[124, 125]).

3.2 Detection of macroscopic superpositions

We focus here on the detection of macroscopic superpositions of phase states created during the quenched dynamics of the BJJ, i.e. the states given in Eqs.(2.25), (2.27), for various numbers of components q, with $\alpha = 1$ ($|\theta = \pi/2, \phi = 0\rangle$ is thus the initial state). We address in particular the question of how to distinguish them from mixtures of coherent states. Our approach, substantially different from the one of Ref. [101] which is devoted to map out the Husimi distribution, is based on the analysis of the distributions of angular momentum eigenvalues. The results of this work are presented in Ref. [32].

3.2.1 Distributions of the eigenvalues of angular momentum operators in the equatorial plane

Consider the probability distribution of the eigenvalues r (taking integer values in the interval $[-N/2, N/2]$) of the spin operator $\hat{J}_r$, satisfying $\hat{J}_r|r\rangle = r|r\rangle$, where $\hat{r}$ is the

generic direction in the (xOy) plane defined in Eq.(1.33) (see also the bottom panel in Fig.3.2). This probability distribution for a pure state is given by

$$P_\phi(r) = |\langle r|\psi\rangle|^2; \tag{3.13}$$

for a generic density matrix $\hat{\rho}$, $P_\phi^{\hat{\rho}}(r) = \mathrm{Tr}(\hat{\rho}|r\rangle\langle r|)$. Indeed, we shall see that the shape of the distribution $P_\phi(r)$ reflects the phase content of the state projected along the direction specified by the vector $\hat{r}$.

It is instructive to calculate the probability distribution $P_\phi(r)$ starting from its generating function, defined as

$$h_\phi(\eta) = \langle e^{-i\eta\hat{J}_r}\rangle = \langle \hat{e}^{-i\eta(J_x\sin\phi - J_y\cos\phi)}\rangle = \langle \hat{R}(\zeta)\rangle \tag{3.14}$$

where $\zeta = \eta e^{-i\phi}$, $\hat{R}(\zeta)$ is the displacement operator introduced in Eq.(1.32), and $\langle ...\rangle$ indicates the quantum average over the state of the system. For a statistical mixture $h_\phi(\eta) = \mathrm{tr}\left[\hat{\rho}e^{-i\eta\hat{J}_r}\right]$. The function $h_\phi(\eta)$ generates the moments of the distribution, since

$$\langle \hat{J}_r^k\rangle = i^k \left(\frac{d}{d\eta}\right)^k h_\phi(\eta)\ |_{\eta=0}\ . \tag{3.15}$$

Let us consider for simplicity a pure state $|\psi\rangle$. Expanding Eq.(3.14) in terms of the eigenstates $|r\rangle$ of $\hat{J}_r$ yields

$$h_\phi(\eta) = \sum_{r=-N/2}^{N/2} e^{-i\eta r}|\langle\psi|r\rangle|^2 = \sum_{r=-N/2}^{N/2} e^{-i\eta r}P_\phi(r). \tag{3.16}$$

The probability distribution $P_\phi(r)$ is then readily obtained as Fourier coefficients relative to the expansion (3.16).

$$P_\phi(r) = \frac{1}{2\pi}\int_{-\pi}^{\pi} h_\phi(\eta)e^{i\eta r}d\eta; \tag{3.17}$$

note that clearly from the definition (3.14) it follows that $h_\phi(\eta+2\pi) = h_\phi(\eta)$, which allows to take finite extrema in the integral of Eq.(3.17). This approach, based on the *full counting statistics* of the probability distribution $P_\phi(r)$, allows us to stress that the knowledge of $P_\phi(r)$ contains the information equivalent to the knowledge of all the moments of the distribution itself. In turn, the latter are known once the generating function is known, as shown by Eq.(3.15) [126].

The generating function Eq.(3.14) can be calculated analytically both for coherent superpositions and incoherent mixtures. The calculation is detailed in Appendix A.1. We obtain as a final result for the generating functions

$$h_\phi^{\mathrm{mixt}}(\eta) = \frac{1}{q}\sum_{k=0}^{q-1} \tag{3.18}$$
$$\left\{|\cos\frac{\eta}{2}| + i\sin\frac{\eta}{2}\ \mathrm{sign}\left[\cos\frac{\eta}{2}\right]\sin\left(\frac{2\pi k}{q}+\frac{\pi}{q}-\phi\right)\right\}^N$$

for the incoherent mixture and

$$h_\phi^{\rm cats}(\eta) = h_\phi^{\rm mixt}(\eta) \tag{3.19}$$
$$+|\tilde{u}_0|^2 \sum_{k\neq k'=0}^{q-1} \frac{\tilde{c}_k \tilde{c}_{k'}^*}{2^N} \left\{ |\cos\frac{\eta}{2}| \left(1 + e^{-i\frac{2\pi(k-k')}{q}}\right) \right.$$
$$\left. + \sin\frac{\eta}{2}\ \mathrm{sign}\left[\cos\frac{\eta}{2}\right] \left(e^{i(\frac{2\pi k'}{q}+\frac{\pi}{q}-\phi)} - e^{-i(\frac{2\pi k}{q}+\frac{\pi}{q}-\phi)}\right) \right\}^N$$

for the coherent superposition, in the case of an odd number of components q (the even-q case is given in Appendix A.1).

As an example, we focus on the three-component superposition $|\psi(t_3)\rangle$ given in Eq.(2.27), formed at a time $t_3 = T/6$ during the quenched dynamics of the BJJ, as we have seen in Sec.2.5.1. Considering also the corresponding mixture, we calculate the probability distributions of the eigenvalues in the x and y direction, namely $P_{\pi/2}(r)$ and $P_\pi(r)$ respectively, by using Eq.(3.17) and (3.19). As illustrated in the top panels of Fig.3.3, these distributions are peaked around the semiclassical values given in Eq.(1.30), i.e., in the specific case $\langle \hat{J}_x \rangle = (N/2)\cos(\pm\pi/3)$, $(N/2)\cos(\pi)$ and $\langle \hat{J}_y \rangle = (N/2)\sin(\pm\pi/3)$, $(N/2)\sin(\pi)$. The distribution $P_{\pi/2}(r)$ displays a noticeable difference between the mixture and the coherent superposition: the latter displays oscillations which are absent in the former. The presence of fringes in the distribution of the eigenvalues of angular momentum operators for superposition states was also noticed in the context of the dynamics of the quantum non-linear rotor by Sanders [127]. The function $P_\pi(r)$ instead does not display fringes for the three-component superposition because its components do not overlap when projected along the y-direction (see Fig.3.2, bottom panel); as a result no interference effect takes place in this case.

This analysis extends to higher-component superpositions (see for instance the bottom panels of Fig.3.3, in which we plot the $P_{\pi/2}(r)$ and $P_\pi(r)$ probability distributions for the four-component cat state $|\psi(t_4)\rangle$).

We note that the two-component phase cat state $|\psi(t_2)\rangle$ given in Eq.(2.26) (with $\alpha = 1$), cannot instead be distinguished from the corresponding incoherent mixture by this method, due to the specific form of its state components (see Section 3.2.1.b).

Finally, the full counting statistics of the operator $\hat{J}_z$ could also be defined, but does not yield any useful information about the considered superpositions of phase states as it coincides with the binomial distribution $P_{\phi=0}(r) = \frac{1}{2^N}\binom{N}{\frac{N}{2}+r}$ of the initial coherent state. This can be easily understood since, as mentioned in Sec.2.5.1, the quenched dynamics leading to the creation of phase cat states conserves the number operator, and hence all of its moments.

3.2.1.a Experimental realization of this method

For each choice of the angle ϕ the probability distribution $P_\phi(r)$ can be experimentally accessed by repeated measurements of the corresponding angular momentum operator $\hat{J}_r$. Indeed, since the eigenstates of $\hat{J}_r$ form an orthonormal basis, each superposition state decomposes as $|\psi_q\rangle = \sum_{r=-N/2}^{N/2} c_r^q |r\rangle$ with $c_r^q = \langle r|\psi_q\rangle$. Then, according to the postulates of quantum mechanics, after a (projective) measurement of $\hat{J}_r$ the state jumps to the state

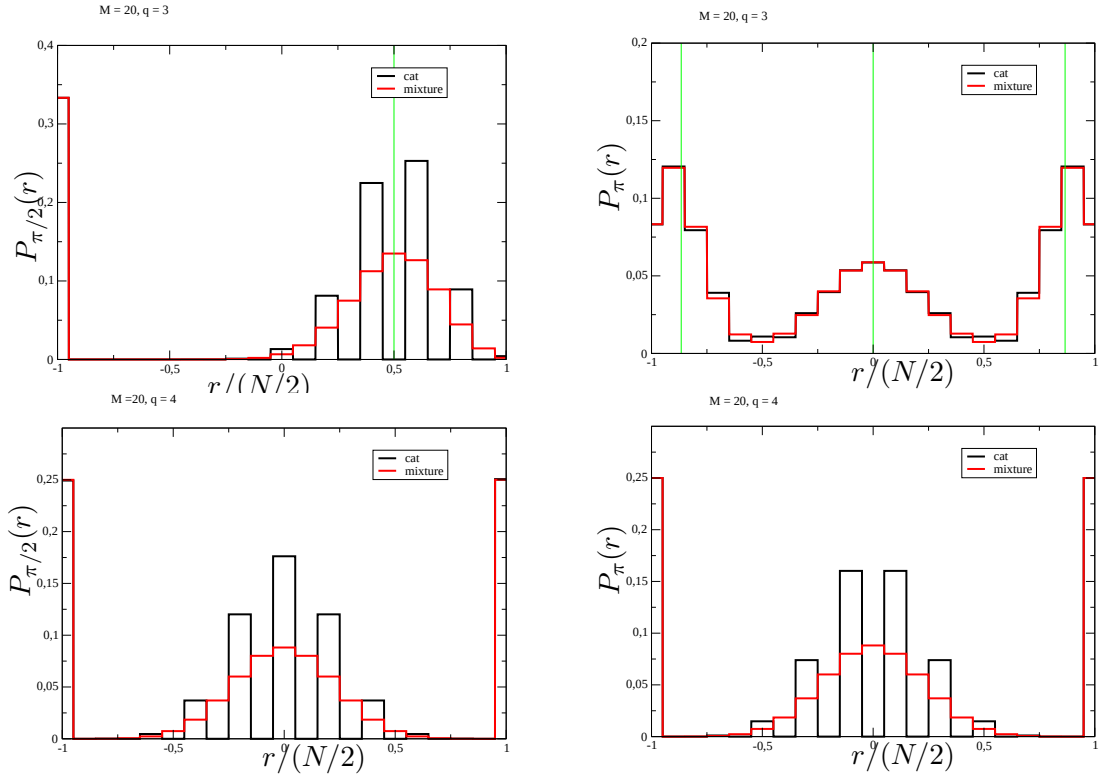

Figure 3.3: Top panels: eigenvalue distribution $P_\phi(r)$ corresponding to $\hat{J}_x$ ($\phi = \pi/2$) and $\hat{J}_y$ ($\phi = \pi$) for the three-component coherent superposition (black lines) as well as for the incoherent mixture of the same phase states (red lines) with $N = 20$. The vertical lines correspond to the semiclassical values for $\langle \hat{J}_x \rangle$ and $\langle \hat{J}_y \rangle$ for the coherent states entering the superposition. Bottom panels: analogous distributions for the four-component case.

$|r\rangle$ with probability $P_\phi(r) = |c_r^q|^2$ and the corresponding outcome of the measurement is r. The full distribution $P_\phi(r)$ is obtained by repeating this procedure many times, each time preparing the system in the same initial state[1]. The measurement of $\hat{J}_r$ for a generic angle ϕ can be achieved by measuring the population imbalance $\hat{J}_z$ between the two modes after proper rotations of the state over the Bloch sphere, as explained in Sec. 1.4.4.

One of the first questions arising about the experimental feasibility of this protocol, which would provide an interesting extension of our work, is how robust the probability distributions of cat states are, if we take into account a possible error in the times at which the shots (i.e., the measurements of $\hat{J}_r$) are taken. A rough estimate of that effect is provided in Appendix A.2.

In Sec.5.1.3.c we will discuss how the probability distributions $P_\phi(r)$ for macroscopic superpositions are affected by the presence of noise.

3.2.1.b Detection of the NOON state

In Reference [128] a similar method has been proposed for the detection of a NOON state as the one given in Eq.(2.13), or with a possible relative phase between the two components, i.e.

$$|\psi_{\mathrm{NOON}_\beta}\rangle = \frac{(|\theta = 0, \phi = 0\rangle + e^{i\beta}|\theta = \pi, \phi = 0\rangle)}{\sqrt{2}}. \tag{3.20}$$

In this case, the probability distribution $P_\phi(r)$ corresponds to the profile of the NOON state when projected on an axes in the equatorial plane, and can be more easily calculated by rotating both the superposition state and the eigenstates of the angular momentum operators by $\pi/2$ on the Bloch sphere, i.e. by transforming the eigenstates $|r\rangle$ in Fock states and the state $|\psi_{\mathrm{NOON}_\beta}\rangle$ in a phase cat state with components along the direction identified by ϕ, $|\psi_{\mathrm{PHASE}_{\phi,\beta}}\rangle = (|\theta = \pi/2, \phi\rangle + e^{i\beta}|\theta = \pi/2, \phi + \pi\rangle)/\sqrt{2}$. Thus we obtain

$$\langle r|\psi_{\mathrm{NOON}_\beta}\rangle = \langle n|\psi_{\mathrm{PHASE}_{\phi,\beta}}\rangle = \frac{1}{2^{\frac{N+1}{2}}}\binom{N}{\frac{N}{2}+n}^{\frac{1}{2}} e^{-i\phi(\frac{N}{2}+n)}\left[1 + e^{i\beta}(-1)^{(\frac{N}{2}+n)}\right], \tag{3.21}$$

which leads to

$$P_\phi(r) = \frac{1}{2^N}\binom{N}{\frac{N}{2}+r}\left[1 + \cos\beta(-1)^{(\frac{N}{2}+r)}\right]. \tag{3.22}$$

As seen in Eq.(3.22), the probability distribution $P_\phi(r)$ does not depend on the direction ϕ and hence is isotropic in the (xOy) plane. The contrast of the interference fringes depends on the relative phase β between the two components of the state. Note in particular that for $\beta = \pi/2$ the distribution $P_\phi(r)$ does not display any fringes, despite the fact that it is a macroscopic superposition. A similar argument can be applied to explain the absence of fringes in the distribution $P_{\pi/2}(r)$ for the two-component phase state. For $\beta = 0$ the contrast is maximal and we obtain

$$P_\phi(r) = \begin{cases} \frac{1}{2^{N-1}}\binom{N}{\frac{N}{2}+r} & \text{if } r \text{ is even} \\ 0 & \text{if } r \text{ is odd} \end{cases} \tag{3.23}$$

[1]Technically, in typical experiments the system is destroyed after a measurement of $\hat{J}_r$. Therefore, one should model the process by a Positive Operator Valued Measure (POVM) rather than by a projective measurement [89]. However, here we are only interested in the outcomes r. These are predicted to be the same for both POVM and projective measurements, even if the latter do not describe properly the state of the system after the measurement.

This corresponds to a binomial envelope centered at $n = 0$, with interference fringes having a unit spacing.

3.2.2 Quasi-probability distribution in spin variables

In our work, Ref. [32], we have addressed the issue of the two-dimensional (2D) tomographic reconstruction $f(x, y)$ of the phase content of a state in the (xOy) plane. This is based on the concept of the Radon transform, also exploited in medical imaging [129–132]. The same principle has been also used for coherent superpositions with cavity photons [133]. The idea is to obtain a 2D distribution function $f(x, y)$ using all the one-dimensional projections $P_\phi(r)$ at each ϕ in the interval $[0, 2\pi]$.

We define the two-dimensional distribution $f(x, y)$ by the implicit expression

$$P_\phi(r) = \int_{-\infty}^{\infty} f(x,y)ds = \int_{-\infty}^{+\infty} dx \int_{-\infty}^{+\infty} dy f(x,y)\delta(r - x\sin\phi + y\cos\phi), \tag{3.24}$$

where $s = x\cos\phi + y\sin\phi = \vec{l}\cdot\hat{p}_1$ with $\vec{l} = x\hat{x} + y\hat{y}$ and $\hat{p}_1$ identifies the direction in the equatorial plane of the Bloch sphere perpendicular to $\hat{r}$, as expressed by the first line of Eq.(2.7). Equation (3.24) can be inverted using the definition of the generating function in Eq. (3.16). In order to do this, it is convenient to express $P_\phi(r)$ as the Fourier transform of a non-periodic characteristic function, obtained by multiplying it by a window $\chi(\eta)$ of width 2π. Namely, we define

$$\tilde{h}_\phi(\eta) = h_\phi(\eta)\chi_{[-\pi,\pi]}(\eta), \tag{3.25}$$

with $\chi_{[-\pi,\pi]}(\eta) = \frac{1}{2}\left(H(-(\eta+\pi) + H(\eta-\pi))\right)$, and $H(x)$ the Heaviside function. This modified generating function is related to the probability distribution as

$$\tilde{h}_\phi(\eta) = \int_{-\infty}^{\infty} P_\phi(r)e^{-i\eta r}dr, \tag{3.26}$$

and inversely $P_\phi(r) = \frac{1}{2\pi}\int_{-\infty}^{\infty}\tilde{h}(\eta,\phi)e^{i\eta r}d\eta$. An important remark is that the physical values of $P_\phi(r)$ are only the ones taken for integer values of the variable r, which correspond to the eigenvalues of a certain angular momentum operator defined by ϕ. In between, it assumes interpolating values; in the same way, for $r > N/2$ or $r < -N/2$, $P_\phi(r)$ oscillates in such a way so to recover zero for integers values of r (see Fig.3.4).

Now we seek the explicit expression of $f(x, y)$ in terms of the characteristic function $h_\phi(\eta)$. We substitute Eq.(3.24) in Eq.(3.26) and we use the integral representation of the delta function, $\delta(r - x\sin\phi + y\cos\phi) = \int_{-\infty}^{\infty}\frac{d\omega}{2\pi}e^{i\omega(r - x\sin\phi + y\cos\phi)}$, obtaining

$$\tilde{h}_\phi(\eta) = \int_{-\infty}^{\infty} dr \int_{-\infty}^{\infty} dxdy f(x,y) \int \frac{d\omega}{2\pi} e^{-i(\eta-\omega)r}e^{-i\omega(x\sin\phi - y\cos\phi)}. \tag{3.27}$$

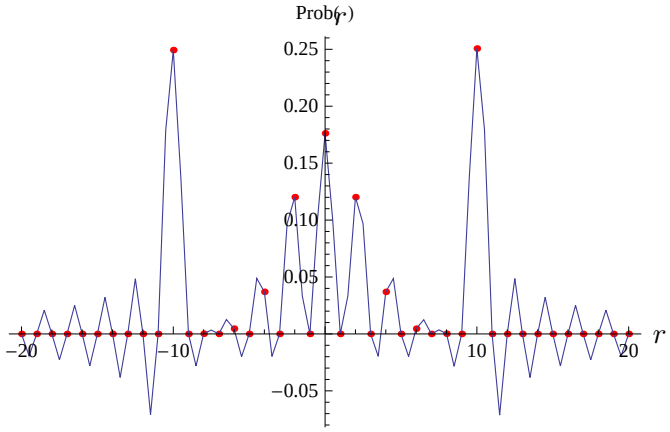

Figure 3.4: Eigenvalue distribution $P_\phi(r)$ corresponding to $\hat{J}_x$ ($\phi = \pi/2$) for the four-component coherent superposition (solid lines) with $N = 40$. The red dots are the physical values corresponding to the discrete eigenvalues, also reported in Fig.3.3, while the blue line shows the extension on the real field of the function $P_\phi(r)$.

Using that $\frac{1}{2\pi}\int_{-\infty}^{\infty} e^{-i(\eta-\omega)r}dr = \delta(\omega-\eta)$ and performing the integral in $d\omega$, yields[2]

$$\begin{aligned}\tilde{h}_\phi(\eta) &= \int_{-\infty}^{\infty} dxdy f(x,y) e^{-i\eta(x\sin\phi - y\cos\phi)} = \\ &= \mathcal{F}^*\left[f(x,y)\right](\eta\sin\phi, -\eta\cos\phi). \end{aligned} \tag{3.29}$$

We have now to invert the Fourier transform in Eq.(3.29). Defining the variables

$$\begin{aligned}\eta\sin\phi &= \omega_x \\ -\eta\cos\phi &= \omega_y, \end{aligned} \tag{3.30}$$

readily leads us to

$$f(x,y) = \left(\frac{1}{2\pi}\right)^2 \int_{-\infty}^{\infty} d\omega_x d\omega_y \tilde{h}_\phi(\eta) e^{i(\omega_x x + \omega_y y)}. \tag{3.31}$$

The definition (3.30) implies that $|\eta| = \sqrt{\omega_x^2+\omega_y^2}$ and $\phi = \arctan\left(-\frac{\omega_x}{\omega_y}\right)$. Rewriting Eq.(3.31) in terms of these variables makes appear the Jacobian of the transformation, and we obtain

$$\begin{aligned} f(x,y) &= \left(\frac{1}{2\pi}\right)^2 \int_{-\infty}^{\infty} d\eta|\eta| \int_0^{\pi} d\phi \tilde{h}_\phi(\eta) e^{i\eta(\sin\phi x - \cos\phi y)} \\ &= \left(\frac{1}{2\pi}\right)^2 \int_{-\pi}^{\pi} d\eta|\eta| \int_0^{\pi} d\phi h_\phi(\eta) e^{i\eta(\sin\phi x - \cos\phi y)}, \end{aligned} \tag{3.32}$$

[2] We choose here the definitions:

$$\begin{aligned}\mathcal{F}\left[f(x)\right](\omega) &= \frac{1}{2\pi}\int_{-\infty}^{\infty} dx f(x) e^{i\omega x} \\ \mathcal{F}^*\left[g(\omega)\right](x) &= \int_{-\infty}^{\infty} d\omega g(\omega) e^{-i\omega x}. \end{aligned} \tag{3.28}$$

$f(x,y)=\left(\frac{1}{2\pi}\right)^2\int_C d^2\zeta \mathrm{tr}[\hat{\rho}\hat{R}(\zeta)]e^{-2i(x\zeta_2+y\zeta_1)}$	$W(x,p)=\left(\frac{1}{\pi}\right)^2\int d^2\lambda \mathrm{tr}[\hat{\rho}\hat{D}(\lambda)]e^{-2i(x\lambda_2-p\lambda_1)}$
$\hat{R}(\zeta)=e^{\zeta\hat{J}_+-\zeta^*\hat{J}_-} \qquad \hat{J}_+=\hat{J}_x+i\hat{J}_y$	$\hat{D}(\lambda)=e^{\lambda\hat{a}^\dagger-\lambda^*\hat{a}} \qquad \hat{a}^\dagger=\hat{x}-i\hat{p}$
$\lvert\zeta\rangle=\hat{R}(\zeta)\lvert -J\rangle \qquad \zeta=\zeta_1+i\zeta_2$	$\lvert\lambda\rangle=\hat{D}(\lambda)\lvert 0\rangle \qquad \lambda=\lambda_1+i\lambda_2$
$\int_{-\infty}^{\infty}dx f(x,y)=P(y)=\langle y\lvert\hat{\rho}\rvert y\rangle$	$\int_{-\infty}^{\infty}dx W(x,p)=P(p)=\langle p\lvert\hat{\rho}\rvert p\rangle$
$\int_{-\infty}^{\infty}dy f(x,y)=P(x)=\langle x\lvert\hat{\rho}\rvert x\rangle$	$\int_{-\infty}^{\infty}dp W(x,p)=P(x)=\langle x\lvert\hat{\rho}\rvert x\rangle$

Table 3.1: Comparison illustrating the analogies between the 2D distribution function $f(x,y)$ and the quantum-optics Wigner function. By $\int_C d^2\zeta$ we mean $\int_0^\pi d\eta\eta\int_0^{2\pi}d\phi$. We denoted here $P_\pi(r)$ as $P(y)$ and $P_{\pi/2}(r)$ as $P(x)$ and the eigenstates satisfying $\hat{J}_{x,y}|r\rangle = r|r\rangle$ as $|x\rangle$ and $|y\rangle$ respectively, which should be taken on integer values only.

where in the last step we made use of Eq.(3.25). It is possible to rewrite Eq.(3.32) in terms of the natural intervals of definition of the variables η and ϕ, according to Ref.[71]. The calculation, detailed in Appendix A.3, yields as a final result

$$f(x,y)=\frac{1}{(2\pi)^2}\int_0^\pi \eta d\eta\int_0^{2\pi}d\phi\, h_\phi(\eta)e^{i\eta(x\sin\phi-y\cos\phi)}. \tag{3.33}$$

Equation (3.33) represents a quasi-probability distribution for the non-commuting operators J_x and J_y. It is closely analogous to the quantum optics Wigner function, which also can be expressed from the characteristic function of the probability distribution of the quadratures (see Table 3.1, and also Eq.(3.8) in Ref.[131]). In terms of SU(2) Wigner functions it could be regarded as the two-dimensional projection on the equatorial plane of the Bloch sphere of the Wigner function defined in Eq.(3.11). Indeed, as shown in Appendix A.4, integrating Eq.(3.11) along the variable x_3 renders a two-dimensional function with structure similar to Eq.(3.33).

Figure 3.5 illustrates the 2D quasi-probability distribution $f(x,y)$ for the three and four component coherent superpositions, and for the corresponding incoherent mixtures. In the top left panel $f(x,y)$ shows three pronounced maxima in correspondence with the coherent states composing the three-component macroscopic superposition. It also displays oscillations between the maxima, due to interferences between the components. The 2D quasi-probability function evaluated for the corresponding incoherent mixture (bottom left) also exhibits the main peaks but the fringes are strongly suppressed, the small remaining oscillations being intrinsically due to the definition of the function $f(x,y)$ as a Fourier transform in angular variables on a compact interval.

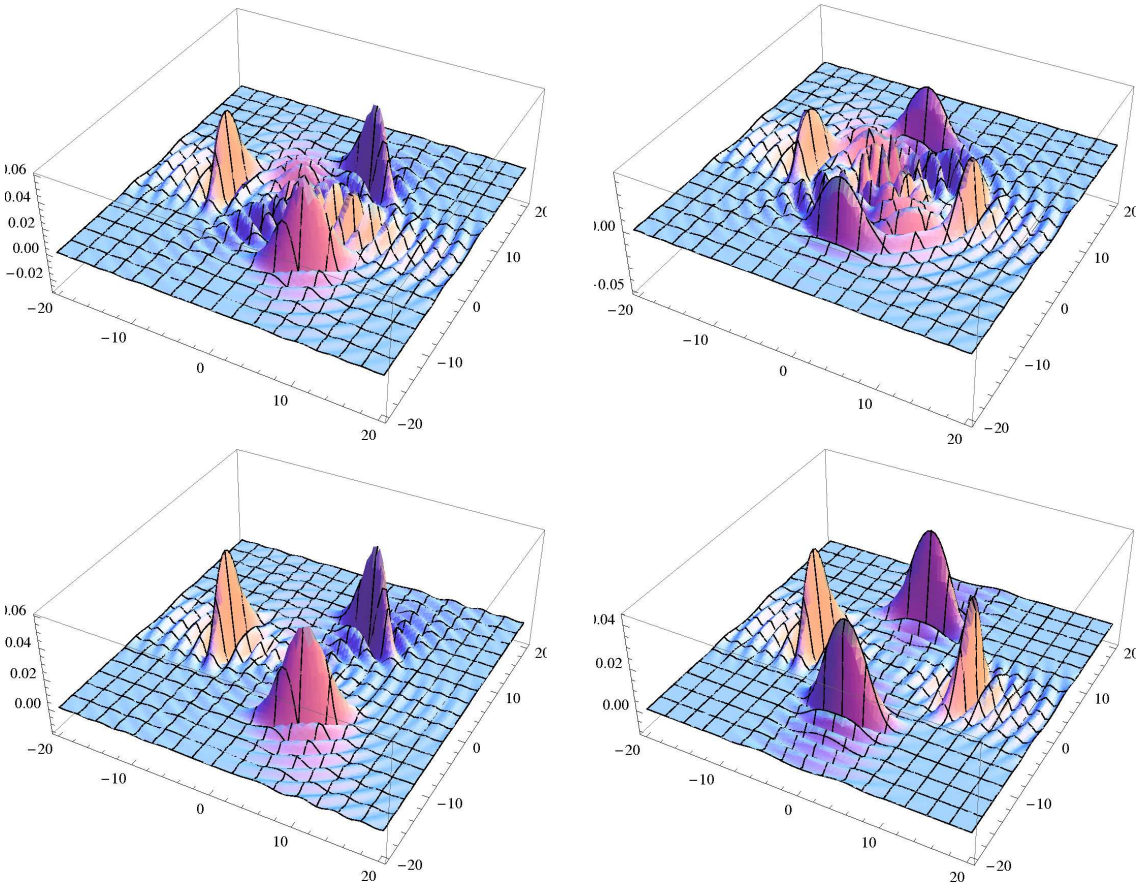

Figure 3.5: Dimensionless 2D quasi-probability distribution $f(x, y)$ in the $(x0y)$ plane (dimensionless) for the three- (left panels) and four- (right panels) component coherent superpositions with $N = 20$ particles (top panels), and for the corresponding incoherent mixtures (bottom panels).

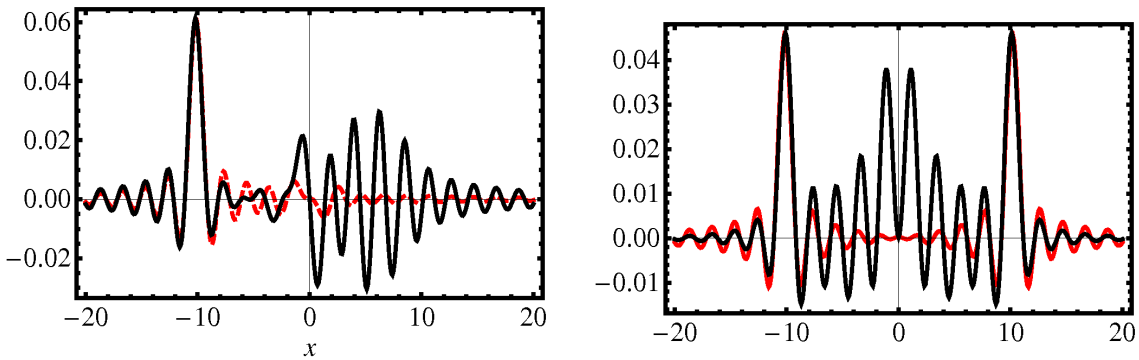

Figure 3.6: Sections $f(x, 0)$ of the quasi-probability distributions of Fig. 3.5 (solid line) in the direction $y = 0$ for the-three component superposition (left) and the four-component superposition (right). The dashed line represents the quasi-probability function $f(x, 0)$ for the corresponding incoherent mixture of the same three coherent states.

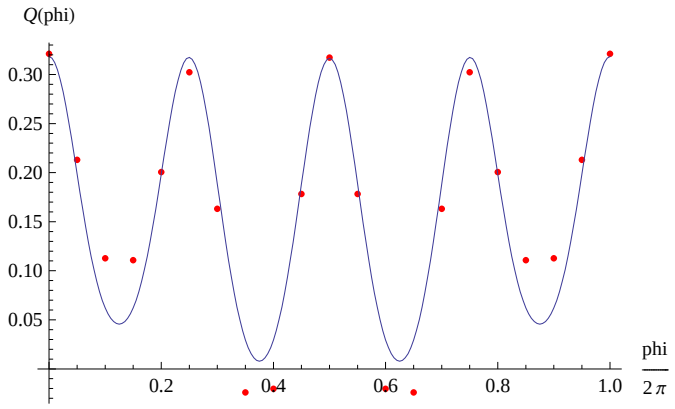

Figure 3.7: Reconstruction of the Husimi distribution $Q(\theta = \pi/2, \phi)$ of a four component superposition with $N = 20$ by means of the overlap property in terms of the function $f(x, y)$. The red dots correspond to the points reconstructed this way, while the solid blue curve is the exact Husimi function.

A complete tomographic protocol allowing for the full reconstruction of the quantum state requires the measurement of angular momentum operators in *all* the directions of the Bloch sphere, and not only in the equatorial plane (see Ref.[115, 131, 134]).

Although the function $f(x, y)$ is not in one-to-one correspondence with the state of the system, for the specific superpositions of phase states which we consider here it yields the main information about the phase structure of the state, and shares many properties with a Wigner function. For example, the definition (3.24) automatically implies that the marginal probability distribution $P_\phi(r)$ can be obtained by integration of $f(x, y)$ along the perpendicular direction, in analogy to the quantum optics Wigner function (see Table 3.1, and Eq.(A.43)-(A-44) in Ref.[135]).

Furthermore, the phase profile of the state (i.e., the Husimi distribution on the equator of the Bloch sphere $Q(\theta = \pi/2, \phi)$) can be qualitatively reconstructed by exploiting the overlap property similarly to Eq.(3.12). An indication of this fact for the four-component cat state is provided in Fig.3.7. The reconstruction shown therein is however only qualitative because we have used as an estimate of the phase profile the function $\sum_x \sum_y \tilde{f}^{\psi}(x, y)\tilde{f}^{\phi}(x, y)$, where $\tilde{f}(x, y) = \left(\frac{1}{2\pi}\right)^2 \Delta_x \Delta_y \sum_{k_x=1}^{P} \sum_{k_y=1}^{P} \tilde{W}\left(\frac{\zeta_1(k_x)}{2}, \frac{\zeta_2(k_y)}{2}\right)$ $\times e^{-iy\zeta_1(k_x)} e^{-ix\zeta_2(k_y)}$ is a discretized version of the function $f(x, y)$, and where the summation interval is taken to be a square instead of a circle.

Note also that the two-dimensional probability distribution $f(x, y)$ could be in principle experimentally reconstructed. This should be done by reconstructing the $P_\phi(r)$ along many different directions with the protocol presented in Sec.3.2.1.a; the knowledge of the values assumed by this function for integers r allows to reconstruct $h_\phi(\eta)$ with the use of Eq.(3.16); then, the two-dimensional distribution $f(x, y)$ can be reconstructed by using the Radon inverse transformation given in Eq.(3.33). Note that a direct inversion of Eq.(3.24) to obtain $f(x, y)$ from $P_\phi(r)$ would involve an improper integral, to be taken in the sense of a principal value [130].

In the case of an external BJJ set-up, a more direct fashion to obtain the 1D profiles $P_\phi(r)$ in any direction of the $(x0y)$ plane could be implemented, based on the measurement of the atomic momentum distribution. This idea is drawn from the similarity between

the expression for the momentum distribution in the two-mode model, Eq.(1.44), and the expression for the angular momentum operator in the plane (xOy), Eq.(1.33). This follow-up of our work is described in Chap. 6.

Chapter 4

Exploitation of useful entangled states

In this chapter we introduce atom interferometry, and we recall the criterium which defines the usefulness of a quantum state for phase estimation. In particular, we recall that squeezed states, macroscopic superposition states and Fock states are useful quantum states, and can be used in metrology to outperform the classical limit of precision. In this spirit, we then quantify the usefulness of various states of the BJJ: first, its ground state, and then the states which are created during its time evolution under the quenched dynamics introduced in Sec.2.5.1. The details of the latter analysis can also be found in our work Ref.[25].

Dans ce chapitre nous introduisons l'interférométrie atomique, et nous rappelons le critères qui définissent l'utilité d'un état quantique pour l'estimation de phase. En particulier nous rappelons que les états comprimés, les superpositions d'états cohérents et les états de Fock sont des états quantiques utiles, qui peuvent être utilisés en métrologie pour surmonter la limite standard de précision. Dans cet esprit, nous quantifions ensuite l'utilité de plusieurs états quantiques de la BJJ; tout d'abord, de son état fondamental, et ensuite des états qui sont créés pendant l'évolution dynamique trempée introduite en section 2.5.1. Les détails de cette analyse peuvent aussi être trouvés dans notre publication Ref.[25].

4.1 Atom interferometry

4.1.1 The general interferometric procedure

The goal in interferometry, which is part of the *theory of estimation of a parameter*, is to estimate an unknown phase shift φ with the highest possible precision. Since there is no observable associated with the phase shift, some other observable is measured in the output state; out of one or more such measurements, the original phase shift is then inferred.

In atom interferometry, an input state is first transformed into a superposition of two modes, analogous to the two arms of an optical interferometer. These modes acquire distinct phases φ_1 and φ_2 during the subsequent quantum evolution. They are are finally recombined to read out interference fringes, from which the phase difference $\varphi = \varphi_1 - \varphi_2$

is inferred. The interferometric sequence can be described by means of rotation matrices acting on the two-mode vector state, that is, by SU(2) rotation matrices in the Schwinger representation introduced in Sec.1.4 [74]; the generators of the rotations are the angular-momentum operators $\hat{J}_x$, $\hat{J}_y$, and $\hat{J}_z$ defined in Eq.(1.22). The total number N of atoms in the condensate is assumed to be fixed.

Let us give a practical example. Consider as an initial state of the interferometric sequence the state in which all atoms are initially in one of the two modes - say, the mode $j = 1$. The input state is then the Fock state $|n = N/2\rangle$, coinciding with the coherent state at the north pole of the Bloch sphere; an interferometric sequence with a different initial state is analyzed for instance in Ref. [74]. A rotation of the atomic state around the y-axes by an angle of $\pi/2$ radians is then applied to the input state, leading to the phase state $|\theta = \pi/2, \phi = 0\rangle$. As explained in Chap. 1, this amounts in the internal BJJ set-up to the application of a $\pi/2$ pulse with frequency in resonance with the two internal levels, while in the external BJJ set-up a rotation around $\hat{J}_y$ would be possible by combining successive rotations around $\hat{J}_x$ and $\hat{J}_z$. This plays the role of a beam splitter in optical interferometers. Then the state is rotated around the z-axes by the free time evolution, the phase accumulation being due to a different energy shift between the two states. For instance, placing an external BJJ in the vertical direction provides an energy difference of the two modes proportional to the gravity constant g [136]. This rotation is the analog of the different phase paths in the two arms of an optical interferometer. Finally, by recombining the two paths, the state is rotated again around the y-axes by an angle of $-\pi/2$ radians. The consecutive rotations of the input state on the Bloch sphere are represented in Fig.4.1. The interferometric sequence can thus be described by a succession of three rotations, and the output state of the linear interferometer is

$$|\psi_{\rm out}\rangle = e^{-i\frac{\pi}{2}\hat{J}_y} e^{-i\varphi\hat{J}_z} e^{i\frac{\pi}{2}\hat{J}_y} |\psi_{\rm in}\rangle = e^{-i\varphi\hat{J}_x}|\psi_{\rm in}\rangle, \tag{4.1}$$

where $|\psi_{\rm in}\rangle$ is the input state, assumed here to be pure. Note that performing rotations of the kind presented in this section requires the non-linear term in the Hamiltonian (1.24) to be ineffective. In the internal BJJ set-up the rotations are typically realized fast enough to neglect the non-linear effects induced by the interactions [8], while in the external set-up Feschbach resonances may be employed. The residual effect of interactions on the interferometric sequence has been recently addressed in Refs. [137, 138].

In a typical experiment one has access to the probability distribution associated with the operator $\hat{J}_z$ measured with respect to the output state. Note however that due to the argument presented in Sec.1.4.4 in practice the angular momentum in any direction can be detected, by means of a suitable further rotation of the quantum state preceeding the measurement of $\hat{J}_z$. The quantum distribution of the measured observable depends on the phase shift φ. In the simple example under consideration, the average value $\langle \hat{J}_z \rangle_{\rm out}$ in the output state gives

$$\begin{aligned} \langle \hat{J}_z \rangle_{\rm out} &= \langle \psi_{\rm in}| e^{i\varphi\hat{J}_x} \hat{J}_z e^{-i\varphi\hat{J}_x} |\psi_{\rm in}\rangle \\ &= \cos\varphi \langle \hat{J}_z \rangle_{\rm in} + \sin\varphi \langle \hat{J}_y \rangle_{\rm in} = -\frac{N}{2}\cos\varphi, \end{aligned} \tag{4.2}$$

which displays Ramsey fringes as a function of the phase shift φ, and in the last step we have made use of Eq.(1.26) for the input state considered. The variance $(\Delta \hat{J}_z)^2_{\rm out} =$

$\langle \hat{J}_z^2 \rangle_{\rm out} - (\langle \hat{J}_z \rangle_{\rm out})^2$ reads

$$\begin{aligned}(\Delta \hat{J}_z)^2_{\rm out} &= \langle \psi_{\rm in}| e^{i\varphi \hat{J}_x} \hat{J}_z^2 e^{-i\varphi \hat{J}_x} |\psi_{\rm in}\rangle - \cos^2\varphi \langle \hat{J}_z^2 \rangle_{\rm in} \\ &= \sin^2\varphi \langle \hat{J}_y^2 \rangle_{\rm in} + \cos\varphi \sin\varphi \langle (\hat{J}_z \hat{J}_y + \hat{J}_y \hat{J}_z) \rangle_{\rm in} \\ &= \frac{N}{4} \sin^2\varphi. \end{aligned} \tag{4.3}$$

The phase shift is then determined by means of a statistical estimator, i.e. an arbitrary function $\varphi_{\rm est}(n_1, n_2, ..., n_m)$ of the m outcomes of the measurements on the output state, in our example of the observable $\hat{J}_z$. Such an estimator is said to be *unbiased* if, when repeating many times the experiment, the average value obtained corresponds to the true value of the phase shift, i.e.

$$\langle \varphi_{\rm est} \rangle = \int dn_1 dn_2 ... dn_m \varphi_{\rm est}(n_1, n_2, ..., n_m) P(n_1, n_2, ..., n_m|\varphi) = \varphi, \tag{4.4}$$

where for independent measurements the probability of the outcomes $(n_1, n_2, ..., n_m)$ under the phase shift φ can be expressed as a product of the *likelihoods*

$$P(n|\varphi) = |\langle n|\psi_{\rm out}\rangle|^2 = |\langle n| e^{-i\varphi \hat{J}_x} |\psi_{\rm in}\rangle|^2, \tag{4.5}$$

i.e. $P(n_1, n_2, ..., n_m|\varphi) = \prod_{i=1}^m P(n_i|\varphi)$ [1]. An example of unbiased estimator is the maximum likelihood φ_{ML}, i.e. the value of φ which maximizes $P(n_1, n_2, ..., n_m|\varphi)$ [2]. Details about the practical experimental determination of the likelihoods and the construction of the corresponding estimator can be found in Ref. [139].

The phase precision, given by the mean square fluctuations

$$(\Delta\varphi)^2 = \int dn_1 dn_2 ... dn_m (\langle \varphi_{\rm est} \rangle - \varphi_{\rm est}(n_1, n_2, ..., n_m))^2, \tag{4.6}$$

depends on the chosen estimator, on the input state and on the measurement performed on the output state. For the maximum likelihood estimator a possible choice is to take the 30 % confidence interval.

A heuristic argument to calculate the phase precision, valid when the input state is gaussian (as e.g. it is the case for coherent states and squeezed states) is based on linear error propagation, which yields [14, 74]

$$\Delta\varphi = \frac{(\Delta \hat{J}_z)_{\rm out}}{{\rm d}\langle \hat{J}_z \rangle_{\rm out}/{\rm d}\varphi}. \tag{4.7}$$

In particular, for the input coherent state $|n = N/2\rangle$ that we are considering in our example, Eqs.(4.2) and (4.3), Eq.(4.7) render

$$\Delta\varphi = \Delta\varphi_{\rm best} = \frac{1}{\sqrt{N}} \equiv \Delta\varphi_{SN}, \tag{4.8}$$

corresponding to the *shot-noise limit* [15], i.e. the typical precision obtained with the use of coherent states. Here the suffix "best" indicates that in our example of interferometric scheme expressed by Eq.(4.1), the observable $\hat{J}_z$ which we are supposing to measure in the output state yields the most precise estimation. We shall clarify and generalize this point it in Sec.4.1.3.

[1] We have denoted the average in Eq.(4.4) via an integral to be more general and include the case of continuous outcomes. In the case of our experiment the values of the output are discrete and the integral can be replaced by a summation.

[2] An alternative unbiased estimator, more suitable than the maximum likelihood in the case in which only few outcomes are available, is a baesyan estimator [16].

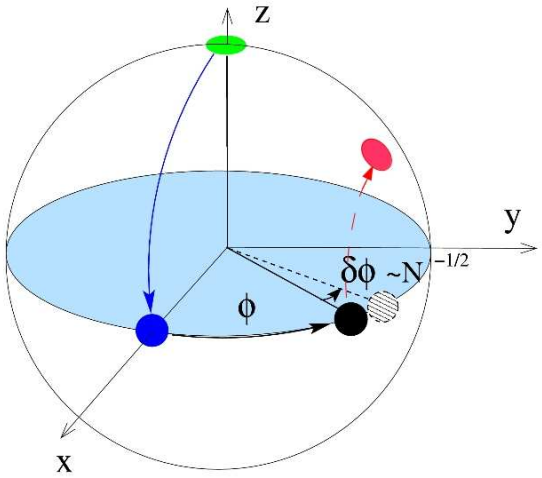

Figure 4.1: Rotations on the Bloch sphere in the interferometric scheme: the input coherent state at the north pole (green disk) is rotated around the y-axes by an angle $\pi/2$ (blue disk) and afterwards around the z-axes by the unkown phase φ (black disk). The precision $\Delta\varphi$ on the estimation of φ is larger than the size $\sqrt{N}/2$ of the disk, representing the angular momentum fluctuations, divided by the radius $N/2$ of the sphere. In the output state (red disk) the number operator is measured.

4.1.2 Use of squeezed states in atom interferometry

If instead of a coherent state we use as input state for the interferometer a squeezed state, an enhanced precision in the inferred phase can be obtained [14]. The squeezed state should be suitably chosen, such that in the output state the fluctuations in the measured direction are reduced. This can be intuitively understood by looking at Fig. 4.2: the squeezing in the y direction is translated in reduced fluctuations of $\hat{J}_z$ in the output state, which lead to an enhancement of the precision in the phase estimation according to Eq.(4.7). Indeed, it can be proved that *for a squeezed state*

$$\Delta\varphi_{\rm best} = \frac{\xi_{\hat{n}}}{\sqrt{N}} = \xi_{\hat{n}}\Delta\varphi_{SN}, \tag{4.9}$$

where we recall that $\xi_{\hat{n}}$ is the squeezing parameter, defined in Eq.(2.6). It follows that the squeezing condition $\xi_{\hat{n}} < 1$ implies $\Delta\varphi_{\rm best} < \Delta\varphi_{SN}$. Indeed, Eq.(2.9) provides a sufficient (but not necessary for more general states) condition for sub-shot noise sensitivity [14] - in addition to being a sufficient condition for multiparticle entanglement, as seen in Sec.2.3.1. We stress that to take a full advantage of such a resource, the angular momentum operator must be measured in the direction of squeezing in the output state.

4.1.3 Cramér-Rao lower bound and quantum Fisher information

The output state of a more general atom interferometer is

$$\hat{\rho}_{\rm out}(\varphi) = e^{-i\varphi\hat{J}_n}\hat{\rho}_{\rm in}e^{i\varphi\hat{J}_n}, \tag{4.10}$$

where $\hat{\rho}_{\rm in}$ is the input density matrix and $\hat{n}$ the unit vector representing the effective rotation axes associated with a given interferometric sequence. The likelihood is now

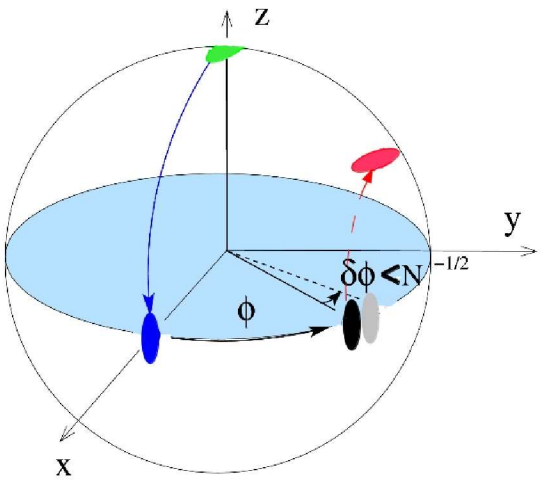

Figure 4.2: Rotations on the Bloch sphere in the interferometric scheme when the input state is a squeezed state: the input state, squeezed along the y direction (green ellipse), is rotated around the y-axes by an angle $\pi/2$ (blue ellipse) and afterwards around the z-axes by the unknown phase φ (black disk). The precision $\Delta\varphi$ on the estimation of φ is of the order of the thinner axes of the ellipse, representing the angular momentum fluctuations, divided by the radius $N/2$ of the sphere. In the output state (red disk) the number operator is measured, which renders clear that the number fluctuations are smaller as compared to a coherent state.

$P(\eta|\varphi) = \mathrm{tr}[\hat{E}(\eta)\hat{\rho}_{\mathrm{out}}]$, where $\hat{E}(\eta)$ is a general positive operator satisfying $\int d\eta \hat{E}(\eta) = \mathbf{1}$.

It can be demonstrated [140] that a general bound - the *Cramér-Rao lower bound* - exists on the phase precision ($\Delta\varphi$) defined in Eq.(4.6), which under the hypothesis of independent measurements and unbiased estimator reads

$$\Delta\varphi \geq \frac{1}{\sqrt{m}\sqrt{F\left[\hat{\rho}_{\mathrm{in}}, \hat{J}_n\right]}}, \tag{4.11}$$

where m is the number of measurements and $F\left[\hat{\rho}_{\mathrm{in}}, \hat{J}_n\right] = \int d\eta \frac{1}{P(\eta|\varphi)\left(\frac{\partial P(\eta|\varphi)}{\partial\varphi}\right)^2}$ is the *Fisher information* [140]. This quantity clearly depends on the measurement $\hat{E}(\eta)$ performed on the output state. We can define the *quantum Fisher information* as the maximum value taken by the Fisher information optimizing over all possible measurements $\hat{E}(\eta)$ [140, 141], i.e.

$$F_Q\left[\hat{\rho}_{\mathrm{in}}, \hat{J}_n\right] = \max_{\hat{E}(\eta)} F\left[\hat{\rho}_{\mathrm{in}}, \hat{J}_n\right] = 2 \sum_{l,m,p_l+p_m>0} \frac{(p_l - p_m)^2}{p_l + p_m} |\langle l|\hat{J}_n|m\rangle|^2 , \tag{4.12}$$

$\{|l\rangle\}$ being an orthonormal basis diagonalizing $\hat{\rho}_{\mathrm{in}} = \sum_l p_l |l\rangle\langle l|$ (with $p_l \geq 0$ and $\sum_l p_l = 1$). The calculation is detailed in Ref. [140], where it is also demonstrated that the general operator $\hat{E}(\eta)$ which optimizes the Fisher information reduces to a projective measurement - in our simple scheme, to the measurement of the collective angular momentum operator in some direction. Note that the quantum Fisher information (4.12) still depends on the input state and on the direction $\hat{n}$ of the interferometer.

Substituting the inequality $F\left[\hat{\rho}_{\rm in},\hat{J}_n\right] \leq F_Q\left[\hat{\rho}_{\rm in},\hat{J}_n\right]$ in Eq.(4.13) leads to a more advantageous bound on the phase precision, i.e. the best precision that can be achieved in principle for a given input state $\hat{\rho}_{\rm in}$

$$\Delta\varphi \geq (\Delta\varphi)_{\rm best} = \frac{1}{\sqrt{m}\sqrt{F_Q\left[\hat{\rho}_{\rm in},\hat{J}_n\right]}}, \tag{4.13}$$

also called the *quantum Cramér-Rao lower bound*. The saturation of the bound (4.13) requires both a suitable classical post-processing on the m outcomes of the measurements (e.g. the maximum likelihood estimation in the limit of large m [140]) and the knowledge of the optimum observable to measure. This latter task can be difficult as the optimum measurement may depend on the phase shift itself [140, 141].

For pure input states $|\psi_{\rm in}\rangle$, the quantum Fisher information given in Eq.(4.12) reduces to the quantum fluctuation $(\Delta J_n)^2 = \langle\psi_{\rm in}|\hat{J}_n^2|\psi_{\rm in}\rangle - \langle\psi_{\rm in}|\hat{J}_n|\psi_{\rm in}\rangle^2$ of $\hat{J}_n$,

$$F_Q\left[|\psi_{\rm in}\rangle,\hat{J}_n\right] = 4(\Delta J_n)^2\,. \tag{4.14}$$

This allows to reinterpret the Cramér-Rao lower bound (4.13) as a generalized uncertainty principle

$$\Delta\varphi\,\Delta J_n \geq \frac{1}{2\sqrt{m}}\,, \tag{4.15}$$

in which the generator $\hat{J}_n$ of the transformation (4.10) and the phase shift φ play the role of two conjugate variables - φ being here not an observable but a parameter [140]. For instance, for the phase state $|\psi_{\rm in}\rangle = |\theta = \pi/2, \phi\rangle$ the quantum fluctuations in the directions $\hat{n} = \hat{x}$, $\hat{y}$, and $\hat{z}$ are equal to $(N\sin^2\phi)/4$, $(N\cos^2\phi)/4$, and $N/4$, respectively. According to (4.15), for this state the best precision that can be achieved on the phase shift for $m = 1$ corresponds to the shot-noise limit in Eq.(4.8).

Due to Eq.(4.13), the inequality

$$F_Q\left[\hat{\rho}_{\rm in},\hat{J}_n\right] > N \tag{4.16}$$

is a necessary and sufficient condition for sub-shot noise sensitivity $(\Delta\varphi)_{\rm best} < (\Delta\varphi)_{SN}$. In what follows, the input states satisfying this inequality are called *useful states* for interferometry (or, more briefly, "useful states").

4.1.3.a Interpretation of the quantum Fisher information

The quantum Fisher information is related to the Bures distance [142]

$$d^2_{\rm Bures}(\hat{\rho}_1,\hat{\rho}_2) = 2(1-\sqrt{\mathcal{F}(\hat{\rho}_1,\hat{\rho}_2)}), \tag{4.17}$$

where

$$\mathcal{F}(\hat{\rho}_1,\hat{\rho}_2) = (\mathrm{tr}[\sqrt{\sqrt{\hat{\rho}_1}\hat{\rho}_2\sqrt{\hat{\rho}_1}}])^2 \tag{4.18}$$

is the fidelity, via the relation

$$d^2_{\rm Bures}(\hat{\rho}_{\rm in},\hat{\rho}_{d\varphi}) = F_Q[\hat{\rho}_{\rm in},\hat{J}_n](d\varphi)^2 \tag{4.19}$$

when two neighboring states are considered, one displaced by $d\varphi$ from the other on the curve (4.10) parameterized by φ, i.e. $\hat{\rho}_{d\varphi} = e^{-id\varphi J_n}\hat{\rho}_{\rm in}e^{id\varphi J_n}$ [140]. While Eq.(4.19) holds

for a general density matrix, it is particularly simple to prove it for pure states. Consider the displaced pure state

$$|\psi_{d\varphi}\rangle = e^{-id\varphi J_n}\varphi|\psi_{\rm in}\rangle \sim (1 - id\varphi\hat{J}_n - \frac{(d\varphi)^2}{2}\hat{J}_n^2)|\psi_{\rm in}\rangle. \tag{4.20}$$

Then the fidelity (4.18) reduces to the overlap of the two states (as we have already seen in Eq.(2.31)), and is given by

$$\mathcal{F}(\psi_{\rm in}, \psi_{d\varphi}) = |\langle\psi_{\rm in}|\psi_{d\varphi}\rangle|^2 \sim 1 - (d\varphi)^2(\Delta J_n)^2 = 1 - (d\varphi)^2\frac{F_Q[|\psi_{\rm in}\rangle, \hat{J}_n]}{4} \tag{4.21}$$

where in the last step we made use of Eq.(4.14). Substitution of Eq.(4.21) in the definition of the Bures metric (4.17) yields Eq.(4.19).

From Eq.(4.19) it can be seen that the quantum Fisher information has the meaning of the square of a "speed" $F_Q[\hat{\rho}_{\rm in}, \hat{J}_n] = \left(\frac{d_{\rm Bures}(\hat{\rho}_{\rm in}, \hat{\rho}_{d\varphi})}{d\varphi}\right)^2$, at which the state evolves along the curve defined by Eq.(4.10) in the space of density matrices when the parameter φ is varied [16, 140]: if one increases φ starting from $\varphi = 0$, the larger is quantum Fisher information of the input state $\hat{\rho}_{\rm in}$, the faster the state (4.10) becomes distinguishable from $\hat{\rho}_{\rm in}$, the smaller is the change in the parameter φ which can be detected. This is further seen from Eq.(4.18), in which we see that the state $|\psi_{d\varphi}\rangle$ becomes orthogonal from $|\psi_{\rm in}\rangle$ when $(d\varphi)^2 F_Q \sim 1$; for $F_Q \sim N$, this happens for $d\varphi \sim 1/\sqrt{N}$, while for $F_Q \sim N^2$, $|\langle\psi_{\rm in}|\psi_{d\varphi}\rangle|^2 \sim 0$ already for $d\varphi \sim 1/N$. Hence the bound (4.13) relates the problem of estimating a phase shift in an interferometer to the problem of distinguishing neighboring quantum states [140].

The link between the quantum Fisher information and the distinguishability of quantum states has also been applied to study the Zeno effect in Ref. [143].

4.1.4 Interplay usefulness in phase estimation and entanglement

It can be shown [15, 16] that for any separable input state $\hat{\rho}_{\rm in}$, $F_Q[\hat{\rho}_{\rm in}, \hat{J}_{\vec{n}}] \leq N$, so that (4.16) is a sufficient condition for $\hat{\rho}_{\rm in}$ to be entangled according to the definition in Eq.(2.1). In other words, $F_Q - N$ is an entanglement witness [3].

It is worthwhile to stress that the inequality (4.16) is not a necessary condition for entanglement: indeed, there exists entangled states which are not useful for interferometry, that is, with a Fisher information $F_Q \leq N$ [16, 76]. The criteria for entanglement and sub-shot noise sensitivity are summarized in Table 4.1.4.

Because of the criterium (4.16) and the bound (4.13), the quantum Fisher information can be seen as an entanglement parameter, quantifying the amount of quantum correlations useful for interferometry. Note however that F_Q is not a proper entanglement measure, because it violates one of the postulates which are typically required in the definition of a measure [144] - namely, it can increase under local operations [76].

The quantum Fisher information is bounded by N^2. This is easy to show for pure states by noticing that the largest square fluctuation of $\hat{J}_{\vec{n}}$ in Eq.(4.14) is smaller or equal to $N^2/4$ (see [15]); for mixed states this follows from the convexity of F_Q (see [16]). According

[3] Strictly speaking, the term "witness" only applies for pure states, where F_Q is an observable, being given by the fluctuations of the angular momentum operator. For mixed states, the entanglement criterium (4.16) still holds, but F_Q is given by the more complicated expression (4.12).

Phase estimation	Entanglement
$F_Q[\hat{\rho}_{\rm in}] > N \Leftrightarrow (\Delta\varphi)_{\rm best} < (\Delta\varphi)_{SN}$	$F_Q[\hat{\rho}_{\rm in}] > N \Rightarrow \hat{\rho}_{\rm in} \neq \hat{\rho}_{\rm sep}$
$\xi^2[\hat{\rho}_{\rm in}] < 1 \Rightarrow (\Delta\varphi)_{\rm best} < (\Delta\varphi)_{SN}$	$\xi^2[\hat{\rho}_{\rm in}] < 1 \Rightarrow \hat{\rho}_{\rm in} \neq \hat{\rho}_{\rm sep}$

Table 4.1: Necessary and/or sufficient conditions for sub-shot noise phase sensitivity in an atom interferometer and multiparticle entanglement in terms of the quantum Fisher information and spin-squeezing parameter.

to Eq.(4.13), the best sensitivity that can be achieved in linear interferometers [145] is then

$$(\Delta\varphi)_{\rm best} = (\Delta\varphi)_{HL} \equiv \frac{1}{N}. \tag{4.22}$$

This corresponds to the so-called *Heisenberg limit*. As it will become clear in the next paragraph, this limit can be reached using highly entangled atoms as input state.

4.1.4.a Macroscopic superpositions

Macroscopic superpositions such as the NOON state defined in Eq.(2.13) provide an example of states which are useful for interferometry according to the criterium (4.16), but which are not recognized as useful by the squeezing criterium (2.9). Indeed, with the use of Eq.(4.14) it is easy to derive

$$F_Q\left[|\psi_{\rm NOON}\rangle, \hat{J}_z\right] = N^2, \tag{4.23}$$

which substituted in the quantum Cramér-Rao lower bound (4.13) yields the highest possible phase resolution, expressed by the Heisenberg limit (4.22).

It is instructive to compare this result with the value of the quantum Fisher information for a statistical mixture of the same states, $\hat{\rho}_{\rm NONO} = (|N,0\rangle\langle N,0| + |0,N\rangle\langle 0,N|)/2$. The latter is found with the help of Eq.(4.12) to be equal to N in all directions $\hat{n}$ in the (xOy) plane and to vanish in the direction $\hat{z}$. Therefore, the scaling of F_Q like N^2 for $\hat{\rho}_{\rm NOON} = |\psi_{\rm NOON}\rangle\langle\psi_{\rm NOON}|$ is due to the presence of the off-diagonal terms $\hat{\rho}_{\rm NOON} - \hat{\rho}_{\rm NONO} = (|N,0\rangle\langle 0,N| + |0,N\rangle\langle N,0|)/2$. In Chap. 5 we will make use of this different scaling of the quantum Fisher information with N, depending on the presence or absence of the off-diagonal terms, to quantify the effect of decoherence on macroscopic superpositions.

The two-component phase cat state shares the same value of the quantum Fisher information as for the NOON state, since it is simply a rotation of the NOON state on the Bloch sphere, and entanglement is conserved by *collective* local operations [76] (see also section 4.2). The quantum Fisher information for macroscopic superpositions with a larger number of components will be explicitly calculated in Sec.4.4.

The fact that macroscopic superpositions are useful for interferometry can be ascribed to the fact that their likelihood probabilities defined in Eq.(4.5) display substructures of order $1/N$, which translates into a small angle of rotation needed to make the state orthogonal to the initial one [16]. For instance, for a NOON state, the state shifted in the $\hat{J}_z$ direction by an angle φ reads

$$|\psi_{\rm out}\rangle = e^{-i\varphi\hat{J}_z}|\psi_{\rm in}\rangle = \frac{1}{\sqrt{2}}\left(e^{-i\varphi\frac{N}{2}}|\frac{N}{2}\rangle + e^{i\varphi\frac{N}{2}}|-\frac{N}{2}\rangle\right), \tag{4.24}$$

which apart from a global phase factor is the same state as the one in Eq.(3.20), with $\beta = N\varphi$. Its likelihood probabilities according to any direction in the (xOy) plane are hence given by Eq.(3.22) with $\beta = N\varphi$, which as a function of φ displays fast oscillations. As a consequence, the overlap $|\langle\psi_{\rm in}|\psi_{\rm out}\rangle|^2 = \cos^2(N\varphi/2)$ vanishes at $\varphi \sim 1/N$.

Finally, we note that the fact that the NOON state is recognized as entangled by the Fisher information criterium, which for pure states reads $4(\Delta J_n)^2 > N$ according to Eqs.(4.14) and (4.16), may seem in contradiction with the statement that the inequalities (2.3) are complete in the sense defined in Sec.2.2: i.e., that there is no other inequality based on first and second moments only capable of detecting entangled states which are not already detected by Eq.(2.3). It is indeed readily verified that the NOON state does not violate such inequalities. The solution of this apparent "paradox" relies on the fact that Eq.(4.14) only holds for *pure* states; however, in order to establish that the state under consideration is pure, and hence that Eq.(4.14) can be applied, one should dispose of higher moments, e.g. performing a quantum tomography, so that the contradiction is removed [146].

4.1.4.b Fock states

The quantum Fisher information of a Fock state can also be calculated with the use of Eq.(4.14), and yields

$$F_Q\left[|n\rangle, \hat{J}_r\right] = N\left(\frac{N}{2}+1\right) - 2n^2 \tag{4.25}$$

in any direction r of the (xOy) plane defined by Eq.(1.33) [4]. In particular, the twin-Fock state $|n=0\rangle$ is highly entangled as

$$F_Q[|n=0\rangle, \hat{J}_r] = N\left(\frac{N}{2}+1\right) \tag{4.26}$$

is of order N^2, and leads thus to the Heisenberg limit. The extremal Fock states $n = \pm N/2$, instead, become separable as they coindice with the coherent states at the poles, so that $F_Q[|n=\pm\frac{N}{2}\rangle, \hat{J}_r] = N$.

In connection with the discussion presented in Sec.2.3.3, we remark that in Ref. [85] the dependence is studied of the quantum Fisher information of a Fock state on the spatial separation of the wells of a BJJ, when the degrees of freedom to be exploited for sub shot-noise interferometry are additional (internal) degrees of freedom.

4.1.4.c Squeezed states

The property that squeezed states are useful for interferometry beyond the shot noise limit, discussed in Sec.4.1.2, is readily demonstrated using the concept of quantum Fisher information. Indeed, as we shall see in Secs.4.4 and 4.3.1, the quantum Fisher information of a squeezed state is approximatively given by $F_Q \simeq F_\xi$ [16, 25], where the parameter F_ξ is defined as

$$F_\xi = \frac{N}{\xi^2}. \tag{4.27}$$

This indicates that for squeezed states the parameters F_Q and ξ provide essentially the same information (see also Fig.4.4). Furthermore, for these states the Fisher information

[4] For what concerns the z-direction, since Fock states are eigenstates of the $\hat{J}_z$ operator, we obtain instead $F_Q[|n\rangle, \hat{J}_z] = 0$ for each n.

is maximum in a direction perpendicular to the one of minimum squeezing. This has a clear physical interpretation: when the state is squeezed, the quantum Fisher information is maximum in the direction of highest angular momentum fluctuations, which is perpendicular to the direction of lowest fluctuations yielding the best squeezing (see Fig.4.2 for a sketch).

Use of Eq.(4.13) yields Eq.(4.9) for the phase uncertainty, demonstrating the usefulness of squeezed states for atom interferometry.

4.2 Optimum coherent spin squeezing and quantum Fisher information

As it is clear from the previous discussion, both the quantum Fisher information F_Q and the coherent spin squeezing parameter ξ depend on the direction of the generator which defines the interferometric sequence (4.10). For instance, for a NOON state $F_Q[|\psi_{\rm NOON}\rangle, \hat{J}_x] = F_Q[|\psi_{\rm NOON}\rangle, \hat{J}_y] = N$, while Eq.(4.23) shows that the NOON state is maximally entangled. Hence, in order to quantify the useful correlations of a quantum state, one needs to optimize F_Q and ξ over all the possible directions by defining [76]

$$\xi^2\left[\hat{\rho}_{\rm in}\right] \equiv \min_{\hat{n}} \xi^2_{\hat{n}}\left[\hat{\rho}_{\rm in}\right] \ , \ F_Q\left[\hat{\rho}_{\rm in}\right] \equiv \max_{\hat{n}} F_Q\left[\hat{\rho}_{\rm in}, \hat{J}_n\right] . \tag{4.28}$$

Let us consider the 3×3 real symmetric covariance matrix $\gamma[\hat{\rho}_{\rm in}]$ with matrix elements

$$\gamma_{ij}\left[\hat{\rho}_{\rm in}\right] = \frac{1}{2} \sum_{l,m,p_l+p_m>0} \frac{(p_l - p_m)^2}{p_l + p_m} \Re{\rm e} \ \left[\langle l|\hat{J}_i|m\rangle\langle m|\hat{J}_j|l\rangle\right] \tag{4.29}$$

where $\{|l\rangle\}$ is the orthonormal eigenbasis of $\hat{\rho}_{\rm in}$ as in Eq.(4.12). According to standard linear algebra, the maximum of $F_Q[\hat{\rho}_{\rm in}, \hat{J}_n] = 4(\hat{n}, \gamma\left[\hat{\rho}_{\rm in}\right]\hat{n})$ over all unit vectors $\hat{n}$ is equal to

$$F_Q\left[\hat{\rho}_{\rm in}\right] = 4\gamma_{\rm max} \, , \tag{4.30}$$

$\gamma_{\rm max}$ being the largest eigenvalue of the matrix $\gamma[\hat{\rho}_{\rm in}]$. In the following it will be useful to define also the matrix

$$G_{ij}[\hat{\rho}] \equiv \frac{1}{2}\langle \hat{J}_i\hat{J}_j + \hat{J}_j\hat{J}_i\rangle - \langle \hat{J}_i\rangle\langle \hat{J}_j\rangle, \tag{4.31}$$

where $\langle \ldots \rangle = {\rm tr}(\ldots \hat{\rho})$, with $\hat{\rho}$ being the system density matrix. Note that for pure input states $|\psi_{\rm in}\rangle$ the matrix $\gamma_{ij}[|\psi_{\rm in}\rangle]$ reduces to the matrix $G_{ij}[|\psi_{\rm in}\rangle\langle\psi_{\rm in}|]$, which is easier to compute than the more general expression (4.29). The optimum quantum Fisher information is then given (up to a factor four) by the largest uncertainty of the angular momentum operators $\hat{J}_n$ (see Eq.(4.14)).

For the sake of brevity, in the following we will omit both the adjective "optimum" and the explicit dependence on the input state, designating the optimum coherent spin squeezing and the optimum quantum Fisher information respectively by ξ^2 and F_Q, unless where source of confusion.

4.3 Quantum Fisher information and spin squeezing in the ground state

In this section, we calculate the squeezing parameter and the quantum Fisher information in the ground state of the BJJ, modeled by the two-mode Hamiltonian (1.24). This pro-

vides an indication of the usefulness of the ground state of the BJJ for sub-shot noise phase estimation in atom interferometry. The extension of the previous scenario to include the effect of temperature within the same simple two-mode model is discussed in Appendix C.

Let us focus on the case of symmetric modes $\lambda = 0$, corresponding to the vertical section of the number fluctuation phase diagram presented in Fig.1.6. We start with the analysis of the limiting cases, namely the limit of non-interacting atoms and the limit of non-coupled modes, for which an analytical solution can be provided; we will then turn to the general case, to be addressed numerically.

4.3.1 Non-coupled modes

In the limit $K = 0$ (left bottom point in the diagram of Fig.1.6), the ground state is the twin Fock state $|n = 0\rangle$, as explained in Sec.1.5.1. Hence, the optimum quantum Fisher information is given by Eq.(4.26), displaying a N^2 scaling, and it is optimum in any direction contained in the (xOy) plane. The ground state in this regime is thus highly "usefully" entangled.

The coherent spin squeezing along the z axes in the same regime is an indeterminate expression, since the coherence factor in the denominator of Eq.(2.6) vanishes, as well as the number fluctuations in the numerator. The limiting value for $K \to 0$ can be calculated with second order perturbation theory. The calculation, detailed in Appendix C.1, yields as a result that the ground state displays the largest squeezing degree of the phase diagram in this limit, as anticipated in Sec.(2.4.1), namely

$$\xi^2 = \frac{1}{\left(\frac{N}{2}+1\right)} \tag{4.32}$$

(see also Ref. [96]). Evaluating the Fisher-like parameter (4.27) yields $F_\xi = F_Q$, given by Eq.(4.26), showing that in this regime the two parameters provide the same information, according to the discussion presented in Sec.4.1.4.c.

4.3.2 Non-interacting atoms

The ground state of the system in the limit of non-interacting atoms is, as already expressed by Eq.(1.37), the maximum eigenstate of $\hat{J}_x$, i.e. the coherent state $|\alpha = 1\rangle$. Then the ground state in this regime is separable, and the Fisher information is $F_Q = N$, optimum in the plane (yOz). Correspondingly, the squeezing is isotropic in the plane (xOy) and its value is $\xi^2 = 1$.

4.3.3 Intermediate regime

In the general case in which the parameters K and χ of the Hamiltonian (1.24) are competing, the values of the optimum quantum Fisher information and of the optimum coherent spin squeezing have to be determined numerically. The result is shown in Fig.4.3. As already mentioned in Sec. 2.4.1, the ground state of the BJJ is *always* a squeezed state at any point of the phase diagram with $\chi \neq 0$. Hence, for the discussion in Sec. 4.3.1, F_Q and ξ provide the same information, which translates into the fact that no substantial difference can be seen between the two numerical curves.

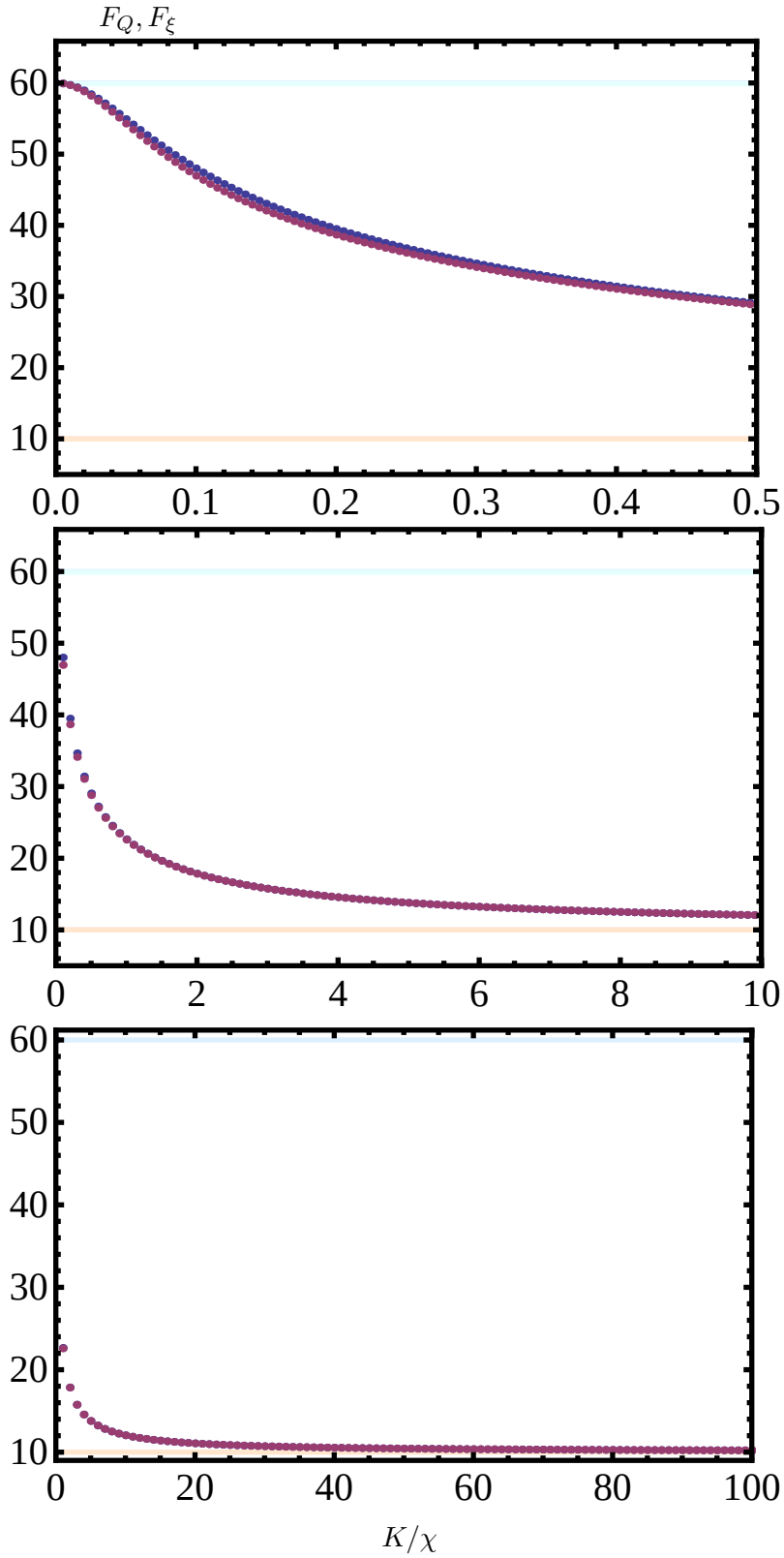

Figure 4.3: $N = 10$. Optimum quantum Fisher information (blue) and optimum Fisher-like measure N/ξ^2 (purple) as a function of $r = K/\chi$ ($\chi = 1$) at $T = 0$. Top panels: zoom at shorter $r = K/\chi$ scales. Blue gridline: $K = 0, \lambda = 0$ limit given by Eq.(4.26). Orange gridline: shot noise limit $F_Q = N$ ($\chi = 0$).

To summarize, the analysis based on the quantum Fisher information allows us to conclude that, increasing the ratio between the tunneling and the interactions, the ground state undergoes a cross-over from a highly entangled state at strong interactions (with $F_Q \simeq N^2/2$) to a separable state (with $F_Q = N$) when the coupling is dominating. This analysis reminds of the studies of Refs. [147, 148], where an entanglement measure is used to analyze phase transitions in spin systems: by changing the external fields and the coupling, the ground state crosses over from an entangled state to a fully factorizable one.

A different use of the quantum Fisher information in the context of phase transitions has been made in Ref. [149]. There, a metric based on the Fisher information is used to detect the line of phase transition, using the fact that perpendicularly to such a line the state is changing with a maximal "speed".

The Fisher information in the ground state of the BJJ has also been studied in Refs.[150–152], to explore the cross-over of the model when the sign of the interatomic interactions is changed from positive to negative.

4.4 Quantum Fisher information and coherent spin squeezing during the quenched dynamics

We now address the question how much the quantum states produced during the quenched dynamics of the BJJ presented in Sec.2.5.1 are useful for interferometry. For this purpose, based on the discussion of the previous sections, we evaluate the quantum Fisher information and the coherent spin squeezing parameter. The results presented in this section are reported in Ref. [25]. In this section we are going to use the suffix "(0)" for the dynamical quantities calculated in the absence of noise, in order to distinguish them from the same quantities calculated in the presence of noise, which will be presented in the next chapter.

Since the atoms are in a pure state $|\psi^{(0)}(t)\rangle$ during all the dynamical evolution, the covariance matrix $\gamma^{(0)}(t)$ associated with this state is thus given by Eq.(4.31), and analytical expressions can be obtained for the quantum Fisher information and the coherent spin squeezing as a function of time.

We consider in particular the case of an initial coherent state with $\alpha = 1$, i.e. the phase state $|\theta = \pi/2, \phi = 0\rangle$. Thus, the quenched dynamics takes place along the equator of the Bloch sphere only, and the average value of the number operator is zero at all times, as we have seen in Sec.2.5.1. Furthermore, the state is also always symmetric with respect to the y direction. Hence, use of Eqs. (2.19) leads to

$$\langle \hat{J}_y(t)\rangle^{(0)} = \langle \hat{J}_z(t)\rangle^{(0)} = 0, \tag{4.33}$$

where $\langle ..\rangle_t^{(0)} = \mathrm{tr}(...\hat{\rho}^{(0)}(t))$. Using also Eq.(2.20), the angular-momenta covariance matrix (4.31) reads

$$\gamma^{(0)}(\tau) = \begin{pmatrix} \gamma_x^{(0)}(\tau) & 0 & 0 \\ 0 & -\frac{N}{8}\left[(N-1)\cos^{N-2}(2\tau) - (N+1)\right] & \frac{N(N-1)}{4}\cos^{N-2}(\tau)\sin(\tau) \\ 0 & \frac{N(N-1)}{4}\cos^{N-2}(\tau)\sin(\tau) & \frac{N}{4} \end{pmatrix} \tag{4.34}$$

where we have introduced the rescaled time $\tau = 2\pi t/T = \chi t$ and

$$\gamma_x^{(0)}(\tau) \equiv \langle (\Delta \hat{J}_x)^2 \rangle_\tau^{(0)} = \frac{N}{8}\left[(N-1)\cos^{N-2}(2\tau) + (N+1) - 2N\cos^{2(N-1)}(\tau)\right]. \quad (4.35)$$

The two other eigenvalues of the matrix (4.34) are given in terms of its elements $\gamma_{ij}^{(0)}$ by

$$\gamma_\pm^{(0)} = \frac{\left(\gamma_{yy}^{(0)} + \gamma_{zz}^{(0)}\right) \pm \sqrt{\left(\gamma_{yy}^{(0)} - \gamma_{zz}^{(0)}\right)^2 + 4\gamma_{yz}^{(0)2}}}{2}, \quad (4.36)$$

or, more explicitly,

$$\begin{aligned}\gamma_\pm^{(0)}(\tau) &= \frac{N}{16}\big[-(N-1)\cos^{N-2}(2\tau) + (N+3) \\ &\quad \pm (N-1)\sqrt{(\cos^{N-2}(2\tau)-1)^2 + 16\cos^{2(N-2)}(\tau)\sin^2(\tau)}\big]. \quad (4.37)\end{aligned}$$

We remark that the matrix (4.34) has the property that its eigenvalues at times τ and $\pi - \tau$ (and, similarly, at $2\pi - \tau$) coincide, hence it suffices to discuss its behavior at times t belonging to the interval $[0, T/4]$ (i.e., $\tau \in [0, \pi/2]$).

According to Eq.(4.30), the quantum Fisher information is given by the largest eigenvalue,

$$F_Q(\tau) = 4\max\left\{\gamma_x^{(0)}(\tau)\,,\, \gamma_+^{(0)}(\tau)\right\}. \quad (4.38)$$

We demonstrate in Appendix B.1 that the coherent spin squeezing (2.6) is always optimum along a direction contained in the (yOz) plane. The optimal spin squeezing parameter (4.28) is thus related to the lowest eigenvalue $\gamma_-^{(0)}(\tau)$ of the submatrix $\gamma^{(0)\prime}(\tau)$ obtained by removing the first line and column in the matrix (4.34). Using Eqs.(4.33) and (2.20), we obtain

$$\xi^{(0)2}(\tau) = \frac{4\gamma_-^{(0)}(\tau)}{N\nu^{(0)2}(\tau)}. \quad (4.39)$$

The direction of optimum squeezing is given by the eigenvector associated with the eigenvalue $\gamma_-^{(0)}$,

$$\hat{n}_\xi^{(0)}(\tau) = \hat{n}_-^{(0)}(\tau) = -\sin\theta_\xi^{(0)}(\tau)\,\hat{y} + \cos\theta_\xi^{(0)}(\tau)\,\hat{z}. \quad (4.40)$$

From the diagonalization of the matrix $\gamma^{(0)}$ we find

$$\hat{n}_\pm^{(0)} = \left(0, \frac{-\gamma_{yz}^{(0)}}{\sqrt{\gamma_{yz}^{(0)2} + (\gamma_{yy}^{(0)} - \gamma_\pm^{(0)})^2}}, \frac{(\gamma_{yy}^{(0)} - \gamma_\pm^{(0)})}{\sqrt{\gamma_{yz}^{(0)2} + (\gamma_{yy}^{(0)} - \gamma_\pm^{(0)})^2}}\right), \quad (4.41)$$

which, via comparison with Eq.(4.40), leads to $\tan\theta_\xi^{(0)} = \left(-\frac{n_y^{(0)}}{n_z^{(0)}}\right)$ and then to the angle of optimization of the squeezing parameter

$$\begin{aligned}\theta_\xi^{(0)}(\tau) &= \arctan\left(\frac{\gamma_{yz}^{(0)}(\tau)}{\gamma_{yy}^{(0)}(\tau) - \gamma_-^{(0)}(\tau)}\right) \\ &= \frac{1}{2}\arctan\left(\frac{\langle\{\hat{J}_y, \hat{J}_z\}\rangle_\tau^{(0)}}{\langle \hat{J}_y^2\rangle_\tau^{(0)} - \langle \hat{J}_z^2\rangle_\tau^{(0)}}\right) \quad (4.42)\end{aligned}$$

where $\{\cdot,\cdot\}$ denotes the anticommutator, and where in the second step we have used the trigonometric identity $\tan 2x = 2\tan x/(1-\tan^2 x)$.

The direction of optimization $\hat{n}_F^{(0)}$ of the quantum Fisher information is either given by $\hat{x}$ (if $\gamma_x^{(0)} > \gamma_+^{(0)}$) or by the eigenvector $\hat{n}_+^{(0)}$ associated with the eigenvalue $\gamma_+^{(0)}$ (if $\gamma_x^{(0)} < \gamma_+^{(0)}$). The latter condition is satisfied at times shorter than t^*, see Appendix B.2. As both these eigenvectors are orthogonal to $\hat{n}_-^{(0)}$ (since the matrix $\gamma^{(0)}$ is symmetric), it follows that coherent spin squeezing and quantum Fisher information are optimized in perpendicular directions.

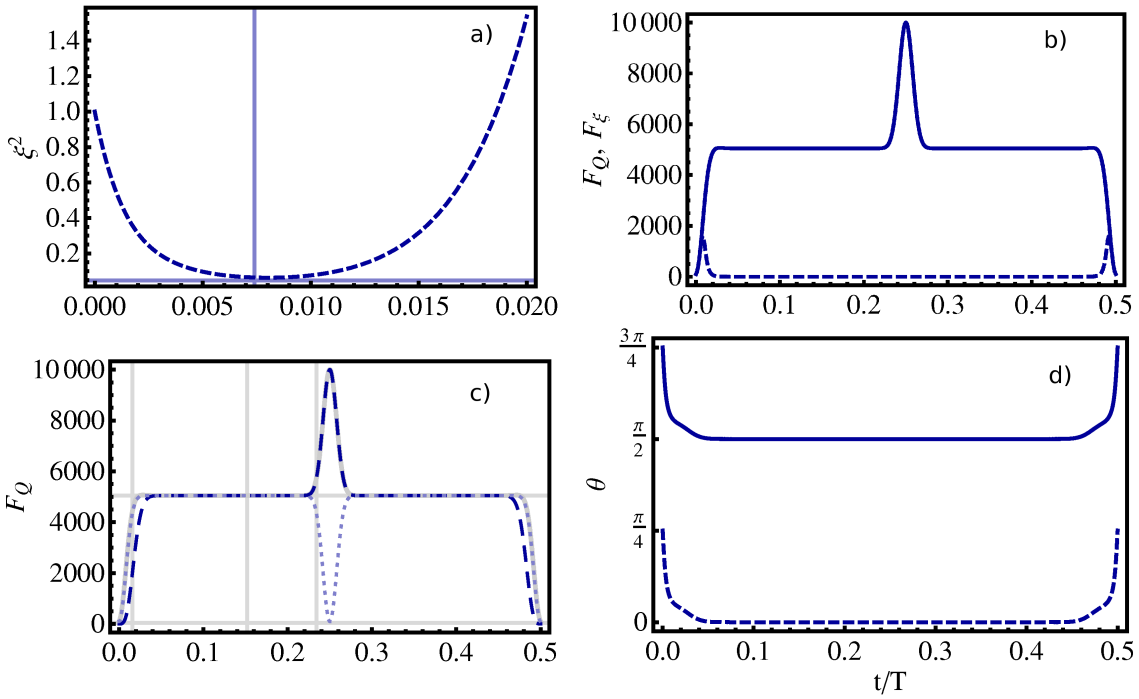

Figure 4.4: a) Coherent spin squeezing and b) quantum Fisher information during the quenched dynamics of a BJJ with $N = 100$ atoms as a function of time (in units of the revival time T) in the absence of noise. The dashed line in the second panel represents the parameter $F_\xi = N/\xi^2$. Horizontal and vertical gridlines in panel a): minimum of the coherent spin squeezing and corresponding time $t_{\min}$ (see text). c) Non-optimized quantum Fisher information along the x-axes (dashed line) and the y-axes (dotted line). For comparison, the optimum quantum Fisher information of panel b) is also shown (gray solid line). The vertical gridlines correspond from right to left to the time $t = t_{fs}$ of formation of the first macroscopic superposition, see Eq.(2.28); to $t = t^*$, see Appendix B.2; and to $t = T/4 - t_{fs}$. The horizontal gridline shows the shot-noise level $F_Q = N$. d) Angles $\theta_\xi^{(0)}$ in Eq.(4.42) (dashed line) and $\theta_F^{(0)}$ (solid line) giving the optimizing direction for the spin squeezing and the quantum Fisher information as a function of time.

At short times, when the state of the system is a squeezed state (see panels (a) and (b) in Fig. 4.4), this can be understood again with the argument discussed in Sec.4.1.4.c; i.e. that for a squeezed state the quantum Fisher information is maximum in the direction of maximal angular momentum fluctuations, perpendicularly to the direction of lowest fluctuations yielding the best squeezing. In this short-time regime, the two parameters provide essentially the same information. This fact can be visualized in panel (b) of

Fig. 4.4, in which at short times the Fisher information (4.38) and squeezing parameter $F_\xi = N/\xi^2$, calculated with the help of Eqs.(4.39), (4.35), (2.20) and (4.37) are shown to coincide. A rigorous demonstration of this fact can be found in Ref.[25].

At time $\tau_{\min}^{(0)} = 3^{1/6}N^{-2/3}$ the squeezing parameter reaches its minimum value, $(\xi_{\min}^{(0)})^2 \simeq (3/N)^{2/3}/2$, as was calculated in Ref.[11].

At larger times, the squeezing parameter grows to values larger than one (that is, F_ξ decreases and becomes smaller than N). This does not imply that the atomic state is not useful for interferometry since, as described in Sec.4.1.2, the squeezing criterion is only a sufficient condition for useful entanglement [16]. Indeed, the quantum Fisher information increases above the shot noise level $F_Q = N$ until it reaches a plateau, at a time of order of t_{fs} given in Eq. (2.28), corresponding to the appearance of the first macroscopic superposition. The value of the Fisher information on the plateau can be easily calculated since in the time regime $\delta t \leq t \leq T/4 - \delta t$ with $\delta t \gg t_{fs}$, the covariance matrix (4.34) takes the simple following form in the limit $N \gg 1$

$$\gamma^{(0)}(\tau) \simeq \begin{pmatrix} \frac{1}{8}N(N+1) & 0 & 0 \\ 0 & \frac{1}{8}N(N+1) & 0 \\ 0 & & \frac{1}{4}N \end{pmatrix}. \tag{4.43}$$

Hence the Fisher information has a plateau at the value

$$F_Q^{(0)}(\tau) = \frac{N(N+1)}{2}. \tag{4.44}$$

We have shown in Appendix B.1 that if N is even, the optimizing direction $\hat{n}_F^{(0)}(\tau)$ of the Fisher information changes as τ increases from the (yOz)-plane to the x-axes at the time $\tau^* \simeq \arccos(1/\sqrt{3})$ defined by $\gamma_x^{(0)}(\tau^*) = \gamma_+^{(0)}(\tau^*)$. Note, however, that any direction in the (xOy)-plane gives a Fisher information almost equal to the optimized value $N(N+1)/2$, as it is clear from the structure of the matrix (4.43), leading to almost degenerate eigenvalues $\gamma_x^{(0)}$ and $\gamma_+^{(0)}$. This reflects the structure of multicomponent superpositions, symmetric in the (yOx) plane. This result is visualized in panel c) of Fig.4.4, displaying the Fisher information in the directions $\hat{x}$ and $\hat{y}$.

It is seen in Fig.4.4 that F_Q displays a sharp maximum at $t = t_2 = T/4$, in correspondence to the two-component macroscopic superposition (2.26), which has the highest possible Fisher information $F_Q = N^2$, as expected in view of the discussion in Sec.4.1.4.a. As one approaches the two-component superposition, the optimizing direction changes to the x-axes, which is the direction of maximal angular momentum fluctuations for the state (2.26).

In panel d) of Fig.4.4, the angle $\theta_\xi^{(0)}$ giving the direction of highest spin squeezing in the (yOz) plane is represented as a function of time together with the corresponding angle $\theta_F^{(0)}$ for the Fisher information, which gives the optimizing direction $\hat{n}_F^{(0)}$ of the Fisher information according to Eq.(2.8). Table 4.4 summarizes the aforementioned results.

To recapitulate, during the quenched dynamics of the BJJ, starting from a (separable) phase state, due to non-linear interactions entangled states are formed. The characteristic time for squeezing scales as $t \propto N^{-2/3}$, which leads to typical values of the quantum Fisher information of $F_Q \sim F_\xi \propto N^{5/3}$, while the first macroscopic superpositions appear at $t \propto N^{-1/2}$, leading to a scaling $F_Q \propto N^2$. The quantum Fisher information reaches its maximum value $F_Q = N^2$ at $t = t_2 = \pi/2$ (independent on N), in correspondence of the formation of the two-component superposition. Hence, in the perspective of exploiting

Time	Optimum quantum Fisher information F_Q	Optimizing direction
$t = 0$	N	degenerate in (yOz) plane
$0 \leq t \lesssim \frac{T}{N}$	$4\gamma_+^{(0)}(\tau) \simeq N\left[1 + \left(\frac{N^2\tau^2}{2} + N\tau\sqrt{1 + \frac{N^2\tau^2}{4}}\right)\right]$	$-\cos\theta_\xi^{(0)}(t)\,\hat{y} - \sin\theta_\xi^{(0)}(t)\,\hat{z}$
$\frac{T}{N} \ll t \leq t_{\min}$	$4\gamma_+^{(0)}(\tau)$ (see above)	$\simeq \hat{y}$
$t_{\min} < t \lesssim t_{fs}$	$3^{1/3}N^{5/3} < F_Q \lesssim 0.4323N^2$	$\simeq \hat{y}$
$t_{fs} \ll t \leq t^*$	$F_Q \simeq N(N+1)/2$	$\simeq \hat{y}$
$t^* < t \leq \frac{T}{4}$	$N(N+1)/2 \lesssim F_Q \leq F_Q(T/4) = N^2$	$\hat{x}$
Time	Optimum coherent spin squeezing $F_\xi \equiv N/\xi^2$	Optimizing direction
$t = 0$	N	degenerate in (yOz) plane
$0 \leq t \lesssim \frac{T}{N}$	$F_\xi \simeq F_Q$	$-\sin\theta_\xi^{(0)}(t)\,\hat{y} + \cos\theta_\xi^{(0)}(t)\,\hat{z}$
$\frac{T}{N} \ll t \leq t_{\min}$	$N < F_\xi \leq F_\xi(t_{\min}) = 2N^{5/3}3^{-2/3}$	$\simeq \hat{z}$
$t_{\min} < t \lesssim t_{fs}$	$Ne^{-1/2} \lesssim F_\xi < 2N^{5/3}3^{-2/3}$	$\simeq \hat{z}$
$t_{fs} \ll t \leq t^*$	$N/3^{N/2-1} \leq F_\xi \ll N$	$\simeq \hat{z}$
$t^* < t \leq \frac{T}{4}$	$0 < F_\xi < N/3^{N/2-1}$	$\simeq \hat{z}$

Table 4.2: Optimum coherent spin squeezing parameter, optimum quantum Fisher information and corresponding optimizing directions during the quenched dynamics of a Bose Josephson junction in the absence of noise for $N \gg 1$. The arrows indicate whether the function is increasing or decreasing with time in a given time interval. In this Table, N is taken to be even. The calculation of the numerical prefactors and the short-time, large N expansion of F_Q in the second and third line can be found in Ref.[25].

the quantum state created during the quenched dynamics using it as an input state of an atomic interferometer, in the absence of any noise sources the highest phase resolution is reached using the state formed at $t = t_2 = \pi/2$ - the two-component phase state. In Chap. 5 we will address the question how this situation is modified by the presence of noise.

Chapter 5

Decoherence of useful entangled states

Cold atoms experiments are affected by various noise sources, which limit the lifetime of the condensate and induce spurious effects, eventually menacing the feasibility of quantum information protocols. The main sources of noise in cold atoms experiments are particle losses [22, 23], phase noise [24, 25], collisions with thermal atoms [26, 27], interaction with the electromagnetic field [28, 29], and random fluctuations of the trapping potentials [30].

In this work we will focus on two sources of noise: phase noise and particle losses, which seem to be the major noise sources in the experiments of Refs. [8, 9, 13]. We will focus in particular on their effect on the creation of useful states (squeezed states and macroscopic superpositions) based on the quenched dynamics of the BJJ introduced in Chap.2. We will address how much the useful quantum correlations of such states, which allow in principle to outperform the classical limit of precision in the interferometric applications presented in Chap.4, are degraded by the presence of noise. We will address the effect of phase noise in Sec. 5.1, while particle losses are discussed in Sec. 5.2. The concluding section 5.3 presents an analytical method to treat both noise sources on the same footing.

Before starting with this program we remark that in this chapter we will focus on the effect of phase noise and particle losses on the *preparation* of the useful input state only. For studies of the effect of noise during the rotations of the interferometric procedure presented in Chap. 4, or during the measurements, see references [153] and [145].

Les expériences d'atomes froids sont affectées par plusieurs sources de bruit, qui limitent le temps de vie du condensat et qui induisent des effets non désirés, en menaçant la faisabilité des protocoles d'information quantique. Les principales sources de bruit sont la perte de particules [22, 23], le bruit de phase [24, 25], les collisions avec les atomes thermiques [26, 27], l'interaction avec les champs électromagnétiques [28, 29], et les fluctuations aléatoires des potentiels de piégage [30].

Dans cette thèse nous nous focaliserons sur deux sources de bruit: le bruit de phase et la perte de particules, qui semblent être les sources de bruit dominantes dans les expériences des Refs. [8, 9, 13].

Nous focaliserons en particulier sur leur effet sur la création d'états quantiques utiles (états comprimés et superpositions macroscopiques) basée sur la dynamique

trempée de la jonction introduite dans le chapitre 2. Nous aborderons comment les corrélations utiles de ces états, qui permettent de surmonter la limite de précision standard dans les applications à l'interférométrie présentées dans le chapitre 4, sont dégradées par la présence de bruit. Nous aborderons l'effet du bruit de phase dans la Sec. 5.1, tandis que les pertes de particules seront examinées en Sec. 5.2. La section conclusive présente une méthode analytique qui permet de traiter ces deux sources de bruit en même temps.

Avant de commencer avec ce programme, nous faisons remarquer que dans ce chapitre nous nous interessons à l'effet du bruit de phase et de la perte de particules sur la préparation *de l'état quantique utile seulement. Pour des études de l'effet du bruit pendant les rotations qui composent la séquence interférométrique présentée dans le chapitre 4, ou pendant les mesures, nous renvoyons aux références [153] et [145].*

5.1 Phase noise

In this section we consider the effects of phase noise on the states formed during the quenched dynamics of the BJJ. The original work associated with this subject is presented in our Refs.[24, 25]. First, we model phase noise, and we analyze its effect on the visibility. Then, we show that macroscopic superpositions of phase states in BJJs are relatively robust with respect to phase noise, their decoherence rate being independent on the total number of atoms in the condensate. Then, we show that these long-lived states can be useful in interferometry to improve phase sensitivity even in the presence of phase noise, by calculating the quantum Fisher information and the coherent spin squeezing as introduced in the previous chapter. In particular, we compare the best possible phase sensitivity obtained with the state of the BJJ at the times of formation of macroscopic superpositions to the one obtained at earlier times when squeezed states are produced. This allows us to determine which are the most useful quantum states for interferometric applications in the presence of phase noise. Throughout this chapter, in the same notation as in the previous one, we will denote by a suffix "$^{(0)}$" the quantities calculated in the absence of noise.

5.1.1 Model

Phase noise is caused by a randomly fluctuating energy difference $\Delta E(t)$ between the two modes, which is modeled by taking the parameter λ in the Hamiltonian (1.24) as stochastically time-dependent. In the single-well experiment [8] (internal BJJ), such a noise is induced by fluctuations of the magnetic field, which by quadratic Zeeman effect cause a shift in the hyperfine energies (see Eq.(1.3)), whereas in the double-well experiment [13] (external BJJ) it is induced by fluctuations of the orientation of the laser beam producing the double-well potential with respect to the trapping potential (see first line in Eq.(1.17)). We will be especially interested in the effect of phase noise on the production of useful entangled states (squeezed states and macroscopic superpositions of phase states) during the quenched dynamics of the BJJ, according to the protocol reported in Sec.(2.5.1). Hence, we focus on the time-dependent Hamiltonian

$$\hat{H}(t) = \chi \hat{J}_z^{\,2} - \lambda(t)\hat{J}_z. \tag{5.1}$$

Note that by the definition (1.25) also a fluctuation of the interaction difference $U_1 - U_2$ would provide a stochastically varying term $\lambda(t)$ in the Hamiltonian (5.1). We will however neglect such fluctuations, as this seems justified in the experiments [8, 9, 13].

5.1.1.a Derivation of the density matrix in the presence of phase noise

Even in presence of phase noise, the time evolution following the quench can be exactly integrated, since the noise term $\lambda(t)\hat{J}_z$ commutes with the noiseless Hamiltonian $\chi\hat{J}_z^{\,2}$ [24]. For a given realization of the stochastic process $\lambda(t)$, the state of the atoms at time t is given by Eq.(2.29); i.e, the effect of a fluctuating energy imbalance in a single realization is a rotation of the state $|\psi^{(0)}(t)\rangle$ formed in the absence of noise, given in Eq.(2.19), by a phase $\phi(t) = -\int_0^t d\tau\lambda(\tau)$ around the z axes.

The system density matrix is then obtained by $\hat{\rho}(t) = \overline{|\psi(t)\rangle\langle\psi(t)|} = \int dP\,[\lambda]\,|\psi(t)\rangle\langle\psi(t)|$, where the overline denotes the average over the noise realizations. The introduction of the distribution probability for the random angle $\phi(t)$,

$$f(\phi,t) = \int dP\,[\lambda(t)]\,\delta(\phi - \phi(t)) \tag{5.2}$$

allows to write it as

$$\hat{\rho}(t) = \int_{-\infty}^{\infty} d\phi\, f(\phi,t)\, e^{-i\phi\hat{J}_z}\hat{\rho}^{(0)}(t)e^{i\phi\hat{J}_z}\,, \tag{5.3}$$

where $\hat{\rho}^{(0)}(t) = |\psi^{(0)}(t)\rangle\langle\psi^{(0)}(t)|$ is the density matrix in the absence of noise. Let us compute explicitly the probability distribution $f(\phi,t)$ of the angle $\phi(t)$, defined in Eq.(5.2) as an average over the noise realizations induced by the functional $P[\lambda(t)]$. By Fourier expansion we have

$$f(\phi,t) = \int dP\,[\lambda(t)]\,\delta\left(-\int_0^t \lambda(\tau)d\tau - \phi\right) = \frac{1}{2\pi}\int dP\,[\lambda(t)]\int_{-\infty}^{\infty} du\, e^{-iu\phi(t)}e^{i\phi u}\,. \tag{5.4}$$

We are left with the evaluation of the Fourier transform of the average $\overline{e^{-iu\phi(t)}} = \int dP[\lambda(t)]\, e^{-iu\phi(t)}$. This is readily done under the hypothesis of a gaussian noise; since for gaussian variables with $\overline{\xi} = 0$ one has $\overline{e^{iu\xi}} = e^{-\frac{u^2}{2}\overline{\xi^2}}$, the average in Eq.(5.4) can be worked out as

$$\begin{aligned}\overline{e^{-iu\phi(t)}} &= \overline{e^{-iu(\phi(t)-\overline{\phi(t)})}}e^{-iu\overline{\phi(t)}} \\ &= e^{-\frac{u^2}{2}\overline{(\phi(t)-\overline{\phi(t)})2}}e^{-iu\overline{\phi(t)}}.\end{aligned} \tag{5.5}$$

Let us introduce the noise correlation function

$$h(\tau,\tau') = \overline{\lambda(\tau)\lambda(\tau')} - \overline{\lambda}^2 = \overline{\Delta E(\tau)\Delta E(\tau')} - \overline{\Delta E}^2, \tag{5.6}$$

where $\overline{\lambda} = \overline{\Delta E} + (N-1)(U_2 - U_1)/2$. Note that $h(\tau,\tau')$ depends only on the time difference $\tau - \tau'$ by the stationarity of the stochastic process $\lambda(t)$, which also implies $\overline{\lambda(t)} = \overline{\lambda(0)} \equiv \overline{\lambda}$; moreover, $h(\tau,\tau')$ decreases to zero at sufficiently long times. Defining also the variance

$$a^2(t) = \int_0^t d\tau \int_0^t d\tau' h(\tau - \tau') \tag{5.7}$$

allows to rewrite Eq.(5.5) as $\overline{e^{-iu\phi(t)}} = e^{-\frac{u^2}{2}\int_0^t d\tau\int_0^t d\tau' h(\tau-\tau')}e^{iu\overline{\lambda}t} = e^{-\frac{u^2}{2}a^2(t)}e^{iu\overline{\lambda}t}$. Substitution of this expression in (5.4) leads to

$$f(\phi,t) = \frac{1}{2\pi}\int_{-\infty}^{\infty} du\, e^{i(\phi+\overline{\lambda}t)u}e^{-\frac{u^2}{2}a^2(t)}\,, \tag{5.8}$$

which, after performing the gaussian integral, gives finally

$$f(\phi,t)=\frac{1}{\sqrt{2\pi}a(t)}e^{-\frac{(\phi+\overline{\lambda}t)^2}{2a^2(t)}}. \tag{5.9}$$

Equation (5.9) is a gaussian distribution, in which the noise parameter $a(t)$ plays the role of the variance. From Eqs.(5.3) and (5.9) we can see that the effect of phase noise after averaging over many realizations of the stochastic process $\lambda(t)$ is a *spread* of the state with respect to the noisless case, combined with a possible rigid rotation around the $\hat{z}$ axes if $\bar{\lambda}\neq 0$. A visualization of such an effect is represented in Fig.5.3 (where $\bar{\lambda}=0$) for a two-component and a four-component phase cat states.

By projecting Eq.(5.3) on the Fock basis $\{|n\rangle\}$ we obtain

$$\langle n|\hat{\rho}(t)|n'\rangle=e^{-\frac{a^2(t)(n-n')^2}{2}}e^{i\overline{\lambda}t(n-n')}\langle n|\hat{\rho}^{(0)}(t)|n'\rangle. \tag{5.10}$$

Equation (5.10) contains all the information about the state formed in the presence of phase noise. Several peculiar properties of phase noise will be deduced by the structure of Eq.(5.10) in Secs.5.1.2-5.1.4. Notice that under our hypothesis, $a(t)$ and thus the decoherence factor (given by the first exponential in the right-hand side of Eq.(5.10)) is independent on the number of atoms N in the BJJ. This is in contrast with the usual scenario for decoherence which predicts stronger decoherence as the number of particles in the system is increased. As a consequence of this fact, macroscopic superpositions of phase states, of the form (2.25),(2.27), are robust against phase noise, as will be detailed in Sec.5.1.3 below. A generalization of this model to treat non gaussian noise is discussed in Ref.[24].

5.1.1.b Variance in different noise regimes

Before analyzing the effect of phase noise on the state of the atoms we briefly discuss the properties of the noise variance $a(t)$. First, let us note that Eq.(5.7) can be rewritten as

$$a^2(t)=2\int_0^t d\tau\int_0^\tau d\tau' h(\tau-\tau'). \tag{5.11}$$

Let us denote by t_c the largest time such that $h(\tau)\simeq h(0)=\delta\lambda(0)^2\equiv\delta\lambda^2$ and by T_c the characteristic time at which $h(\tau)$ vanishes. If the time evolution occurs on a short scale such that $t<t_c$ then the colored nature of the noise plays an important role (non-markov regime) and from Eq.(5.11) we obtain

$$a^2(t)\simeq 2\int_0^t d\tau\int_0^\tau d\tau' h(0)=h(0)t^2=\delta\lambda^2t^2. \tag{5.12}$$

If instead the time evolution occurs on a time scale much larger than the noise correlation time T_c we obtain the same result as for white noise,

$$a^2(t)\simeq 2t\int_0^\infty h(y)dy, \tag{5.13}$$

which corresponds to the Markov approximation.

The effect of phase noise can be partially suppressed by using a so-called spin-echo protocol [154]. This strategy was followed in a recent experiment [8]. The analysis discussed in Sec. 5.1.1.a can be adapted to take into account the residual effect of phase noise when spin echo pulses are applied, see Appendix D.1.

5.1.2 Effect of phase noise on the visibility

Under the effect of the noise, the visibility (1.45) acquires an additional decaying factor due to the above-mentioned phase spreading. Indeed, one easily obtains from (5.10)

$$\nu(t) = \frac{2}{N}\mathrm{tr}[\hat{\rho}(t)\hat{J}_x] = e^{-\frac{a^2(t)}{2}}\cos\left(\overline{\lambda}t\right)\nu^{(0)}(t). \tag{5.14}$$

The dephasing factor $e^{-a^2(t)/2}$ displays a Gaussian decay at short times $t \leq t_c$, corresponding to the universal regime of Ref. [93], and an exponential decay at long times $t \gg T_c$ (Markov regime). A Gaussian decay of the visibility (5.14) has been observed experimentally in the internal BJJ even at small values of the interactions χ [62]. This indicates that in the time regime $0 \leq t \lesssim t_{fs}$ in which the experiment was performed the phase noise has strong time correlations (colored noise), corresponding to a non-markovian regime. An estimate of the noise is extracted from the fit of the visibility decay data in Fig.4.15 of Ref. [62] to our prediction given by Eq.(5.14). The resulting value for the noise correlations is $h(0)^{1/2} \simeq 8$Hz, obtained for a small value of the interactions χ, thus in a regime in which the decay is mainly due to the phase noise. The effect of phase noise on the visibility decay in this regime is shown in Fig.5.1, for experimentally relevant parameters [62].

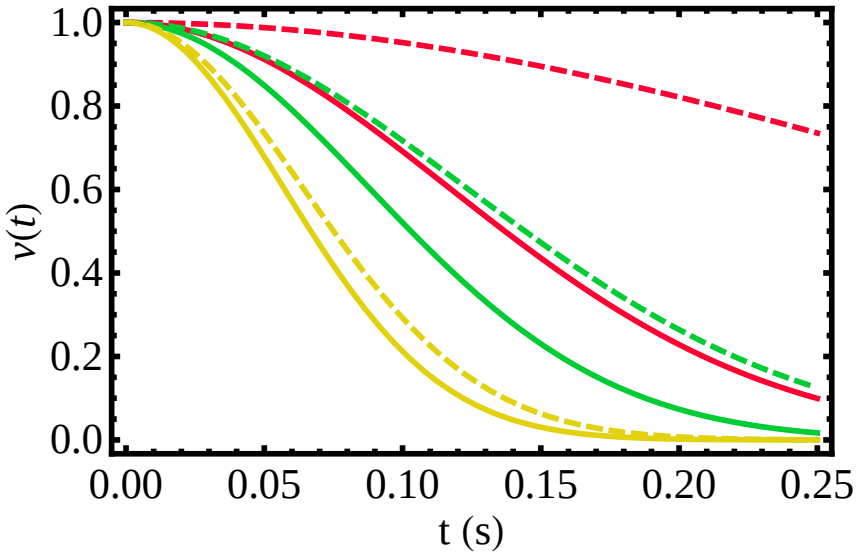

Figure 5.1: Visibility $\nu(t)$ as a function of time (in units of seconds) for $\chi = \pi \cdot 0.05$Hz, $\pi \cdot 0.13$Hz, $\pi \cdot 0.25$Hz (from top to bottom), $N = 400$. Solid lines: decay of $\nu(t)$ in Eq.(5.14) in the limit $\chi t \ll 1$ and $\overline{\lambda}t \ll 1$ with $a^2(t) = h(0)t^2$ and $h(0)^{1/2} = 8$Hz. Dashed lines: decay of $\nu^{(0)}(t)$ under the unitary evolution only. For small values of the interactions the decay is mainly due to the phase noise.

5.1.3 Effect of phase noise on multicomponent macroscopic superpositions of phase states

We proceed now to study the nature of the state of the atoms under phase noise at the specific times t_q which in the noiseless BJJ correspond to the formation of multicomponent superpositions of phase states. We first illustrate the effect of the noise on the structure of

the density matrix, then we visualize our results by means of the probability distributions of the eigenvalues of the angular momentum operators presented in Sec.3.2.1.

5.1.3.a Structure of the density matrix in the Fock basis

In the absence of noise the quenched dynamics of the Bose Josephson junction leads to the formation of coherent superpositions with q components as given by Eqs.(2.25),(2.27). The corresponding density matrix $\hat{\rho}^{(0)}(t_q) = |\psi^{(0)}(t_q)\rangle\langle\psi^{(0)}(t_q)|$ has the form $\hat{\rho}^{(0)}(t_q) = \sum_{k,k'} \hat{\rho}^{(0)}_{kk'}(t_q)$, where the indices k and k' label the various components of the superposition and $\hat{\rho}^{(0)}_{kk'}(t_q) = q^{-1} c_{k,q} c^*_{k',q} |\pi/2, \phi_{k,q}\rangle\langle\pi/2, \phi_{k',q}|$. For general decoherence processes one expects that, by increasing the intensity of the noise, $\hat{\rho}^{(0)}(t_q)$ will evolve into the statistical mixture of phase states $\sum_k \hat{\rho}^{(0)}_{kk}(t_q)$; moreover, the larger the atom number N the weaker should be the noise strength at which this occurs [155]. It was found in [24] that for the phase noise considered in Sec.5.1.1.a the actual scenario for decoherence is different from the usual one. Indeed, the typical noise intensity at which the coherences between distinct phase states $|\pi/2, \phi_{k,q}\rangle$ are lost turns out to be independent on the atom number. This is a consequence of the fact that the decoherence factor $a(t)$ is independent on N, as shown in Sec.5.1.1.a. Furthermore, for superpositions with a large number of components q, this intensity is *larger than* the noise intensity at which phase relaxation occurs. In what follows we discuss the origin of this fact.

Since the noise is expected to destroy correlations between different components of the macroscopic superposition, we decompose the density matrix in its diagonal (intra-component) and off-diagonal (intercomponent) parts, focussing on the latter one to quantify the decoherence. We have then $\hat{\rho}^{(0)} = \hat{\rho}^{(0)}_{\rm d} + \hat{\rho}^{(0)}_{\rm od}$ where

$$\hat{\rho}^{(0)}_{\rm d}(t_q) = \sum_{k=0}^{q-1} \hat{\rho}^{(0)}_{kk}(t_q) \tag{5.15}$$

and

$$\hat{\rho}^{(0)}_{\rm od}(t_q) = \sum_{k,k'=0;k\neq k'}^{q-1} \hat{\rho}^{(0)}_{kk'}(t_q). \tag{5.16}$$

Let us consider for simplicity the case q,N even; the general case can be found in Ref.[25]. Using Eqs.(2.25) and (1.28) and the identity $\sum_{k=0}^{q-1} e^{2ik(n'-n)\pi/q} = q$ if $n = n'$ modulo q and 0 otherwise, the matrix elements of $\hat{\rho}^{(0)}_{\rm d}(t_q)$ in the Fock basis are

$$\langle n|\hat{\rho}^{(0)}_{\rm d}(t_q)|n'\rangle = \begin{cases} \dfrac{1}{2^N} \binom{N}{\frac{N}{2}+n}^{\frac{1}{2}} \binom{N}{\frac{N}{2}+n'}^{\frac{1}{2}} & \text{if } n' = n + pq \\ 0 & \text{if } n' \neq n \bmod q \end{cases} \tag{5.17}$$

where p is an integer. By using $\hat{\rho}^{(0)}_{\rm od}(t_q) = e^{-i\pi \hat{J}_z^2/q} |\theta = \pi/2, \phi = 0\rangle\langle\theta = \pi/2, \phi = 0| e^{i\pi \hat{J}_z^2/q} - \hat{\rho}^{(0)}_{\rm d}(t_q)$, we also get

$$\langle n|\hat{\rho}^{(0)}_{\rm od}(t_q)|n'\rangle = \begin{cases} 0 & \text{if } n' = n + pq \\ \dfrac{e^{i\frac{\pi}{q}(n'^2-n^2)}}{2^N} \binom{N}{\frac{N}{2}+n}^{\frac{1}{2}} \binom{N}{\frac{N}{2}+n'}^{\frac{1}{2}} & \text{if } n' \neq n \bmod q \end{cases} \tag{5.18}$$

The use of Eq.(5.10) allows to obtain the corresponding expressions in the presence of noise,

$$\langle n|\hat{\rho}_{\rm d,od}(t_q)|n'\rangle = e^{-\frac{a_q^2(n-n')^2}{2}}\langle n|\hat{\rho}^{(0)}_{\rm d,od}(t_q)|n'\rangle \tag{5.19}$$

up to a phase factor irrelevant for decoherence, with $a_q \equiv a(t_q)$. In the strong noise limit $a_q \gg 1$, the off-diagonal part $\hat{\rho}_{\rm od}$ of the atom density matrix vanishes whereas the diagonal part $\hat{\rho}_{\rm d}$ tends to a matrix which is diagonal in the Fock basis,

$$\begin{aligned}\hat{\rho}_{\rm d}(t_q) \to \hat{\rho}_\infty &= \sum_{n=-N/2}^{N/2} \frac{1}{2^N}\binom{N}{\frac{N}{2}+n}|n\rangle\langle n| \\ &= \int_0^{2\pi}\frac{d\phi}{2\pi}\,|\theta=\pi/2,\phi\rangle\langle\theta=\pi/2,\phi|\,.\end{aligned} \tag{5.20}$$

This means that for large noise intensity (or for long times) the phase ϕ is uniformly spread on $[0, 2\pi]$, as is the case for Fock states (Fig.5.3, right panels).

From Eqs.(5.17) and (5.18) we obtain a peculiar result, i.e. that the diagonal part of the atom density matrix decays faster than the off-diagonal part for increasing noise strengths [24]. This is readily explained by examining the structure of the noiseless density matrices in Eqs.(5.17) and (5.18). The first off-diagonal elements of $\hat{\rho}_{\rm d}(t_q)$ in the Fock basis are those for which $n' = n \pm q$ while the first off-diagonal elements of $\hat{\rho}_{\rm od}(t_q)$ satisfy $n' = n \pm 1$. Hence, it results from Eq.(5.19) that the off-diagonal elements of $\hat{\rho}_{\rm d}$ vanish at the noise scale $a \simeq 1/q$ while the off-diagonal elements of $\hat{\rho}_{\rm od}$ vanish at the larger noise scale $a \simeq 1$. In other words, the noise is more effective in letting $\hat{\rho}_{\rm d}$ converge to $\hat{\rho}_\infty$ than in suppressing $\hat{\rho}_{\rm od}$, and this effect is more pronounced the higher is the number of components in the superposition. An illustration of such anomalous decoherence is given in Fig.5.2. The middle panels show that for intermediate noise strengths, $\hat{\rho}_{\rm d}$ has already acquired its asymptotic diagonal form (5.20), while $\hat{\rho}_{\rm od}$ has not yet vanished. As we will see in Sec.5.1.4 below, these results imply that, for moderate strengths of phase noise, macroscopic superpositions are formed and provide quantum correlations useful for interferometry.

5.1.3.b Husimi distribution

The phase relaxation of macroscopic superpositions of phase states can be visualized by means of the projected Husimi distribution $Q(\theta = \pi/2, \phi)$ introduced in Sec.3.1.1.c. For a two-component phase cat state it is particularly simple to calculate this function, as it is exactly given by the diagonal part of the density matrix $\hat{\rho}_{\rm d}(t_2)$ only. The calculation is reported in Appendix D.2, and gives as a result for $\bar{\lambda} = 0$, $N \gg 1$, and $N^{-1/4} \ll a_2 \ll N^{-1/2}$

$$Q(\frac{\pi}{2},\phi) = \frac{\sqrt{2\pi}}{2a_2}Q_{cost}\Theta_3\left(-\phi, e^{-2a_2^2}\right), \tag{5.21}$$

with Θ_3 the Theta function [156] and $Q_{cost} = \frac{1}{\sqrt{\pi}}\frac{\Gamma\left(\frac{1}{2}+N\right)}{\Gamma(1+N)}$ the distribution of the state (5.20) (see Appendix D.2). $Q(\pi/2, \phi)$ is plotted for various values of a_2 in Fig.5.3. In the absence of noise it shows peaks at $\phi = 0$ and π, which correspond to the two coherent states of the superposition. The peaks are smeared at increasing a_2, and finally at $a_2 \gg 1$ the Husimi distribution reaches the flat profile $Q(\pi/2, \phi) = Q_{cost}$.

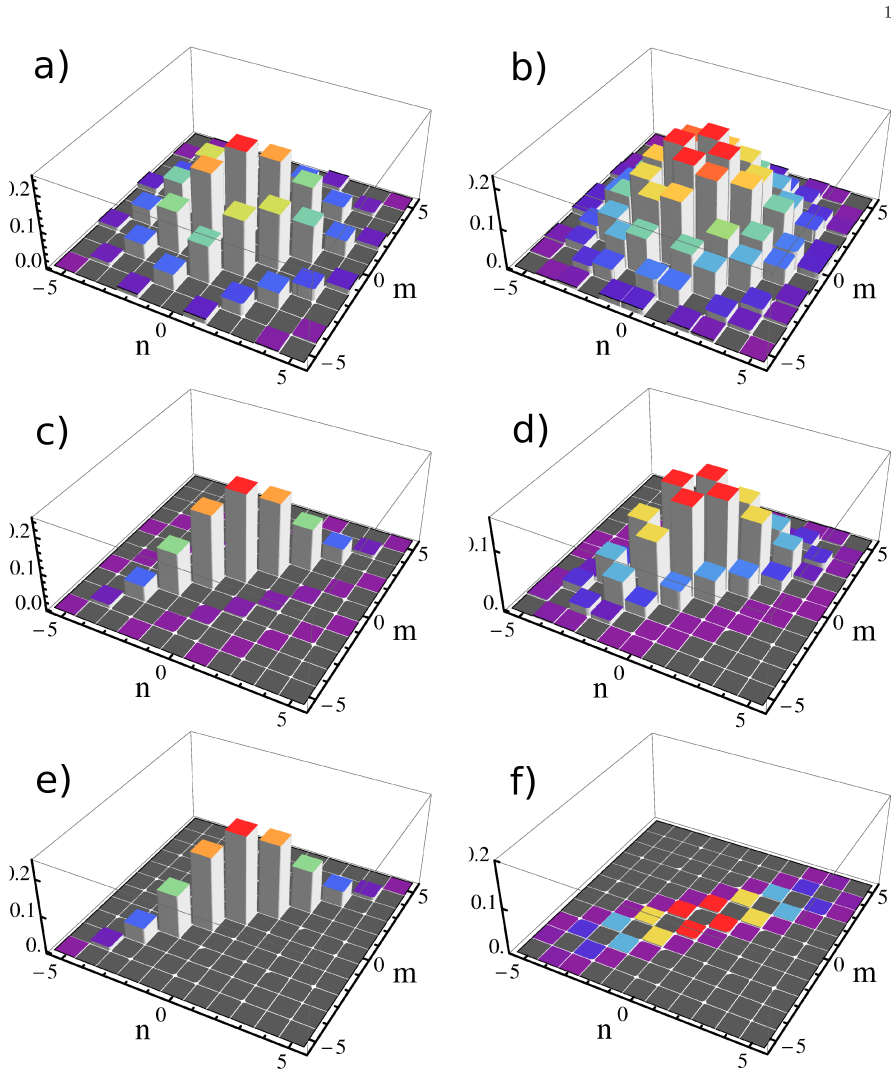

Figure 5.2: Matrix elements of the diagonal (intracomponent) part $\hat{\rho}_{\rm d}(t_3)$ (panels a),c),e)) and the off-diagonal (inter-component) part $\hat{\rho}_{\rm od}(t_3)$ (panels b),d),f)) of the density matrix in the Fock basis at time $t = t_3$ as the noise is increased from $a_3 = 0$ (a),b)) to $a_3 = 0.9$ (c),d)) and $a_3 = 2.9$ (e),f)).

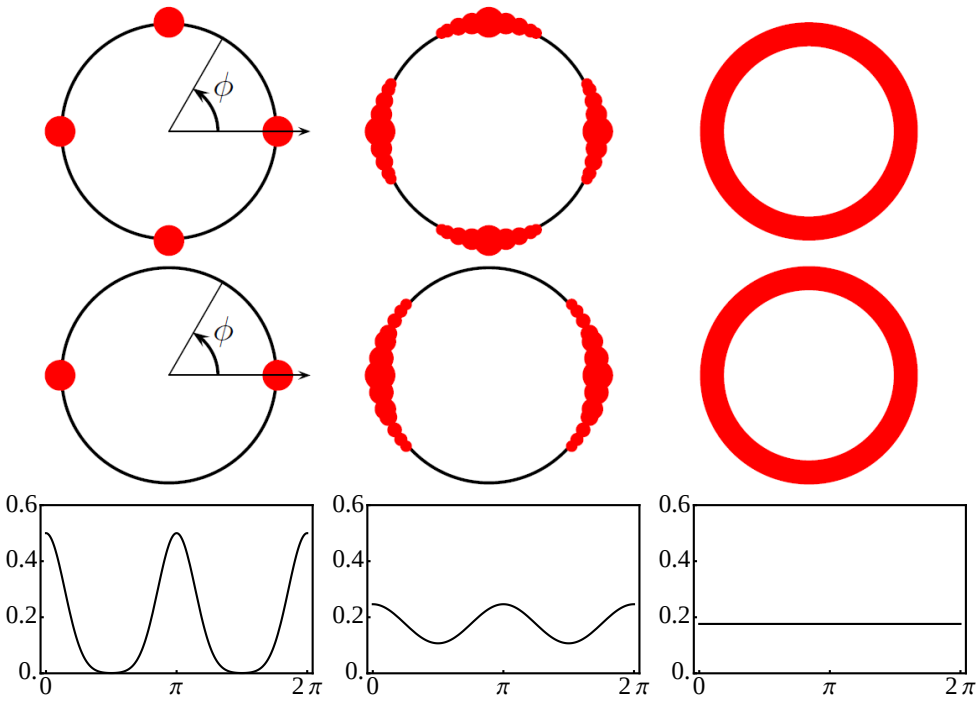

Figure 5.3: Phase relaxation of the $q = 4$ and $q = 2$ macroscopic superpositions in the presence of noise sketched along the equator $\theta = \pi/2$ of the Bloch sphere. Top panels: $q = 4$ ($t_4 = T/8$) and $a_4 = 0$, 0.64, 2.05 (from left to right). Middle panels: $q = 2$ ($t_2 = T/4$) for the same noise intensities $\int_0^\infty d\tau h(\tau)$ in the Markov regime ($a_2 = 0$, 0.9, 2.9). The circle sizes illustrate qualitatively the phase distribution $f(\phi, t_{2,4})$. For intermediate noise (middle column), the superposition is closer to the steady state (last column) for $q = 4$ than for $q = 2$. Bottom panels: Husimi distribution $Q(\theta = \pi/2, \phi)$ for $q = 2$ for the same values of a_2. Here $\overline{\lambda} = 0$ and $N = 10$.

5.1.3.c Angular momentum distributions

The anomalous decoherence of the atomic state can be visualized by plotting the probability distribution $P_\phi(r)$ of the eigenvalues of the angular momentum operators $\hat{J}_r = \hat{J}_x \sin\phi - \hat{J}_y \cos\phi$ in an arbitrary direction of the equatorial plane of the Bloch sphere. Indeed, as presented in Sec.3.2.1, the presence of correlations among the components of the superposition formed at time t_q is revealed by interference fringes in these distributions, which would be absent if the atoms would be in a statistical mixture of phase states.

The probability distribution of $\hat{J}_r$ in the state $\hat{\rho}$ can be calculated by a straightforward generalization of the calculation in Sec. 3.2.1 as the Fourier coefficient of the characteristic function $h_\phi(\eta, t) = \mathrm{tr}[e^{-i\eta \hat{J}_r}\hat{\rho}(t)]$, namely,

$$P_\phi(r;t) = \frac{1}{2\pi}\int_{-\pi}^{\pi} d\eta\, h_\phi(\eta;t) e^{i\eta r}. \tag{5.22}$$

For the quenched dynamics of the Bose Josephson junction in the presence of noise, the characteristic function reads

$$h_\phi(\eta;t) = \sum_{n,n'=-N/2}^{N/2} g_{nn'}(t)\langle n|\hat{\rho}^{(0)}(t)|n'\rangle \times D_{n'n}(-\phi,\eta,\phi) \tag{5.23}$$

where $g_{nn'}(t) = e^{-a^2(t)(n-n')^2/2} e^{i\bar{\lambda}t(n-n')}$ and $D_{n'n}(-\phi,\eta,\phi)$ is the matrix element of the rotation operator $e^{-i\eta J_\phi}$ in the Fock basis, which is given by (see e.g. [71], Eq. (D6))

$$D_{n'n}(-\phi,\eta,\phi) = \langle n'|e^{-i\eta J_\phi}|n\rangle = \sum_{k=\max\{0,n-n'\}}^{\min\{N/2-n',N/2+n\}} (-1)^k \binom{N}{\frac{N}{2}+n}^{-\frac{1}{2}} \binom{N}{\frac{N}{2}+n'}^{-\frac{1}{2}}$$
$$\times \frac{N!}{(\frac{N}{2}-n'-k)!(\frac{N}{2}+n-k)!k!(k+n'-n)!} \times \left(\sin\frac{\eta}{2}\right)^{2k+n'-n} \left(\cos\frac{\eta}{2}\right)^{N+n-n'-2k} e^{-i\phi(n'-n)}.$$

The probability distribution in the absence of noise derived in Sec. 3.2.1 is recovered by setting $g_{nn'}(t) = 1$ in Eq.(5.23).

As an example, the distribution $P_{\pi/2}(r,t_3) = |\langle n_x = r|\psi^{(0)}(t_3)\rangle|^2$ of the eigenvalues of $\hat{J}_x$ (satisfying $\hat{J}_x|n_x = r\rangle = r|n_x = r\rangle$) is shown in Fig.5.4 for the three-component superposition of phase states, for $\bar{\lambda} = 0$. As we have presented in Sec.3.2.1, in the absence of noise (panel a)) its profile displays two peaks corresponding to the projections on the x-axes of the phase states $|\theta = \pi/2, \phi = \phi_{k,3}\rangle$, $\phi_{k,3} = \pi, \pm\pi/3$ (the "phase content" of the state, accounted for by $\hat{\rho}_{\mathrm{d}}(t_3)$) and interference fringes, due to the coherences between these phase states (contained in $\hat{\rho}_{\mathrm{od}}(t_3)$). In the presence of noise (b)-c)), the phase profile of each component of the superposition spreads and the characteristic peaks of the distribution are smeared out (phase relaxation). At strong noise intensities, $\hat{\rho}_{\mathrm{d}}(t_q)$ approaches the steady-state given by the density matrix (5.20), which is symmetric in the (xOy)-plane. As a consequence, the corresponding probability distribution $P_\phi(r,\infty) \equiv P(r,\infty) = \mathrm{tr}[\hat{\rho}_\infty|n_x = r\rangle\langle n_x = r|]$ is independent on ϕ. In the semi-classical limit $N \gg 1$, this distribution can be easily calculated since $\hat{J}_x$ takes the values $N\cos\phi/2$ in the phase states $|\pi/2,\phi\rangle$ apart from small relative fluctuations of the order of $1/\sqrt{N}$ (see Eq.(1.30)). Hence, recalling that $\hat{\rho}_\infty$ is a statistical mixture of the states $|\pi/2,\phi\rangle$ with

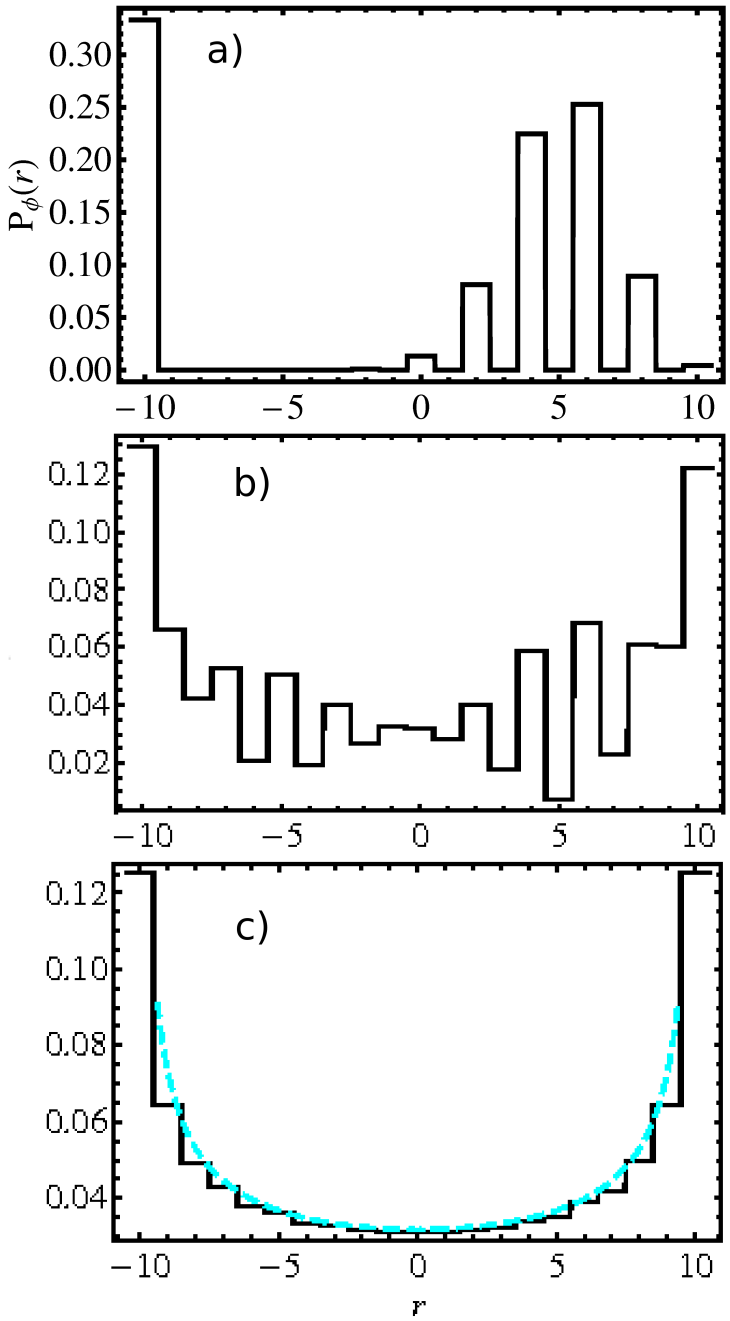

Figure 5.4: Probability distribution $P_{\pi/2}(r, t_3)$ of the eigenvalues of $\hat{J}_x$ for the three-component coherent superposition (solid lines) at increasing noise strength from $a_3 = 0$ (a), to $a_3 = 0.9$ (b) and $a_3 = 2.9$ (c) with $N = 20$ atoms. The blue dashed curves indicate the large-noise intensity and large N limit given by Eq.(5.24).

equal probabilities (see Eq.(5.20)),

$$P(r,\infty) = c\int_0^{2\pi} d\phi\,\delta\left(\frac{N}{2}\cos\phi - r\right) = \frac{1}{\pi}\frac{1}{\sqrt{\left(\frac{N}{2}\right)^2 - r^2}} \tag{5.24}$$

where c is a normalization factor. The semi-circle law (5.24) is indicated by the blue dashed curve in panel c) of Fig.5.4. For finite N, one finds

$$P(r,\infty) = \binom{N}{\frac{N}{2}+r}\frac{1}{\pi}\frac{\Gamma\left[\frac{N}{2}+\frac{1}{2}-r\right]\Gamma\left[\frac{N}{2}+\frac{1}{2}+r\right]}{\Gamma\left[N+1\right]}.$$

On the other hand, the vanishing of $\hat{\rho}_{\rm od}(t_q)$ tends to diminish the contrast of the fringes in the distribution $P_\phi(r,t_q)$, until they are completely washed out in the asymptotic distribution (panel c) of Fig.5.4). The fact that phase relaxation occurs at a lower noise strength than decoherence is evident in the panel b), where the profile of $P_\phi(r,t_q)$ is close to the asymptotic distribution $P(r,\infty)$ corresponding to $\hat{\rho}_\infty$, while interference fringes due to $\hat{\rho}_{\rm od}(t_q)$ are still visible.

The surprising fact that decoherence is not enhanced by increasing the atom number N is specific to the noise considered. Indeed, such a noise is applied perpendicularly to the equator of the Bloch sphere where the phase states of the superpositions lay. As a result, the noise is insensitive to the separation between these states, which scales with N. However, such superpositions are very fragile under a noise applied parallel to the equatorial plane, which resolves the separation between the components. This yields an indication as to which classical noise to reduce to preserve the coherence in superpositions of the phase states: this is the noise in directions parallel to this plane. For example, stochastic fluctuations on the tunnel amplitude K give rise to rapid decoherence of the macroscopic superposition $(|\alpha=1\rangle + e^{i\gamma}|\alpha=-1\rangle)/\sqrt{2}$ at a rate increasing with the atom number, without inducing relaxation. By rotation of the same argument, the same fate is followed by a NOON state under the action of phase noise, as we will show in Appendix D.4.

5.1.4 Quantum Fisher information and coherent spin squeezing during the quenched dynamics of the BJJ

We present in this section the calculation of the useful quantum correlations which are formed during the quenched dynamics of the Bose Josephson junction, when phase noise is affecting the system. Hence, in analogy with what the calculation presented in Sec.4.4 for the noiseless case, we evaluate the quantum Fisher information and the coherent spin squeezing parameter as a function of time. We take for simplicity $\bar{\lambda} = 0$.

5.1.4.a Coherent spin squeezing in the presence of phase noise

For coherent spin squeezing the calculation can be carried out analytically. We start with the observation that even in the presence of noise $\langle\hat{J}_y\rangle_t = \langle\hat{J}_z\rangle_t = 0$ and more generally the angular-momentum covariance matrix G defined in Eq.(4.31) has the same structure as the matrix (4.34) in the noiseless case. Therefore, the arguments used in Appendix B.1 can be taken over to the noisy case. We thus conclude that the squeezing parameter ξ^2 is minimum in the (yOz)-plane, and is given by Eq.(4.39), evaluated for the corresponding quantities in the presence of noise. In particular, the bare visibility $\nu^{(0)}$, Eq.(2.20), should

be replaced by the visibility ν in the presence of noise which is given in Eq.(5.14) with $\bar{\lambda} = 0$, and $\gamma_-^{(0)}$ by the lowest eigenvalue G_- of the restriction of the covariance matrix G to the (yOz)-plane.

We are now going to compute G_- and the spin squeezing parameter explicitly. In order to do so, we need to perform the averages in the presence of noise using the full density matrix $\hat{\rho}(t)$: $\langle \ldots \rangle_t = \mathrm{tr}(\ldots \hat{\rho}(t))$. These are related to those in the absence of noise according to

$$\langle \hat{J}_i \rangle_t = \int_{-\infty}^{\infty} d\phi \, f(\phi, t) \langle e^{i\phi \hat{J}_z} \hat{J}_i e^{-i\phi \hat{J}_z} \rangle_t^{(0)} \tag{5.25}$$

where the expectation value inside the integral is taken for the pure state $|\psi^{(0)}(t)\rangle$ in the absence of noise. The rotated angular momentum operators in the above expectation value are equal to $\cos\phi \hat{J}_x - \sin\phi \hat{J}_y$, $\sin\phi \hat{J}_x + \cos\phi \hat{J}_y$, and $\hat{J}_z$ for $i = x, y$, and z, respectively. A similar derivation holds for $\langle \{\hat{J}_i, \hat{J}_j\} \rangle_t = \mathrm{tr}[\hat{\rho}(t)\{\hat{J}_i, \hat{J}_j\}]$. We are left with integrals of trigonometric functions with the gaussian envelope given by Eq.(5.9), yielding the result

$$\begin{aligned}
\langle \hat{J}_z^2 \rangle_t &= \langle \hat{J}_z^2 \rangle_t^{(0)} = \frac{N}{4} \\
\langle \hat{J}_y^2 \rangle_t &= \frac{1 - e^{-2a^2(t)}}{2} \langle \hat{J}_x^2 \rangle_t^{(0)} + \frac{1 + e^{-2a^2(t)}}{2} \langle \hat{J}_y^2 \rangle_t \\
\langle \{\hat{J}_y, \hat{J}_z\} \rangle_t &= e^{-a^2(t)/2} \langle \{\hat{J}_y, \hat{J}_z\} \rangle_t^{(0)} \\
\langle \{\hat{J}_x, \hat{J}_y\} \rangle_t &= \langle \{\hat{J}_x, \hat{J}_z\} \rangle_t = 0 \,.
\end{aligned} \tag{5.26}$$

Finally, the submatrix matrix $G'(t)$ reads

$$G'(\tau) = \begin{pmatrix} \frac{N}{8}\left[-e^{-2a^2(\tau)}(N-1)\cos^{N-2}(2\tau) + (N+1)\right] & \frac{1}{4}e^{-\frac{a^2(\tau)}{2}} N(N-1)\cos^{N-2}(\tau)\sin(\tau) \\ \frac{1}{4}e^{-\frac{a^2(\tau)}{2}} N(N-1)\cos^{N-2}(\tau)\sin(\tau) & \frac{N}{4} \end{pmatrix} . \tag{5.27}$$

Thus, by Eqs.(4.39), (5.14) and (5.27), one has

$$\begin{aligned}
\xi^2(\tau) &= \frac{1}{4{\nu^{(0)}}^2(\tau)} \Big[-e^{-a^2(\tau)}(N-1)\cos^{N-2}(2\tau) + e^{a^2(\tau)}(N+3) \\
&\quad -(N-1)e^{a^2(\tau)} \sqrt{(1 - e^{-2a^2(\tau)}\cos^{N-2}(2\tau))^2 + 16 e^{-a^2(\tau)} \cos^{2(N-2)}(\tau)\sin^2(\tau)} \Big] .
\end{aligned} \tag{5.28}$$

The angle which identifies the optimal squeezing direction is given by Eq.(4.42), in which the matrix $\gamma^{(0)'}$ should be replaced by G'.

We proceed by illustrating our results for the squeezing parameter in the presence of phase noise. For the calculations we have chosen a noise range of direct experimental relevance, as extracted from the fit of the visibility decay data mentioned in Sec.5.1.2 (see also caption of Fig.5.1 and forthcoming Sec. 6.2.2). For the noise variance $a^2(\tau)$ we have taken the short-time behavior $a^2(\tau) = (\delta\lambda/\chi)^2\tau^2$ expressed by Eq.(5.12) since the experimental visibility exhibits a gaussian decay even for small interactions χ [62] (see Sec.5.1.2). The squeezing parameter as a function of time is shown in Fig.5.5-a). As seen in the figure, the presence of noise degrades the squeezing, as its minimum value increases at increasing noise strength. We also notice that the time for optimal squeezing $t_{\min}$ is slightly shorter than in the noiseless case. Analytical estimates of the minimum value reached by the squeezing parameter and of the corresponding time can be found in

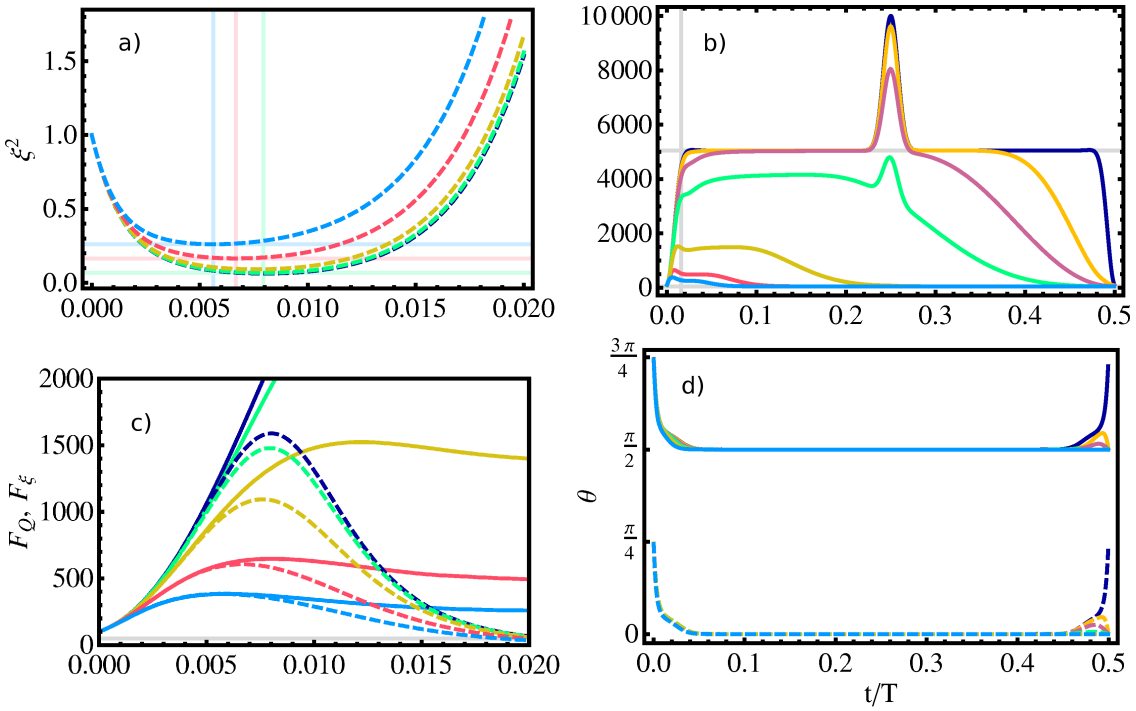

Figure 5.5: Coherent spin squeezing and quantum Fisher information in the presence of noise as a function of time in units of T during the quenched dynamics of a BJJ. The parameters used are $N = 100$, $\chi = \pi\,\mathrm{Hz}$. a) Spin squeezing ξ^2 for (from top to bottom) $\delta\lambda = 15, 10, 5,$ and $0\,\mathrm{Hz}$. Horizontal and vertical gridlines: minimum of ξ^2 and corresponding time $t_{\min}$. b) Fisher information F_Q for (from top to bottom) $\delta\lambda = 0, 0.4, 1, 2, 5, 10,$ and $15\,\mathrm{Hz}$; the horizontal and vertical gridlines correspond to $F_Q = N(N+1)/2$ and $t = t_{fs} = T/\sqrt{N}$. c) Zoom on the quantum Fisher information (solid lines) and $F_\xi = N/\xi^2$ (dashed lines) for $\delta\lambda = 0, 2, 5, 10,$ and $15\,\mathrm{Hz}$ (from top to bottom). d) Angles θ_F and θ_ξ giving the optimizing direction of F_Q (solid lines) and ξ^2 (dashed lines) as a function t/T, for the same noise levels.

Ref.[25]. The angle $\theta_\xi(t)$ which identifies the optimizing squeezing direction is represented in dashed lines for various noise levels in Fig.5.5-d).

In the experiments of Refs.[8, 9], affected by phase noise, the squeezing degree has been measured at a fixed time, as a function of the angle θ. This motivates the theoretical calculation of the curve $\xi^2(\theta)$, which is reported in appendix D.3.

5.1.4.b Quantum Fisher information in the presence of phase noise

The evaluation of the optimum quantum Fisher information (4.29) requires a numerical diagonalization of the density matrix $\hat{\rho}(t)$ given by Eq.(5.10). For the time dependence of $a^2(t)$ we take again the short-time approximation given in Eq.(5.12), even if there is no experimental evidence that justifies such a choice at times $t \sim T$. This choice corresponds to the worst possible scenario for decoherence, as in the markovian regime the dependence of $a^2(t)$ is weaker (see Eq.(5.13)) [24]. The behavior of F_Q as a function of time in the presence of noise results from the competition of two phenomena: (i) in the absence of noise, at short times the quantum Fisher information grows from its initial value $F_Q = N$ to the plateau value $F_Q = N(N+1)/2$ in a time interval $t_{fs} \sim T/\sqrt{N}$ which shrinks as N becomes larger, and (ii) the decoherence exponent $a^2(t)$ is independent on N and also grows with time. As a result, F_Q reaches a local maximum at a time $t_{\max} \sim t_{sf}$, with a value which increases with N and decreases with the noise fluctuation $\delta\lambda^2$.

The quantum Fisher information as a function of time for various noise levels is shown in Fig. 5.5. The short-time evolution is similar to the one found for the noiseless case, the accumulation of noise correlations being not yet effective. In particular, one observes that F_Q coincides with the squeezing parameter $F_\xi = N/\xi^2$ at sufficiently small times (panel c). For not too large noise intensities, F_Q displays a plateau at those times which in the noiseless BJJ correspond to the formation of macroscopic superpositions. The value on the plateau is smaller than in the absence of noise but it is still much above the shot noise level $F_Q = N$. This indicates the presence of useful correlations which remain in spite of the decoherence effects induced by the noise. This effect is due to the robustness of the multicomponent superpositions with respect to phase noise discussed in Sec.5.1.3 above. For higher noise levels, the width of the plateau is reduced and the peak at $t_2 \equiv T/4$ corresponding to the two-component superposition in the absence of noise disappears completely, meaning that decoherence has washed out the useful quantum correlations at t_2 (three bottom curves in the Fig.5.5-b)). In the limit of very large noise intensities the Fisher information at times t_q of formation of q-component superpositions in the noiseless BJJ is degenerate in the (xOy) plane and tends to the asymptotic value

$$F_Q[\hat{\rho}_\infty] = \frac{N(N-1)}{2N+2}\,, \tag{5.29}$$

which can be readily obtained from Eqs.(4.30) and (5.20). As illustrated in Fig.5.6, apart from short times and around the peak at t_2, the optimization direction is in the (xOy)-plane and F_Q is almost degenerate in all directions of this plane, as in the noiseless case.

As a partial summary, the analysis of the time evolution of the quantum Fisher information indicates the build-up of useful quantum correlations at times beyond the spin-squeezing regime. In the following we quantify this effect by studying the dependence of F_Q with the noise strength and the particle number.

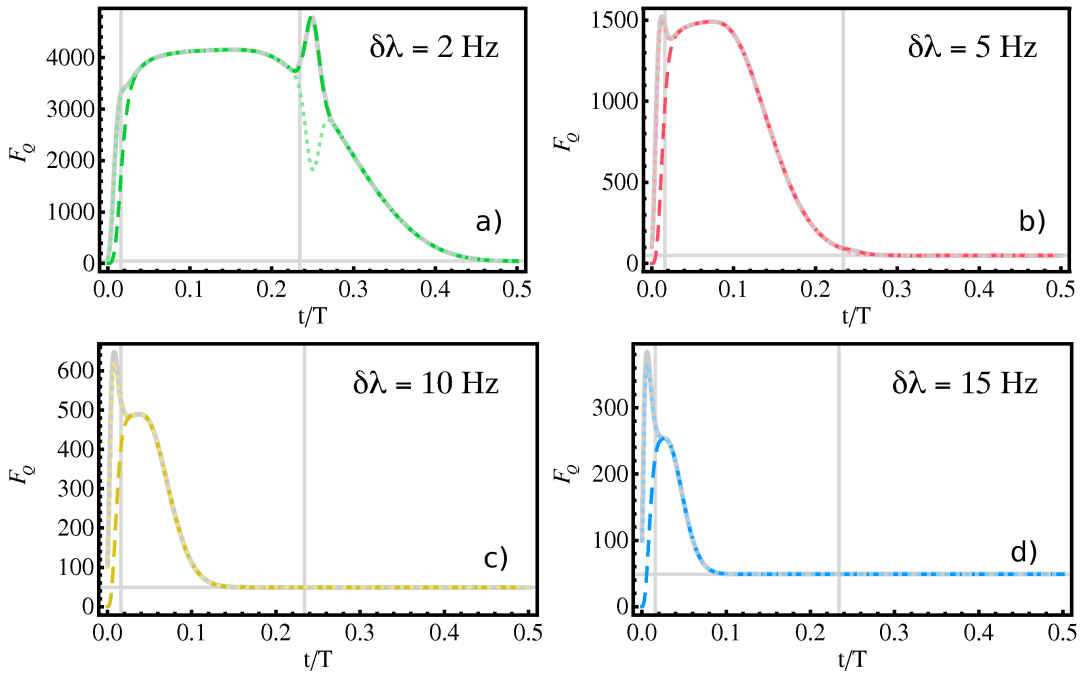

Figure 5.6: Direction-dependent quantum Fisher information in the presence of noise as a function of time in units of T during the quenched dynamics of a BJJ with $N = 100$ atoms and $\chi = \pi$Hz for: a) $\delta\lambda = 2$Hz, b) 5Hz, c) 10Hz and d) 15Hz, calculated along the $\hat{x}$ direction (dashed lines), the $\hat{y}$ direction (dotted lines) and the optimizing direction (light-gray solid line). After a time $t \sim T/\sqrt{N}$ (left vertical gridlines) the three values are almost the same, showing that the Fisher information is almost degenerate in the (xOy) plane, except around $t = T/4$ if F_Q has a peak at this value (panel a)). The vertical and horizontal gridlines represent the times $t = t_{fs}$ and $t = T/4 - t_{fs}$ and the value of the Fisher information in the limit of large noise intensities given by Eq.(5.29).

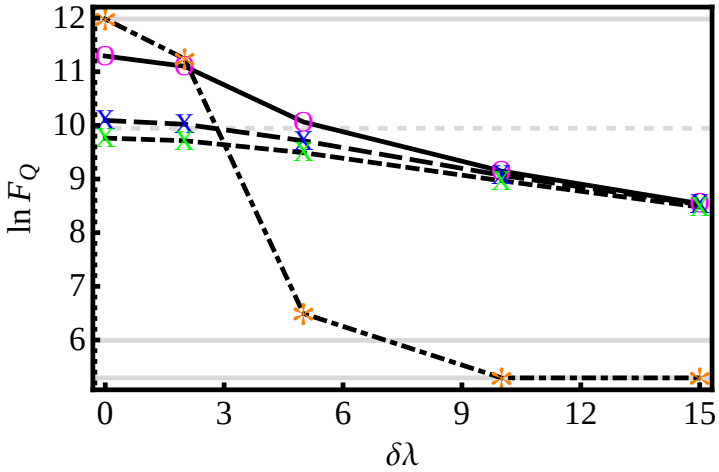

Figure 5.7: Values of the Fisher information at its local maximum at time $t_{\max}$ (solid line, circle markers), at time t_2 (dot-dashed line, star markers) and at the time $t_{\min}$ of maximal squeezing (long-dashed line, blue cross markers) in a logarithmic scale, as a function of the energy fluctuation $\delta\lambda$ (in Hz). For comparison we also plot the squeezing parameter $F_\xi = N/\xi^2$ at the time $t_{\min}$ (dashed line, green cross markers) in a logarithmic scale. Gridlines, from top to bottom: Heisenberg limit N^2 (solid), approximate value $(2/3^{2/3})N^{5/3}$ of $F_\xi(t_{\min})$ in the absence of noise, see Sec.4.4 (dashed), shot noise limit (solid), and limit of F_Q for large noise intensities (solid) given by Eq.(5.29). The parameters used are $N = 400$ and $\chi = \pi$ Hz.

5.1.4.c Quantum correlations vs particle number and phase noise

Figure 5.7 shows $F_Q(t)$ on a logarithmic scale, evaluated at the time $t = t_2 \equiv T/4$ of formation of the two-component superposition in the noiseless BJJ, as well as the maximum $(F_Q)_{\max}$ of $F_Q(t)$ in the time interval $0 < t < T/8$. This maximum corresponds roughly to the value at the plateau in Fig.5.5, that is, to the value of $F_Q(t)$ at the times of formation of the first multicomponent superpositions. It can be seen that in the range of noise considered $(F_Q)_{\max}$ stays above the shot noise level, and is also larger than the value $F_Q(t_{\min})$ at the time $t_{\min}$ of highest squeezing. The two-component superposition, formed much after the superpositions with a large number of components, appears to be too much degraded by noise to lead to any advantage in interferometry with respect to separable states. Hence, in this regime multicomponent macroscopic superpositions provide a convenient alternative to both the squeezed states and the two-component macroscopic superposition.

We next study the scaling of the quantum Fisher information with the particle number, taken at the time $t_{\max}$ as before. As it is illustrated in Fig.5.8, at this time F_Q displays a power-law behavior $F_Q \sim N^\beta$ with an exponent β depending on the noise strength. This exponent is extracted from a log-linear fit of the numerical data, varying N between 50 and 400 [1], the latter value being realistic in the experiments [8]. We notice that in the noise range considered β is larger or equal to 5/3, which is the exponent corresponding to the squeezed state at $t = t_{\min}$ in the absence of noise (see Sec.4.4). For the chosen interval of noise strengths, the analysis of the scaling $F_Q = cN^\beta$ is meaningful as the multiplying constant c, which also depends on the noise, is large enough to ensure that $F_Q(t_{\max}) \gg$

[1] We cannot exclude here that slightly different values of β would appear for larger N's.

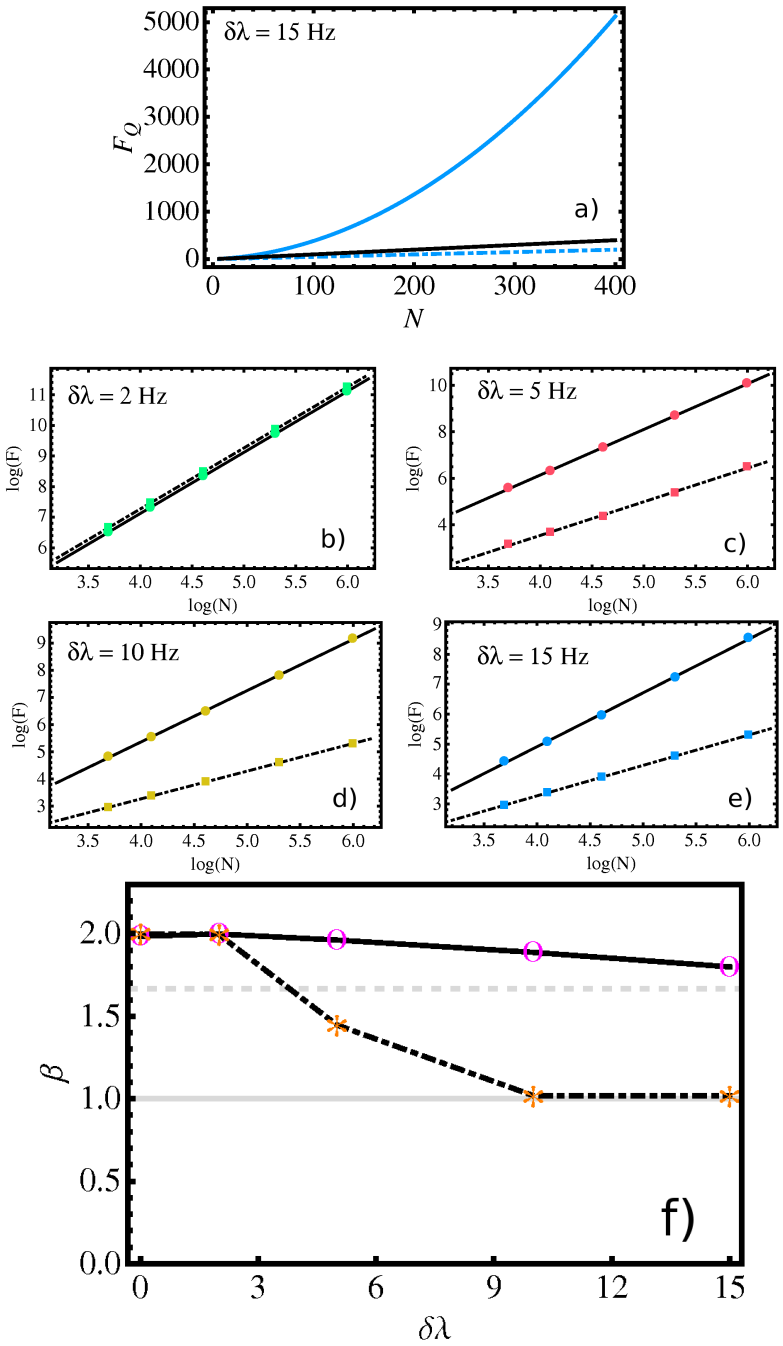

Figure 5.8: a) Quantum Fisher information evaluated at the time of its local maximum $t_{\max}$ (blue solid line) and at the time t_2 (blue dashed line) as a function of the number of particles N for $\delta\lambda = 15\,\mathrm{Hz}$, as compared to the shot noise limit (black solid line). Panels b),c),d),e): same as in a) in a semi-logarithmic scale, for various noise strengths $\delta\lambda = 2, 5, 10$, and $15\,\mathrm{Hz}$ (from left to right and top to bottom). f) Exponent β, extracted by a log-linear fit of the data in a), as a function of the energy fluctuations $\delta\lambda$ (in Hz) for $t = t_{\max}$ (solid line, circle markers) and for $t = t_2$ (dot-dashed line, star markers). We used $\chi = \pi\,\mathrm{Hz}$.

N, as shown in the first panel in Fig.5.8. This confirms the potential improvement in interferometry given by the state at time $t_{\max}$ with respect to the use of squeezed states in the presence of phase noise. For comparison, we also show the scaling of F_Q at the time t_2. At that time, β decays faster with the noise strength, reaching rapidly the shot noise limit $\beta = 1$. This is due to the fact that the noise exponent $a^2(t)$ increases with time.

To recapitulate, multicomponent superpositions of phase states appear to be "twice" robust against phase noise: 1) because of the independence of the decoherence rate on the particle number, a feature shared with the two-component superposition; 2) because they are formed at short times $\propto 1/\sqrt{N}$, when the noise correlations did not become effective yet for decoherence (for experimentally relevant values of noise $\delta\lambda$); this is not the case for the two-component superposition, formed at $t_2 = \pi/(2\chi)$. As a consequence, the analysis based on the quantum Fisher information has indicated these states as the most suitable for interferometric applications when phase noise is affecting the preparation of the input state based on the quenched dynamics of the BJJ.

To conclude this section, we mention that a work similar in spirit has been presented in Ref.[19], in which a new class of entangled states has been shown to be more robust than the two-component macroscopic superposition against decoherence, induced by a single particle (qubit) process. Analogously to our multicomponent superposition states, these states are still highly entangled and lead to advantage over the use of classical resources for quantum technology applications.

5.2 Particle losses

Several loss processes can induce the simultaneous expulsion of one, two or even three particles out of the condensate. One-body loss processes are generally due to scattering with impurities; spin-relaxation is instead a two-body process, in which two atoms collide and can change their spin state, with a high kinetic energy gain which ejects them out of the trap [157]; finally, when three atoms collide two of them form a molecule, and again the third acquires a large kinetic energy which overcomes the trap height [158, 159].

Generally, atom losses in optical lattices are theoretically treated by means of the master equation in the Lindblad form [160]

$$\partial_t\hat{\rho} = -\frac{i}{\hbar}\left[H^{(0)},\hat{\rho}\right] + \gamma^{(m)}\sum_k\left(\left[(\hat{a}_k)^m,\hat{\rho}(\hat{a}_k^\dagger)^m\right] + \left[(\hat{a}_k)^m\hat{\rho},(\hat{a}_k^\dagger)^m\right]\right), \tag{5.30}$$

where $m = 1,2,3$ is the order of the loss process, $(\hat{a}_k)^m$ is the annihilation operator destroying m atoms at site k and $\gamma^{(m)}$ is the loss rate. This loss rate has been measured in ^{87}Rb for $m = 1$ and $m = 3$ [161], while two-body collisions have been studied in Ref. [157]. Equation (5.30) generally implies the rotating-wave approximation and it only describes the dynamics in the Markov regime. A microscopic derivation of the master equation (5.30) can be found for $m = 3$ in Ref. [159] and for $m = 1$ in Ref. [162].

We will focus here on the effect of one-body atom losses, and we will particularly study their effect on the quenched dynamics of the bosonic Josephson junction and on the formation of Schroedinger cat states. In this particular example of quantum dynamics it is possible to solve the master equation exactly with analytical techniques. This analytical solution has been provided for one-body losses in Ref.[162] in the case of symmetric wells and interaction energies ($\lambda = 0$). In what follows we generalize this treatment to the asymmetric case $\lambda \neq 0$, where λ can be a time-varying parameter, which will allow us in

Sec.5.3 to treat particle losses and phase noise at the same time. An analytical solution of the master equation for the quenched dynamics in the presence of two-body and three-body losses is also available [163]. Further results on two-body losses will be given in appendix E.4.

5.2.1 Master equation for one-body particle losses

For the case of one-body losses ($m = 1$), we present here and in the following section the analytical solution for the density matrix. We rename $\gamma^{(1)} \equiv \gamma$; the density matrix in the presence of one-body losses is referred to as $\hat{\rho}$. The master equation of the BJJ is given by the two-site case of Eq.(5.30),

$$\partial_t \hat{\rho} = -\frac{i}{\hbar}\left[H^{(0)}, \hat{\rho}\right] + \gamma \sum_{k=1}^{2} \left(\left[\hat{a}_k, \hat{\rho}\hat{a}_k^\dagger\right] + \left[\hat{a}_k\hat{\rho}, \hat{a}_k^\dagger\right]\right). \tag{5.31}$$

For the external BJJ, the unitary Hamiltonian $H^{(0)}$ appearing in Eq.(5.31) is given by Eq.(1.16), with $K = 0$

$$H^{(0)} = \sum_{k=1}^{2} E_k \hat{a}_k^\dagger \hat{a}_k + \sum_{k=1}^{2} \frac{U_k}{2} \hat{a}_k^\dagger \hat{a}_k^\dagger \hat{a}_k \hat{a}_k, \tag{5.32}$$

where $(E_1 - E_2)(t)$ can be time dependent. As initial state of the dynamics we take as usual the phase state $|\theta = \pi/2, \phi = 0\rangle = \frac{1}{2^{N/2}} \sum_{k=0}^{N} \binom{N}{k}^{1/2} |k, N-k\rangle$, belonging to the $(N+1)$-dimensional Hilbert space of N bosons, as explained in Sec.1.4.2, where N is the initial total number of particles (not necessarily even).

During the dynamics of the BJJ, as soon as particle losses become effective, other sub-spaces of the total Fock space $\mathcal{H} = \prod_{\otimes m=0}^{N} \mathcal{H}^{(m)}$ become populated (where m labels the $(m+1)$-dimensional Hilbert space associated with m particles), possibly involving also the vacuum state $|0\rangle$ in which no atoms are left. The dimension of the total Hilbert space to which the BJJ has access in the presence of one-body losses is hence $\dim(\mathcal{H}) = \sum_{m=0}^{N}(m+1) = \frac{1}{2}(N+1)(N+2)$. For this larger space we can still use the Fock basis $|n_1, n_2\rangle$, but here $n_1 + n_2$ does not necessarily sum to N, rather it can take any integer value between 0 and N. In what follows we will denote the general density matrix element in this basis as $\rho_{k,l+p}^{k+r,l} \equiv \langle n_1 = k, n_2 = l+p|\hat{\rho}(t)|n_1 = k+r, n_2 = l\rangle$.

Projection of the master equation (5.31) on the Fock basis yields

$$\begin{aligned}
\partial_t \rho_{k,l+p}^{k+r,l} &= \left\{ -i\left[(E_2 p - E_1 r) + \frac{U_2}{2}p(p-1) - \frac{U_1}{2}r(r-1)\right] - \gamma(r+p)\right\}\rho_{k,l+p}^{k+r,l} \\
&+ \left\{(-iU_2 lp - 2\gamma l)\rho_{k,l+p}^{k+r,l} + 2\gamma\sqrt{(l+1)(l+p+1)}\rho_{k,l+p+1}^{k+r,l+1}\right\} \\
&+ \left\{(+iU_1 kr - 2\gamma k)\rho_{k,l+p}^{k+r,l} + 2\gamma\sqrt{(k+r+1)(k+1)}\rho_{k+1,l+p}^{k+r+1,l}\right\},
\end{aligned} \tag{5.33}$$

while the expansion of the initial state on the Fock basis leads to the initial condition

$$\rho_{k,l+p}^{k+r,l}(0) = \frac{1}{2^N}\binom{N}{k}^{\frac{1}{2}}\binom{N}{k+r}^{\frac{1}{2}}\delta_{r,p}\delta_{k+r,N-l}. \tag{5.34}$$

The effect of the cross-interaction term $U_{12}\hat{a}_1^\dagger\hat{a}_1\hat{a}_2^\dagger\hat{a}_2$ appearing in the Hamiltonian of the internal BJJ Eq.(1.19) adds to the master equation (5.33) the term $-iU_{12}(kr - lr)\rho_{k,l+p}^{k+r,l}$.

Hence, we see in Eq.(5.33) that this term can be treated by a renormalization of the interaction constants $U_i \to U_i - U_{12}/2$ with $i = 1, 2$.

Note that the presence of the term $\delta_{r,p}$ in Eq.(5.34) expresses the absence of correlations between sub-spaces at different particle numbers in the initial state. Since no such correlation will be built during the dynamics described by Eq.(5.31), the state will never be a coherent superposition of states at different particle number. This implies that the only non-zero elements of the density matrix satisfy $n_1 + n_2 = n_1' + n_2' \equiv m$, which labels the m-particles sub-space. This allows for the decomposition in blocks of the density matrix, as

$$\hat{\rho} = \sum_{m=0}^{N} \hat{\rho}_m = \sum_{m=0}^{N} w_m \bar{\rho}_m, \tag{5.35}$$

where we defined the normalized density matrix in the m-supspace $\bar{\rho}_m = \hat{\rho}_m / \mathrm{tr}[\hat{\rho}_m]$. The resulting block structure of the density matrix is represented in the first panel of Fig.5.9 (see also Sec.5.2.2).

5.2.2 Exact solution of the one body-losses master equation by the characteristic method

In this paragraph we generalize the solution of the master equation (5.34), presented in Ref.[162], to the case $E_1 \neq E_2$, $U_1 \neq U_2$. Let us introduce the generating function

$$h_p^r(x, y, t) = \sum_{k,l}^{\infty} x^k y^l \sqrt{\frac{(k+r)!(l+p)!}{k!l!}} \rho_{k,l+p}^{k+r,l}(t), \tag{5.36}$$

from which the elements of the density matrix can be retrieved by derivation as

$$\hat{\rho}_{k,l+p}^{k+r,l}(t) = \frac{1}{(k!l!(k+r)!(l+r)!)^{\frac{1}{2}}} \partial_x^k \partial_y^l h_p^r(0, 0, t). \tag{5.37}$$

By multiplying Eq.(5.34) by $x^k y^l$ and summing over k, l, the master equation can be expressed in terms of the generating function h_p^r as

$$\begin{aligned} \partial_t h_p^r &= \left\{ -i \left[(E_1(t)p - E_2(t)r) + \frac{U_2}{2} p(p-1) - \frac{U_1}{2} r(r-1) \right] - \gamma(r+p) \right\} h_p^r \\ &+ \left[(iU_1 r - 2\gamma)\, x + 2\gamma \right] \partial_x h_p^r + \left[(-iU_2 r - 2\gamma)\, y + 2\gamma \right] \partial_y h_p^r. \end{aligned} \tag{5.38}$$

Let us define the shifted generating function $h_p^r = e^{-\int_0^t c(r,p,\tau) d\tau} \tilde{h_p^r}$, where the parameter $c(r, p, t)$ is given by

$$c(r, p, t) = i \left[(E_1(t)p - E_2(t)r) + \frac{U_2}{2} p(p-1) - \frac{U_1}{2} r(r-1) \right] + \gamma(r+p). \tag{5.39}$$

The further definitions

$$\begin{aligned} \zeta_{1,r} &= 2\gamma - iU_1 r \\ \zeta_{2,p} &= 2\gamma + iU_2 p \end{aligned} \tag{5.40}$$

allow us to rewrite the master equation (5.38) as a linear partial differential equation of the first order

$$\partial_t \tilde{h_p^r} = (-\zeta_{1,r} x + 2\gamma)\, \partial_x \tilde{h_p^r} + (-\zeta_{2,p} y + 2\gamma)\, \partial_y \tilde{h_p^r}. \tag{5.41}$$

The solution for $\tilde{h_p^r}$, obtained with the methods of the characteristics as in Ref. [162], is reported in appendix E.1, and reads

$$\tilde{h_p^r}(x,y,t) = \frac{1}{2^N}\frac{N!}{(N-r)!}\left[\frac{2\gamma-(2\gamma-\zeta_{1,r})e^{-\zeta_{1,r}t}}{\zeta_{1,r}} + \frac{2\gamma-(2\gamma-\zeta_{2,p})e^{-\zeta_{2,p}t}}{\zeta_{2,p}}\right]^{(N-r)}\delta_{r,p}. \tag{5.42}$$

Then, by use of Eq.(5.37), we obtain the solution for the density matrix

$$\begin{aligned}\hat{\rho}_{k,l+p}^{k+r,l} = \quad & \frac{N!e^{-\int_0^t(E_1-E_2)(\tau)d\tau r}e^{-\left(\frac{\zeta_{2,r}+\zeta_{1,r}}{2}\right)(r-1)t}e^{-\zeta_{1,r}kt}e^{-\zeta_{2,r}lt}e^{-2\gamma t}}{2^N(N-r-k-l)!(k!l!(k+r)!(l+r)!)^{\frac{1}{2}}} \\ & \times\left[\frac{2\gamma}{\zeta_{1,r}}(1-e^{-\zeta_{1,r}t})+\frac{2\gamma}{\zeta_{2,r}}(1-e^{-\zeta_{2,r}t})\right]^{(N-r-k-l)}\delta_{r,p},\end{aligned} \tag{5.43}$$

where we have also used that the combination of parameters $\frac{U_2-U_1}{2}r(r-1)$ appearing in the definition (5.39) when $p=r$ can be rewritten as $\left(\frac{U_2-U_1}{2}r(r-1)\right) = \left(\frac{\zeta_{2,r}+\zeta_{1,r}}{2}\right)(r-1)+2\gamma$.

We can rewrite the solution (5.43) in a simplified form by using that, accordingly to the discussion in Sec.5.2.1, due to the term $\delta_{r,p}$ we have $k+r+l = k+l+p = m$, which leads to

$$\begin{aligned}\hat{\rho}_{k,m-k}^{k+r,m-(k+r)}(t) \quad = \quad & e^{-\int_0^t(E_1-E_2)(\tau)d\tau r}\frac{N!e^{-2\gamma mt}}{2^{(N-m)}(N-m)!} \\ & \left[\frac{1-e^{-2\gamma t}e^{iU_1rt}}{1-iU_1r/(2\gamma)}+\frac{1-e^{-2\gamma t}e^{-iU_2rt}}{1+iU_2r/(2\gamma)}\right]^{(N-m)}\hat{\rho}_{k,m-k}^{(0)\ k+r,m-(k+r)}(t).\end{aligned} \tag{5.44}$$

Here $\hat{\rho}^{(0)}(t) = |\psi^{(0)}(t)\rangle\langle\psi^{(0)}(t)|$ is the density matrix corresponding to the unitary evolution under the Hamiltonian (5.32) with m particles and $E_1 = E_2$, i.e.

$$\hat{\rho^{(0)}}_{k,m-k}^{k+r,m-(k+r)}(t) = \frac{1}{2^m}\binom{m}{k}^{\frac{1}{2}}\binom{m}{k+r}^{\frac{1}{2}}e^{-i\left(\frac{U_2-U_1}{2}\right)r(r-1)t}e^{-i(U_2(m-k-r)-U_1k)rt}. \tag{5.45}$$

The reason to separate the contribution due to an energy imbalance E_1-E_2 from the unitary part will become clear in Sec.5.3.

Note that for $m=N$ the factor $\left[\frac{2\gamma}{\zeta_{1,r}}(1-e^{-\zeta_{2,r}t})+\frac{2\gamma}{\zeta_{2,r}}(1-e^{-\zeta_{2,r}t})\right]^{(N-r-k-l)}$ in Eq.(5.44) is equal to 1, and the effect of particle losses on the corresponding block is only to "dump" it (i.e., to reduce its weight), without affecting its inner dynamics, which then corresponds to the unitary dynamics.

From Eq.(5.44) we can calculate the weights of each block of the density matrix, appearing in Eq.(5.35). The diagonal elements are identified by $r=0$, which leads to

$$\hat{\rho}_{k,m-k}^{k,m-k}(t) = \frac{N!e^{-2\gamma mt}}{2^m(N-m)!k!(m-k)!}(1-e^{-2\gamma t})^{(N-m)}, \tag{5.46}$$

from which the weights w_m can be immediately obtained as

$$w_m = \mathrm{tr}[\hat{\rho}_m] = \sum_k \hat{\rho}(t)_{k,m-k}^{k,m-k} = \frac{N!e^{-2\gamma mt}}{m!(N-m)!}(1-e^{-2\gamma t})^{(N-m)}. \tag{5.47}$$

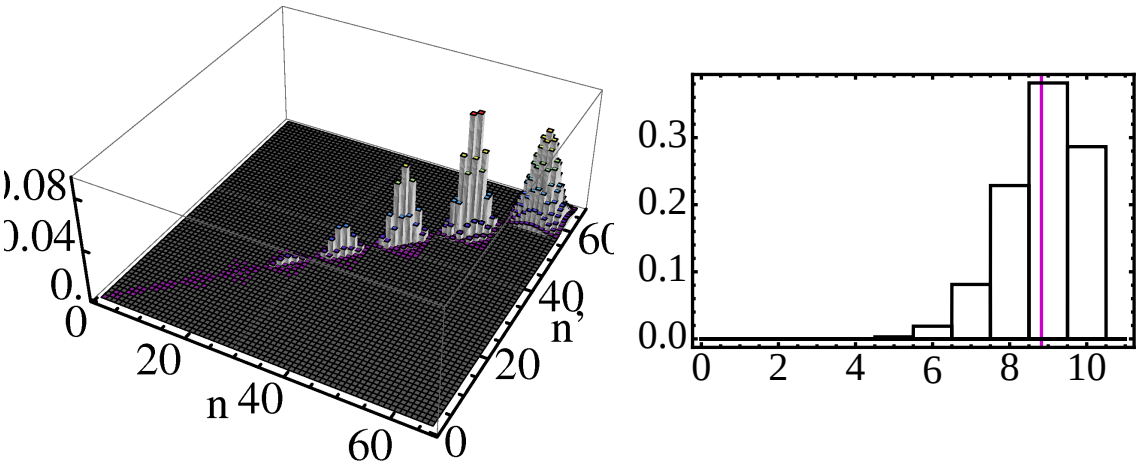

Figure 5.9: Density matrix in the Fock basis of the total Hilbert space (left panel), and weights of the density matrix as a function of the label of the subspace, i.e. the number of particles m (right panel). Values of the parameters: $N = 10$, $\gamma T = 0.25$, $U_1 = U_2 = 4\pi$Hz, $t = t_2$.

From Eq.(5.47) we can calculate the decay of the average atom number with time, which is given by

$$\langle \hat{m} \rangle = \sum_{m=0}^{N} w_m m = \sum_{m=0}^{N} \binom{N}{m} e^{-2\gamma m t} (1 - e^{-2\gamma t})^{(N-m)} m = N e^{-2\gamma t}. \tag{5.48}$$

Equation (5.48) shows that, as expected for one-body losses, the atom number decays exponentially with time, with a decay rate given by γ.

5.2.3 Effect of particle losses on the visibility

The visibility in the presence of one-body atom losses can be calculated by generalizing Eq.(2.20) to $\nu(t) = \mathrm{tr}[\hat{\rho}(t)\hat{J}_x]/\sqrt{\mathrm{tr}[\hat{\rho}(t)\hat{n}_1]\mathrm{tr}[\hat{\rho}(t)\hat{n}_2]}$, where in the denominator we have replaced N by the averages of the atom number $\hat{n}_i$ in each mode $i = 1, 2$. This calculation has been performed in Ref. [162] for optical lattices. The two-site case yields

$$\nu_{\mathrm{1body}}(t) = \left\{ \frac{\gamma^2 + \left[\gamma \frac{\chi}{2} \sin(\chi t) + (\frac{\chi}{2})^2 \cos(\chi t)\right] e^{-2\gamma t}}{\gamma^2 + (\frac{\chi}{2})^2} \right\}^{N-1}. \tag{5.49}$$

A short-time expansion of Eq.(5.49) to the third order for $\chi t \equiv \tau \ll 1$ leads to

$$\nu_{\mathrm{1body}}(t) \simeq (1 - \frac{1}{2}\tau^2 + \frac{2}{3}\frac{\gamma}{\chi}\tau^3)^{(N-1)} \simeq e^{(N-1)[1-\frac{1}{2}\tau^2 + \frac{2}{3}\frac{\gamma}{\chi}\tau^3]}. \tag{5.50}$$

In Eq.(5.50) we recognize the gaussian decay of the visibility due to the atomic interactions (the unitary part), which also appears in the short-time expansion of Eq.(2.20), while we see that atom losses provide a positive (cubic) corrections to the visibilty. This counterintuitive effect is due in our model to the fact that the sites occupations in the denominator decrease under the effect of particle losses. However, we expect this effect to disappear in a more rigorous derivation in which the dependence of the microscopic parameters of the BJJ from the particle number would be taken into account (see discussions in Secs.1.3.1.a and 6.2.2).

5.2.4 Effect of particle losses on squeezed states

The effect of particle losses on squeezed states in the bosonic Josephson junction has already been addressed in Refs.[23, 164] for one, two and three-body losses. In Ref.[164] the optimum particle number and the optimum trap frequency allowing to reach the highest possible squeezing in the presence of atom losses have been determined, while in Ref.[23] the best squeezing degree has been calculated when the spatial dynamics of the bimodal condensate cannot be neglected.

5.2.5 Effect of one-body losses on macroscopic superpositions of phase states

We now focus on the formation of macroscopic superpositions of phase states when one-body losses are affecting the BJJ. We want to perform some kind of "spectroscopy" of the density matrix at the specific times of formation of macroscopic superpositions, in the spirit of Ref.[28], with the use of Eq.(5.35) and of the solution Eq.(5.44). For instance, let us fix $t = t_q \equiv T/(2q)$, where $T = T_{even} = 2\pi/\chi$ is the period of the quantum state when the initial particle number N is even. For $q = 2$, in the absence of noise the state at t_2 is a two-component cat state. We want to see whether the state at this time is the sum of terms in which each represents a two-component cat state in the space of m particles. In order to do so, we analyze different quantities: the fidelity, the Husimi function and the quantum Fisher information. From the discussion at the end of Sec.5.2.2 we already partially know the answer: the block with $m = N$ will be a perfect cat state. We study in this section the character of the other blocks of the density matrix.

5.2.5.a Fidelity

Let us consider the state of the system at the time t_2, corresponding to the two-component macroscopic superposition. First, we plot the fidelity of density matrix $\hat{\rho}_m$ of each subspace at m particles, with a perfect m-particle cat state. We define thus $\mathcal{F}_m \equiv \mathcal{F}[\overline{\rho}_m, \hat{\rho}_m^{(0)}] = \mathrm{Tr}[\sqrt{\sqrt{\hat{\rho}_m^{(0)}}\overline{\rho}_m\sqrt{\hat{\rho}_m^{(0)}}}]^2$, where $\hat{\rho}_m^{(0)} = |\psi_m^{(0)}\rangle\langle\psi_m^{(0)}|$ is perfect the two-component cat state in the space of m particles, and we recall that $\bar{\rho}_m = \hat{\rho}_m/\mathrm{tr}[\hat{\rho}_m]$. Then using $\hat{\rho}_m^{(0)2} = \hat{\rho}_m^{(0)}$ and $\mathrm{tr}[\hat{\rho}_m^{(0)}] = 1$ we obtain

$$\mathcal{F}_m = \langle\psi_m^{(0)}|\overline{\rho}_m|\psi_m^{(0)}\rangle = \sum_{n,n'=1}^{m+1} \hat{\rho}_m^{(0)}(n',n)\overline{\rho}_m(n,n'). \tag{5.51}$$

The fidelities $\mathcal{F}_m$ are plotted for $m = 0, 1, ...N = 10$ in Fig.5.10. As we expected, since we have defined $\mathcal{F}_m$ referring to the density matrices in each block renormalized by the respective weight, we have $\mathcal{F}_N = 1$ (trivially, also $\mathcal{F}_0 = 1$ for the vacuum state), as the block at $m = N$ is only dumped by particle losses.

Quite remarkably, we find that the lower blocks with $m < N$, which are populated only by the loss mechanism, have a non-zero fidelity with the corresponding two-component m-particle cat state. Hence, we find that the loss process transfers some quantum correlations [2].

[2] Using Eq.(5.44) we have demonstrated that the fidelity of each block of the density matrix renormalized by its weight $\overline{\rho}_m$ for $m \neq N$ with the density matrix of a perfect cat state *increases* in the limit of infinite

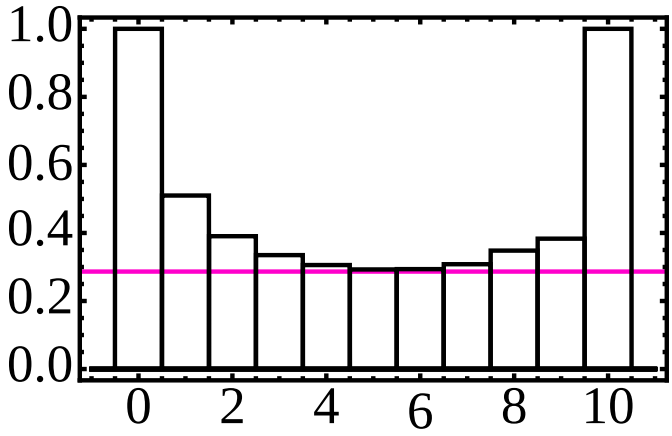

Figure 5.10: Fidelity of each block of the density matrix with an m-particle two-component cat state. The red line corresponds to the total fidelity defined in Eq.(5.52). Values of the parameters: $N = 10$, $\gamma T = 0.25$, $U_1 = U_2 = 4\pi$Hz, $t = t_2$.

Note that the fidelity of the total density matrix with the two-component cat state formed in the absence of losses with N particles $\hat{\rho}_N^{(0)}(t_2)$ is trivially given by the weight w_N expressed by Eq.(5.47), due to the orthonormality of Fock states at different m. Mathematically, expliciting the time-dependence of the density matrix, we have at all times

$$\mathcal{F}[\rho(t), \hat{\rho}^{(0)}(t)] = \sum_{n,n'=1}^{N+1} \hat{\rho}^{(0)}(n', n, t)\rho_N(n, n', t) = \mathcal{F}_N w_N(t) = w_N(t) = e^{-2\gamma N t}, \quad (5.52)$$

to be evaluated at $t = t_2 = T/4$ for the fidelity with the two-component cat state. The total fidelity corresponds to the red horizontal line in Fig. 5.10, coinciding with the last weight in the second panel of Fig. 5.9 by Eq.(5.52).

Note that, since no inner dynamics affects the block at $m = N$ (a part from a global dumping), as already said at t_2 $\overline{\rho}_N$ corresponds to a perfect two-component phase cat state, displaying in particular non-diagonal terms at $r \neq 0$. Hence, no other way to eliminate these off-diagonal elements exists apart from lowering the weight of the block at $m = N$, which means that the decoherence rate coincides with the dumping of this block - i.e., $2\gamma N$, at it results from the last equality in Eq.(5.52).

We may ask whether the effect of a purely lossy dynamics would equally affect the BJJ if initially prepared either in a NOON state, or in a two-component phase cat state. This question is affirmatively answered in appendix E.3, in contrast with what we have found for the case of phase noise (see appendix D.4).

5.2.5.b Projected Husimi distribution

We now visualize the results presented in the previous section by plotting the Husimi function in each subspace. In order to compare the Husimi functions corresponding to subspaces at different particle number m, we define

$$Q_m(\phi) \equiv Q_m(\theta = \frac{\pi}{2}, \phi) = \frac{1}{\text{Norm}_m} {}_m\langle\phi|\bar{\rho}_m|\phi\rangle_m \quad (5.53)$$

loss rate γ. However, in that limit the weights of each block except $m = 0$ go to zero, and this happens faster than the speed at which a $\overline{\rho}_m$ tends to a cat state, so that we recover a physically meaningful result.

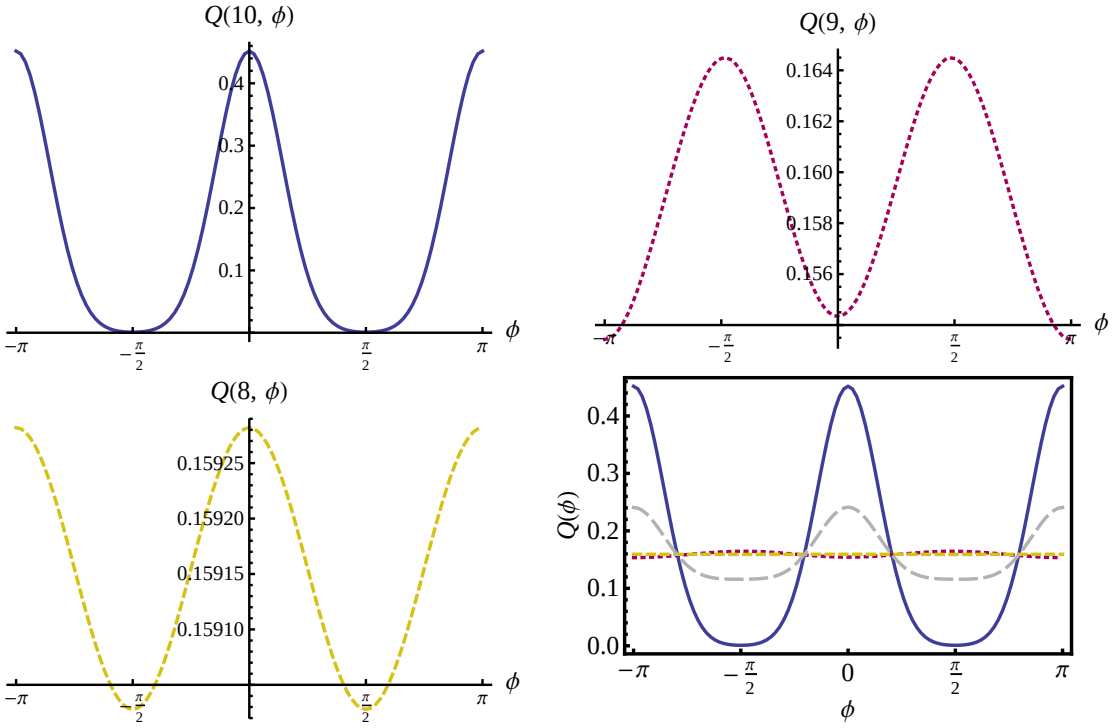

Figure 5.11: First three panels: Husimi distribution $Q_m(\theta = \pi/2, \phi)$ (see Eq.(5.53)) at $t = t_2$ for $m = 10, 9, 8$ respectively. Last panel: All previous curves now at the same scale, plus (gray dashed line) total Husimi distribution $Q(\theta = \pi/2, \phi)$ (see Eq.(3.1)) at $t = t_2$. Values of the parameters: $N = 10$, $\gamma T = 0.25$, $U_1 = U_2 = 4\pi$Hz, $t = t_2$.

where

$$\text{Norm}_m = \frac{2\sqrt{\pi}\Gamma[m + \frac{1}{2}]}{\Gamma[m + 1]} = 2\pi Q_{cost} \tag{5.54}$$

is a normalizing factor obtained with the requirement that the Husimi function $Q_m(\phi)$ associated with $\hat{\rho}_\infty(m) \equiv \frac{1}{2\pi}\int d\phi |\phi\rangle_{mm}\langle\phi|$ is equal to 1, and $|\phi\rangle_m$ is the phase state parameterized by the angle ϕ in the space of m particles (the constant Q_{cost} has already been introduced in Sec.5.1.3.b).

We plot the Husimi functions Q_m for $m = N, N-1, N-2$ in Fig. 5.11. For $m = 10$ we recover the Husimi function of a perfect cat state with 10 particles, due to the aforementioned effect of simple "dumping" of the N-th block of the density matrix. For $m = 9, 8$ we see that the structure of these curves still displays two peaks, corresponding to the components of the cat state. These peaks are placed at $\pi/2$ and $3\pi/2$ for $m = 9$, corresponding to the rotated components of a cat state with an odd number of particles [101]. Note however the different scale on the y-axes in the first, second and third panel in Fig. 5.11; we also find that $Q_9(\phi)$ and $Q_8(\phi)$ are quite different from the corresponding Husimi functions of perfect two-component cat states (the latter are not shown here). As a result, the profile of the total Husimi function $Q(\phi) = \sum_{m=0}^{N} w_m Q_m(\phi)$ (gray curve in the last panel in Fig. 5.11) is smeared out, already for intermediate values of the decoherence rate $\gamma T = 0.25$.

Since the dynamics in the presence of particle losses is not conserving the number imbalance operator, there is a "leaking" of the state along the θ direction also. Hence, it

can be instructive to consider also the full Husimi distribution $Q(\theta, \phi)$. This is addressed in appendix E.2.

5.2.5.c Quantum Fisher information

We want now to quantify the effect of particle losses on the useful quantum correlations of the state of the system as a function of time. To do this, we calculate the quantum Fisher information as a function of time, after optimizing it over all of the possible directions. Since the number of particles is fluctuating, we follow Ref.[165], and calculate the Fisher information as

$$F_Q[\hat{\rho}, \hat{J}_n] = \sum_{m=0}^{N} w_m F_Q[\hat{\rho}_m, \hat{J}_n], \tag{5.55}$$

in analogy with the other quantities calculated in the previous sections. In Ref. [165] it has been shown that in the presence of a super selection rule which forbids coherences between subspaces at different numbers of particles the previous expression is bounded by $\langle \hat{m}^2 \rangle$ and the following implication holds:

$$F_Q[\hat{\rho}, \hat{J}_n] > \langle \hat{m} \rangle \quad \Rightarrow \quad \hat{\rho} \text{ entangled.} \tag{5.56}$$

The Fisher information in each subspace at fixed m is then calculated with the use of Eq.(4.12), which in terms of the sub-space density matrix $\hat{\rho}_m$ reads

$$F_Q[\hat{\rho}_m, \hat{J}_n] = \sum_{k,l=0}^{m} \frac{(p_l - p_k)^2}{p_l + p_k} |\langle l|\hat{J}_n|k\rangle|^2, \tag{5.57}$$

where $|k\rangle$ are the orthonormalized eigenstates which diagonalize the density matrix, satisfying $\hat{\rho}_m|k\rangle = p_k|k\rangle$. Then, we optimize Eq.(5.55) over all the possible directions $\hat{J}_n$. We choose to perform the optimization *after* the summation specified in Eq.(5.55) because this choice seems to us physically more relevant: summing instead Fisher informations optimized at each m in Eq.(5.55) would give an indication of the usefulness of the state $\hat{\rho}$ in interferometric experiments in which the densities matrices $\hat{\rho}_m$ associated with subspaces at different m would be transformed with respect to different directions, which seems hard to be realized in experiments.

In Fig. 5.12 we show the quantum Fisher information for various loss rate γ, for $N = 10$. The black dashed line is the shot noise limit F_Q for the initial number of particles N; the regions in which F_Q is larger than this reference line are such that sub-shot noise phase estimation could be in principle performed even in the presence of particles losses. The gray dotted line is $F_\xi = N/\xi^2$, where ξ^2 is the coherent spin squeezing, showing when the quantum state is in principle more useful than a squeezed state even in the presence of losses (note that here the squeezing is plotted in the ideal lossless case).

The presence of relatively high correlations at long times which can be seen in Fig. 5.12 is associated with our choice of a small initial number of particles. The plot of F_Q for the same parameters, repeated in the case of $N = 100$, displays a more dramatic effect of losses for the same noise parameter, as can be seen in Fig. 5.13. This can be related to the fact that the decay rate of the fidelity with the state formed in the absence of losses scales like N (see Eq.(5.52)).

Finally, in connection with the results of Sec.5.1.4.c, we would like to perform a scaling analysis of the quantum Fisher information as a function of the average number of particles

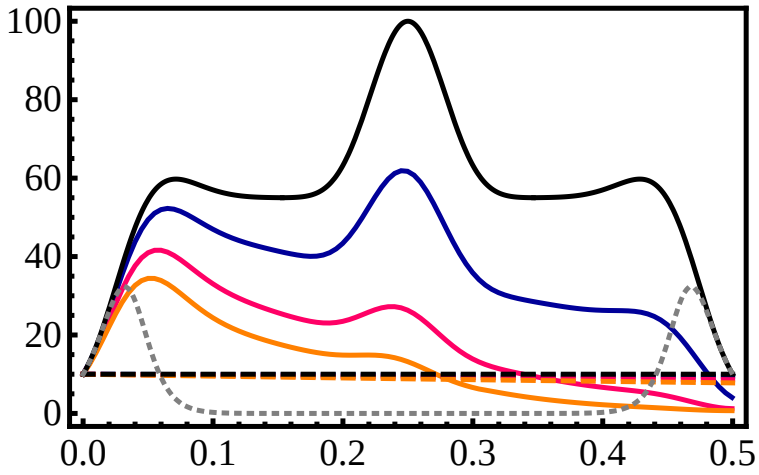

Figure 5.12: Quantum Fisher information given in Eq.(5.55) optimized over $\hat{J}_n$ as a function of t/T, for $\gamma T = 0, 0.05, 0.15, 0.25$ from top to bottom. The dashed lines represent the corresponding average number of atoms as a function of time. Black dashed line: shot noise limit N. Gray dotted line: coherent spin squeezing parameter ξ^2/N in the absence of losses. Value of the parameters: $N = 10$, $U_1 = U_2 = 4\pi$Hz.

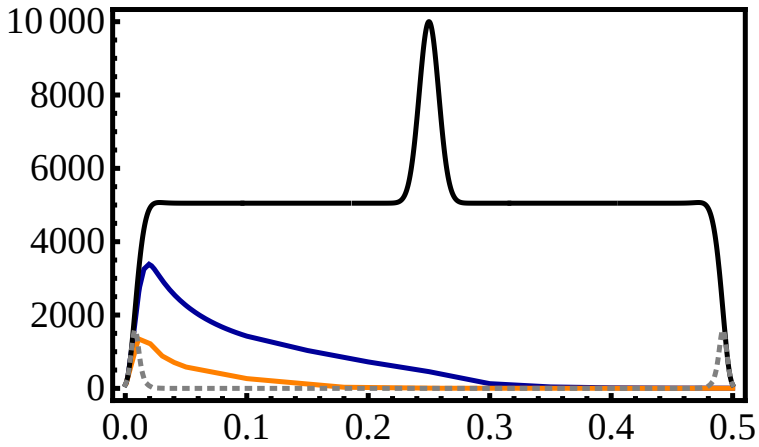

Figure 5.13: Quantum Fisher information given in Eq.(5.55) optimized over $\hat{J}_n$ as a function of t/T, for $\gamma T = 0, 0.05, 0.25$ from top to bottom. Gray dotted line: coherent spin squeezing parameter ξ^2/N in the absence of losses. Values of the parameters: $N = 100$, $U_1 = U_2 = 4\pi$Hz.

$\langle \hat{m} \rangle$ in the present case of a fluctuating total number of particles. This could still be done, but it would provide less clear indications with respect to the case of phase noise, as in this case F_Q is bounded by $F_Q[\hat{\rho}, \hat{J}_n] \leq \langle \hat{m}^2 \rangle$, involving the expectation value of a different operator (m^2) [165]. Note also that in this case the bound on the highest possible phase estimation has to be modified as $\Delta\varphi \geq \max\left[\frac{1}{\sqrt{p\langle \hat{m}^2 \rangle}}, \frac{1}{p\langle \hat{m} \rangle}\right]$ (p being here the number of measurements) [165].

5.3 Treating phase noise and particle losses at the same time

Since in real experiments both particle losses and phase noise are acting simultaneously, it is important to develop a treatment allowing to calculate the density matrix of the system including both sources of noise. We proceed in this direction.

As we deduced in Sec.5.1.2, and as we have already done in Sec.5.1.4, we are going here to assume that phase noise is strongly correlated in the time-regime of interest, leading e.g. to the production of squeezed states and macroscopic superpositions. During this time regime, losses are affecting the system. We assume hence that the phase noise process $\lambda(t) = (E_2 - E_1)(t)$ in one realization is constant during the characteristic time for losses $1/\gamma$, i.e. that $t_c\gamma \gg 1$ (where t_c is the correlation time for phase noise introduced in Sec.5.1.1.b). Hence, we can consider the solution of the master equation (5.44) as "quenched" with respect to phase noise, i.e. as the solution of the lossy dynamics in one realization of the phase noise process. We can indicate it with a "Q" suffix, i.e. we rename $\hat{\rho}_{k,m-k}^{k+r,m-(k+r)}(t) \to \hat{\rho}_{Q\ k,m-k}^{k+r,m-(k+r)}(t)$ in Eq.(5.44), which gives

$$\begin{aligned}\hat{\rho_Q}_{k,l+p}^{k+r,l} = \quad & \frac{N! e^{-i\phi(t)r} e^{-\left(\frac{\zeta_{2,r}+\zeta_{1,r}}{2}\right)(r-1)t} e^{-\zeta_{1,r}kt} e^{-\zeta_{2,r}lt} e^{-2\gamma t}}{2^N (N-r-k-l)!(k!l!(k+r)!(l+r)!)^{\frac{1}{2}}} \\ & \times \left[\frac{2\gamma}{\zeta_{1,r}}(1-e^{-\zeta_{1,r}t}) + \frac{2\gamma}{\zeta_{2,r}}(1-e^{-\zeta_{2,r}t})\right]^{(N-r-k-l)} \delta_{r,p} \end{aligned} \tag{5.58}$$

where we have also defined $\Lambda(t) = (E_2 - E_1)$ and $\int_0^t (E_1 - E_2)(\tau)d\tau = -\int_0^t \Lambda(\tau)d\tau \equiv \phi(t)$. The sign difference with respect to the analogous definition in Sec. 5.1.1.a is due to the fact that in this basis (we recall that $\hat{\rho_Q}_{k,l+p}^{k+r,l} \equiv \langle n_1 = k, n_2 = l+p|\hat{\rho}_Q|n_1 = k+r, n_2 = l\rangle$) in terms of the number imbalance $n = (n_1 - n_2)/2$, we have $(n - n') = ((k - l - r) - (k + r - l))/2 = -r$, to be compared to Eq.(5.10).

Then, $(E_1 - E_2)(t)$ appearing in Eq.(5.58) is considered to be randomly fluctuating, and we have to average with respect to phase noise. The averages are performed as in Sec. 5.1.1.a, and the averaged density matrix is given by

$$\hat{\rho}(t)_{k,l+p}^{k+r,l} = \int dP\,[\Lambda(t)]\,\hat{\rho_Q}_{k,l+p}^{k+r,l} = \int d\phi f(\phi,t)\hat{\rho_Q}_{k,l+p}^{k+r,l} \tag{5.59}$$

where $f(\phi,t)$ is defined as in Eq.(5.4) with the replacement $\lambda \to \Lambda$, and reads $f(\phi,t) = \frac{1}{\sqrt{2\pi}a(t)} e^{-\frac{(\phi+\overline{\Lambda}t)^2}{2a^2(t)}}$, with $a^2(t)$ given by Eq.(5.7) and $h(\tau-\tau') = \overline{\Lambda(\tau)\Lambda(\tau')} - \overline{\Lambda}^2 = \overline{\Delta E(\tau)\Delta E(\tau')} - \overline{\Delta E}^2$ is identical to the correlation function defined in Sec. 5.1.1.a, while $\overline{\Lambda} = \overline{-\Delta E} + (N-1)(U_2 - U_1)/2$.

Substituting the expression of $f(\phi,t)$ in Eq.(5.59) and performing the gaussian integral yields as final result the density matrix of the system in the presence of both phase noise (red contribution) and particle losses (blue contribution)

$$\hat{\rho}_{k,m-k}^{k+r,m-(k+r)}(t) = e^{i\overline{\Lambda}rt}e^{-\frac{a(t)^2r^2}{2}}\frac{N!e^{-2\gamma mt}}{2^{(N-m)}(N-m)!}\left[\frac{1-e^{-2\gamma t}e^{iU_1rt}}{1-iU_1r/(2\gamma)}+\frac{1-e^{-2\gamma t}e^{-iU_2rt}}{1+iU_2r/(2\gamma)}\right]^{(N-m)} \times\hat{\rho}_{k,m-k}^{(0)\ k+r,m-(k+r)}(t),$$

from which we see that in the density matrix in the presence of both one-atom losses and phase noise these two respective contributions appear factorized.

This allows to write the visibility in the presence of both noise sources as

$$\nu(t) = e^{-\frac{a(t)^2r^2}{2}}\nu_{1\text{body}}(t), \tag{5.60}$$

where $\nu_{1\text{body}}$ is given in Eq.(5.49) and we have taken $\Lambda = 0$. A discussion of the possibility to compare this expression to the measured decay of the visibility is presented in Sec. 6.2.2.

Chapter 6

Conclusions and perspectives

6.1 Conclusions

In this thesis we have considered the bosonic Josephson junction in the quantum regime in the framework of the two-mode approximation, studying in particular some aspects connected to quantum information.

Starting with the characterization of the system, in Chap.1 [31] we have studied its "phase diagram", by calculating the fluctuations of number imbalance operator as a function of the ratio between the coupling and inter-atomic interactions, and the asymmetry of the two modes. We have shown that such a phase diagram displays a lobe structure, due to the degeneracy of neighboring Fock states in the strongly interacting regime. The size of the lobes increases at increasing asymmetry, as a consequence of a reduction of the effective coupling; this non-linear effect is absent in superconducting Josephson junctions.

In Chap.2 [31, 33] we have shown that the dynamics driven by the interatomic interactions only ("quenched dynamics"), starting from a single coherent state, leads to the creation of macroscopic superposition of coherent states. These superpositions are placed in planes parallel to the equator of the Bloch sphere - the equator of the Bloch sphere itself if the initial coherent state is number balanced ("phase state") - and they appear at fractions $t_q = T/(2q)$ of the period $T = 2\pi/\chi$, with a number of components q which varies in time (this result has been also reported in Ref.[101]). We have later shown that the creation of macroscopic superpositions can be optimized by means of an optimal control protocol: a two-component phase cat state (as well as a NOON state) can be created with a very high fidelity ($\sim 99\%$) in a time $T' = cT_c$, where $T_c \propto 1/N$ depends inversely on the atom number, and c is a constant (depending in principle on the particle number). For instance, $c = 10$ for $N = 300$, leading to an advantage over the quenched dynamics-based protocol in terms of the time of formation of the superposition. A proper scaling analysis of the constant c as a function of the number of particles is still to be carried out.

In Chap.3 [32] we have addressed the detection of macroscopic superpositions of phase states. We have shown that the probability distributions of the eigenvalues of the collective angular momentum operator in various directions are suitable to detect qualitatively these states. Indeed these probability distributions allow to access the phase content of the state, and to distinguish macroscopic superpositions of phase states from incoherent mixtures, as for the latter the probability distributions do not display fringes. Based on the Radon transform, we have shown that the knowledge of these probability distribu-

tions in each direction of the equatorial plane of the Bloch sphere allows to reconstruct a two-dimensional distribution, analogous to phase-space distributions, yielding the major information about macroscopic superposition states.

In Chap.4 [25] we have addressed the applications to quantum interferometry. We have computed the quantum Fisher information and the squeezing parameter as a function of time during the quenched dynamics of the BJJ, optimizing them with respect to all the possible unitary transformations describing a linear interferometer. This analysis yields qualitatively the same result as reported in Ref.[16], indicating the two component macroscopic superposition as the most useful state in ideal conditions. However, note that in Ref.[16] the quantum Fisher information and the coherent spin squeezing were not optimized. The optimization was for us important in view of the analysis of the decoherence process presented in Chap.5, in order to assign via the quantum Fisher information a value to the correlations of the superpositions - an intrinsec property of the state.

In Chap.5 [25] we have studied how the useful quantum correlations created during the quenched dynamics of the BJJ are affected by the presence of noise, such as phase noise and particle losses. First, we have derived an exact solution for the quantum state of the system at any time during the quenched dynamics in the presence of phase noise. The formation of macroscopic superpositions of phase states has been shown to be robust against phase noise, since decoherence occurs at a rate of the same order as phase relaxation, independently of the total number of particles. As a consequence of this anomalously slow decoherence, a scaling analysis of the optimum quantum Fisher information with the number of particles has allowed us to conclude that, for a realistic choice of noise strengths, multicomponent superpositions are more useful for interferometry than either the two-component superposition or squeezed states. These superpositions are built during the dynamical evolution of a noiseless junction at times longer than for squeezed states, but still depending inversely on the total number of particles, the first macroscopic superposition being formed at a time $\propto 1/\sqrt{N}$. This is not the case for the two-component cat state, which is formed at $T/4$ independent on N, and is thus more affected by the presence of noise. Hence, in experiments aimed at preparing a useful state for interferometric applications based on the quenched dynamics of the BJJ, despite the presence of a decoherence source such as phase noise it would be convenient to wait until times $\propto 1/\sqrt{N}$, beyond the regime of spin squeezing, and reach the regime of formation of the first multicomponent macroscopic superpositions.

We have then considered the effect of one-body particle losses on the production of cat states. We have generalized the exact solution of the density matrix presented in Ref.[162] to the case in which an asymmetry in the parameters of the BJJ is taken into account. Then, we have carried out a "spectroscopy" of the density matrix, revealing that the states with lost particles, which are mixed in the total density matrix to the state in the absence of losses, still display some "cat-like" features. For instance, their Husimi distribution displays peaks, even if smoothened, corresponding to the components of the superposition. The analysis of how much the useful quantum correlation built up during the dynamics are affected by particle losses has been possible only in a qualitative fashion, as no easy scaling relation of the Fisher information with the particle number can be defined in this case. Finally, we have shown that it is possible to treat one-body particle losses and phase noise analytically at the same time. This result can be extended in principle to the case of two- and three-body losses, and is important in view of an accurate comparison with the experiments.

Our study confirms the BJJ as a versatile and promising system in quantum metrology

and for other applications in quantum information.

Dans cette thèse nous avons considéré la jonction Josephson bosonique dans le régime quantique dans le cadre de l'approximation à deux modes, en étudiant en particulier certains aspects en relation avec l'information quantique.

En commençant par la caractérisation du système, dans le premier chapitre nous avons étudié son "diagramme de phase", en calculant les fluctuations de l'opérateur de nombre relatif en fonction du rapport entre le couplage et les interactions interatomiques, et de l'asymétrie des deux modes. Nous avons montré que ce diagramme de phase présente une structure à lobes, causée par la dégénérescence d'états de Fock adjacents dans la limite de hautes interactions. La dimension des lobes augmente avec l'asymétrie, comme conséquence de la réduction du couplage effectif; cet effet non-linéaire ne se trouve pas dans les jonctions Josephson supraconductrices.

Dans le chapitre 2 [31, 33] nous avons montré que la dynamique régie par les interactions interatomiques seulement (dynamique "trempée"), en démarrant avec un seul état cohérent, porte à la création de superpositions macroscopiques d'états cohérents. Ces superpositions sont placées sur des plans parallèles à l'équateur de la sphère de Bloch, notamment le plan équatorial même si l'état cohérent initial est symétrique quant'à occupation atomique moyenne ("état de phase"). Ces états apparaissent à des temps $t_q = T/(2q)$ fractions de la période $T = 2\pi/\chi$, et ont un nombre de composantes q qui varient dans le temps (ce résultat a été démontré également dans la Ref.[101]). Nous avons ensuite montré que la création des superpositions macroscopiques peut être optimisé à l'aide d'un protocole de contrôle optimal: une superposition de deux états de phase (tout comme un état NOON) peut être créée avec une très grande fidélité ($\sim 99\%$) dans un temps $T' = cT_c$, où $T_c \propto 1/N$ dépend inversement du nombre d'atomes, et c est une constante (qui dépends en principe du nombre d'atomes). Par exemple, $c = 10$ pour $N = 300$, ce qui conduit à un avantage par rapport à la dynamique trempée en terme du temps de formation de la superposition. Une analyse détaillée de la loi d'échelle suivie par la constante c avec le nombre d'atomes n'a pas encore été effectuée.

Dans le chapitre 3 [32] nous avons abordé la détection des superpositions macroscopique d'états de phase. Nous avons montré que les distributions de probabilité des valeurs propres de l'opérateur de moment angulaire collectif dans différentes directions sont convenables pour détecter qualitativement ces états. En effet ces distributions de probabilité permettent de caractériser la distribution de la phase de l'état, et de distinguer des superpositions macroscopiques des mélanges incohérents, puisque pour ces dernières les distributions de probabilité n'ont pas de franges. En s'appuyant sur la transformation de Radon, nous avons montré que la connaissance de ces distributions de probabilité dans toutes les directions du plan équatorial permet de construire une distribution bi-dimensionnelle, analogue aux distributions sur l'espace des phases, qui porte les informations essentielles pour les états de superposition macroscopique.

Dans le chapitre 4 [25] nous avons abordé les applications à l'interférométrie. Nous avons calculé l'information de Fisher et le paramètre de compression en fonction du temps pendant la dynamique trempée de la BJJ, en les optimisant par rapport aux possibles transformations unitaires qui décrivent un interféromètre linéaire. Cette

analyse apporte qualitativement les mêmes résultats communiqués en Ref.[16], indiquant que l'état le plus utile dans des conditions idéales est la superposition de deux états cohérents. C'est tout de même à noter que en Ref.[16] l'information de Fisher et le paramètre de compression n'étaient pas optimisés. L'optimisation était pour nous importante en vue de l'analyse du processus de décohérence présenté dans le chapitre 5, pour pouvoir assigner à l'aide de l'information de Fisher une valeur aux corrélations de la superposition, qui sont une propriété intrinsèque de l' état.

Dans le chapitre 5 [25] nous avons étudié comment les corrélations quantiques créées pendant la dynamique trempée de la BJJ sont affectées par la présence de bruits extèrnes, tels que le bruit de phase et la perte de particules. Dans un premier temps, nous avons dérivé une solution exacte pour décrire l'état quantique du système à tout temps pendant la dynamique trempée en présence de bruit de phase. Nous avons montré que la formation des superpositions macroscopiques d'états de phase est robuste vis-à-vis du bruit de phase, étant donné que la décohérence survient avec la même vitesse que la relaxation, et que cette vitesse ne dépend pas du nombre d'atomes. Comme conséquence de cette décohérence lente, une analyse d'échelle de l'information de Fisher optimale avec le nombre d'atomes nous a permis de conclure que pour un choix réaliste de la force du bruit, les superpositions à beaucoup de composantes sont plus utiles pour l'interférométrie que la superposition à deux composantes d'une part, et les états comprimés d'autre part. Ces superpositions apparaissent pendant l'évolution dynamique en l'absence de bruit à des temps plus longs par rapports à ceux des états comprimés, mais qui dépendent encore inversement du nombre total d'atomes, étant donné que la première superposition se forme à un temps $\propto 1/\sqrt{N}$. *Ceci n'est pas le cas pour la superposition macroscopique à deux composantes, qui est formée à* $T/4$ *indépendamment de* N, *et qui donc est plus affectée par la présence de bruit. Donc, dans des expériences qui auraient pour but de préparer un état utile pour l'interférométrie en reposant sur la dynamique trempée de la jonction Josephson bosonique, malgré la présence de bruit de phase il serait convenable d'attendre jusqu'à un temps* $\propto 1/\sqrt{N}$, *au-delà de le régime de spin squeezing, rejoignant la régime de formation des superpositions macroscopiques.*

Ensuite, nous avons considéré l'effet des pertes à une particule sur la production d'états de chat de Schroedinger. Nous avons généralisé la solution pour la matrice densité présentée en Ref.[162] au cas où une asymétrie dans les paramètres de la BJJ est prise en compte. Nous avons fait ainsi une "spectroscopie" de la matrice densité qui a révélé que les états où des particules ont été perdues, qui sont mélangés dans la matrice densité avec l'état en l'absence de perte de particules, ont encore des caractéristiques en commun avec des états de chat. Par exemple, leur distribution de Husimi possède encore des pics, toutefois amortis, qui correspondent aux composantes de la superposition. L'analyse de comment les corrélations utiles produites pendant la dynamique sont affectées par la perte de particules a été possible seulement de manière qualitative, puisqu'il n'est pas simple de définir dans ce cas une loi d'échelle pour l'information de Fisher avec le nombre de particules. Enfin, nous avons montré qu'il est possible de traiter analytiquement les pertes à une particule et le bruit de phase en même temps. Ce résultat peut être en principe étendu au cas de pertes à deux et trois corps, et il est important dans la perspective d'une comparaison quantitative avec les expériences.

Nos études confirment que la jonction Josephson de Bose est un système prometteur pour la métrologie et pour d'autres applications en information quantique.

6.2 Prospective views

Several aspects in the field of bosonic Josephson junctions deserve to be further investigated, especially regarding their application in quantum metrology, towards the implementation of a Heisenberg-limited interferometer, or the realization of Schroedinger's cat states, among others. A few theoretical questions in particular appear as natural extensions of the present thesis. We provide in the following the detailed list.

6.2.1 Efficient reconstruction of macroscopic superpositions via measurement of the momentum distribution

By looking at expression (1.44) and at the expression of the angular momentum operator $\hat{J}_r$ given in Eq.(1.33) one immediately notes their mutual similarity. A very natural question which arises is therefore the following: is it possible to reconstruct the angular momentum eigenvalues distributions in the $x-y$ plane $P_\phi(r)$ introduced in Chap.3 by measuring the momentum distribution?

Let us consider the operator version of Eq.(1.44),

$$\hat{n}(\vec{p}) = |\phi_0(\vec{p})|^2(N + \hat{J}_x \cos(p_x d) - \hat{J}_y \sin(p_x d)), \tag{6.1}$$

where $\langle \hat{n}(\vec{p}) \rangle = n(\vec{p})$ gives Eq.(1.44). As seen in Eq.(6.1), each value of the momentum p_x selects a direction in the $x-y$ plane of the angular momentum space. For instance, fixing $p_x d = \pi$ (we note by $\vec{p}$ the three-dimensional vectors satisfying this condition) leads to $\hat{n}(p_x d = \pi) = |\phi_0(\vec{p})|^2(N + \hat{J}_x)$. Suppose that a one shot measurement of the observable $\hat{n}(\vec{p})$ is performed. Hence, under knowledge of the gaussian envelope $|\phi_0(\vec{p})|^2$ and of the total number of particles N, from the eigenvalue of $\hat{n}(p_x d = \pi)$ we can extract an eigenvalue of $\hat{J}_x$. Analogously, the value at $\hat{n}(p_x d = \pi/2)$ yields an eigenvalue for $\hat{J}_y$, and so on, for each direction. In practice, for each shot the curve $n(\vec{p})$ should be devided in bins; the center of each bin identifies a direction in angular momentum space, while the count in each bin provides an outcome for an angular momentum operator. Repeating many times this procedure would allow to reconstruct the histograms for the angular momentum operators eigenvalues distributions in various directions of the $x-y$ plane $P_\phi(r)$ as explained in Chap.3 (see Fig.3.3), and if wished the two-dimensional quasi-probability distribution $f(x, y)$.

What is surprising with this procedure is that outcomes of observables which are not mutually commuting could be apparently simultaneously obtained with a single shot of the momentum distribution $\hat{n}(\vec{p})$. We expect such a procedure to be realizable in the regime in which the number of particles is large.

A possible recipe to demonstrate the feasability of this protocol is based on references [166, 167]. By using the N-point probability distribution $P(\vec{r}_1, \vec{r}_2, ..., \vec{r}_N) = \langle \hat{\psi}^\dagger(\vec{r}_1)\hat{\psi}^\dagger(\vec{r}_2)...\hat{\psi}^\dagger(\vec{r}_N)\hat{\psi}(\vec{r}_N)...\hat{\psi}(\vec{r}_1)\rangle$ corresponding to the state of interest, one could simulate various shots of the spatial disribution of N-particles after a time of flight, analogously to Refs. [166, 167]. The momentum distribution would be obtained from it via the scaling law $n(\vec{p}t/m) = n(\vec{r})$ [35, 46]. Since this procedure attempts to map out the

correlations in the equatorial plane of the Bloch sphere, it is more useful for states with a structure in that plane, as indeed phase cat states (see Chap.3). A similar procedure has been followed in Ref.[101] to map out the phase profile (i.e., the projected Husimi distribution $Q(\pi/2, \phi)$) of a phase cat state.

Once the simulation described above has shown the reliability of this method, one could try an experimental verification by using available data for the momentum distribution, e.g. by reconstructing the distributions $P_\phi(r)$ in various directions for a phase state. A further questions which arises in this context is how the resolution in the directions which can be reconstructed is related to the total number of particles and to the number of measurements. A finite resolution on the spatial measurement of the particles (size of the detectors) should be also taken into account (see Ref.[166]).

6.2.2 Particle losses and comparison with the experiments

Although in Sec.5.3 we have developed a treatment to include the effect of particle losses and phase noise on the same footing, and we dispose of an analytical expression for the visibility in the presence of both noise sources, a direct comparison with experimental data seems to be difficult. There are mainly two reasons for this: first of all, one would need to dispose of sufficiently good data in order to decide which loss process is the most important between one-, two- or three-body losses. This could be done e.g. by means of a fit of the visibility expression in the presence of different kind of losses separately, and by looking at which one present the best agreement. To do this, an expression of the visibility in the presence of two- and three-body losses analogous to Eq.(5.60) should be derived, which seems to be feasable (one could also think of deriving an expression including the effect of several sources of losses at the same time). Secondly, a precise comparison with the experiments would also require to take into account the dependence of the relevant parameters which enter the BJJ model on the particle number (and on the site occupation in the case of the external BJJ), according to the discussion presented in Sec.1.3.1.a. Despite the fact that we have neglected this dependence in our derivation, the fit of the visibility decay for the internal set-up that we have mentioned in Sec.5.1.2, which allowed us to extract an estimate for the noise correlation function in the non-markov regime, is still qualitatively meaningful. An argument as to why this is the case relies on the fact that at short times the contribution of the unitary dynamics to the damping of the visibility in Eq.(5.14) depends on the factor $N\chi^2$; in the set-up of Ref.[8], an experimental estimation of the dependence of the interaction constant χ from the particle number yields $\chi \propto 1/\sqrt{N}$, so that that the product $N\chi^2$ is approximatively constant at varying N. As a consequence, the visibility decay is not affected by particle losses in a first approximation [168]. A quantitative investigation of this point would be nevertheless interesting.

6.2.3 Controlled creation of cat states in the presence of atom losses and phase noise

As we have mentioned in Ch.2, the present decoherence rate in the experiments is too high to permit the creation of cat states by means of the quenched dynamics of the BJJ, or even by means of our optimal control protocol presented in Sec.2.5.3 (see also Ref.[33]). Once the main sources of noise and their decoherence rates have been identified (see comments above), an ambitious project would be thus to provide a protocol for the controlled creation of cat states, able to take into account the effect of phase noise and particle losses, with the

objective of making the experimental realization of such states possible. One could think to proceed in an analogous way as presented in Sec.2.5.3: first, by a pre-study based on a geometrical approach. To do this, one could use a semi-classical model for the dynamics of the BJJ in the presence of atom losses and phase noise, as developped in Ref.[169]. A verification of the validity of such a protocol by a full numerical calculaton of the fidelity should clearly follow. Then, the geometrical solution for the control field $K(t)$ could be again used as a trial for a full numerical algorythm. Such a full numerical calculation would be probably a challenging task, since as we have seen in Sec.5.2 the dimension of the total Hilbert space when losses are affecting the system scales as N^2.

6.2.4 Dynamics in optical lattices

A further extension of our work would be to study the quantum dynamics of a M-site optical lattice, occupied by N bosons. For instance, one could generalize the calculation of the quantum state produced after a quench which we have presented for the two-sites case in Ch.2, in the case of a M-site lattice. An approximated version of such a calculation has been carried out [101, 104, 170], in which the initial "superfluid" state (the M-site version of the strongly coupled state for the BJJ) is described by the product state $|\psi\rangle = \prod_{i=1}^{M} |\alpha_i\rangle$, where $|\alpha\rangle_i = e^{-|\alpha|^2/2} \sum_n \frac{\alpha^n}{\sqrt{n!}} |n\rangle_i$ is the Glauber coherent state in the site i. This is a good approximation in the case in which the total particle number and the number of sites are large, which is not always the case in experiments [170]. We propose to use a formalism based on generalized SU(M) coherent states [27, 162]. In such a framework, a generalized coherent state is defined as the displacement of a reference state as

$$\begin{aligned} |\vec{y}\rangle &= \hat{R}(\vec{y})|N,0,0....,0\rangle = e^{\sum_{k=2}^{M} y_{1k} J_{k1} - y_{1k}^* J_{k1}^\dagger} |N,0,0....,0\rangle \\ &= \frac{1}{\sqrt{N!}} \left(\sum_{k=1}^{M} x_k \hat{a}_k^\dagger \right)^N , \end{aligned} \tag{6.2}$$

where the SU(M) generators $J_{jk} = \hat{a}_j^\dagger \hat{a}_k$ satisfy $[\hat{J}_{jk}, \hat{J}_{mn}] = \hat{J}_{jn}\delta_{km} - \hat{J}_{mk}\delta_{nj}$, $x_1 = \cos|y|$ and $x_k = \frac{\sin|y|}{|y|} y_k$ for $k \geq 2$ [27]. Note the analogy of Eq.(6.2) with Eqs.(1.32) and (1.29), which are recovered when $M = 2$ by setting $y = \theta/2e^{-i\phi}$. The ground state of the Hamiltonian (5.32) is given by Eq.(6.2) with $x_k = 1$ for each k [162, 170]. The first purpose would be to show that under a quench, after a fraction of the period the state is found in a superposition of generalized coherent states of the form (6.2).

This formalism also allows to treat the 4-mode set-up advanced in Ref.[171], in which two atomic species are trapped in a double-well external potential, so that four modes are naturally involved. Such a system is a promising tool to demonstrate entanglement between spatially separated parties, as in the Einstein-Podolski-Rosen paradox [171, 172].

Appendix A

Detection of macroscopic superpositions

A.1 Generating function of the distributions of the angular momentum operators eigenvalues for macroscopic superpositions and incoherent mixtures of phase states

Let us now evaluate explicitely the generating function (3.14) for the q-component cat state and the corresponding statistical mixture of coherent states. In the following we will assume that N is even. With the definition $\zeta = \eta/2e^{-i\phi}$ [71] and by using Eqs.(2.25), the generating function for cat states with an even number of components can be rewritten as

$$h_{\phi}^{\mathrm{cats}}(\eta) = \langle\psi(t_q)|e^{\zeta\hat{J}_+ - \zeta^*\hat{J}_-}|\psi(t_q)\rangle = |u_0|^2 \sum_{k=0}^{q-1}\sum_{k'=0}^{q-1}\langle\alpha e^{-i\frac{2\pi k'}{q}}|e^{\zeta\hat{J}_+ - \zeta^*\hat{J}_-}|\alpha e^{-i\frac{2\pi k}{q}}\rangle \quad \text{(A.1)}$$

From the disentangling theorem (Eq. (A5) in Ref.[71]) we have

$$e^{\zeta\hat{J}_+ - \zeta^*\hat{J}_-} = e^{-\tau^*\hat{J}_-}e^{-\log(1+|\tau|^2)\hat{J}_z}e^{\tau\hat{J}_+} \quad \text{(A.2)}$$

The operator $e^{\tau\hat{J}_+}$ acts on the coherent state on the right sides of Eq.(A.2) as a changing in the amplitude of the coherent states, due to

$$\begin{aligned} e^{\tau\hat{J}_+}|\alpha\rangle &= \frac{\left(1+|\alpha+\tau|^2\right)^{N/2}}{\left(1+|\alpha|^2\right)^{N/2}}|\alpha+\tau\rangle \\ \langle\alpha'|e^{-\tau^*\hat{J}_-} &= \frac{\left(1+|\alpha'-\tau|^2\right)^{N/2}}{\left(1+|\alpha'|^2\right)^{N/2}}\langle\alpha-\tau| \end{aligned} \quad \text{(A.3)}$$

(similarly for the left hand side of Eq.(A.2)). Then, we need to calculate the action of the operator $e^{\gamma\hat{J}_z}$ over two general coherent states, which gives

$$\begin{aligned} &\langle\beta'|e^{\gamma\hat{J}_z}|\beta\rangle = \\ &= \frac{1}{(1+|\beta|^2)^{N/2}}\frac{1}{(1+|\beta|^2)^{N/2}}\sum_{n=-N/2}^{N/2}\sum_{m=-N/2}^{N/2}\binom{N}{\frac{N}{2}+n}^{1/2}\binom{N}{\frac{N}{2}+m}^{1/2}\beta^{n+\frac{N}{2}}\beta'^{*(m+\frac{N}{2})}\langle m|e^{\gamma\hat{J}_z}|n\rangle \\ &= \frac{e^{-\gamma N/2}}{(1+|\beta|^2)^{N/2}(1+|\beta'|^2)^{N/2}}\left(1+\beta\beta'^*e^{\gamma}\right)^N. \end{aligned} \quad \text{(A.4)}$$

Using Eqs.(A.3) and (A.4), equation (A.2) becomes

$$\langle\alpha'|e^{\zeta\hat{J}_+-\zeta^*\hat{J}_-}|\alpha\rangle = \frac{1}{(1+|\alpha|^2)^{N/2}}\frac{1}{(1+|\alpha'|^2)^{N/2}}e^{-\frac{\gamma N}{2}}\left(1+(\alpha+\tau)\left(\alpha'-\tau\right)^* e^{\gamma}\right)^N \quad (A.5)$$

with

$$\begin{aligned}\tau &= \frac{\zeta}{|\zeta|}\tan|\zeta| \\ \gamma &= -\log\left(1+|\tau|^2\right)\end{aligned} \quad (A.6)$$

Substituting equations (A.5) and (A.6) in Eq.(A.1) and using $\alpha = 1$, we obtain finally for even q

$$h_\phi^{\rm cats}(\eta) = |u_0|^2\frac{e^{-\frac{\gamma N}{2}}}{2^N}\sum_{k=0}^{q-1}\sum_{k'=0}^{q-1}c_k c_{k'}^*\left(1+\left(e^{-i\frac{2\pi k}{q}}+\tau\right)\left(e^{i\frac{2\pi k'}{q}}-\tau^*\right)e^{\gamma}\right)^N \quad (A.7)$$

while the mean over the corresponding mixture gives

$$h_\phi^{\rm mixt}(\eta) = \frac{1}{q}\frac{e^{-\frac{\gamma N}{2}}}{2^N}\sum_{k=0}^{q-1}\left(1+\left(e^{-i\frac{2\pi k}{q}}+\tau\right)\left(e^{i\frac{2\pi k}{q}}-\tau^*\right)e^{\gamma}\right)^N \quad (A.8)$$

and, for odd q

$$\begin{aligned}h_\phi^{\rm cats}(\eta) &= |\tilde{u}_0|^2\frac{e^{-\frac{\gamma N}{2}}}{2^N}\sum_{k=0}^{q-1}\sum_{k'=0}^{q-1}\tilde{c}_k\tilde{c}_{k'}^*\left(1+\left(e^{-i\frac{2\pi k}{q}-i\frac{\pi}{q}}+\tau\right)\left(e^{i\frac{2\pi k'}{q}+i\frac{\pi}{q}}-\tau^*\right)e^{\gamma}\right)^N \\ h_\phi^{\rm mixt}(\eta) &= \frac{1}{q}\frac{e^{-\frac{\gamma N}{2}}}{2^N}\sum_{k=0}^{q-1}\left(1+\left(e^{-i\frac{2\pi k}{q}-i\frac{\pi}{q}}+\tau\right)\left(e^{i\frac{2\pi k}{q}+i\frac{\pi}{q}}-\tau^*\right)e^{\gamma}\right)^N\end{aligned} \quad (A.9)$$

This can be further simplified as

$$\begin{aligned}h_\phi^{\rm mixt}(\eta) &= \frac{1}{q}\sum_{k=0}^{q-1}\left(|\cos\frac{\eta}{2}| + i\sin\frac{\eta}{2}\ \mathrm{sign}\left[\cos\frac{\eta}{2}\right]\sin\left(\frac{2\pi k}{q}-\phi\right)\right)^N \\ h_\phi^{\rm cats}(\eta) &= h_\phi^{\rm mixt}(\eta) \\ &+|u_0|^2\sum_{k\neq k'=0}^{q-1}\frac{c_k c_{k'}^*}{2^N}\left(|\cos\frac{\eta}{2}|\left(1+e^{-i\frac{2\pi(k-k')}{q}}\right)+\sin\frac{\eta}{2}\ \mathrm{sign}\left[\cos\frac{\eta}{2}\right]\left(e^{i(\frac{2\pi k'}{q}-\phi)}-e^{-i(\frac{2\pi k}{q}-\phi)}\right)\right)^N\end{aligned} \quad (A.10)$$

for an even number of components, while for an odd q one obtains Eqs.(3.18) and (3.19) of the main text.

A.2 Effect of time noise in the reconstruction of the probability distribution $P_\phi(r)$

In order to roughly estimate the effect on the reconstruction of the profile $P_\phi(r)$ of an error in the time at which the measurements of the angular momentum operators are performed, we extract N_{meas} values of t distributed normally with a variance σ^2 around the time t_q at

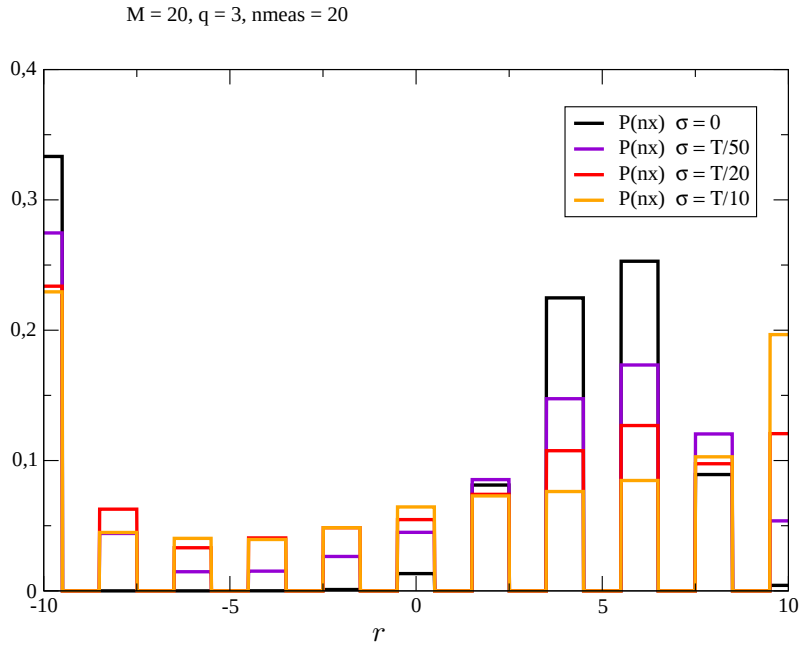

Figure A.1: Eigenvalue distribution $P_\phi(r)$ corresponding to $\hat{J}_x$ ($\phi = \pi/2$) for the three-component coherent superposition with $N = 20$, in the case in which an error in the time of the measurement is taken into account, at various values of the variance σ of the time distribution.

which the q-component cat state is formed, i.e. according to $p(t, t_q) = e^{-\frac{(t-t_q)^2}{2\sigma^2}}/(\sqrt{2\pi}\sigma)$. Then, we average $P_\phi(r, t) = |\langle r|\psi(t)\rangle|^2$ where $|\psi(t)\rangle$ is given by Eq.(2.19), obtaining thus

$$P_\phi(r, t_q) = \frac{1}{N_{meas}} \sum_{i=1}^{N_{meas}} P_\phi(r, t). \tag{A.11}$$

Such an estimate is correct only in the limit of an infinite number of measurement, which allows to sample many times each time t, and to perfectly reconstruct each probability distribution $P_\phi(r, t)$. We illustrate the estimate (A.11) in Fig.(A.1). We see that a standard deviation $\sigma = 1/N$ is somehow critical, in the sense that for lower standard deviations the probability distribution still displais the peaks corresponding to the cat state, while for higher values the recognition of such state fails.

A.3 Rewriting the quasi-probability distribution $f(x, y)$

The probability distribution $f(x, y)$ of Eq.(3.32) can be rewritten to change the interval of integration. To do this, we first separate the contribution for positive and negative η in Eq.(3.32), obtaining

$$f(x, y) = \left(\frac{1}{2\pi}\right)^2 \left(\int_0^\pi d\eta\eta \int_0^\pi d\phi h_\phi(\eta) e^{i\eta(\sin\phi x - \cos\phi y)} + I\right) \tag{A.12}$$

with

$$I=\int_{-\pi}^{0}d\eta\,(-\eta)\int_{0}^{\pi}d\phi h_{\phi}(\eta)e^{i\eta(\sin\phi x-\cos\phi y)}=\int_{0}^{\pi}d\eta'\eta'\int_{0}^{\pi}d\phi h_{\phi}(-\eta')e^{-i\eta'(\sin\phi x-\cos\phi y)}, \tag{A.13}$$

where we set $\eta'=-\eta$. Let us drop the prime. Due to the definition of the generating function Eq.(3.14), the following property follows:

$$\begin{aligned} h_{\phi}(-\eta)e^{-i\eta(\sin\phi x-\cos\phi y)} &= \langle e^{i\eta(J_x\sin\phi-J_y\cos\phi)}\rangle e^{-i\eta(\sin\phi x-\cos\phi y)} \\ &= \langle e^{-i\eta(J_x\sin(\phi+\pi)-J_y\cos(\phi+\pi))}\rangle e^{i\eta(\sin(\phi+\pi)x-\cos(\phi+\pi)y)} \\ &= h_{\phi+\pi}(\eta)e^{i\eta(\sin(\phi+\pi)x-\cos(\phi+\pi)y)}. \end{aligned} \tag{A.14}$$

This allows to rewrite Eq.(A.13), defining also $\phi'=\phi+\pi$, as

$$\begin{aligned} I &= \int_{0}^{\pi}d\eta\eta\int_{0}^{\pi}d\phi h_{\phi}(-\eta)e^{-i\eta(\sin\phi x-\cos\phi y)} \\ &= \int_{0}^{\pi}d\eta\eta\int_{\pi}^{2\pi}d\phi' h_{\phi}(\eta)e^{i\eta(\sin\phi' x-\cos\phi' y)}. \end{aligned} \tag{A.15}$$

Substitution of Eq.(A.15) in Eq.(A.12) yields to equation (3.33) of the main text.

A.4 Connection with the Wigner function

Referring to the definition in Eq.(3.11) taken from Ref.[116], let us consider the projection along the equator, i.e.

$$\begin{aligned} W_s(x_1,x_2) &= \int_{-\infty}^{\infty}dx_3 W_s(\vec{x})=\int_{SU(2)}d\vec{y}s(\xi)\mathrm{tr}\left[e^{i\vec{y}\vec{J}}\hat{\rho}\right]e^{-i(x_1y_1+x_2y_2)}\int_{-\infty}^{\infty}dx_3e^{-ix_3y_3} \\ &= (2\pi)\int_{SU(2)}d\vec{y}s(\xi)\mathrm{tr}\left[e^{i(y_1J_x+y_2J_y)}\hat{\rho}\right]e^{-i(x_1y_1+x_2y_2)}\delta(y_3). \end{aligned} \tag{A.16}$$

Now, with the parametrization of Ref.[116] we have

$$\begin{aligned} y_1 &= \xi\sin\theta\sin\phi \\ y_2 &= \xi\sin\theta\cos\phi \\ y_3 &= \xi\cos\theta. \end{aligned} \tag{A.17}$$

Since

$$\delta(y_3)=\delta(\xi\cos\theta)=\frac{\delta\left(\theta-\frac{\pi}{2}\right)}{\xi}, \tag{A.18}$$

hence from Eq.(A.16) we obtain

$$\begin{aligned} W_s(x_1,x_2) &= \int d\xi\xi s(\xi)\int d\theta\sin\theta\int d\phi\frac{\delta\left(\theta-\frac{\pi}{2}\right)}{\xi} \\ &\quad\times\mathrm{tr}\left[e^{i\xi(\sin\theta\sin\phi J_x+\sin\theta\cos\phi J_y)}\hat{\rho}\right]e^{-i\xi(x_1\sin\theta\sin\phi+x_2\sin\theta\cos\phi)} \\ &= \int d\xi d\phi s(\xi)\mathrm{tr}\left[e^{i\xi(\sin\phi J_x+\cos\phi J_y)}\hat{\rho}\right]e^{-i\xi(x_1\sin\phi+x_2\cos\phi)}, \end{aligned} \tag{A.19}$$

which clearly displais the same structure as Eq.(3.33).

Appendix B

Coherent spin squeezing and quantum Fisher information

B.1 Demonstration of Eq.(4.39) for the spin squeezing parameter

In the following we show that the spin squeezing parameter $\xi^2(t)$ in a Bose Josephson junction is always optimized along a direction contained in the (yOz)-plane.

Let us observe that the angular momentum covariance matrix $G(t)$ defined by Eq.(4.31) has vanishing matrix elements $G_{xy}(t) = G_{xz}(t) = 0$. In fact, in the absence of noise this matrix $G(t) = \gamma^{(0)}(t)$ is given by Eq.(4.34), and we have seen in Sec. 5.1.4 that it preserves the same structure in the presence of phase noise. Due to this special structure of $G(t)$, the fluctuations of the angular momentum operator along an arbitrary direction $\hat{n}$ given by Eq.(2.8) is

$$\begin{aligned} (\Delta J_n(t))^2 &= \sum_{i,j=x,y,z} n_i G_{ij}(t) n_j \\ &= \sin^2\theta \sin^2\phi\, G_{xx}(t) + \sum_{i,j=y,z} n_i G_{ij}(t) n_j \,. \end{aligned} \tag{B.1}$$

The sum over i, j in the second line can be written as $(\sin^2\theta\cos^2\phi + \cos^2\theta)\hat{n}'^T G'(t)\hat{n}'$, where we introduced the notation $G'(t)$ for the two-by-two submatrix of $G(t)$ in the plane (yOz) and the normalized vector

$$\hat{n}' = \frac{n_y\hat{y} + n_z\hat{z}}{\sqrt{\sin^2\theta\cos^2\phi + \cos^2\theta}} \tag{B.2}$$

in this plane. Furthermore, we observe that during the dynamics of the noisy junction one has $\langle\hat{J}_y\rangle_t = \langle\hat{J}_z\rangle_t = 0$ at all times. As a consequence, the expectation values of the angular momentum operators along the directions defined by Eq.(2.7) are given by

$$\begin{aligned} \langle\hat{J}_{p_1}\rangle_t &= \cos\phi\langle\hat{J}_x\rangle_t \\ \langle\hat{J}_{p_2}\rangle_t &= -\cos\theta\sin\phi\langle\hat{J}_x\rangle_t \,. \end{aligned} \tag{B.3}$$

Combining these results and using the fact that $G_{xx}(t) \geq 0$, we obtain from Eq.(2.6)

$$\begin{aligned}
&\frac{N\nu(t)^2}{4}\xi_{\vec{n}}^2(t) = \frac{\sin^2\theta\sin^2\phi\, G_{xx}(t)}{1-\sin^2\phi\sin^2\theta} + \hat{n}'^T G'(t)\hat{n}' \\
&\geq G_-(t) = \min_{\hat{n}'}\left\{\hat{n}'^T G'(t)\hat{n}'\right\} \\
&= \min_{\hat{n}\in(yOz)}\left\{\hat{n}^T G(t)\hat{n}\right\}
\end{aligned} \tag{B.4}$$

where $\nu(t) = 2\langle \hat{J}_x\rangle_t/N$ is the visibility and $G_-(t)$ the smallest eigenvalue of $G'(t)$. Since it is clear that the inequality in Eq.(B.4) is an equality for $\hat{n}$ equal to the corresponding eigenvector $\hat{n}_-(t)$ of $G_-(t)$, this demonstrates that the squeezing is minimized along a direction $\hat{n}_-(t)$ contained in the (yOz)-plane. Combining Eqs.(4.28) and (B.4), we obtain that the optimum coherent spin squeezing is given by Eq.(4.39).

B.2 Determination of the time t^* when the optimization direction of the Fisher information changes in the absence of noise

If the number N of atoms is even, the direction of optimization $\hat{n}_F^{(0)}$ of the Fisher information in a noiseless Bose Josephson junction is along x-axis at the time $t_2 = T/4$ of formation of the superposition of the two phase states $|\theta = \pi/2, \phi = 0\rangle$ and $|\theta = \pi/2, \phi = \pi\rangle$. These phase states are indeed diametrically opposite on the equator of Bloch sphere along this axis. Since $\hat{n}_F^{(0)}(\tau) = \hat{n}_+^{(0)}(\tau)$ is in the (yOz)-plane at times $\tau = 2\pi t/T \ll 1$ (see Sec.4.4), the optimizing direction thus changes abruptly from the (yOz)-plane to the x-axis at some time $\tau^* \in]0, \pi/2[$ satisfying

$$\gamma_x^{(0)}(\tau^*) = \gamma_+^{(0)}(\tau^*)\,. \tag{B.5}$$

In this appendix we determine τ^* explicitely in the limit of large total atom number N, supposed to be even. We may infer from the previous discussion that τ^* is neither close to 0 nor close to $\pi/2$. Consequently, we look for a solution of the implicit equation (B.5) in the interval $\tau \in [N^{-\alpha}, \pi/2 - N^{-\alpha}]$, α being a positive exponent strictly smaller than 1/2. Introducing the variables $u \equiv \cos(\tau) \in [0, \cos(N^{-\alpha})]$ and $v \equiv \cos(2\tau) \in [-\cos(2N^{-\alpha}), \cos(2N^{-\alpha})]$, we obtain with the help of Eqs.(4.35) and (4.37)

$$\begin{aligned}
&\frac{4(\gamma_+^{(0)}(\tau) - \gamma_x^{(0)}(\tau))}{N} = -(N-1)v^{N-2} + Nu^{2N-2} \\
&+2(N-1)u^{2N-4}(1-u^2) + O(Nu^{4N-8}) + O(Nv^{2N-4})\,.
\end{aligned} \tag{B.6}$$

Setting $\gamma_+^{(0)}(\tau) = \gamma_x^{(0)}(\tau)$ gives the equation

$$\left(2 - \frac{1}{u^2}\right)^{N-2} = 2 - u^2\frac{N-2}{N-1} + O(e^{-N^{1-2\alpha}})\,. \tag{B.7}$$

For large N, the right-hand side of Eq.(B.7) is strictly larger than one and is of the order of unity. Hence the solution must satisfy $|2-u^{-2}| > 1$ and $2-u^{-2} \simeq \pm 1$. We may exclude the positive sign as the values $u = \pm 1$ correspond to $\tau \simeq 0$ or $\tau = \pi$ outside the studied time interval. The relevant solution u of Eq.(B.7) is thus close to $1/\sqrt{3}$ and smaller than this number. Let us note that for odd N's, such a solution does not exist; indeed, in this

case Eq.(B.5) has no solution (see Sec.4.4). Let us set $u = 1/(\sqrt{3}(1+\delta))$. Then from Eq.(B.7) we obtain

$$e^{(N-2)\ln(1+6\delta+O(\delta^2))} = \frac{5}{3} + O(\delta) + O\left(\frac{1}{N}\right) \tag{B.8}$$

from which we find

$$\delta = \frac{1}{6N}\ln\left(\frac{5}{3}\right)\left(1 + O\left(\frac{1}{N}\right)\right) \tag{B.9}$$

In terms of the dimensionless time τ^* we get

$$\tau^* = \arccos\left(\frac{1}{\sqrt{3}}\right) + \frac{\ln(5/3)}{6\sqrt{2}N} + O\left(\frac{1}{N^2}\right). \tag{B.10}$$

Appendix C

Quantum Fisher information and coherent spin squeezing at thermal equilibrium

C.1 Squeezing at $T = 0$, $K = 0$

The squeezing in the ground state of the BJJ at $K = 0$ is an indeterminate expression. To evaluate its limiting value, we use the perturbation theory to the second order with unperturbed Hamiltonian $\hat{H}_0 = \chi \hat{J}_z^2$, and $\hat{H}_I = -2K\hat{J}_x$. The ground state is the only non-degenerate state for the unperturbed Hamiltonian. The excited two-fold degenerate levels are given by

$$\begin{aligned} |\psi_n^{(1)}\rangle &= |n\rangle - 2K \sum_{m\neq n} \frac{\langle m|\hat{J}_x|n\rangle}{E_n^{(0)} - E_m^{(0)}} |m\rangle \\ &= |n\rangle + \frac{K}{\chi}\left[\frac{\sqrt{\left(\frac{N}{2}+n+1\right)\left(\frac{N}{2}-n\right)}}{(2n+1)}|n+1\rangle + \frac{\sqrt{\left(\frac{N}{2}-n+1\right)\left(\frac{N}{2}+n\right)}}{(-2n+1)}|n-1\rangle\right], \end{aligned}$$

while the ground state expansion yields

$$|\psi_0^{(1)}\rangle = |0\rangle - 2K \sum_{m\neq n} \frac{\langle m|\hat{J}_x|n\rangle}{E_n^{(0)} - E_m^{(0)}} |m\rangle = |0\rangle + b\left(|-1\rangle + |1\rangle\right), \tag{C.1}$$

where we defined $b = \frac{K}{\chi}\sqrt{\left(\frac{N}{2}+1\right)\frac{N}{2}}$; the normalization is fixed by $\langle\psi_0^{(1)}|\psi_0^{(1)}\rangle = (1+2b^2)$.

Indicating with $\langle \tilde{O} \rangle \equiv \frac{\langle \psi_0^{(1)} | \hat{O} | \psi_0^{(1)} \rangle}{\langle \psi_0^{(1)} | \psi_0^{(1)} \rangle}$, with the use of Eq.(C.1) we obtain

$$\begin{aligned}
\langle \tilde{J}_x \rangle &= \frac{2b}{(1+2b^2)} \sqrt{\left(\frac{N}{2}+1\right)\frac{N}{2}} \\
\langle \tilde{J}_y \rangle &= \langle \tilde{J}_z \rangle = 0 \\
\langle \tilde{J}_x^2 \rangle &= \frac{1}{4(1+2b^2)} \left[N\left(\frac{N}{2}+1\right) + 2b^2 \left(N\left(\frac{N}{2}+1\right) + \left(\frac{N}{2}-1\right)\left(\frac{N}{2}+2\right)\right)\right] \\
\langle \tilde{J}_y^2 \rangle &= \frac{1}{4(1+2b^2)} \left[N\left(\frac{N}{2}+1\right) - 2b^2 \left(\frac{N}{2}-1\right)\left(\frac{N}{2}+2\right)\right] \\
\langle \tilde{J}_z^2 \rangle &= \frac{2b^2}{(1+2b^2)} \\
\langle \tilde{J_x J_y} \rangle &= \langle \tilde{J_x J_z} \rangle = 0 \\
\langle \tilde{J_y J_z} \rangle &= \frac{-b}{i(1+2b^2)} \sqrt{\left(\frac{N}{2}+1\right)\frac{N}{2}}.
\end{aligned} \tag{C.2}$$

Due to Eqs.(C.2), we find that the direction which optimizes the squeezing is z. With the definition (2.6) we then obtain

$$\xi^2 = \xi_z^2 = \frac{N\Delta^2 \hat{J}_z}{\langle \hat{J}_x \rangle^2 + \langle \hat{J}_y \rangle^2} = \frac{N 2b^2}{4b^2\left(\frac{N}{2}+1\right)\frac{N}{2}}, \tag{C.3}$$

which renders Eq.(4.32) of the main text.

C.2 Quantum Fisher information and coherent spin squeezing at thermal equilibrium

We want to calculate the Fisher information and the squeezing (optimized over all the possible directions) at thermal equilibrium when $T = \frac{1}{K_B \beta}$ is non zero, at $\lambda = 0$, in the framework of the two-mode Hamiltonan (1.24) modeling the bosonic Josephson junction. As for Sec.4.3 of the main text, this provides an indication of the usefulness of the equilibrium state of the BJJ for sub-shot noise phase estimation in atom interferometry, when the temperature is finite. We focus again on the case of symmetric modes $\lambda = 0$.

The density matrix at temperature T is

$$\hat{\rho} = \sum_k p_k |k\rangle\langle k| \tag{C.4}$$

where $|k\rangle$ are the $N+1$ eigenstates which diagonalize the Hamiltonian Eq.(1.24) $\hat{H}|k\rangle = E_k|k\rangle$, and the p_ks are given by the Gibbs distribution

$$p_k = \frac{e^{-\beta E_k}}{Z} \tag{C.5}$$

with Z the partition function $Z = \sum_k e^{-\beta E_k}$.

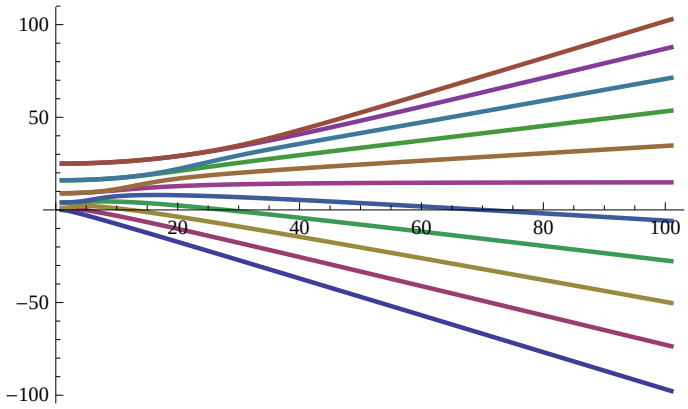

Figure C.1: Energy spectrum from the Hamiltonian diagonalization as a function of $r = K/\chi$, with $N = 10$, $\lambda = 0$. For $r \sim 0$ the spectrum is quadratic (see Sec.C.2.1), while for $r \gg 1$ the level spacing is linear (see Sec.C.2.2).

To compute the Fisher information, we use the covariance matrix (4.29) introduced in Sec.4.2. In reference to Eq.(4.29), we introduce the notation

$$e_{i,j}(l,k) = \langle l|J_i|k\rangle\langle k|J_j|l\rangle, \tag{C.6}$$

which allows to rewrite the covariance matrix as

$$[\gamma_C]_{i,j} = \frac{1}{2}\sum_{l,k}\frac{(p_l - p_k)^2}{p_l + p_k}e_{i,j}(l,k). \tag{C.7}$$

As we have done in Sec.4.3, we first tackle in the next following two subsections the limiting cases of the problem, namely the limit $K = 0$ and $\chi = 0$. We will address numerically the general case.

C.2.1 Limiting case I: $K = 0$, $\lambda = 0$

In this limit the Hamiltonian is reduced to $\hat{H} = \chi \hat{J}_z^2$, with as eigenstates the Fock states given by Eq.(1.26), with double degeneracy except the ground state $n = 0$. Therefore

$$Z = 1 + 2\sum_{n=1}^{\frac{N}{2}} e^{-\chi\beta n^2} \tag{C.8}$$

and $\hat{\rho} = \sum_{n=1}^{\frac{N}{2}} p_n|n\rangle\langle n|$ with $p_n = e^{-\chi\beta n^2}/Z$. From (C.6) it is easy to calculate

$$\begin{aligned}
e_{xx}(l,k) &= \frac{1}{4}\left[(\frac{N}{2}+k+1)(\frac{N}{2}-k)\delta_{l,k+1} + (\frac{N}{2}-k+1)(\frac{N}{2}+k)\delta_{l,k-1}\right] \\
e_{yy}(l,k) &= e_{xx}(l,k) \\
e_{xy}(l,k) &= -\frac{1}{4i}\left[(\frac{N}{2}+k+1)(\frac{N}{2}-k)\delta_{l,k+1} - (\frac{N}{2}-k+1)(\frac{N}{2}+k)\delta_{l,k-1}\right]
\end{aligned} \tag{C.9}$$

The other elements do not contribute since they imply $\delta_{l,k}$, and they appear multiplied by $(p_l - p_k)^2$ in Eq.(4.29). The corresponding probability factors are

$$\begin{aligned}
\frac{(p_{k+1}-p_k)^2}{p_{k+1}+p_k} &= \frac{1}{Z}\frac{(e^{-\chi\beta(k+1)^2}-e^{-\chi\beta k^2})^2}{e^{-\chi\beta(k+1)^2}+e^{-\chi\beta k^2}} = \frac{1}{Z}\frac{2e^{-\frac{\chi\beta}{2}\left(k^2+(k+1)^2\right)}\sinh^2(\frac{\chi\beta}{2}(2k+1))}{\cosh(\frac{\chi\beta}{2}(2k+1))} \\
\frac{(p_{k-1}-p_k)^2}{p_{k-1}+p_k} &= \frac{1}{Z}\frac{(e^{-\chi\beta(k-1)^2}-e^{-\chi\beta k^2})^2}{e^{-\chi\beta(k-1)^2}+e^{-\chi\beta k^2}} = \frac{1}{Z}\frac{2e^{-\frac{\chi\beta}{2}\left(k^2+(k-1)^2\right)}\sinh^2(\frac{\chi\beta}{2}(-2k+1))}{\cosh(\frac{\chi\beta}{2}(-2k+1))}
\end{aligned}$$

and then we obtain

$$\begin{aligned}
\gamma_{xx} &= \frac{1}{4Z}\sum_{k=-\frac{N}{2}}^{\frac{N}{2}}\left[(\frac{N}{2}+k+1)(\frac{N}{2}-k)\frac{e^{-\frac{\chi\beta}{2}(k^2+(k+1)^2)}\sinh^2(\frac{\chi\beta}{2}(2k+1))}{\cosh(\frac{\chi\beta}{2}(2k+1))}+\right. \\
&\left.+(\frac{N}{2}-k+1)(\frac{N}{2}+k)\frac{e^{-\frac{\chi\beta}{2}(k^2+(k-1)^2)}\sinh^2(\frac{\chi\beta}{2}(-2k+1))}{\cosh(\frac{\chi\beta}{2}(-2k+1))}\right] \\
&= \frac{1}{2Z}\sum_{k=0}^{N}(k+1)(N-k)\frac{e^{-\frac{\chi\beta}{2}((k-\frac{N}{2})^2+(k-\frac{N}{2}+1)^2)}\sinh^2(\frac{\chi\beta}{2}(2(k-\frac{N}{2})+1))}{\cosh(\frac{\chi\beta}{2}(2(k-\frac{N}{2})+1))} = \gamma_{yy}
\end{aligned}$$

The covariance matrix is then given by

$$\gamma = \begin{pmatrix} \gamma_{xx} & 0 & 0 \\ 0 & \gamma_{xx} & 0 \\ 0 & 0 & 0 \end{pmatrix} \tag{C.10}$$

which is already diagonal. Therefore the Fisher information is optimum along any degenerate direction in the $\hat{J}_x - \hat{J}_y$ plane, which reflects the fact the Hamiltonian in this limit does not depend on $\hat{J}_x$ nor on $\hat{J}_y$, and its value is

$$F_Q = 4\gamma_{xx}. \tag{C.11}$$

(the squeezing in this regime is calculated numerically).

For $T \to \infty$, we find $\hat{\rho_\infty} = \frac{1}{N+1}\sum_{n=-\frac{N}{2}}^{\frac{N}{2}}|n\rangle\langle n|$, which has optimum Fisher information $F_Q = 0$ as $p_l = p_k$ for each k, l in Eq.(4.29). Here the squeezing parameter is infinite.

C.2.2 Limiting case II: $\chi = 0$

The Hamiltonian in this regime reduceds to $\hat{H} = -2K\hat{J}_x$; its eigenstates are the states $|n_x\rangle$ satisfying $\hat{J}_x|n_x\rangle = n_x|n_x\rangle$, with $-\frac{N}{2} \le n_x \le \frac{N}{2}$. Hence the partition function is given by

$$Z = \sum_{n_x=-\frac{N}{2}}^{\frac{N}{2}} e^{2K\beta n_x} = \frac{\sinh(K\beta(N+1))}{\sinh(K\beta)} \tag{C.12}$$

and $\hat{\rho} = \sum_{n_x=-\frac{N}{2}}^{\frac{N}{2}} p_{n_x}|n_x\rangle\langle n_x|$ with $p_{n_x} = e^{2K\beta n_x}/Z$. To calculate the Fisher information, we rotate the basis (the Fisher information is left unvaried), and we calculate the covariance matrix corresponding to the density matrix $\tilde{\rho} = \sum_{n=-\frac{N}{2}}^{\frac{N}{2}} p_n|n\rangle\langle n|$ where $\hat{J}_z|n\rangle = n|n\rangle$,

and $p_n = e^{2K\beta n}/Z$. The matrix elements (C.6) are the same as in Eq. (C.9), but now the corresponding probability factors are given by

$$\begin{aligned}\frac{(p_{k+1}-p_k)^2}{p_{k+1}+p_k} &= \frac{1}{Z}\frac{(e^{2K\beta(k+1)}-e^{2K\beta k})^2}{e^{2K\beta(k+1)}+e^{2K\beta k}} = \frac{1}{Z}\frac{2e^{2K\beta(k+1/2)}\sinh^2(K\beta)}{\cosh(K\beta)} \\ \frac{(p_{k-1}-p_k)^2}{p_{k-1}+p_k} &= \frac{1}{Z}\frac{(e^{2K\beta(k-1)}-e^{2K\beta k})^2}{e^{2K\beta(k-1)}+e^{2K\beta k}} = \frac{1}{Z}\frac{2e^{2K\beta(k-1/2)}\sinh^2(K\beta)}{\cosh(K\beta)}\end{aligned}$$

Then we obtain

$$\begin{aligned}\tilde{\gamma}_{xx} &= \frac{1}{4Z}\frac{\sinh^2(K\beta)}{\cosh(K\beta)}\sum_{k=-\frac{N}{2}}^{\frac{N}{2}}\left[(\frac{N}{2}+k+1)(\frac{N}{2}-k)e^{2K\beta(k+1/2)}+(\frac{N}{2}-k+1)(\frac{N}{2}+k)e^{2K\beta(k-1/2)}\right] \\ &= \frac{1}{2Z}\frac{\sinh^2(K\beta)}{\cosh(K\beta)}\sum_{k=0}^{N}(k+1)(N-k)e^{2K\beta(k-\frac{(N-1)}{2})} = \tilde{\gamma}_{yy} \qquad \text{(C.13)}\end{aligned}$$

Coming back to the original basis via the identification $\gamma_{zz} = \tilde{\gamma}_{xx}$, $\gamma_{yy} = \tilde{\gamma}_{xx}$ we obtain

$$\gamma = \begin{pmatrix} 0 & 0 & 0 \\ 0 & \gamma_{zz} & 0 \\ 0 & 0 & \gamma_{zz} \end{pmatrix} \qquad \text{(C.14)}$$

From Eq.(C.14) it is easily seen that the Fisher information is optimum along any degenerate direction in the $\hat{J}_y - \hat{J}_z$ plane, reflecting the fact the Hamiltonian does not depend on $\hat{J}_y$ nor on $\hat{J}_z$. Its optimum value is

$$F_Q = 4\gamma_{zz} = 4\tilde{\gamma}_{xx} \qquad \text{(C.15)}$$

.

For $T \to \infty$, $\hat{\rho_\infty} = \frac{1}{N+1}\sum_{n_x=-\frac{N}{2}}^{\frac{N}{2}} |n_x\rangle\langle n_x|$ which has optimum Fisher information $F_Q = 0$ as $p_l = p_k$ for each k, l in Eq.(4.29).

C.2.3 Intermediate regime

In Figs.(C.2.3) and (C.2.3) are presented the results of the numerical calculation of the Fisher information and the squeezing at various temperatures in the intermediate regime, as a function of the ratio $r = K\chi$.

We observe an interesting non monotonic behaviour of the Fisher information for the intermediate temperature regime, e.g. $K_BT/\chi = 1.31$ as in Fig.C.2.3. The Fisher information has in this case a maximum at $r = K/\chi \sim 1$ (for $N = 10$). This can be understood as resulting from the competition between the following two effect: 1) At $T = 0$ the region close to $r = 0$ is more entangled since the state is close to a Fock state; 2) In the same region the energy levels are less separated from each other, and therefore it is easier to populate thermically many of them, compared to the region at high r where the levels are more separated. (see Fig.C.2).

The squeezing exhibits the same behaviour. However, there is some regime (e.g. top panel in Fig.C.2.3) in which the Fisher information is above the shot noise limit (here $N = 10$) and therefore recognizes useful states, while squeezing does not.

We have checked numerically that in the intermediate regime of generic r the squeezing is always optimized in the z-direction, while the Fisher information is optimum in a non trivial direction in angular momentum space which involves all of the components $\hat{J}_i$. Such direction is changed by the presence of temperature.

C.3 Remarks on the validity of the two-mode model

The presence of a finite temperature may induce the population of more than two one-particle levels of the double-well potential realizing the external BJJ, thus invalidating the two-mode approximation. In the experiments of Ref.[13], however, the lowest energy of transversal excitation, set by the trap frequencies, is approximatively twice the temperature, and the two-mode approximation still yields good indications [62].

A multi-mode approach has been followed in Ref.[173] to study the effect of temperature on the dynamical formation of squeezed states (see Ch.2), by means of a fully non perturbative semiclassical field simulation. The result of this analysis is that the scaling of the best spin squeezing $\xi^2_{\rm best}$ with the number of particles N is strongly modified by the finite temperature, and $\xi^2_{\rm best}$ saturates to a constant value independent on N.

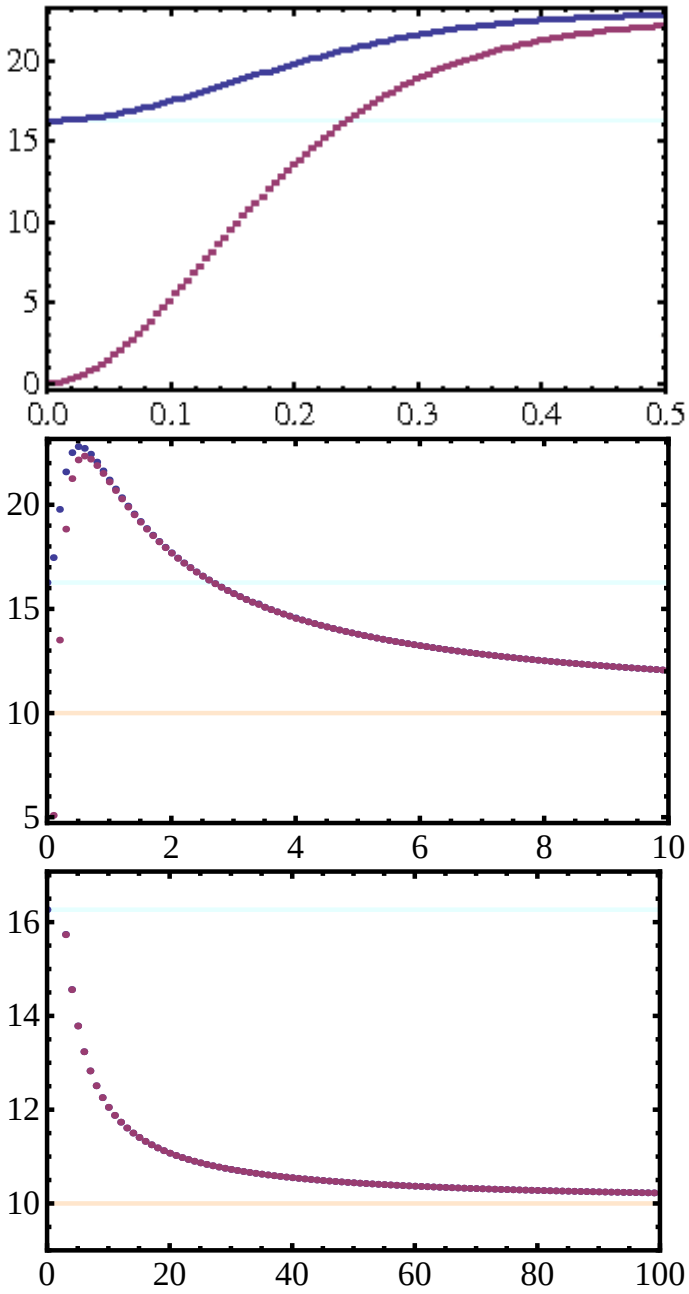

Figure C.2: $N = 10$. Fisher information (blue) and fisher-like measure N/ξ^2 obtained from the squeezing (purple) as a function of $r = K/\chi$ ($\chi = 1$) at $K_B T/\chi = 1.31$ ($T = 10^{-11}$K). Top panels: zoom at shorter $r = K/\chi$ scales. Blue gridline: Eq.(C.11) ($K = 0, \lambda = 0$). Orange gridline: Eq.(C.15) ($\chi = 0$).

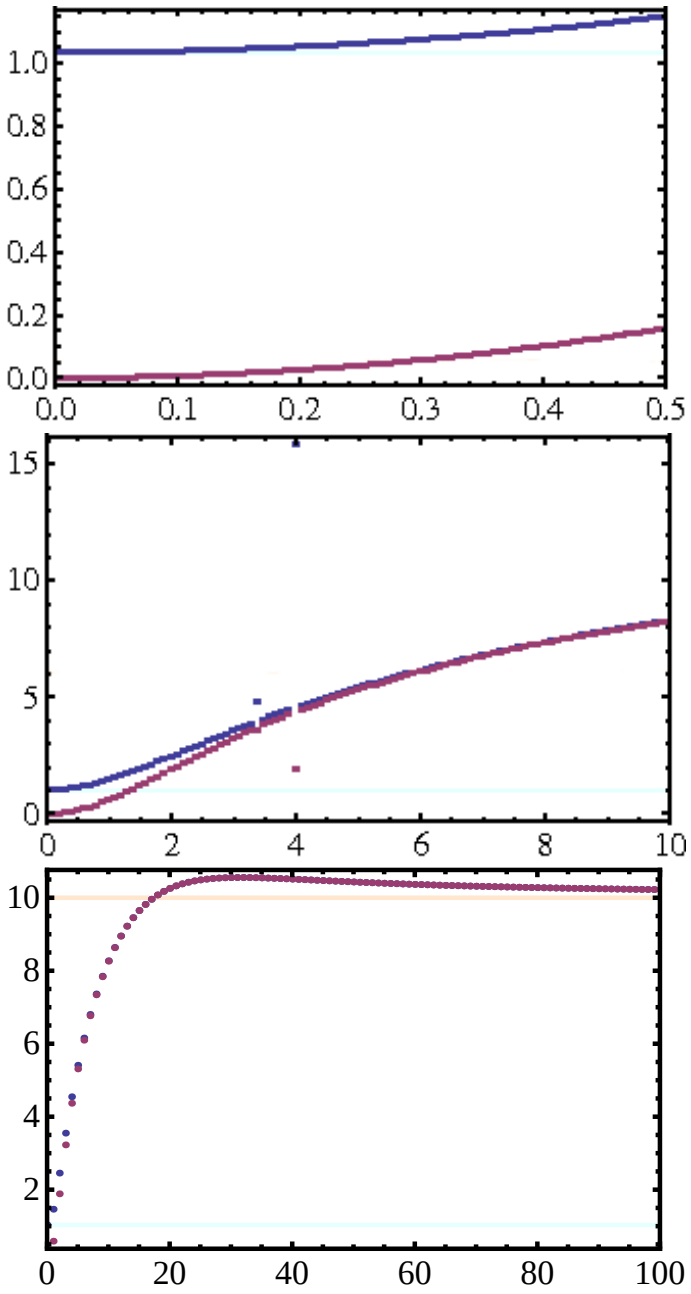

Figure C.3: $N = 10$. Fisher information (blue) and fisher-like measure N/ξ^2 obtained from the squeezing (purple) as a function of $r = K/\chi$ ($\chi = 1$) at $K_B T/\chi = 13.1$ ($T = 10^{-10}$K). Top panels: zoom at shorter $r = K/\chi$ scales. Blue gridline: Eq.(C.11) ($K = 0, \lambda = 0$). Orange gridline: Eq.(C.15) ($\chi = 0$).

Appendix D

Decoherence effects induced by phase noise

D.1 Partial suppression of phase noise by spin-echo pulses

In a recent experiment [8], phase noise was partially suppressed by a spin-echo protocol [154]. Let us assume that the state of interest (for instance, a squeezed state in [8]) is produced after an evolution time t under the Hamiltonian (5.1). In the spin-echo protocol, two short π-pulses are send by a laser in resonance with the energies of the two modes at times $t/2$ and t. The effect of these laser pulses is to reverse the direction of $\hat{J}_z$, mapped into $-\hat{J}_z$, in the evolution between $t/2$ and t. Since the noiseless part of the Hamiltonian (5.1) is quadratic in $\hat{J}_z$, it is not affected by the pulses, while the noise part is linear in $\hat{J}_z$ and is reversed after half of the evolution. This allows to suppress the effect of the noise if it is strongly correlated between the two time intervals $[0, t/2]$ and $[t/2, t]$, which appears to be the case in the experiment of Ref.[8] (see also [62]).

Our model in Sec.5.1.1.a can be easily adapted to take into account the residual effect of phase noise when the spin-echo pulses are applied. The derivation follows the same lines as in the main text. Eq.(5.10) still holds provided that we use $\phi(t) \equiv \int_0^t d\tau \, \mathrm{Sgn}(\tau - t/2)\lambda(\tau)$, with the sign function defined as $\mathrm{Sgn}(x) = \pm 1$ for $\pm x > 0$. This leads to

$$a^2_{\mathrm{echo}}(t) = \int_0^t d\tau \int_0^t d\tau' \, \mathrm{Sgn}(\tau - \frac{t}{2})\mathrm{Sgn}(\tau' - \frac{t}{2}) h(\tau - \tau'). \tag{D.1}$$

We focus on the short time regime $t < t_c$. The approximation $h(\tau) \simeq h(0)$ yields no contribution to $a^2_{\mathrm{echo}}(t)$. An expansion to second order is needed, $h(\tau) = h(0) + \tau h'(0) + \tau^2 h''(0)/2 + O(\tau^3)$. Using the parity $h(-\tau) = h(\tau)$ of the correlation function (which implies $h'(0) = 0$), we obtain

$$a^2_{\mathrm{echo}}(t) = -\frac{h''(0)}{16} t^4 \, . \tag{D.2}$$

Note that $a^2_{\mathrm{echo}}(t)$ is positive since $h''(0) < 0$. This follows from the fact that the correlation function h is of positive type and hence has a positive Fourier transform. Comparing Eqs. (D.2) and (5.12), one sees that the effect of the noise at times $t < t_c$ is considerably reduced with respect to the case in absence of spin echo.

D.2 Husimi distribution of a two-component macroscopic superposition in the presence of phase noise

In this Appendix we want to calculate the projected Husimi function $Q(\phi) \equiv Q(\theta = \pi/2, \phi)$ defined in Chap.3, for the two-component macroscopic superposition (2.26). Let us focus on the case N even. Due to Eq.(2.26) and (5.3), the density matrix of the two-component superposition formed in the presence of noise (assuming $\bar{\lambda} = 0$) is given by

$$\begin{aligned}\hat{\rho}(t_2) &= \frac{1}{2}\int_{-\infty}^{\infty} d\phi_0 f(\phi_0, t_2)\,(|\phi_0\rangle\langle\phi_0| + |\phi_0+\pi\rangle\langle\phi_0+\pi| \\ &\quad + c_0 c_1^* |\phi_0\rangle\langle\phi_0+\pi| + c_1 c_0^* |\phi_0+\pi\rangle\langle\phi_0|)\,, \end{aligned} \tag{D.3}$$

and naturally decomposes in a diagonal part $\hat{\rho}_{\rm d}$, in the sense of the components of the superposition, and an off-diagonal part $\hat{\rho}_{\rm od}$, as we have seen in Sec.5.1.3.a. As a consequence, the Husimi distribution can be expressed as

$$Q(\phi) = \langle\phi|\hat{\rho}_{\rm d}|\phi\rangle + \langle\phi|\hat{\rho}_{\rm od}|\phi\rangle. \tag{D.4}$$

From Eq.(1.31) we have $\langle\phi|\phi_0\rangle = e^{-i\frac{\phi-\phi_0}{2}}\cos^N\left(\frac{\phi-\phi_0}{2}\right)$ and $\langle\phi|\phi_0+\pi\rangle = e^{-i\frac{\phi-\phi_0}{2}}(i)^N\sin^N\left(\frac{\phi-\phi_0}{2}\right)$. Hence from Eqs.(D.3) and (5.9) we obtain for the diagonal contribution in Eq.(D.4)

$$\begin{aligned}\langle\phi|\hat{\rho}_{\rm d}|\phi\rangle &= |u_0|^2\frac{1}{\sqrt{2\pi}a_2}\int_{-\infty}^{\infty} d\phi_0 e^{-\frac{\phi_0^2}{2a_2^2}}(|\langle\phi|\phi_0\rangle|^2 + |\langle\phi|\phi_0+\pi\rangle|^2) \\ &= |u_0|^2\frac{1}{\sqrt{2\pi}}\int_{-\infty}^{\infty} dp e^{-\frac{p^2}{2}}\left(\cos^{2N}\left(\frac{\phi-pa_2}{2}\right) + \sin^{2N}\left(\frac{\phi-pa_2}{2}\right)\right), \end{aligned} \tag{D.5}$$

where we have defined $\phi_0 = pa_2$ and $a_2 \equiv a(t_2)$, $a(t)$ being the noise parameter defined in Eq.(5.7). The off-diagonal part of the superposition yields instead

$$\begin{aligned}\langle\phi|\hat{\rho}_{\rm od}|\phi\rangle &= |u_0|^2\frac{1}{\sqrt{2\pi}a_2}\int_{-\infty}^{\infty} d\phi_0 e^{-\frac{\phi_0^2}{2a_2^2}}(c_0 c_1^*\langle\phi|\phi_0\rangle\langle\phi_0+\pi|\phi\rangle + c_0^* c_1\langle\phi|\phi_0\rangle\langle\phi_0+\pi|\phi\rangle) \\ &= |u_0|^2(c_0 c_1^*\frac{(i)^N}{2^N} + c_0^* c_1\frac{(-i)^N}{2^N})\frac{1}{\sqrt{2\pi}}\int_{-\infty}^{\infty} dp e^{-\frac{p^2}{2}}\sin^N(\phi - pa_2) = 0, \end{aligned} \tag{D.6}$$

where we have used that, due to the particular expression of the coefficients c_k for the two-component superposition, $c_0 c_1^*(i)^N + c_0^* c_1(-i)^N = i(-1)^{N/2}(i)^N - i(-1)^{N/2}(-i)^N = i^{N+1}(1-(-1)^N) = 0$ (see the definition in Eq.(2.25)). Hence, in the case of the two-component phase cat state (2.26), the phase profile is given by the diagonal part of the density matrix only. From Eqs.(D.4), (D.5) and (D.6) we are then left with

$$Q(\phi) = |u_0|^2\frac{1}{\sqrt{2\pi}}\int_{-\infty}^{\infty} dp e^{-\frac{p^2}{2}}\left(\cos^{2N}\left(\frac{\phi-pa_2}{2}\right) + \sin^{2N}\left(\frac{\phi-pa_2}{2}\right)\right). \tag{D.7}$$

The function to be integrated $\cos^{2N}\left(\frac{\phi-pa_2}{2}\right)$ is $2\pi-$periodic and peaked around the value $\frac{\phi-pa_2}{2} = k\pi$, for k integer. Therefore, in the limit of large N we can consider the exponential as a constant function in an interval $-\frac{\pi}{2} + k\pi < \frac{\phi-pa_2}{2} < \frac{\pi}{2} + k\pi$ around the peak

(the regime of validity of this approximation is discussed in detail in Sec.D.2.1). Hence, setting $\frac{\phi-pa_2}{2}=j$, we can write

$$\begin{aligned}\int_{-\infty}^{\infty}dpe^{-\frac{p^2}{2}}\cos^{2N}\left(\frac{\phi-pa_2}{2}\right) &= \frac{2}{a_2}\int_{-\infty}^{\infty}dje^{-\left(\frac{2j-\phi}{a_2}\right)^2/2}\cos^{2N}j\\ &= \frac{2}{a_2}\sum_{k=-\infty}^{\infty}\int_{-\frac{\pi}{2}+k\pi}^{\frac{\pi}{2}+k\pi}dje^{-\left(\frac{2j-\phi}{a_2}\right)^2/2}\cos^{2N}j\\ &\simeq \frac{2}{a_2}\sum_{k=-\infty}^{\infty}e^{-\left(\frac{2k\pi-\phi}{a_2}\right)^2/2}\int_{-\frac{\pi}{2}+k\pi}^{\frac{\pi}{2}+k\pi}dj\cos^{2N}j\\ &= \frac{2}{a_2}\sum_{k=-\infty}^{\infty}e^{-\left(\frac{2k\pi-\phi}{a_2}\right)^2/2}I_1 \end{aligned} \tag{D.8}$$

where $I_1=\int_{\frac{-\pi}{2}}^{\frac{\pi}{2}}dj\cos^{2N}j=\sqrt{\pi}\frac{\Gamma(N+1/2)}{\Gamma(N+1)}$. Analogous considerations hold for the sine function $\sin^{2N}\left(\frac{\phi-pa_2}{2}\right)$, peaked at $\frac{\phi-pa_2}{2}=(2k+1)\frac{\pi}{2}$, yielding to

$$\begin{aligned}\int_{-\infty}^{\infty}dpe^{-\frac{p^2}{2}}\sin^{2N}\left(\frac{\phi-pa_2}{2}\right) &= \frac{2}{a_2}\sum_{k=-\infty}^{\infty}\int_{k\pi}^{k\pi+\pi}dje^{-\left(\frac{2j-\phi}{a_2}\right)^2/2}\sin^{2N}j\\ &\simeq \frac{2}{a_2}\sum_{k=-\infty}^{\infty}e^{-\left(\frac{(2k+1)\pi-\phi}{a_2}\right)^2/2}I_2 \end{aligned} \tag{D.9}$$

with $I_2=\int_{\frac{-\pi}{2}}^{\frac{\pi}{2}}dj\sin^{2N}j=\sqrt{\pi}\frac{\Gamma(N+1/2)}{\Gamma(N+1)}=I_1$. Substituting Eq.(D.8) and (D.9) in Eq.(D.7) gives

$$Q(\phi)=|u_0|^2\frac{\sqrt{2\pi}}{a_2}Q_{cost}\sum_{k=-\infty}^{+\infty}\left(e^{-\left(\frac{2k\pi-\phi}{a_2}\right)^2/2}+e^{-\left(\frac{(2k+1)\pi-\phi}{a_2}\right)^2/2}\right), \tag{D.10}$$

where we have introduced the Husimi function Q_{cost} corresponding to the uniform density matrix $\hat{\rho}_\infty=\frac{1}{2\pi}\int_0^{2\pi}d\phi|\phi\rangle\langle\phi|$ defined in Eq.(5.20),

$$Q_{cost}=\langle\phi|\hat{\rho}_\infty|\phi\rangle=\frac{1}{2\pi}\int_0^{2\pi}d\phi'\cos^{2N}(\phi-\phi')=\frac{1}{2\pi}\frac{2\sqrt{\pi}\Gamma\left(\frac{1}{2}+N\right)}{\Gamma\left(1+N\right)} \tag{D.11}$$

(in Eq.(D.11) we made use of the overlap formula $\langle\phi|\phi'\rangle=\left(\frac{1+e^{-i(\phi'-\phi)}}{2}\right)^N$). Finally, we remark that the two sums appearing in Eq.(D.10) can be expressed as a single sum over all the integers k, i.e.

$$\sum_{k=-\infty}^{+\infty}\left(e^{-\left(\frac{2k\pi-\phi}{a_2}\right)^2/2}+e^{-\left(\frac{(2k+1)\pi-\phi}{a_2}\right)^2/2}\right)=\sum_{k=-\infty}^{+\infty}e^{-\left(\frac{k\pi-\phi}{a_2}\right)^2/2}=\Theta_3\left(-\phi,e^{-2a_2^2}\right), \tag{D.12}$$

where Θ_3 is the Theta function defined as $\Theta_3(u,q)=1+2\sum_{n=1}^{\infty}q^{n^2}\cos(2nu)$ [156]. Substituting Eq.(D.12) in Eq.(D.10), and noticing that $|u_0|^2=1/2$, finally yields expression (5.21) of the main text for the projected Husimi distribution of the two-component phase cat state.

D.2.1 Regime of validity of the approximation

We want now to discuss when the approximation that we have done to derive Eq.(D.8) is valid, i.e. where we are allowed to identify

$$\int_{-\frac{\pi}{2}}^{\frac{\pi}{2}} dj e^{-\left(\frac{2j-\phi}{a_2}\right)^2/2} \cos^{2N} j \simeq e^{-\left(\frac{\phi}{a_2}\right)^2/2} \int_{-\frac{\pi}{2}}^{\frac{\pi}{2}} dj \cos^{2N} j, \tag{D.13}$$

considering as constant the exponetial function in the interval. First, we note that since the cosine function is strongly peaked for large N, we have to assume this fact only in the interval in which the cosine is well above zero. We can take such an interval to be the width at half amplitude of the cosine function in the variable j around each peak, defined by the condition

$$\cos^N j = \left(1 - \frac{j^2}{2} + o(j^4)\right)^N \simeq e^{N \ln\left(1-\frac{j^2}{2}\right)} \sim e^{-N\frac{j^2}{2}} \equiv \frac{1}{2}, \tag{D.14}$$

from which we derive $j = \sqrt{\frac{2\ln 2}{N}} \sim \frac{1}{\sqrt{N}}$. Now, in integrals of the kind $\frac{2}{a}\int_{-\infty}^{\infty} dj e^{-\left(\frac{2j-\phi}{a}\right)^2/2} \cos^{2N} j$, the exponential function can be considered constant in the region $-\frac{1}{\sqrt{N}} < j < \frac{1}{\sqrt{N}}$ if the condition

$$a \ll \frac{1}{\sqrt{N}} \tag{D.15}$$

is satisfied. At the same time, we want $e^{-\left(\frac{2j-\phi}{a}\right)^2/2} = e^{-\frac{2j^2}{a^2}} e^{-\frac{\phi^2}{a^2}} e^{\frac{2j\phi}{a^2}} \sim e^{-\frac{\phi^2}{a^2}}$, which is true if $|2j(\phi - j)| \ll a^2$. Since we want this condition to hold for each ϕ, we have to choose the strongest version $j \ll a^2$, which in the interval of interest implies

$$a^2 \gg \frac{1}{\sqrt{N}}. \tag{D.16}$$

Condition (D.16), together with the condition Eq.(D.15), yields as a regime in which we expect our approximation to be valid the range of noise correlations $N^{-1/4} \ll a \ll N^{-1/2}$.

D.3 Squeezing as a function of the angle under the action of phase noise

As we have seen in Sec.5.1.4, during the quenched dynamics of the BJJ, possibly in the presence of phase noise, squeezed states are developed at short times. The squeezing degree and the direction of optimum squeezing vary with time. Stimulated by the measurements reported in Refs.[8, 9] from the definition (2.6) we can compute the spin squeezing parameter as a function of the direction, parametrized by the angle θ, at fixed time. As demonstrated in Appendix B.1, the direction of squeezing is contained in the plane (yOz), and we have $\mathrm{tr}\left[\hat{\rho}\hat{J}_z\right] = \mathrm{tr}\left[\hat{\rho}\hat{J}_y\right] = 0$. Hence, using the definition 4.40 for the angle θ, the squeezing degree as a function of the angle is given by

$$\xi^2(t) = 4\frac{\left(\Delta\hat{J}_n(\theta)\right)^2}{N\nu(t)}, \tag{D.17}$$

where the visibility $\nu(t)$ is given in Eq.(5.14), and $\left(\Delta\hat{J}_n(\theta)\right)^2$ are the fluctuations of the collective angular momentum operator in the direction θ. The latter can be calculated as

$$\begin{aligned}\left(\Delta\hat{J}_n(\theta)\right)^2 &= \left[\sin^2\theta\mathrm{tr}\left[\hat{\rho}\hat{J}_y^2\right]+\cos^2\theta\mathrm{tr}\left[\hat{\rho}\hat{J}_z^2\right]-\cos\theta\sin\theta\mathrm{tr}\left[\hat{\rho}\hat{J}_y\hat{J}_z+\hat{\rho}\hat{J}_z\hat{J}_y\right]\right]\\ &= \left[-\frac{\cos 2\theta}{2}(\mathrm{tr}\left[\hat{\rho}\hat{J}_y^2\right]-\mathrm{tr}\left[\hat{\rho}\hat{J}_z^2\right])-\frac{\sin 2\theta}{2}\mathrm{tr}\left[\hat{\rho}\left\{\hat{J}_y,\hat{J}_z\right\}\right]+\frac{\mathrm{tr}\left[\hat{\rho}\hat{J}_y^2\right]+\mathrm{tr}\left[\hat{\rho}\hat{J}_z^2\right]}{2}\right]\\ &= -\left(\frac{\tilde{A}}{2}\cos 2\theta+\frac{\tilde{B}}{2}\sin 2\theta\right)+\frac{C}{2}\\ &= \frac{C}{2}-\frac{\sqrt{\tilde{A}^2+\tilde{B}^2}}{2}\cos\left(2(\theta-\delta)\right)\end{aligned} \tag{D.18}$$

where we defined

$$\begin{aligned}\tilde{A} &= (\mathrm{tr}\left[\hat{\rho}\hat{J}_y^2\right]-\mathrm{tr}\left[\hat{\rho}\hat{J}_z^2\right])=G'_{yy}-G'_{zz}=\frac{N(N-1)A}{8}\\ \tilde{B} &= \mathrm{tr}\left[\hat{\rho}\left\{\hat{J}_y,\hat{J}_z\right\}\right]=G'_{yz}+G'_{zy}=\frac{N(N-1)B}{8}\\ C &= \mathrm{tr}\left[\hat{\rho}\hat{J}_z^2\right]+\mathrm{tr}\left[\hat{\rho}\hat{J}_y^2\right]=G'_{yy}+G'_{zz}\\ \delta &= \frac{1}{2}\arctan\frac{\tilde{B}}{\tilde{A}},\end{aligned} \tag{D.19}$$

G' being the fluctuation matrix given in Eq.(5.27). The last step is demonstrated using that $\cos 2(\theta-\delta)=\cos 2\theta\cos 2\delta+\sin 2\theta\sin 2\delta=(\tilde{A}\cos 2\alpha+\tilde{B}\sin 2\theta)/\sqrt{\tilde{A}^2+\tilde{B}^2}$; the quantities A, B and δ have been previously defined in Ref.[11].

The spin squeezing as a function of the angle θ at various noise levels is represented in Fig.D.1. We see that the presence of phase noise shifts the position of the minimum with respect to the noisless case, and increases the value of the minimum squeezing reached, as can be expected. The analytical calculation of the correction of the minimum value reached by the squeezing in the presence of noise for a large number of particles can be found in Ref.[25].

The issue of a direct comparison of Eq.(D.18) with the experimental results presented in Refs.[8, 9] is discussed in Sec.6.2.2.

D.4 Decoherence of a NOON state and a phase cat state under phase noise

In this section, we analyze the decoherence process to which a NOON state and a phase cat state undergo when the two states, taken as initial states, are subjected to phase noise only, with no other additional dynamics; i.e, we consider as initial state $|\psi(0)\rangle$ the two states

$$\begin{aligned}|\psi_{\mathrm{PHASE}_\beta}\rangle &= \frac{1}{\sqrt{2}}(|\phi=0\rangle+e^{i\beta}|\phi=\pi\rangle)\\ |\psi_{\mathrm{NOON}_\beta}\rangle &= \frac{1}{\sqrt{2}}(|N,0\rangle+e^{i\beta}|0,N\rangle),\end{aligned} \tag{D.20}$$

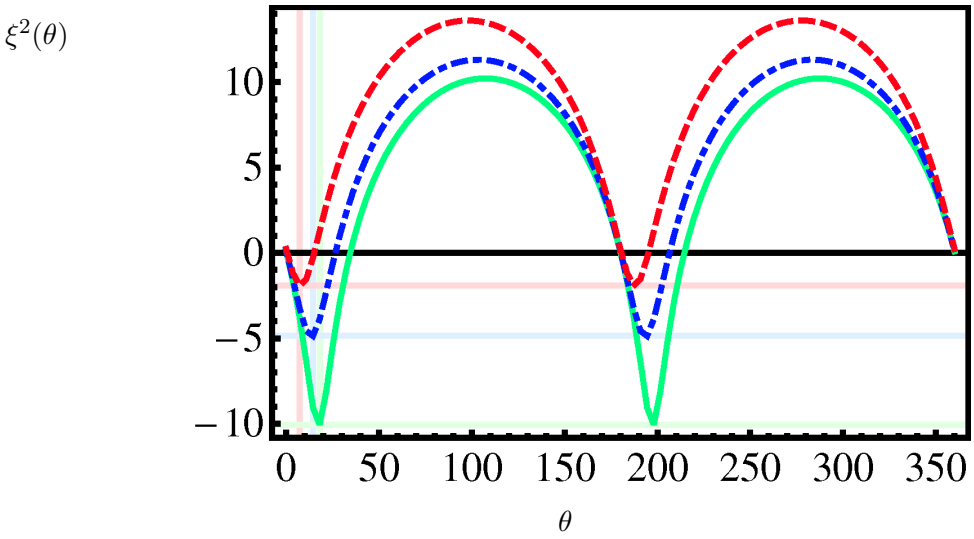

Figure D.1: Coherent spin squeezing as a function of the angle θ at $t = 18$ms. Solid green line: $\delta\lambda = 0$; blue dotdashed line: $\delta\lambda = 5$Hz; red dashed line: $\delta\lambda = 10$Hz. Here we have considered values of the parameters close to the experimental ones: $N = 400$, $\chi = 0.13\pi$.

and we assume that they are evolving under the action of the Hamiltonian $H = -\lambda(t)\hat{J}_z$, where $\lambda(t)$ is a stochastic process (we will assume here for simplicity that $\overline{\lambda} = 0$). Everything goes exaclty as in Sec.5.1 with the setting $H^{(0)} = 0$, which implies in particular that Eq.(5.10) for the system density matrix as a function of time is still valid, with $\hat{\rho}^{(0)}(t) = \hat{\rho}(0)$, i.e.

$$\langle n|\hat{\rho}(t)|n'\rangle = e^{-\frac{a^2(t)(n-n')^2}{2}}\langle n|\hat{\rho}(0)|n'\rangle. \tag{D.21}$$

Let us first discuss the case of an initial phase cat state. The structure of the density matrix $\hat{\rho}(0)$ of macroscopic superpositions of phase states has been analyzed in detail in Sec.5.1.3.a. In particular, decomposing the initial density matrix into its diagonal and off-diagonal parts $\hat{\rho}(0) = \hat{\rho}_{\rm d}(0) + \hat{\rho}_{\rm od}(0)$, from Eq.(5.17) we have shown that the elements in $\hat{\rho}_{\rm d}(0)$ which are the less affected by the noise are placed at $n' = n + 2$ for the case of a two component superposition of phase states ($q = 2$), such as the one given in the first line of Eq.(D.20). Hence, they are dumped by a factor $e^{-2a^2(t)}$. For the off-diagonal part $\hat{\rho}_{\rm od}(0)$ given in Eq.(5.18), instead, the first non-zero elements out of the diagonal are placed at $n' = n + 1$, yielding an effective decoherence factor of $e^{-\frac{a^2(t)}{2}}$, inferior (but of the same order of magnitude) to the one for relaxation, and independent on N.

For the case of an initial NOON state (second line of Eq.(D.20)), Eq.(D.21) is still valid, but the structure of the initial density matrix $\hat{\rho}(0)$ is dramatically different with respect to the case of a phase cat state. Indeed, separating the diagonal and off-diagonal parts of the density matrix in same way as we have done for the two-component phase cat state yields to the identifications

$$\begin{aligned}\hat{\rho}_{\rm d}(0) &= \frac{1}{2}(|0,N\rangle\langle 0,N| + |N,0\rangle\langle N,0|)\\ \hat{\rho}_{\rm od}(0) &= \frac{1}{2}(e^{i\beta}|0,N\rangle\langle N,0| + e^{-i\beta}|N,0\rangle\langle 0,N|).\end{aligned} \tag{D.22}$$

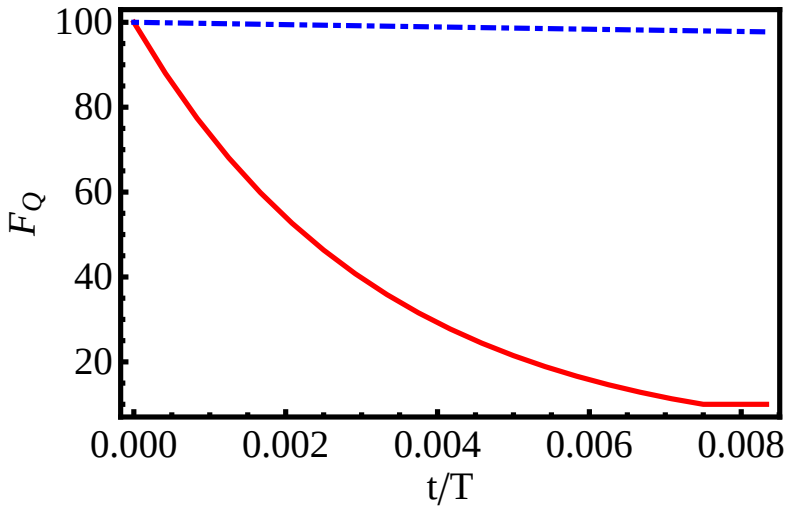

Figure D.2: Optimum quantum Fisher information as a function of time for an initial NOON state (red solid line) and an initial phase cat state (blue dot-dashed line). In the former case the decay is exponential, with a rate equal to $a^2(t)N^2$, while in the latter case the decay is slower. The saturation of F_Q to the value $N = 10$ for the NOON state is due to the fact that we are calculating here the optimized quantum Fisher information: when all the coherences of the initial NOON state are lost, we are left with a statistical mixture of two coherent states (see first line in Eq.(D.22)), the optimum Fisher information of which is N. We have taken here $a^2(t) = 2ct$, where $c = \int_0^\infty h(y)dy$, defined in the markov regime of Eq.(5.13).

Thus, from Eq.(D.21) we easily obtain

$$\begin{aligned}\langle n|\hat{\rho}(t)|n'\rangle &= \frac{1}{2}e^{-\frac{a^2(t)(n-n')^2}{2}}\left[(\delta_{n,\frac{N}{2}}\delta_{n',\frac{N}{2}}+\delta_{n,-\frac{N}{2}}\delta_{n',-\frac{N}{2}})+(e^{i\beta}\delta_{n,\frac{N}{2}}\delta_{n',-\frac{N}{2}}+e^{i\beta}\delta_{n,-\frac{N}{2}}\delta_{n',\frac{N}{2}})\right]\\ &= \langle n|\hat{\rho}_{\rm d}(0)|n'\rangle + e^{-\frac{a^2(t)N^2}{2}}\langle n|\hat{\rho}_{\rm od}(0)|n'\rangle. \qquad \text{(D.23)}\end{aligned}$$

From Eq.(D.23) we see that the coherences of the NOON state are lost with a rate $a^2(t)N^2/2$, proportional to the number of particles, while the diagonal part of the superposition is not affected by the phase noise - a purely dephasing process for the such a cat state. This situation is in apparent contrast with the case of the two-component phase cat states.

As we have discussed in Sec.5.1, the difference between the two situations can be ascribed to the fact that phase noise acts perpendicularly with respect to the plane in which the two-component phase cat state is contained - the equatorial plane, and hence is insensitive to the separation between its components. This separation is instead resolved in the case of a NOON cat state, as its components are placed along the z-direction, to which the noise couples.

As a consequence of the fact that the coherences of the NOON state decay exponentially in time under the effect of phase noise (Eq.(D.23)), the optimum quantum Fisher information also decays exponentially for such an initial state, with a rate equal to $a^2(t)N^2$. Instead, the decay is slower in the case of an initial phase cat state. This fact can be visualized in Fig.D.2.

Appendix E

Decoherence effects induced by particle losses

E.1 Solution of the Master equation by the characteristic method

In this section, we provide a solution of the linear partial differential equation of the first order Eq.(5.41) by means of the methods of the characteristic, as given in Ref.[162].

Let us define the characteristic function $F(s) = \tilde{h_p^r}(x(s), y(s), t(s))$, depending on a parameter s. The condition for its first derivative to be zero $F'(s) = 0$ translates in terms of the function $\tilde{h_p^r}$ into

$$\partial_t \tilde{h_p^r} = \frac{\partial \tilde{h_p^r}}{\partial x}\frac{\partial x}{\partial s} + \frac{\partial \tilde{h_p^r}}{\partial y}\frac{\partial y}{\partial s}, \tag{E.1}$$

given the choice $\partial_t/\partial_s = -1$, or equivalently $t = t_0 - s$, where $t_0 = t(s = 0)$. The identification of the coefficients in Eqs.(E.1) and (5.41) provides the set of equations

$$\begin{cases} \frac{\partial x}{\partial s} = -\zeta_1 x + 2\gamma \\ \frac{\partial y}{\partial s} = -\zeta_2 x + 2\gamma \end{cases} \tag{E.2}$$

which has solution

$$\begin{cases} x(s) = \frac{2\gamma}{\zeta_1} + \left(x_0 - \frac{2\gamma}{\zeta_1}\right) e^{-\zeta_1 s} \\ y(s) = \frac{2\gamma}{\zeta_2} + \left(y_0 - \frac{2\gamma}{\zeta_2}\right) e^{-\zeta_2 s} \end{cases} \tag{E.3}$$

where we have set $x(s = 0) = x_0$ and $y(s = 0) = y_0$. By definition, the function $F(s)$ is constant along the curve (E.3). Hence

$$\tilde{h_p^r}(x_0, y_0, t_0) = \tilde{h_p^r}(x(t_0), y(t_0), 0). \tag{E.4}$$

The last term expresses the initial condition (5.34) in terms of the generating function (5.36), which reads

$$\tilde{h_p^r}(x, y, 0) = \frac{1}{2^N}\frac{N!}{(N-r)}(x+y)^{(N-r)}\delta_{r,p} = h_p^r(x, y, 0). \tag{E.5}$$

Substituting the curves (E.3) in Eq.(E.5) according to the prescription (E.4), with the redefinition $(x_0, y_0, t_0) \to (x, y, t)$, gives Eq.(5.42) of the main text.

E.2 Full Husimi function for cat states in the presence of particle losses

In analogy to the definitions in Sec.5.2.5.b, we define the full Husimi function for each of the density matrices in the various m-particle subspaces as

$$Q_m(\theta,\phi) \equiv {}_m\langle\theta,\phi|\bar{\rho}_m|\theta,\phi\rangle_m, \tag{E.6}$$

satisfying the normalization condition $\frac{1}{4\pi}\int d\Omega Q_m(\theta,\phi) = 1$. The total Husimi function is

$$Q(\theta,\phi) = \sum_{m=0}^{N} w_m Q_m(\theta,\phi). \tag{E.7}$$

The Husimi function at time t_2 for $\gamma T_{even} = 0.25$ is represented in Fig. E.1. The first panel corresponds to the Husimi function of the block $m = N$ of the density matrix, coinciding with that of a perfect superposition of two coherent states with N particles formed in the absence of losses. The other panels represent the Husimi function corresponding to the blocks $m = N-1$ and $m = N-2$, according to Eq.(E.6). The last panel is the total Husimi function defined in Eq.(E.7), which is still displaying a two-peak structure. A discussion qualitatively similar to the case of the Husimi distribution projected on $\theta = \pi/2$ presented in Sec. 5.2.5.b can be put in advance. Note that the total Husimi function in the presence of losses (forth panel of Fig. E.1) is more spread in the θ direction than the corresponding Husimi function in the lossless case, represented in the first panel (see color scale). This is due to the fact that the number imbalance is not conserved by the lossy quenched dynamics of the BJJ, contrarily to the lossless case.

E.3 Decoherence of a NOON state and a phase cat state under particle losses

In this section we analyze the decoherence of a phase cat state and a NOON state (Eq.(D.20)) when such states are taken as initial states, and are later subjected to particle losses only with no other additional (unitary) dynamics, as we have done in Sec.D.4 for phase noise. In particular, we are interested in the question whether the two states share the same decoherence rate or not. To do so, we first present the solution of the master equation in the presence of one-body losses, following the lines of Sec.5.2.2. This allows us to calculate the decay of the quantum Fisher information. Then, we provide a calculation (for the NOON state only) based on the technique of quantum jumps, to directly access the decay of the off-diagonal part of the density matrix.

E.3.1 Solution of the master equation by the method of the characteristics

We proceed by solving the master equation (5.31) with $H^{(0)} = 0$. The initial condition can be derived from Eq.(D.20) with the use of the expansion Eq.(1.28), in which by setting $k = n + N/2$ the sum involved can be rescaled as $|\theta,\phi\rangle = (1+|\alpha|^2)^{-\frac{N}{2}} \sum_{k=0}^{N} \binom{N}{k}^{\frac{1}{2}} \alpha^k |k; N-k\rangle$,

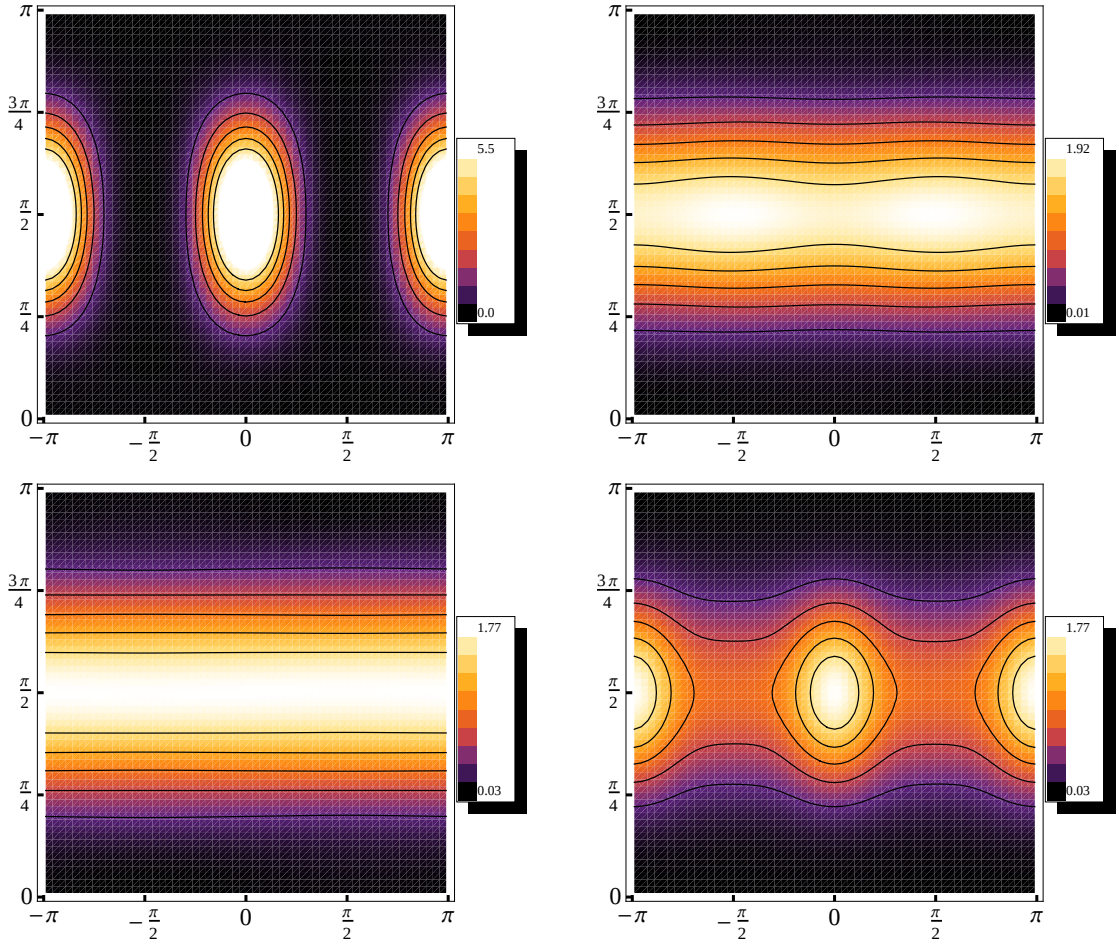

Figure E.1: First three panels: Husimi distribution $Q_m(\theta,\phi)$ (see Eq.(E.6)) at $t=t_2$ for $m=10,9,8$ respectively. Last panel: Husimi distribution $Q(\theta,\phi)$ (see Eq.(E.7)) at $t=t_2$. Value of the parameters: $N=10$, $\gamma T_{even}=0.25$, $U_1=U_2=4\pi$Hz, $t=t_2$.

and read respectively

$$\begin{aligned}
\rho_1{}^{k+r,l}_{k,l+p}(0) &= \frac{1}{2}\frac{1}{2^N}\binom{N}{k}^{\frac{1}{2}}\binom{N}{k+r}^{\frac{1}{2}}[1+(-1)^r+e^{i\beta}(-1)^k+e^{-i\beta}(-1)^{k+r}]\delta_{r,p}\delta_{k+r+l,N}\\
\rho_2{}^{k+r,l}_{k,l+p}(0) &= \frac{1}{2}[\delta_{k,N}\delta_{r,0}+\delta_{k,0}\delta_{r,0}+e^{i\beta}\delta_{k,0}\delta_{r,N}+e^{-i\beta}\delta_{k,N}\delta_{r,-N}]\delta_{r,p}\delta_{k+r+l,N}. \qquad \text{(E.8)}
\end{aligned}$$

The generating functions h_1 and h_2 corresponding to the two different initial states can still be defined as in Eq.(5.36), and they both satisfy Eq.(5.38) with $E_1=E_2=U_1=U_2=0$. Hence, the solution is provided by Eq.(E.3) in the absence of unitary terms, i.e.

$$\begin{cases} x(s) = 1+(x_0-1)\,e^{-2\gamma s} \\ y(s) = 1+(y_0-1)\,e^{-2\gamma s} \end{cases} \qquad \text{(E.9)}$$

where we have used the same definition of $\tilde{h_{1,2}}{}^r_p$ as in Sec.5.2.2, with $c(r,p,t)=\gamma(r+p)$. The initial condition in terms of such generating functions is obtained with the use of

Eq.(E.8) and (5.36), and reads

$$
\begin{aligned}
h_{1_p}^r(x,y,0) &= \frac{1}{2}\frac{1}{2^N}\frac{N!}{(N-r)}\left[(1+(-1)^r)(x+y)^{(N-r)}+(e^{i\beta}+e^{-i\beta}(-1)^r)(-x+y)^{(N-r)}\right]\delta_{r,p} \\
h_{2_p}^r(x,y,0) &= \frac{1}{2}(x^N\delta_{r,0}+y^N\delta_{r,0}+N!e^{i\beta}\delta_{r,N}+\frac{e^{-i\beta}}{N!}x^N y^N\delta_{r,-N})\delta_{r,p}. \qquad \text{(E.10)}
\end{aligned}
$$

Following the line of Sec.E.1, and in particular with the use of Eq.(E.4), we obtain as solutions

$$
\begin{aligned}
h_{1_p}^r(x,y,t) &= e^{-2\gamma r t}\frac{1}{2^{(N+1)}}\frac{N!}{(N-r)!}\Big[(1+(-1)^r)\left(2+(x-1)e^{-2\gamma t}+(y-1)e^{-2\gamma t}\right)^{(N-r)} \\
&+ (e^{i\beta}+e^{-i\beta}(-1)^r)e^{-2\gamma(N-r)t}(-x+y)^{(N-r)}\Big]\delta_{r,p} \\
h_{2_p}^r(x,y,t) &= e^{-2\gamma r t}\frac{1}{2}\left[(1+(x-1)e^{-2\gamma t})^N\delta_{r,0}+(1+(y-1)e^{-2\gamma t})^N\delta_{r,0}\right. \\
&+ \left. N!e^{i\beta}\delta_{r,N}+\frac{e^{-i\beta}}{N!}(1+(x-1)e^{-2\gamma t})^N(1+(y-1)e^{-2\gamma t})^N\delta_{r,-N}\right]\delta_{r,p} \qquad \text{(E.11)}
\end{aligned}
$$

Using the definition (5.37), from Eq.(E.11) we obtain the solution for the density matrix of the two states as a function of time

$$
\begin{aligned}
\hat{\rho_1}_{k,l+p}^{k+r,l} &= \frac{N!e^{-2\gamma r t}}{2^{(N+1)}(N-r-k-l)!(k!l!(k+r)!(l+r)!)^{\frac{1}{2}}} \\
&\times \Big[(1+(-1)^r)e^{-2\gamma t(l+k)}2^{N-r-l-k}(1-e^{-2\gamma t})^{N-r-l-k} \\
&+ (e^{i\beta}+e^{-i\beta}(-1)^r)e^{-2\gamma(N-r)t}(-1)^k\delta_{N,r+l+k}\Big]\delta_{r,p} \\
\hat{\rho_2}_{k,l+p}^{k+r,l} &= \frac{N!e^{-2\gamma r t}}{2(k!l!(k+r)!(l+r)!)^{\frac{1}{2}}} \\
&\times \left[\frac{e^{-2\gamma k t}}{(N-k)!}(1-e^{-2\gamma t})^{(N-k)}\delta_{r,0}\delta_{l,0}+\frac{e^{-2\gamma l t}}{(N-l)!}(1-e^{-2\gamma t})^{(N-l)}\delta_{r,0}\delta_{k,0}\right. \\
&+ \left. e^{i\beta}\delta_{r,N}\delta_{l,0}\delta_{k,0}+e^{-i\beta}\frac{(1-e^{-2\gamma t})^{(2N-k-l)}e^{-2\gamma(l+k)t}}{(N-l)!(N-k)!}\delta_{r,-N}\right]\delta_{r,p}. \qquad \text{(E.12)}
\end{aligned}
$$

Thanks to the exact solution (E.12) for the density matrix of an initial noon state and an initial phase state in the presence of one-body losses, we can calculate the optimum quantum Fisher information as a function of time. This is shown in Fig.E.2, where we see that for both initial states the quantum Fisher information decays exponentially, with a rate $4\gamma N$, thus depending on the initial number of particles. Note that this result is different with respect to what we had found in Sec.D.4 for the case of phase noise, where for the phase cat state the decay of the quantum Fisher information was much slower than the for the NOON state.

E.3.2 Decoherence of a NOON state via the method of quantum jumps

As we have presented in Secs.5.1 and D.4 for the case of phase noise, the decay of the useful quantum correlations of a macroscopic superposition under the effect of noise can be related to the decay of the off-diagonal part of its density matrix, in the sense of the

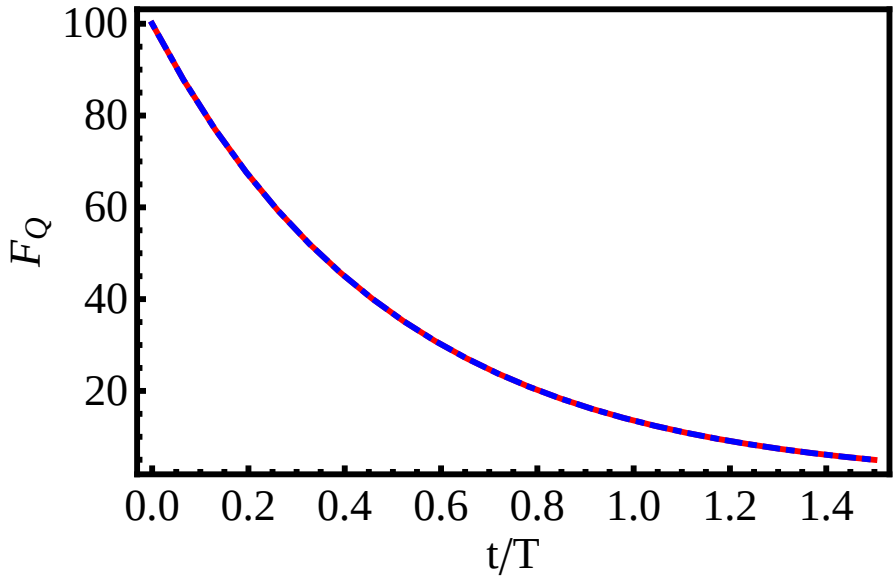

Figure E.2: Optimum quantum Fisher information (5.55) as a function of time, for an initial NOON state (red solid curve) and an initial phase cat state (blue dot-dashed curve) subjected to one-body particle losses. The two curves are superposed.

components of the superposition - the coherences of the superposition (see e.g. Eq.(D.23)). Unfortunately, in the exact solutions (E.12) for the density matrix of an initial noon state and an initial phase state in the presence of one-body losses, such diagonal and off-diagonal contributions are not easily recognizeable.

However, in the case of a NOON state we can easily derive the decay of the off-diagonal part of the density matrix by means of a *quantum jumps* approach [135, 174]. In this framework, the effective Hamiltonian accounting for the dissipative dynamics corresponding to the master equation (5.31) (with $H^{(0)} = 0$) is defined as

$$H_{\rm eff} = -i\gamma \sum_{i=1}^{2} \hat{a}_i^\dagger \hat{a}_i, \tag{E.13}$$

and the state of the system evolves along each *trajectory* - corresponding to a single realization the stochastic loss process - according to the following prescription:

$$|\psi(t)\rangle = \begin{cases} |\psi_{nj}(t)\rangle = \frac{e^{-itH_{\rm eff}}|\psi(0)\rangle}{\|e^{-itH_{\rm eff}}|\psi(0)\rangle\|} = |\psi(0)\rangle \quad \text{if no jump is occurred} \\ \\ |N-1,0\rangle \qquad \text{if a jump is occurred on the site i = 1} \\ |0,N-1\rangle \qquad \text{if a jump is occurred on the site i = 2.} \end{cases} \tag{E.14}$$

The first line of Eq.(E.14) can be easily verified by direct calculation of the action of the effective Hamiltonian (E.13) on the NOON state in Eq.(D.20), i.e. $H_{\rm eff}|\psi(0)\rangle = -i\gamma(\hat{n}_1+\hat{n}_2)\frac{1}{\sqrt{2}}(|N,0\rangle + e^{i\beta}|0,N\rangle) = -i\gamma N|\psi(0)\rangle$, which implies

$$e^{-itH_{\rm eff}}|\psi(0)\rangle = e^{-\gamma N t}|\psi(0)\rangle, \tag{E.15}$$

leading to the first line in Eq.(E.14).

From Eq.(E.14) we see that the trajectories in which at least one jump has occurred in the time interval $[0,t]$ lead to a mixture of Fock states $\hat{\rho}_{\rm mixt}$, while only the trajectory in which no jump occurred in $[0,t]$ keeps trace of the coherences of the initial superposition, i.e.

$$\hat{\rho}(t) = P_{nj}([0,t])|\psi(0)\rangle\langle\psi(0)| + \hat{\rho}_{\rm mixt}, \tag{E.16}$$

where $P_{nj}([0,t])$ is the probability that no jumps occurred between the time 0 and t. In order to evaluate the rate at which the coherence of the superposition is lost, we have thus to calculate $P_{nj}([0,t])$. This probability satisfies the equation

$$P_{nj}([0,t]) - P_{nj}([0,t+dt]) = \sum_{i=1,2} dp_i(t) P_{nj}([0,t]), \tag{E.17}$$

where $dp_i(t)$ is the probability that a jump occurs at site i in a time interval $[t,t+dt]$, which we assume to be symmetric (i.e. $dp_1(t) = dp_2(t) \equiv dp(t)$). The latter probability is given by [174]

$$dp(t) = 2\gamma \|\hat{a}_i|\psi_{nj}(t)\rangle\|^2 dt, \tag{E.18}$$

where $|\psi_{nj}(t)\rangle$ is defined in Eq.(E.14). Deviding each member of Eq.(E.17) by $dtP_{nj}([0,t])$ we obtain

$$-\frac{d\ln P_{nj}([0,t])}{dt} = 2\frac{dp(t)}{dt}. \tag{E.19}$$

From a direct calculation, using that $H_{\rm eff}^\dagger = -H_{\rm eff}$, we obtain that

$$\begin{aligned}
\frac{d}{dt}\ln\|e^{-itH_{\rm eff}}|\psi(0)\rangle\|^2 = & \quad \frac{d}{dt}\ln\langle\psi(0)|e^{-i2tH_{\rm eff}}|\psi(0)\rangle \\
= & \quad \frac{-2i\langle\psi(0)|e^{-itH_{\rm eff}}H_{\rm eff}e^{-itH_{\rm eff}}|\psi(0)}{\|e^{-itH_{\rm eff}}|\psi(0)\rangle\|^2} \\
= & \quad \frac{-2i\|e^{-itH_{\rm eff}}|\psi(0)\rangle\|^2\langle\psi_{nj}(t)|H_{\rm eff}|\psi_{nj}(t)\rangle}{\|e^{-itH_{\rm eff}}|\psi(0)\rangle\|^2} \\
= & \quad -2i\langle\psi_{nj}(t)|H_{\rm eff}|\psi_{nj}(t)\rangle \\
= & \quad -2\gamma\sum_{i=1}^{2}\|\hat{a}_i|\psi_{nj}(t)\rangle\|^2 = -\frac{2dp}{dt}
\end{aligned} \tag{E.20}$$

where we have made use of the first line of Eq.(E.14), of the definition (E.13), and of Eq.(E.18). By comparing Eqs.(E.19) and (E.20) we can finally make the identification

$$P_{nj}([0,t]) = \|e^{-itH_{\rm eff}}|\psi(0)\rangle\|^2 = e^{-2\gamma Nt}, \tag{E.21}$$

where in the last step we have used Eq.(E.15). From Eq.(E.21) we see that the coherences of the superposition are lost at a rate $2\gamma N$, directly related to the exponential decay of the Fisher information presented in Fig.(E.2). Incidentally, we remark that the fidelity of the system density matrix during the quenched dynamics leading to the formation of cat states in the presence of losses with the state formed in the absence of losses decays with the same rate (see Eq.(5.52)).

The calculation may be repeated for the phase cat state, yielding the same final result. In Ref.[159] the decoherence rate for the case of three-body losses has been calculated, and turns out to be $\propto \gamma^{(3)}N^3$. We expect by analogy a decoherence rate $\propto \gamma^{(2)}N^2$ for a cat state in the presence of two-body losses.

E.4 Solution for two body losses

An analytical solution of the master equation (5.30) for the quenched dynamics in the presence of two- and three-body losses is also available [163]. Here we do not provide that derivation, but we apply the solution found in case of two-body losses to the calculation of various quantities characterizing the state of the system at the time of formation of the two-component macroscopic superposition, analogously to what we have done in Sec. 5.2.5 for the case of one-body losses. These are the fidelity with the two-component superposition (Fig. E.4), the projected Husimi distribution (Fig. E.5), the full Husimi distribution (Fig. E.6) and the optimum quantum Fisher information as a function of time (Fig. E.7).

Similarly to the case of one-body losses, coherences between states at different number of particles are forbidden. As a consequence, the density matrix in the Fock basis displays a block structure, as can be seen in Fig. E.3. In the present case, though, the Hilbert space accessible to the system only comprehends subspaces at m sharing the same parity as the initial number of particles N. This fact is clearly visualized in Fig. E.3.

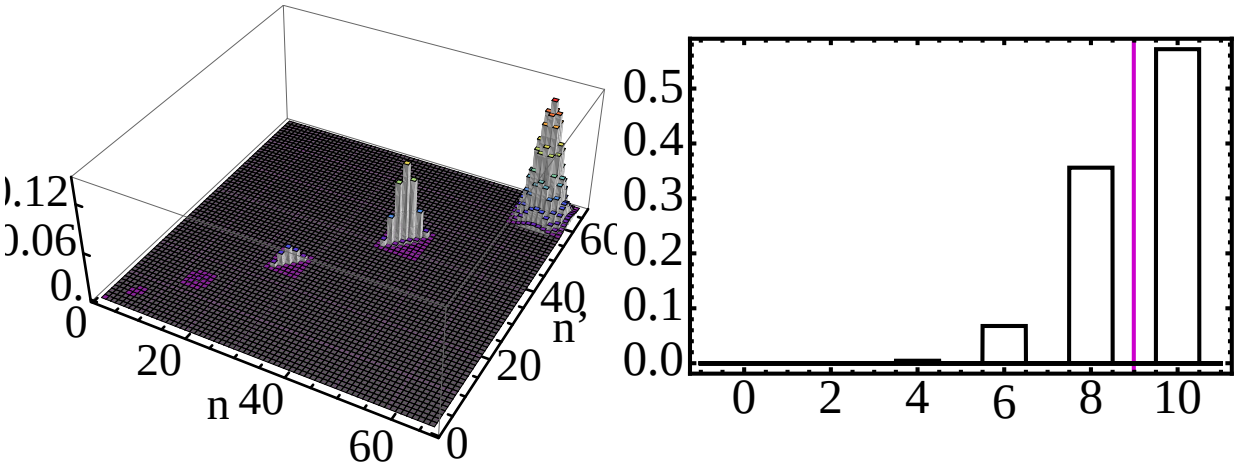

Figure E.3: Density matrix in the Fock basis of the total Hilbert space (left panel), and weigths of the density matrix as a function of the label of the subspace, i.e. the number of particles m (right panel). Values of the parameters: $N = 10$, $\gamma T_{even} N = 0.25$, $U_1 = U_2 = 4\pi\text{Hz}$, $t = t_2$.

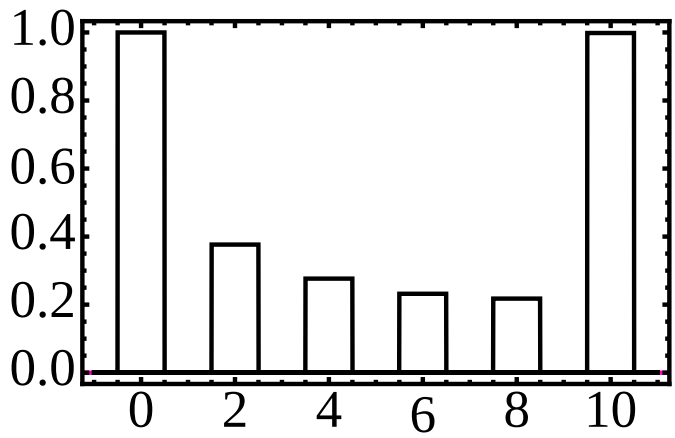

Figure E.4: Fidelity given in Eq.(5.51). The red line corresponds to Eq.(5.52). Values of the parameters: $N = 10$, $\gamma T_{even} N = 0.25$, $U_1 = U_2 = 4\pi$Hz, $t = t_2$.

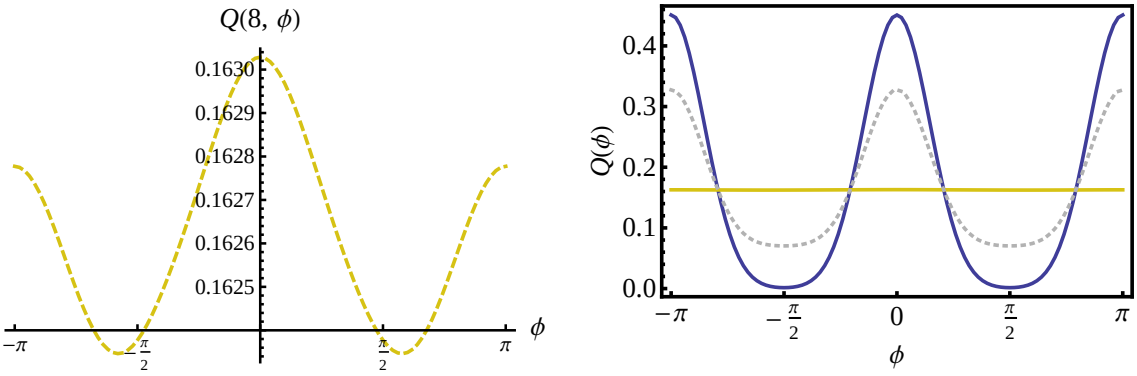

Figure E.5: First panel: Husimi distribution $Q_m(\theta = \pi/2, \phi)$ (see Eq.(5.53)) at $t = t2$ for $m = 8$; second panel: same curve (yellow solid line) superposed to the Husimi function for $m = 10$, i;e. $Q_{10}(\theta = \pi/2, \phi)$ (blue solid line), and to the total Husimi distribution $Q(\theta = \pi/2, \phi)$ (gray dashed line, see Eq.(3.1)). Values of the parameters: $N = 10$, $\gamma T_{even} N = 0.25$, $U_1 = U_2 = 4\pi$Hz, $t = t_2$.

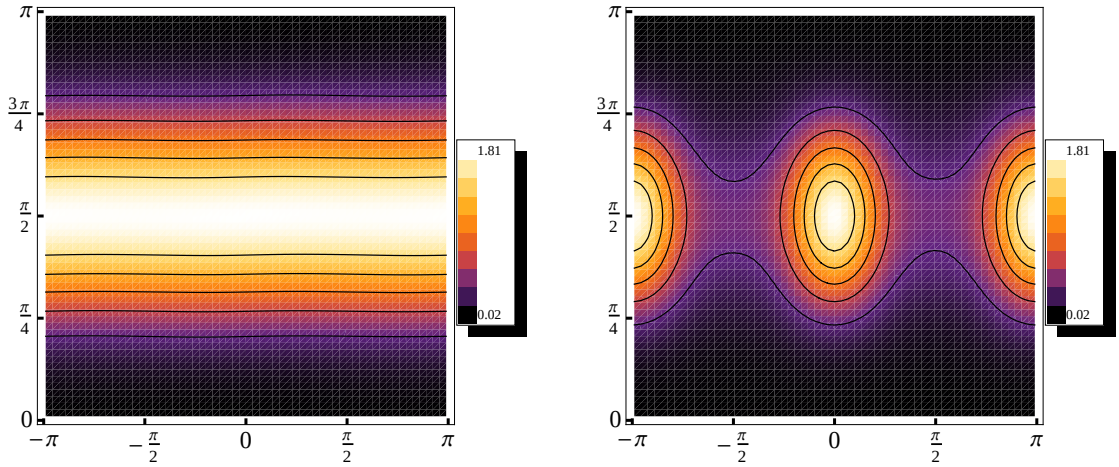

Figure E.6: Husimi distribution $Q_m(\theta, \phi)$ (see Eq.(E.6)) at $t = t_2$ for $m = 8$ (first panel), and total Husimi distribution $Q(\theta, \phi)$ (see Eq.(E.7)). Values of the parameters: $N = 10$, $\gamma T_{even} N = 0.25$, $U_1 = U_2 = 4\pi$Hz, $t = t_2$.

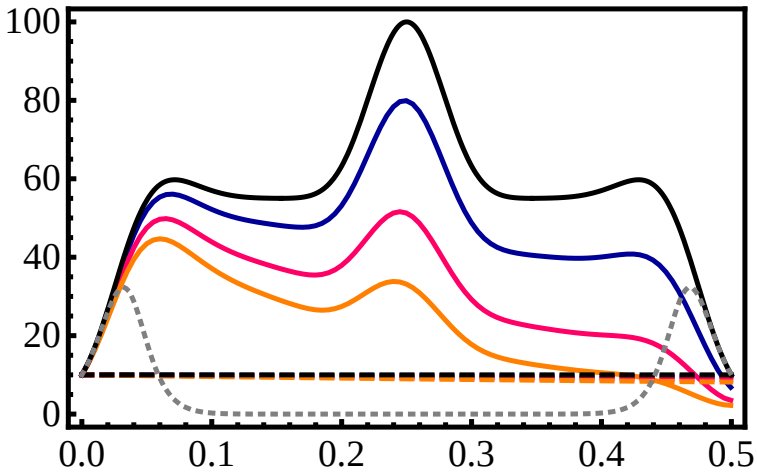

Figure E.7: Fisher information given in Eq.(5.55) optimized over $\hat{J}_{\vec{n}}$ as a function of t/T_{even}, for $\gamma T_{even} N = 0, 0.05, 0.15, 0.25$ from top to bottom. The dashed lines represent the corresponding average number of atoms as a function of time. Black dashed line: shot noise limit N. Values of the parameters: $N = 10$, $U_1 = U_2 = 4\pi$Hz.

Bibliography

[1] I. Lesanovsky and W. Von Klitzing, *Time-Averaged Adiabatic Potentials: Versatile Matter-Wave Guides and Atom Traps*, Phys. Rev. Lett. **99**, 083001 (2007).

[2] J. Fortágh and C. Zimmermann, *Magnetic microtraps for ultracold atoms*, Rev. Mod. Phys. **79**, 235 (2007).

[3] C. Chin, R. Grimm, P. Julienne, and E. Tiesinga, *Feshbach resonances in ultracold gases*, Rev. Mod. Phys. **82**, 1225 (2010).

[4] I. Bloch, J. Dalibard, and W. Zwerger, *Many-body physics with ultracold gases*, Rev. Mod. Phys. **80**, 885 (2008).

[5] W. Wasilewski, K. Jensen, H. Krauter, J. J. Renema, M. V. Balabas, and E. S. Polzik, *Quantum Noise Limited and Entanglement-Assisted Magnetometry*, Phys. Rev. Lett. **104**, 133601 (2010).

[6] J. Appel, P. J. Windpassinger, D. Oblak, U. B. Hoff, N. Kjærgaard, , and E. S. Polzik, *Mesoscopic atomic entanglement for precision measurements beyond the standard quantum limit*, PNAS **106**, 10960 (2009).

[7] M.H. Schleier-Smith, I.D. Leroux, and V. Vuletic, *States of an Ensemble of Two-Level Atoms with Reduced Quantum Uncertainty*, Phys. Rev. Lett. **104**, 073604 (2010).

[8] C. Gross, T. Zibold, E. Nicklas, J. Estève, and M. K. Oberthaler, *Nonlinear atom interferometer surpasses classical precision limit*, Nature **464**, 1165 (2010).

[9] M. F. Riedel, P. Bohi, Y. Li, T. W. Hansch, A. Sinatra, and P. Treutlein, *Atom-chip-based generation of entanglement for quantum metrology*, Nature **464**, 1170 (2010).

[10] J. J. Sakurai. *Meccanica quantistica moderna*. Zanichelli, (2003).

[11] M. Kitagawa and M. Ueda, *Squeezed spin states*, Phys. Rev. A **47**, 5138 (1993).

[12] A. Sørensen, L.-M. Duan, J. I. Cirac, and P. Zoller, *Many-particle entanglement with Bose-Einstein condensates*, Nature **409**, 63 (2001).

[13] J. Estève, C. Gross, A. Weller, S. Giovanazzi, and M. K. Oberthaler, *Squeezing and entanglement in a Bose-Einstein condensate*, Nature **455**, 1216 (2008).

[14] D. J. Wineland, J. J. Bollinger, W. M. Itano, and D. J. Heinzen, *Squeezed atomic states and projection noise in spectroscopy*, Phys. Rev. A **50**, 67 (1994).

[15] V. Giovannetti, S. Lloyd, and L. Maccone, *Quantum Metrology*, Phys. Rev. Lett. **96**, 010401 (2006).

[16] L. Pezzé and A. Smerzi, *Entanglement, Nonlinear Dynamics, and the Heisenberg Limit*, Phys. Rev. Lett. **102**, 100401 (2009).

[17] W. Dür, C. Simon, and J. I. Cirac, *Effective Size of Certain Macroscopic Quantum Superpositions*, Phys. Rev. Lett. **89**, 210402 (2002).

[18] W. Dür and H-J. Briegel, *Stability of Macroscopic Entanglement under Decoherence*, Phys. Rev. Lett. **92**, 180403 (2004).

[19] F. Fröwis and W. Dür, *Stable Macroscopic Quantum Superpositions*, Phys. Rev. Lett. **106**, 110402 (2011).

[20] A. P. Hines, R. McKenzie, and G. J. Milburn, *Entanglement of two-mode Bose-Einstein Condensates*, Phys. Rev. A **67**, 013609 (2003).

[21] T. Hwang, C.-C. Hwang, and C.-M. Li, *Multiparty quantum secret sharing based on GHZ states*, Physica Scripta **83**, 45004 (2011).

[22] A. Sinatra and Y. Castin, *Phase dynamics of Bose-Einstein condensates: Losses versus revivals*, Eur. Phys. J. D **4**, 247 (1998).

[23] Y. Lin, P. Treutlein, J. Reichel, and A. Sinatra, *Spin squeezing in a bimodal condensate: spatial dynamics and particle losses*, Eur. Phys. J. D **68**, 365 (2008).

[24] G. Ferrini, D. Spehner, A. Minguzzi, and F. W. J. Hekking, *Noise in Bose Josephson junctions: Decoherence and phase relaxation*, Phys. Rev. A **82**, 033621 (2010).

[25] G. Ferrini, D. Spehner, A. Minguzzi, and F. W. J. Hekking, *Effect of phase noise on quantum correlations in Bose Josephson junctions*, Phys. Rev. A **84**, 043628 (2011).

[26] J. Anglin, *Cold, Dilute, Trapped Bosons as an Open Quantum System*, Phys. Rev. Lett. **79**, 6 (1997).

[27] D. Witthaut, F. Trimborn, and S. Wimberger, *Dissipation-induced coherence and stochastic resonance of an open two-mode Bose-Einstein condensate*, Phys. Rev. A **79**, 033621 (2009).

[28] Y. P. Huang and M. G. Moore, *Creation, detection and decoherence of macroscopic quantum superposition states in double-well Bose-Einstein condensates*, Phys. Rev. A **73**, 023606 (2006).

[29] M. G. Benedict and A. Czirjàk, *Wigner functions, squeezing properties, and slow decoherence of a mesoscopic superposition of two-level atoms*, Phys. Rev. A **60**, 4034 (1999).

[30] Y. Khodorkovsky, G. Kurizki, and A. Vardi, *Decoherence and entanglement in a bosonic Josephson junction: Bose-enhanced quantum Zeno control of phase diffusion*, Phys. Rev. A **80**, 023609 (2009).

[31] G. Ferrini, A. Minguzzi, and F. W. J. Hekking, *Number squeezing, quantum fluctuations, and oscillations in mesoscopic Bose Josephson junctions*, Phys. Rev. A **78**, 023606 (2008).

[32] G. Ferrini, A. Minguzzi, and F. W. J. Hekking, *Detection of coherent superpositions of phase states by full counting statistics in a Bose Josephson junction*, Phys. Rev. A **80**, 043628 (2009).

[33] M. Lapert, G. Ferrini, and D. Sugny, *Optimal control of quantum superpositions in a bosonic Josephson junction*, arXiv:1106.2316 (2011).

[34] B. D. Josephson, *Possible new effects in superconductive tunnelling*, Phys. Lett. **1**, 251 (1962).

[35] L. P. Pitaevskii and S. Stringari. *Bose-Einstein Condensation.* Oxford University Press, (2003).

[36] M. H. Anderson, J. R. Ensher, M. R. Matthews, C. E. Wieman, and E. A. Cornell, *Observation of Bose-Einstein condensation in a dilute atomic vapor*, Science **269**, 198 (1995).

[37] K. Davis, M. O. Mewes, M. Andrews, N. van Druten, N. Durfee, D. Kurn, and W. Ketterle, *Bose-Einstein Condensation in a Gas of Sodium Atoms*, Phys. Rev. Lett. **75**, 1687 (1995).

[38] C. J. Pethick and H. Smith. *Bose-Einstein condensation in atomic gases.* Cambridge University Press, (2002).

[39] J. Fortágh and C. Zimmermann, *Magnetic microtraps for ultracold atoms*, Rev. Mod. Phys. **79**, 235 (2007).

[40] T. Schumm, S. Hofferberth, L. M. Andersson, S. Wildermuth, S. Groth, I. Bar-Joseph, J. Schmiedmayer, and P. Kruger, *Matter-wave interferometry in a double well on an atom chip*, Nature **1**, 57 (2005).

[41] P. Bohi, M. F. Riedel, J. Hoffrogge, J. Reichel, T. W. Hänsch, and P. Treutlein, *Coherent manipulation of Bose-Einstein condensates with state-dependent microwave potentials*, Nat. Phys. **5**, 592 (2009).

[42] G. Jo, Y. Shin, S. Will, T. A. Pasquini, M. Saba, W. Ketterle, and D. E. Pritchard, *Long phase coherence time and number squeezing of two Bose-Einstein condensates on an atom chip*, Phys. Rev. Lett. **95**, 030407 (2007).

[43] C. A. Regal and D. S. Jin, *Measurement of Positive and Negative Scattering Lengths in a Fermi Gas of Atoms*, Phys. Rev. Lett. **90**, 230404 (2003).

[44] C. A. Regal, M. Greiner, and D. S. Jin, *Observation of Resonance Condensation of Fermionic Atom Pairs*, Phys. Rev. Lett. **92**, 040403 (2004).

[45] L. V. Hau, B. D. Bush, C. Liu, Z. Dutton, M. M. Burns, and J. A. Golovchenko, *Near-resonant spatial images of confined Bose-Einstein condensates in a 4-Dee magnetic bottle*, Phys. Rev. A **58**, R54 (1998).

[46] W. Zhang and L.-M. Duan, *Tomography of correlation functions for ultracold atoms via time-of-flight images*, Phys. Rev. A **80**, 063614 (2009).

[47] J. Javanainen, *Oscillatory exchange of atoms in traps containing Bose Condensates*, Phys. Rev. Lett. **57**, 3164 (1986).

[48] A. Smerzi, S. Fantoni, S. Giovanazzi, and S. R. Shenoy, *Quantum Coherent Atomic Tunneling between Two Trapped Bose-Einstein Condensates*, Phys. Rev. Lett. **79**, 4951 (1997).

[49] S. Raghavan, A. Smerzi, S. Fantoni, and S. R. Shenoy, *Coherent oscillations between two weakly coupled Bose-Einstein Condensates: Josephson effects, π-oscillations, and macroscopic quantum self trapping*, Phys. Rev. A **59**, 620 (1999).

[50] S. Giovanazzi, A. Smerzi, and S. Fantoni, *Josephson Effects in Dilute Bose-Einstein Condensates*, Phys. Rev. A **84**, 4521 (2000).

[51] S. Levy, E. Lahoud, I. Shomroni, and J. Steinhauer, *The a.c. and d.c. Josephson effects in a Bose–Einstein condensate*, Nature **449**, 06186 (2007).

[52] M. Albiez, R. Gati, J. Fölling, S. Hunsmann, M. Cristiani, and M. K. Oberthaler, *Direct Observation of Tunneling and Nonlinear Self-Trapping in a single Bosonic Josephson Junction*, Phys. Rev. Lett. **95**, 010402 (2005).

[53] D. S. Hall, M. R. Matthews, J. R. Ensher, C. E. Wieman, and E. A. Cornell, *Dynamics of Component Separation in a Binary Mixture of Bose-Einstein Condensates*, Phys. Rev. Lett. **1539**, 81 (1998).

[54] L. Pitaeskii and S. Stringari, *Interference of Bose-Einstein Condensates in Momentum Space*, Phys. Rev. Lett. **83**, 4237 (1999).

[55] L. Pitaeskii and S. Stringari, *Thermal vs Quantum Decoherence in Double Well Trapped Bose-Einstein Condensates*, Phys. Rev. Lett. **87**, 180402 (2001).

[56] Y. Castin and J. Dalibard, *Relative phase of two Bose-Einstein condensates*, Phys. Rev. A **55**, 4330 (1997).

[57] R. Gati and M. K. Oberthaler, *A bosonic Josephson junction*, J. Phys. B **40**, 61 (2007).

[58] W. H. Louisell, *Amplitude and phase uncertainty relations*, Phys. Lett. **7**, 60 (1963).

[59] P. Carruthers and M. M. Nieto, *Coherent states and the number-phase uncertainty relation*, Phys. Rev. Lett. **14**, 387 (1965).

[60] R. Lynch, *The quantum phase problem: a critical review*, Phys. Rep. **256**, 367 (1995).

[61] T. Zibold, E. Nicklas, C. Gross, and M. K. Oberthaler, *Classical Bifurcation at the Transition from Rabi to Josephson Dynamics*, Phys. Rev. Lett. **105**, 204101 (2010).

[62] C. Gross. *Ph.D. thesis.* Heidelberg, (2010).

[63] G. J. Milburn, J. Corney, E. M. Wright, and D. F. Walls, *Quantum dynamics of an atomic Bose-Einstein condensate in a double-well potential*, Phys. Rev. A **55**, 4318 (1997).

[64] K. Sakmann, A. I. Streltsov, O. E. Alon, and L. S. Cederbaum, *Exact Quantum dynamics of a Bose Josephson junction*, Phys. Rev. Lett. **103**, 220601 (2009).

[65] K. Sakmann, A. I. Streltsov, O. E. Alon, and L. S. Cederbaum, *Quantum dynamics of attractive versus repulsive bosonic Josephson junctions: Bose-Hubbard and full-Hamiltonian results*, Phys. Rev. A **82**, 013620 (2010).

[66] D. Ciampini, O. Morsch Oliver, and E. Arimondo, *Quantum Control in Strongly Driven Optical Lattices*, International Journal of Quantum Information **9**, 139 (2011).

[67] A. Eckardt, T. Jinasundera, C. Weiss, and M. Holthaus, *Analog of Photon-Assisted tunneling in a Bose-Einstein Condensate*, Phys. Rev. Lett. **95**, 200401 (2005).

[68] H.J. Lipkin, N. Meshkov, and A.J. Glick, *Validity of many-body approximation methods for a solvable model*, Nucl. Phys. **62**, 188 (1965).

[69] S. Ghose, R. Stock, P. Jessen, R. Lal, and A. Silberfarb, *Chaos, entanglement, and decoherence in the quantum kicked top*, Phys. Rev. A **78**, 042318 (2008).

[70] R. W. Spekkens and J. E. Sipe, *Spatial fragmentation of a Bose-Einstein condensate in a double-well potential*, Phys. Rev. A **59**, 3868 (1999).

[71] F. T. Arecchi, E. Courtens, R. Gilmore, and H. Thomas, *Atomic coherent states in quantum optics*, Phys. Rev. A **6**, 2212 (1972).

[72] W-M. Zhang, D. H. Feng, and R. Gilmore, *Coherent states: theory and some applications*, Rev. Mod. Phys. **62**, 867 (1990).

[73] Y. P. Huang and M. G. Moore, *Optimized Double-Well Quantum Interferometry with Gaussian Squeezed States*, Phys. Rev. Lett. **100**, 250406 (2008).

[74] T.Kim, O. Pfister, M. J. Holland, J. Noh, and J. L. Hall, *Influence of decorrelation on Heisenberg-limited interferometry with quantum correlated photons*, Phys. Rev. A **57**, 4004 (1998).

[75] A. J. Leggett, *Bose-Einstein condensation in the alkali gases: Some fundamental concepts*, Rev. Mod. Phys. **73**, 307 (2001).

[76] P. Hyllus, O. Guhne, and A. Smerzi, *Not all pure entangled states are useful for sub-shot-noise interferometry*, Phys. Rev. A **82**, 012337 (2010).

[77] M. P. A. Fisher, P. W. Weichmann, G. Grinstein, and D. S. Fisher, *Boson localization and the superfluid-insulator transition*, Phys. Rev. B **40**, 546 (1989).

[78] S. Sachdev. *Quantum Phase transitions.* Cambridge University Press, (1999).

[79] E. P. Gross, *Structure of a quantized vortex in boson systems*, Il Nuovo cimento **20**, 454 (1961).

[80] L. P. Pitaevskii, *Vortex Lines in an Imperfect Bose Gas*, Soviet Phys. JETP **13**, 451 (1961).

[81] Konstantin K. Likharev. *Dynamics of Josephson Junctions and Circuits.* Gordon and Breach Publishers, (1986).

[82] G. Toth, C. Knapp, O. Gühne, and H. J. Briegel, *Optimal Spin Squeezing Inequalities Detect Bound Entanglement in Spin Models*, Phys. Rev. Lett. **99**, 250405 (2007).

[83] K. Eckert, J. Schliemann, D. Bruß, and M. Lewenstein, *Quantum Correlations in Systems of Indistinguishable Particles*, Ann. Phys. **299**, 88 (2002).

[84] F. Benatti, R. Floreanini, and U. Marzolino, *Sub-shot-noise quantum metrology with entangled identical particles*, Ann. Phys. **325**, 924 (2010).

[85] P. Hyllus, A. Smerzi, D. Schlenk, and H. Weinfurter, *Sub shot-noise phase sensitivity with symmetrization-entanglement*, preprint (2011).

[86] J. K. Korbicz, O. Gühne, M. Lewenstein, H. Häffner, C. F. Roos, and R. Blatt, *Generalized spin-squeezing inequalities in N-qubit systems: Theory and experiment*, Phys. Rev. A **74**, 052319 (2006).

[87] A. Sørensen and K. Mølmer, *Entanglement and extreme spin squeezing*, Phys. Rev. Lett. **86**, 4431 (2001).

[88] G. Vitagliano, P. Hyllus, I. L. Egusquiza, and Geza Toth, *Optimal Spin Squeezing Inequalities Detect Bound Entanglement in Spin Models*, arXiv:1104.3147v1 (2011).

[89] M. A Nielsen and I. L. Chuang. *Quantum Computation and Quantum Information.* Cambridge University Press, (2000).

[90] C. Bodet, J. Estève, M. K. Oberthaler, and T. Gasenzer, *Two-mode Bose gas: Beyond classical squeezing*, Phys. Rev. A **81**, 063605 (2010).

[91] T.-C. Wei and P. M. Goldbart, *Geometric measure of entanglement and applications to bipartite and multipartite quantum states*, Phys. Rev. A **68**, 042307 (2003).

[92] M. Aulbach, D. Markham, and M. Murao, *The maximally entangled symmetric state in terms of the geometric measure*, New J. Phys. **12**, 073025 (2010).

[93] J. Martin, O. Giraud, P. A. Braun, D. Braun, and T. Bastin, *Multiqubit symmetric states with high geometric entanglement*, Phys. Rev. A **81**, 062347 (2010).

[94] W. Dür, G. Vidal, and J. I. Cirac, *Three qubits can be entangled in two inequivalent ways*, Phys. Rev. A **62**, 062314 (2000).

[95] S. Haroche. 4ème leçon du cours 2006-2007. In *Cours au Collège de France, Physique Quantique*.

[96] L. Pezzé, L. A. Collins, A. Smerzi, G. P. Berman, and A. R. Bishop, *Sub-shot-noise phase sensitivity with a Bose-Einstein condensate Mach-Zehnder interferometer*, Phys. Rev. A **72**, 043612 (2005).

[97] C. Menotti, J. R. Anglin, J. I. Cirac, and P. Zoller, *Dynamic splitting of a Bose-Einstein condensate*, Phys. Rev. A **63**, 023601 (2001).

[98] J. I. Cirac, M. Lewenstein, K. Mølmer, and P. Zoller, *Quantum superposition states of Bose-Einstein condensates*, Phys. Rev. A **57**, 1208 (1998).

[99] T-L. Ho and C. V. Ciobanu, *The Schrödinger Cat Family in Attractive Bose Gases*, J. Low Temp. Phys. **135**, 257 (2004).

[100] M. Kitagawa et Y. Yamamoto, *Number-phase minimum-uncertainty state with reduced number uncertainty in a Kerr nonlinear interferometer*, Phys. Rev. A **34**, 3974 (1986).

[101] F. Piazza, L. Pezzé, and A. Smerzi, *Macroscopic superpositions of phase states with Bose-Einstein condensates*, Phys. Rev. A **78**, 051601(R) (2008).

[102] B. Yurke and D. Stoler, *Generating Quantum Mechanical Superpositions of Macroscopically Distinguishable States via Amplitude Dispersion*, Phys. Rev. Lett. **57**, 13 (1986).

[103] C. C. Gerry, *Schrödinger cat states in a Josephson junction*, Phys. Rev. B **57**, 7474 (1997).

[104] M. W. Jack, *Effect of atom loss on collapse and revivals of phase coherence in small atomic samples*, Phys. Rev. A **67**, 043612 (2003).

[105] G. S. Agarwal, R. R. Puri, and R. P. Singh, *Atomic Schrödinger cat states*, Phys. Rev. A **56**, 2249 (1997).

[106] C. Weiss and N. Teichmann, *Differences between Mean-Field Dynamics and N-particle Quantum Dynamcis as a Signature of Entanglement*, Phys. Rev. Lett. **100**, 140408 (2008).

[107] V. O. Nesterenko, A. N. Novikov, A. Y. Cherny, F. F. de Souza-Cruz, and E. Suraud, *An adiabatic transport of Bose–Einstein condensates in double-well traps*, J.Phys.B: At. Mol. Opt. Phys. **42**, 235303 (2009).

[108] A. Micheli, D. Jaksch, J. I. Cirac, and P. Zoller, *Many-particle entanglement in two-component Bose-Einstein condensates*, Phys. Rev. A **67**, 013607 (2003).

[109] U. Boscain and B. Piccoli. *Optimal syntheses for control systems on 2-D manifolds*. Springer-Verlag, Berlin, (2004).

[110] J. Werschnik and E. K. U. Gross, *Quantum optimal control theory*, J. Phys. B: At. Mol. Opt. Phys. **40**, 175 (2007).

[111] R. Gilmore. Wigner distribution on su(2). In *Lecture Notes in Physics, 278, pag.211.* Springer, (1987).

[112] M. O. Scully and K. Wódkiewicz, *Spin Quasi-distribution Functions*, Foundation of Physics **24**, 85 (1994).

[113] J. P. Dowling, G. S. Agarwal, and W. P. Schleich, *Wigner distribution of a general angular-momentum state: Applications to a collection of two-level atoms*, Phys. Rev. A **49**, 4101 (1994).

[114] S. M. Chumakov, A. B. Klimov, and K. B. Wolf, *Connection between two Wigner functions for spin systems*, Phys. Rev. A **61**, 034101 (2000).

[115] R. Schmied and P. Treutlein, *Tomographic reconstruction of the Wigner function on the Bloch sphere*, arXiv:1101.4131 (2011).

[116] S. M. Chumakov, A. Frank, and K. B. Wolf, *Finite Kerr medium: Macroscopic quantum superposition states and Wigner functions on a sphere*, Phys. Rev. A **60**, 1817 (1999).

[117] C.-W. Lee and H. Jeong, *Quantification of Macroscopic Quantum Superpositions within Phase Space*, Phys. Rev. Lett. **106**, 220401 (2011).

[118] J. Gong, *Comment on "Quantification of Macroscopic Quantum Superpositions within Phase Space"*, arXiv:1106.0062v2 (2011).

[119] A. Kenfack and K. Zyczkowski, *Negativity of the Wigner function as an indicator of non-classicality*, J. Opt. B: Quantum Semiclass. Opt. **6**, 396 (2004).

[120] A. Biswas and G. S. Agarwal, *Non-classicality and decoherence of photon subtracted squeezed states*, Phys. Rev. A **75**, 032104 (2007).

[121] W. Schleich, M. Pernigo, and F. Le Kien, *Non-classical states from two pseudo-classical states*, Phys. Rev. A **44**, 2172 (1991).

[122] R. L. Hudson, *When is the Wigner quasi-probability density non-negative?*, Rep. Math Phys. **6**, 249 (1974).

[123] M. S. Kim, E. Park, P. L. Knight, and H. Jeong, *Non-classicality of a photon-subtracted gaussian field*, Phys. Rev. A **71**, 043805 (2005).

[124] W. Vogel, *Non-classical states: an observable criterion*, Phys. Rev. Lett. **84**, 1849 (2000).

[125] T. Richter and W. Vogel, *Observing the non-classicality of a quantum state*, Journal Opt. B: Quantum Semiclass. Opt. **5**, 371 (2003).

[126] L. E. Reichl. *A modern course in Statistical Physics.* Cambridge University Press, (1984).

[127] B. C. Sanders, *Quantum dynamics of the non-linear rotator and the effect of continual spin measurement*, Phys. Rev. A **40**, 2417 (1989).

[128] T. J. Haigh, A. J. Ferris, and K. K. Olsen, *Demonstrating mesoscopic superpositions in double-well Bose-Einstein condensates*, Opt. Comm. **283**, 3540 (2010).

[129] F. Natterer. *The Mathematics of Computerized Tomography.* Wiley-Chichester, (1986).

[130] E. W. Weisstein. Radon transform. In *From MathWorld–A Wolfram Web Resource. http://mathworld.wolfram.com/RadonTransform.html.* (1987).

[131] G. M. D'Ariano, M. G. A. Paris, and M. F. Sacchi, *Quantum Tomography*, arXiv:quant-ph/0302028v1 (2003).

[132] K. Vogel and H. Risken, *Determination of quasiprobability distributions in terms of probability distributions for the rotated quadrature phase*, Phys. Rev. A **40**, 2847 (1989).

[133] S. Deléglise, I. Dotsenko, C. Sayrin, J. Bernu, M. Brune, J.-M. Raimond, and S. Haroche, *Reconstruction of non-classical cavity field states with snapshots of their decoherence*, Nature **455**, 510 (2008).

[134] G. M. D'Ariano, *Universal quantum estimation*, Phys. Lett. A **268**, 151 (2000).

[135] S. Haroche and J. M. Raimond. *Exploring the quantum*. Oxford Graduate texts, (2008).

[136] A. D. Cronin, J. Schmiedmayer, and D. E. Pritchard, *Atom Interferometers*, Rev. Mod. Phys. **81**, 1051 (2009).

[137] J. Grond, U. Hohenester, J. Schmiedmayer, and A. Smerzi, *Mach-Zehnder interferometry with interacting trapped Bose-Einstein condensates*, arXiv:1010.3273 (2010).

[138] I. Tikhonenkov, M. G. Moore, and A. Vardi, *Optimal Gaussian squeezed states for atom interferometry in the presence of phase diffusion*, Phys. Rev. A **82**, 043624 (2010).

[139] L. Pezzé, A. Smerzi, G. Khoury, J. F. Hodelin, and D. Bouwmeester, *Phase detection at the quantum limit with multiphoton Mach-Zender Interferometry*, Phys. Rev. Lett. **99**, 223602 (2007).

[140] S. L. Braunstein and C. M. Caves, *Statistical Distance and the Geometry of Quantum States*, Phys. Rev. Lett. **72**, 3439 (1994).

[141] S. L. Braunstein, C. M. Caves, and G. J. Milburn, *Generalized Uncertainty Relations: Theory, Examples, and Lorentz Invariance*, Ann. Phys. **247**, 135 (1996).

[142] A. Uhlmann, *The Transition Probability in the State Space of a *-Algebra*, Rep. Math. Phys. **9**, 273 (1976).

[143] A. Smerzi, *Zeno Dynamics and Distinguishability of Quantum States*, arXiv:1002.2760v1 (2010).

[144] R. Horodecki, P. Horodecki, M. Horodecki, and K. Horodecki, *Quantum entanglement*, Rev. Mod. Phys. **81**, 865 (2009).

[145] V. Giovannetti, S. Lloyd, and L. Maccone, *Advances in Quantum Metrology*, arXiv:1102.2318 (2011).

[146] P. Hyllus. *Private communication*.

[147] S. M. Giampaolo, G. Adesso, and F. Illuminati, *Separability and ground-state factorization in quantum spin systems*, Phys. Rev. B **79**, 224434 (2009).

[148] L. Amico and R. Fazio, *Entanglement and magnetic order*, J. Phys. A: Math. Theor. **42**, 504001 (2009).

[149] P. Zanardi, L. Campos Venuti, and P. Giorda, *Bures metric over thermal state manifolds and quantum criticality*, Phys. Rev. A **76**, 062318 (2007).

[150] G. Mazzarella, L. Salasnich, A. Parola, and F. Toigo, *Coherence and entanglement in the ground state of a bosonic Josephson junction: From macroscopic Schrödinger cat states to separable Fock states*, Phys. Rev. A **83**, 053607 (2011).

[151] J. Ma and X. Wang, *Fisher information and spin squeezing in the Lipkin-Meshkov-Glick model*, Phys. Rev. A **80**, 012318 (2009).

[152] R. Orùs, S. Dusuel, and J. Vidal, *Equivalence of Critical scaling laws for many-body entanglement in the Lipkin-Meshkov-Glick model*, Phys. Rev. Lett. **101**, 025701 (2008).

[153] U. Dorner, *Quantum frequency estimation with trapped ions and atoms*, arXiv:1102.1361 (2011).

[154] L. Viola and S. Lloyd, *Dynamical suppression of decoherence in two-state quantum systems*, Phys. Rev. A **58**, 2733 (1998).

[155] E. Joos, H. D. Zeh, C. Kiefer, D. Giulini, J. Kupsch, and I.-O. Stamatescu. *Decoherence and the appearance of a Classical World in Quantum Theory.* Springer, (1996).

[156] M. Abramowitz and I. A. Stegun. *Handbook of mathematical functions.* Dover, (1972).

[157] A. Widera, Fabrice Gerbier, Simon Fölling, Tatjana Gericke, Olaf Mandel, and Immanuel Bloch, *Coherent collisional spin dynamics in optical lattices*, Phys. Rev. Lett. **95**, 190405 (2005).

[158] D. M. Stamper-Kurn, M.R. Andrews, A.P. Chikkatur, S. Inouye, H.-J. Miesner, J. Stenger, and W. Ketterle, *Optical Confinement of a Bose-Einstein Condensate*, Phys. Rev. Lett. **80**, 2027 (1998).

[159] M. W. Jack, *Decoherence due to Three-Body Loss and its Effect on the State of a Bose-Einstein Condensate*, Phys. Rev. Lett. **89**, 140402 (2002).

[160] A. Sinatra and Y. Castin, *Phase dynamics of Bose-Einstein condensates: Losses versus revivals*, Eur. Phys. J. D **4**, 247 (1998).

[161] E. A. Burt, R. W. Ghrist, C. J. Myatt, M. J. Holland, E. A. Cornell, and C. E. Wiemann, *Coherence, Correlations, and Collisions: What One Learns about Bose-Einstein Condensates from Their Decay*, Phys. Rev. Lett. **79**, 337 (1997).

[162] K. Pawlovski and K. Rzazewski, *Background atoms and decoherence in optical lattices*, Phys. Rev. A **81**, 013620 (2010).

[163] K. Pawlovski, *Unpublished*, (2011).

[164] Y. Lin, Y. Castin, and A. Sinatra, *Optimum Spin squeezing in Bose-Einstein Condensates with particle losses*, Phys. Rev. Lett. **100**, 210401 (2008).

[165] P. Hyllus, L. Pezzé, and A. Smerzi, *Entanglement and sensitivity in Precision Measurements with States of a Fluctuating Number of Particles*, Phys. Rev. Lett. **105**, 120501 (2010).

[166] R. Bach and K. Rzazewski, *Correlations in Atomic Systems: Diagnosing Coherent Superpositions*, Phys. Rev. Lett. **92**, 200401 (2004).

[167] J. Javanainen, *Quantum Phase of a Bose-Einstein Condensate with an arbitrary number of atoms*, Phys. Rev. Lett. **76**, 161 (1996).

[168] C. Gross. *Private communication.*

[169] Y. Hao and Q. Gu, *Dynamics of two-components Bose-Einstein condensates coupled with the environment*, Phys. Rev. A **83**, 043620 (2011).

[170] M. Greiner, O. Mandel, T. W. Hansch, and I. Bloch, *Collapse and revival of the matter wave field of a Bose–Einstein condensate*, Nature **419**, 51 (2002).

[171] N. Bar-Gill, C. Gross, I. Mazets, M. Oberthaler, and G. Kurizki, *Einstein-Podolsky-Rosen correlations of ultracold atomic gases.*, Phys. Rev. Lett. **106**, 120404 (2011).

[172] Q. Y. He, M. D. Reid, T. G. Vaughan, C. Gross, M. Oberthaler, and P. D. Drummond, *Einstein-Podolsky-Rosen Entanglement Strategies in Two-Well Bose-Einstein Condensates*, Phys. Rev. Lett. **106**, 120405 (2011).

[173] A. Sinatra, E. Witkowska, J.-C. Dornstetter, Y. Lin, and Y. Castin, *Limit of spin squeezing in finite temperature Bose-Einstein condensates*, arXiv:1104.1871 (2011).

[174] K. Molmer, Y. Castin, and J. Dalibard, *Monte Carlo wave-function method in quantum optics*, J. Opt. Soc. Am. B **10**, 524 (1993).

Thanks to...

First, I would like to thank all the members of the jury of my defense. Thanks to Wiebke Guichard, for having accepted to be the president of the jury during my defense. I especially would like to thank Augusto Smerzi for having revised my manuscript, for all the discussions that we had, and for his encouragements. His work is a strong source of motivation and inspiration to me, and I strongly hope that we will have more scientific exchanges and collaborations in the future! Then, I would like to warmly thank Nicolas Pavloff for having accepted to revise my manuscript, despite the subject was not precisely within his own interests. I have really appreciated this, as well as the quality of his revision. I thank Claude Fabre for having been an examinator of my defense and, together with Nicolas Treps and all their team, for the wonderful reception which I have found at my arrival in the LKB.

In these years I had the chance to meet and to be supported by several wonderful persons; I would like to take the occasion to sincerely thank them.

I start with my supervisors, Anna Minguzzi and Frank W.J. Hekking. They have been two exceptional supervisors. Both of them are models to me and I highly esteem them, both as scientists and as persons. I would especially like to thank them for having always supported and encouraged me, despite my often pessimistic attitude and my limits. They have always been extremely generous, literally spoiling me, and offering me the occasion to travel around Europe for a long list of conferences, in which they have always encouraged me to present my (our) results. Among the other things, I would like to thank them also for the help with the writing of the manuscript of the thesis and of our last paper.

Then I would like to thank Dominique Spehner for the exciting experience of my first fruitful scientific collaboration, and for his generosity in according to me several interesting and precise explanations. He has also always encouraged and supported me and he has been always extremely willing to help me. He is a model to me for his versatility, being interested both in mathematical and experimental aspects of physics, and for his rigour.

I would then like to thank Dominique Sugny and Marc Lapert because they have been confident on me, accepting to work together, and for all the work that they have done on our common project. I have really enjoyed the collaboration with them.

I also would like to thank Krzysiek Pawlowski, who has been especially kind to me and so enthusiastic about our collaboration.

Thanks to Frédéric Faure for his generosity in many explanations at the beginning of my phd.

Thanks to Pu Jian for the corrections of the french translations contained in this manuscript, and for her kindness and help.

Then, I would like to thank some of the exceptional persons which I have met along during the conferences. A huge thank to Christian Gross, who has been so kind in providing me with so many explanations about experimental (and unfortunately, even theoretical, sigh!!) aspects of the BJJ. He is an exceptional scientist and I hope I will have other occasions to discuss physics with him. Many thanks to Philipp Hyllus, who has also been extremely helpful with his several interesting, precise and timely explanations, and with whom it has been nice to share some very nice moment around. Thanks also to Alessio Recati, Paolo Zanardi, Marietta Pezzoli, which was a pleasure to meet. A sincere thank to Jan Chwedenczuk for his kindness and his hospitality! ...and a fond thank to Armand Niederberger, to whom I ought even more than an explanation in physics.

I would also like to thank all the people in the LPMMC who have made pleasant my stay there. A huge thank to Jean Daniel and Françoise, always extremely helpful, kind and efficient in solving my several informatic problems. Thanks to Laurence and Michelle for all the practical help and for her kindness. Thanks to Sandrine, both for the help with the "école doctorale" bureaucracy, and for the nice moments spent together outside!

Among all the members of the lab, I would especially like to thank the others phd students, with which I have shared the office and many nice moments: thank to Nicolas Pauget for the wonderful dinners he prepared us. Thanks to Nicolas Didier for being a dear friend (even if for sure I cannot thank him for listening to my stories... :P). I would like to thank Arthur Goetschy for the help with more french translations (among which the summary in the back page of the manuscript), the daily help and support and for all the stories he told me, which opened up my mind!

I would like to thank all my friends in Grenoble: Lise, Laurent, Simon, Guillaume, Hélène... for all the nice time spent together. Thanks to Valeria and Khaldoun too, the good times are going on in Paris now!

Special thanks to our genoan friends, my "Magister" Alessandro Gaddalella Cartapeta, whose intelligence and rationality is a guide for me since almost 15 years! Thanks to Elena, Giulia, Patty, Pippo, Giorgio, Giulia Bista, Gigi, Romina, Carlotta... and all the other friends with which is wonderful to keep in touch along the path, despite the kilometers separating us. I am proud of all of them for the great job that each of them is doing, in the respective fields.

Thanks to Chiara, Tessa and Lara, close friends since many, many years, even if not always "close" in the geographical sense. At least at the moment we are in the same country! It's always a pleasure to meet them, either in Italy or in France.

The warmest thank to Melisdjane; she is in my highest esteem, and she deeply influenced and inspired me. Thanks for offering me the skirt "which every girl would desire"!

Thanks to my family for the support, especially to my sister Anna and to dad. Thanks to zio Mario for the wonderful party after the defense!

Finally, thanks to Ale, my "Cic", for loving me and for taking so much care of me since almost 9 years.

MACROSCOPIC QUANTUM COHERENT PHENOMENA IN BOSE JOSEPHSON JUNCTIONS

In recent years, cold atomic systems have been recognized as very promising tools for quantum simulators and for applications in quantum technology. In particular, a Bose Josephson junction (BJJ) - a system of ultracold dilute bosons which can occupy two modes - has been used to realize an atomic interferometer, allowing to estimate a phase shift with a precision beyond the classical limit. In this thesis we study theoretically the production, detection and decoherence of entangled states which can be used for high-precision interferometry in a Bose Josephson junction. Among such useful quantum states are atomic squeezed states and macroscopic superpositions of coherent states. In the first part of the thesis, after demonstrating that macroscopic superpositions of coherent states can be created during the dynamics following a "quench" of the coupling between the two modes of the junction, we study protocols for their experimental detection. In the experiments there are unavoidable sources of noise, the major sources being phase noise, induced by stochastic fluctuations of the energies of the two modes of the BJJ, and particle losses. The presence of noise induces decoherence and degrades the quantum correlations of these states. In the second part of the thesis we analyze in detail how the useful quantum correlations of squeezed states and macroscopic superpositions are degraded by phase noise. We show that for moderate phase noise intensities multicomponent superpositions of coherent states are interesting candidates for high-precision atom interferometry. Finally, we address the effect of atom losses on the formation of macroscopic superpositions, showing how decoherence affects the system density matrix.

EFFETS DE COHÉRENCE QUANTIQUE MACROSCOPIQUE DANS LES JONCTIONS JOSEPHSON BOSONIQUES

Dans les annés récentes, les systèmes d'atomes froids ont été reconnus comme des candidats prometteurs pour réaliser des simulateurs quantiques, ainsi que pour différentes applications en information quantique. Dans cette perspective, la jonction Josephson bosonique, un système de bosons ultrafroids dilués qui peuvent occuper deux modes, a été employée pour réaliser un interféromètre atomique, qui a permit d' estimer un déphasage avec une précision allant au delà de la limite classique. Dans cette thèse nous étudions d'un point de vue théorique la production, la détection et la décohérence d'états intriqués qui peuvent être utilisés pour l'interférométrie de haute précision dans une jonction Josephson bosonique. Parmi ces états quantiques utiles se trouvent les états comprimés et les superpositions macroscopiques d'états cohérents. Dans la première partie du manuscrit, nous démontrons que les superpositions macroscopiques d'états cohérents peuvent être crées pendant la dynamique qui suit un arrêt soudain du couplage entre les deux modes de la jonction, puis nous étudions des protocoles de détection expérimentale. Les expériences souffrent inévitablement de sources de bruit, les principaux étant le bruit de phase, induit par des fluctuations des énergies des deux modes, et la perte d'atomes. La présence de bruit induit de la décohérence et dégrade les corrélations quantiques des états manipulés. Dans la deuxième partie du manuscrit, nous analysons en détail comment les corrélations quantiques utiles des états comprimés et des superpositions macroscopiques sont dégradées par le bruit de phase. Nous montrons que, pour des intensités de bruit modérées, les superpositions d'états cohérents formées de nombreuses composantes sont des candidates intéressantes pour l'interférométrie de précision. Enfin, nous étudions l'effet de la perte d'atomes sur la formation des superpositions macroscopiques, en montrant comment la décohérence agit sur la matrice densité du système.